Maryland Sea Grant Research Experiences for Undergraduates

Final Student Papers Summer 2018

Edited by
Mike Allen and Olivia Isaacs

Sponsored by
Maryland Sea Grant

Maryland Sea Grant College
Publication number UM-SG-TS-2018-02

Copies of this publication are available from:

Maryland Sea Grant College Program
4321 Hartwick Road, Suite 300
College Park, MD 20740

For more information, visit the Maryland Sea Grant web site:
http://www.mdsg.umd.edu/

This publication, produced by the Maryland Sea Grant College Program, is a compilation of the final REU student fellow papers produced for summer 2018.

This report was prepared under awards OCE-1756244 from the National Science Foundation and NA18OAR4170070 from the National Oceanic and Atmospheric Administration, U.S. Department of Commerce. The statements, findings, conclusions and recommendations are those of the author(s) and do not necessarily reflect the views of Maryland Sea Grant, the National Science Foundation, the National Oceanic and Atmospheric Administration or U.S. Department of Commerce.

Contents

Contents..... 2

Chesapeake Biological Laboratory

Acoustical analysis of bottlenose dolphin signature whistles off Ocean City, Maryland..... 5
Elizabeth Grzyb, REU Fellow
Mentor: Helen Bailey, Research Associate Professor

Viability of Epinephrine as an Inducer of Metamorphosis on the Oyster *Crassostrea virginica*..... 25
Justin Guider, REU Fellow
Mentor: Carys Mitchelmore, Professor

Quantifying energetics and scope for growth of different strains of the Eastern Oyster, *Crassostrea virginica*..... 49
Hannah Haskell, REU Fellow
Mentor: Thomas Miller, Professor and Director

Greenhouse gas release from permafrost soil incubations under aerobic and anaerobic conditions at relevant soil temperatures..... 59
Lillian Henderson, REU Fellow
Mentor: Laura Lapham, Associate Professor

Sargassum as an Important Source of Methylmercury in Aquatic Systems..... 76
Kenna D. Leonzo, REU Fellow
Mentor: Andrew Heyes, Associate Research Professor

Photochemical ammonium production from dissolved organic matter in anthropogenic, freshwater, and estuarine sources……..... 88
Shirley Ma, REU Fellow
Mentor: Michael Gonsior, Associate Professor & Leanne Powers, Assistant Research Scientist

Extracting Microplastics in Archived Sediment Samples from Baltimore Harbor..... 111
Katherine Mitchell, REU Fellow
Mentor: Johan Schijf, Associate Professor

Impacts of Oxygen Depletion on Phosphorus Cycling in Rock Creek, an Aerated Tidal Tributary of the Patapsco River.....123
Curtis Szewczyk, REU Fellow
Mentor: Jeremy Testa, Assistant Professor

Horn Point Laboratory

Inducing Mixotrophy in the Dinoflagellate *Heterocapsa rotundata*.....147
Alexius Dingle, REU Fellow
Mentor: Emily Brownlee, Postdoctoral Researcher & Sairah Malkin, Assistant Professor

Examining the Effects of 3-D Reef Structures on the Mixing and Reaeration of Hypoxic Waters.....157
Ella A. Kaplan, REU Fellow
Mentor: Larry Sanford, Professor

Coupling Plastic Degradation with Coastal Processes…………………..……………....................... 177
Benjamin William Stalheim Lane, REU Fellow
Mentor: William Nardin, Assistant Professor & Corinne Corbau, Visiting Scholar

Tracking microbial contaminants in Baltimore Harbor: Are current techniques sufficient for assessing human risk?.. 192
Norberto Latorre Arzola, REU Fellow
Mentor: Judith O'Neil, Associate Research Professor

Relationships among sediments, nutrients, and submersed aquatic vegetation in Upper Chesapeake Bay……………………………………………………………………………………………………… 224
Margaret Martinez, REU Fellow
Mentor: Cindy Palinkas, Associate Professor

Evaluating the effect of nutrient enrichment on phytoplankton growth rate in the Chesapeake Bay……………………………………………………………………………..………………….. 237
Kristin Ratliff, REU Fellow
Mentor: Greg Silsbe, Assistant Research Professor

Statistically Downscaling the Community Climate Systems 4 Global Climate Model to Project Hypoxia in the Chesapeake Bay……………………………………………………………………………...... 252
Samantha Roth, REU Fellow
Mentor: Ming Li, Professor & Wenfei Ni, Graduate Assistant & Andrew C. Ross, Postdoctoral Research Associate

A deployable sutonomous CO2 sensor (DACS): Improving pCO2 spatial resolution in Chesapeake Bay, Maryland.. 276
Victoria Williams, REU Fellow
Mentor: Matthew Gray, Associate Professor

University of Maryland
Center for Environmental Science
Chesapeake Biological Laboratory

Acoustical analysis of bottlenose dolphin signature whistles off Ocean City, Maryland

Elizabeth Grzyb, REU Fellow
Maryland Sea Grant

Helen Bailey, Research Associate Professor
Chesapeake Biological Laboratory, University of Maryland Center for Environmental Science

Abstract

The common bottlenose dolphin, *Tursiops truncatus,* is a highly social and vocal species that uses a variety of acoustic signals to aid communication, foraging, and orientation. Bottlenose dolphins have the ability to convey identity information via signature whistles—an individually specific whistle that is unique to individual dolphins. These bottlenose dolphin signature whistles play a similar role in identity communication as unique names for individual humans. Based on a bout analysis method of signature whistle identification, we identified signature whistles in audio recordings collected via passive acoustic monitoring between July 2016 and October 2017 off Ocean City, Maryland, U.S.A., within a proposed wind energy area. Through signature whistle analysis we estimated the minimum abundance of dolphins within our detection area as 174 dolphins with the highest number in summer 2016 and the most frequent re-occurrence of individuals during winter 2017. These results can be used to inform assessments of the potential exposure of bottlenose dolphins to high levels of noise associated with offshore wind farm construction.

Introduction

Water restricts the propagation of light, limiting visual communication in the underwater environment. As a result, many cetaceans (whales, dolphins, and porpoises) rely on acoustic signals for communication (Kishida et al. 2007). In contrast to light, sound waves travel more quickly and effectively through water than through air, making acoustic signals a good alternative to visual communication. One of the most studied cetacean species, the common bottlenose dolphin *Tursiops truncatus* uses a variety of acoustic signals in the form of clicks, whistles, and buzzes to aid in orientation, foraging, and social communication. Bottlenose dolphins have the additional ability to encode individual identity information through the frequency modulation patterns of their whistles (Janik 2009).

These frequency-modulated whistles, known as signature whistles, are unique to each individual bottlenose dolphin. Signature whistles are developed early in the dolphin's life as a means of communicating identity and maintaining group cohesion (Deecke and Janik 2006). Once a calf develops its own signature whistle, the whistle remains stable for many years, if not the rest of the dolphin's life (Sayigh et al. 1990). Previous researchers have found that the identity information of these whistles is independent of individual vocal characteristics because other bottlenose dolphins will repeat the signature whistles of conspecifics (Quick and Janik

2012). This suggests that dolphins can refer to other dolphins by imitating their whistles. In the wild, almost half of all whistles emitted by bottlenose dolphins can be classified as signature whistles (Buckstaff 2004). The frequency of occurrence of these whistles increases upon meeting other dolphins and during periods of separation from other individuals (Quick and Janik 2012).

In the North Atlantic Ocean along the Eastern coast of the United States, the coastal morphotype of bottlenose dolphin populating the region from Florida to New Jersey can be categorized into five different stocks based on geographic location (Waring et al. 2014). The Northern migratory coastal stock, which this study focuses on, migrates seasonally between the mouth of the Chesapeake Bay and Long Island in the summer, and the region between southern North Carolina and southern Virginia in the winter. This stock of bottlenose dolphins has been depleted partially due to an epizootic in the 1980s, and is now considered a strategic stock under the Marine Mammal Protection Act (Waring et al. 2014). In the past, researchers have monitored the movement, activity, and seasonal migration of these dolphins via photo identification (Janik 2000), genetic analysis (Rosel et al. 2009), and satellite telemetry (Waring et al. 2014). As more research has been done on the properties of the unique signature whistles emitted by dolphins, it may now be possible to monitor movement, activity, and population structure from audio recordings of signature whistles.

The process of autonomous recording is known as passive acoustic monitoring. This powerful tool allows for ocean monitoring at all times of day and year in all conditions. Submersible acoustic monitoring units consist of two main components: a transducer in the form of a hydrophone to convert acoustic sound waves into electrical signals, and a recording unit to convert the electrical signals into digital information to be stored on a storage device (Rumsey and McCormick 2010). A submersible unit can stay in the ocean unattended for weeks to months at a time. By deploying passive acoustic recorders over multiple years, researchers can create a long-term monitoring network that would be difficult to achieve with other methods (Davis et al. 2017).

Previous studies have used underwater recording and analysis methods to successfully identify signature whistles (Sayigh et al. 1990; Deecke and Janik 2006; Quick and Janik 2012; Gridley et al. 2014). By applying signature whistle identification methods described in these studies to long term passive acoustic data sets, it may be possible to monitor dolphins over long periods of time. This acoustic analysis gives insights into the movement, population, and frequency of occurrence of individuals within the detection area, and allows for any changes to be tracked over time.

Using signature whistle identification methods as described by Janik (2006), the goal of this study was to analyze acoustic data collected off the coast of Ocean City, Maryland between July 2016 and September 2017 to provide information about individual dolphin occurrence within that timeframe. An offshore wind farm site has been proposed for construction in this area by 2020. This study could aid in the environmental assessment of the potential exposure of dolphins to loud noises and increased vessel traffic that would occur as a result of constructing an offshore wind farm. From analyzing bottlenose dolphin signature whistles from acoustic data, we aimed to:

- Determine the number of unique signature whistles collected via passive acoustic monitoring to estimate the number of dolphins in the detection area over the time span July 2016 to September 2017.

- Determine how frequently individual dolphins visit our study area based on matching identical signature whistles during our acoustic recording time series to identify whether there is site fidelity.

- Determine whether the same dolphins are returning to this site every year and amongst seasons by comparing signature whistles from 2016 and 2017 during summer and winter.

Materials and Methods

Data Collection

The northern migratory coastal stock of bottlenose dolphins reside in areas up to 40 kilometers offshore at depths between 20 and 40 meters (Garrison et al. 2002). This migratory path includes the proposed wind energy area off Ocean City, Maryland. In the summer of 2016 between July 27th, and September 24th, an SM3M submersible acoustic recorder was deployed 27 meters below the ocean surface, 30 kilometers off the coast of Ocean City, Maryland at a latitude and longitude of 38.336° N, 74.722° W (Figure 1). Two additional deployments at this site occurred during the winter of 2017 on 11th January to 5th April, and the summer of 2017 on 7th June to 2nd October.

For the deployments, the SM3M was configured to have a sensitivity of -165 dB re 1V/µPa, a preamplifier gain of 12dB, a recording bit depth of 16 bit, and a peak to peak voltage range of 1.9997 V. The recording sampling rate was set to 48kHz, with a duty cycle of 2 minutes on, 4 minutes off during the first deployment and 5 minutes on, 10 minutes off in the subsequent deployments. Bottlenose dolphin's signature whistles occur at frequencies between 1kHz and 27.3kHz (Buckstaff 2004; Esch et al. 2009), and it was important to use a sampling rate that would be capable of recording within that frequency range. By using a sampling rate of 48kHz, sounds up to 24kHz could be captured on the recordings. In general when recording audio, the higher the sampling rate, the more digital storage space and battery power the recording will require (Rumsey and McCormick 2010). To offset high sampling rates and conserve battery life, the duty cycle was implemented to lengthen deployments by periodically activating and deactivating the SM3M. Although the sampling rate chosen for this deployment didn't cover the entire potential range of a signature whistle, it captured the majority of their frequency range while taking up less storage space and maximizing deployment time.

Defining and Detecting Signature Whistles

Previous studies have defined signature whistles as the most common whistle emitted by dolphins when isolated (Caldwell 1965; Sayigh et al. 2007). Often, when a bottlenose dolphin is separated from others, it calls out its signature whistle to reconnect with the group (Quick 2012). Our study did not allow for visual monitoring, making it difficult to determine if dolphins may be separated from each other. Instead, we drew from definitions by Janik et al. (2013), and Gridley et al. (2014) to identify signature whistles. Our identification process heavily relied on a bout analysis method of signature whistle identification known as SIGnature IDentification (SIGID), developed by Janik et al. (2013). SIGID is a conservative signature whistle identification method, but highly restricts the likelihood of false positives.

Whistles emitted by dolphins can be broken into smaller fragments called contours. These contours are narrow band tonal signals with the fundamental frequency above 3kHz. In our

analysis, we included contours that were greater than 1 ms in duration and excluded any harmonics (Gridley et al. 2014). Dolphins often form whistles by looping these contours multiple times continuously, or looping them with a separation gap of less than 250 ms. Sometimes contours are not looped at all and instead form a standalone whistle. This looping of contours is characteristic of both signature and non-signature whistles (Figure 2).

The whistle's context partly separates signature whistles from whistles of other types. Often, these signature whistles are delivered in bout patterns where the same whistle is repeated multiple times (Figure 3). A bout pattern of signature whistles can be described as a group of consecutive signature whistles where the start of one whistle is between 1 and 10 seconds after the end of the immediately preceding whistle in the bout. This gap between whistles is known as the inter-whistle interval (IWI). In this study, bouts of signature whistles were identified when there were three or more consecutive signature whistles, with each whistle having an IWI of 1-10s (Gridley et al. 2014; Janik et al. 2013). By identifying these bouts of whistles, we were able to identify individual signature whistles contained within bouts.

Following these signature whistle definitions and detection guidelines, signature whistles were detected manually in Raven Pro 1.4, a sound analysis software created by researchers at the Cornell Lab of Ornithology. With the duty cycle, the SM3M recorded audio for either two minutes or five minutes at a time depending on the deployment. Individual audio files from the SM3M were combined into longer one-hour sections containing all the individual two or five minute recordings from that hour to make the analysis more time-efficient. This allowed us to more precisely keep track of the timing of the whistles, quickly identify changes in activity at different times of day, and minimize computing time. Each hour-long clip was opened into its own Raven Workspace. Once a clip was loaded into Raven, signature whistles were highlighted using the selection tool to automatically record start times and end times of each signature whistle. If a bout of signature whistles was identified, each signature whistle within the bout was selected separately. Selections were only made on clearly defined whistles with high signal to noise ratios (Heiler et al. 2016). After selecting signature whistles, a custom-written computer script was used to cut smaller individual audio clips containing individually identified signature whistles.

Categorization of Signature Whistles

Once signature whistles were identified, they were compared and sorted into groups based on similarities in frequency modulation pattern. Since signature whistles are unique to individual bottlenose dolphins, each group represented the presence of a unique dolphin. There have been various approaches to signature whistle categorization which can be classified broadly into two methods: manual sorting where one or more people sort whistles into groups visually, and unsupervised automated sorting through the use of computer software or a neural network. Many studies report using a combination of the two methods (Quick and Janik 2012; Janik et al. 2013; Gridley et al. 2014). In our approach, we relied heavily on the use of automated sorting via a neural network. After automated sorting, we reviewed the results and verified categories manually.

Before conducting neural network categorization of the signature whistles, the contours of each signature whistle were extracted using the Beluga software. Beluga is a sound analysis program written in Matlab by researchers at the University of St. Andrews, and is specifically designed to extract contours for neural network sorting. Each signature whistle audio clip collected in Raven was loaded into Beluga. Once clips were loaded, the software generated spectrograms with an FFT length of 2048, a frame length of 512, and an overlap of 87% between frames. From these

spectrograms, signature whistles were extracted and saved as Matlab readable files for neural network sorting.

After contour extraction in Beluga, signature whistles were sorted using ARTwarp (Deecke and Janik 2006), a Matlab based neural network. ARTwarp uses two main variables to fine tune the sorting process. First, the time warping function allows each contour to be slightly sped up or slowed down. Frequency modulation patterns of signature whistles of the same type have little variation, but the duration of identical whistles may vary slightly (Janik 1994). This warping function takes into account small changes in whistle duration by speeding up or slowing down contours to test them more accurately against signature whistles with the same modulation pattern. Second, the vigilance parameter dictates the degree of similarity between whistles required to be considered part of the same category (Deecke and Janik 2006). In our study, a warping function of three was used in combination with a vigilance parameter of 94% based on parameters used by Janik et al. (2013) and Gridley et al. (2014). Upon running signature whistle contours through ARTwarp, categories of signature whistles were generated and manually verified.

Data Analysis

After signature whistle categorization via ARTwarp, we analyzed the number of unique categories of signature whistles. These unique categories each represented a group of identical signature whistles emitted by an individual bottlenose dolphin, and the number of unique categories gives information on the minimum number of bottlenose dolphins in our study area. Additionally, each signature whistle was associated with the date and time of detection through filename. By analyzing the date of occurrence of signature whistles within signature whistle categories, we examined whether bottlenose dolphins were returning to the study area and how frequently.

To determine the detection range of our acoustic recorder, we selected 20 high-quality, clearly defined signature whistles. Based on the loudness and clarity of these selected whistles, we assumed that the dolphins emitting these whistles were in close proximity to our acoustic recorder. Using Raven bioacoustics software, we then examined the acoustic recordings from the same type of device at sites located 3 km, 8 km, and 20 km from our recorder to determine if the same whistle was detected across different sites.

Results

Signature whistle identification from 309 hours of acoustic data resulted in 398 confirmed signature whistles across all deployments (Table 1). Neural network sorting in ARTwarp categorized these 398 signature whistles into 141 unique categories. By manually verifying and correcting ARTwarp's sorting, we re-sorted 57 signature whistles from the existing ARTwarp categories into an additional 33 categories. The final sorting resulted in a total of 174 unique signature whistle types (Figure 4). Of the 174 dolphin signature whistles types, 77 of these dolphins were detected during the summer 2016, 55 during the winter 2017, and 42 in the summer 2017.

Of the 174 signature whistle categories, 160 signature whistle categories (92%) exclusively contained signature whistles in which all whistle occurrences within that category were on the same day (Figure 5). Signature whistles in these 160 categories were not identified again on any other days across all three deployments. The remaining 14 categories included whistles that were identified on at least one other day. All 14 of these signature whistle recurrences were

within their deployment of initial detection and occurred up to 79 days apart. More than half (57%) of the recurrences appeared between 1 and 20 days after the first identification of the signature whistle, and the majority (71%) of all recurrences were during the winter 2017 deployment (Table 2). 10 signature whistles recurred twice and four signature whistles recurred three times. The mean time interval between recurrences was 25 days (SD= 21 days).

Our analysis of the detection range of our acoustic recorder revealed that the same whistles could be detected 100% of the time at a recorder 3km away, 37% of the time at our site 8 km away, and were not detected (0%) at the site 20 km away (Figure 6). Based on this analysis, we estimate a 50% detection rate at 7km away from our recorder (Figure 6).

Discussion

Bottlenose Dolphin Occurrence

In this study, we estimated that at least 174 dolphins passed through our study area between July 2016 and October 2017. This serves as a minimum estimate of the number of dolphins occurring in the study area, although it is likely that this underestimates the total number of dolphins visiting this location. According to an estimate in the 2013 stock assessment, the population of dolphins in the Northern Migratory Coastal Stock is approximately 11,548 (Waring et al. 2014). In our study, the detection of signature whistles is limited by the hydrophone's detection range, the amount of data analyzed, and the requirement that dolphins emit signature whistles when passing through our site. While it is unlikely that the entire Northern Migratory Coastal stock of bottlenose dolphins migrates through our area, the limitations of this study suggest the number of dolphins traveling through our detection area is at least 174 dolphins.

When analyzing dolphin occurrence within individual deployment periods, a much smaller number of dolphins were found during the summer of 2017 than the summer of 2016. Our results even suggested a smaller number of dolphins in our study area during the summer of 2017 than the winter of 2017, which is surprising given that dolphins are generally observed more frequently during the summer in the mid-Atlantic (Toth et al. 2011). This decrease in the number of individual bottlenose dolphins identified during the summer of 2017 may be related to an increased level of underwater noise in our study area. Audio recordings from the summer of 2017 had an overall higher level of low frequency background noise than all other deployments (Figure 7), potentially causing avoidance by dolphins (Buckstaff 2004), and affecting their calling behavior or reducing our ability to detect their signature whistles.

Analysis of recurrence of dolphins within our detection range showed that the majority (71%) of all recurrences happened during the winter 2017 deployment (Table 2). While further research must be conducted on a larger time scale, this finding suggests that the bottlenose dolphins appearing in our study area in the winter may be returning to this area more frequently and exhibiting higher fine-scale site fidelity than those in the summer. We also found that of these 14 recurring dolphin detections, 8 detections recurred within 20 days of the dolphin's first appearance. This may also indicate that when dolphins are returning to our study area, the amount of time between visits tends to be relatively short and high site fidelity is not exhibited across years. All recurring bottlenose dolphins were detected within the same deployment. This could indicate that bottlenose dolphins have flexibility in the specific path they take during migration and may not always pass through our 7 km detection range. The Northern Migratory Coastal stock of bottlenose dolphins are a highly mobile population of bottlenose dolphins (Waring et al. 2014), and these results may reflect this migratory behavior. While our results reflect the mobility of this stock, it is also important to note that the amount of acoustic data

analyzed was limited to 309 hours, and that the whistle detection range of our acoustic recorder was limited to 7 km. Additional analysis of data at this site and data at surrounding sites is likely to reveal more bottlenose dolphin recurrences.

Signature Whistle Analysis

Using similar methods, previous studies have successfully grouped signature whistles into stereotyped categories associated with individual dolphins (Gridley et al. 2014; Janik et al. 2013). Our study supports that signature whistle identification and matching has the potential to aid in the tracking of individual bottlenose dolphins over time. There has been substantial research on bottlenose dolphin signature whistles, especially with the use of visual aid (Sayigh et al. 1999). Much less research has been done on signature whistle identification in the wild without relying on visual aid (Gridley et al. 2014; Janik et al. 2013). This study utilizes existing knowledge of signature whistles, but is limited to bout analysis: a highly accurate signature whistle identification method that avoids risk of false positives (Janik et al. 2013). Bout analysis, however, tends to be conservative and may not always detect all signature whistles. Further studies on the properties and context of signature whistles could help improve signature whistle identification when visual aid is not possible.

A large number of different signature whistles were detected from acoustic data that spanned over more than a year. This led to the detection of many signature whistle that were similar, but not similar enough to be considered the signature whistle of the same dolphin. Previously, an ARTwarp categorization vigilance parameter of 91% has been used (Gridley et al. 2014), but in our study this threshold created many incorrect signature whistle matches that required manual adjustment. We gradually increased the vigilance parameter to 94%, which produced the most accurate sorting. It avoided grouping together signature whistles that did not match while still detecting similarity between signature whistles of the same type. Even with this increased vigilance parameter, some whistles were still inaccurately put into the same category and had to be corrected manually. This increased vigilance parameter helped distinguish these similar signature whistles from each other, but it was still important to consider the ARTwarp results as a starting point requiring manual oversight.

Passive acoustic monitoring offers the great benefit of delivering huge quantities of data. The greatest limitation of working with this data stems from restrictions on time, as much of the process of signature whistle identification must be done manually by a human observer. This limitation presents itself in our study, where estimates of population and dolphin recurrence rely on the amount of acoustic data analyzed. Computer algorithms utilizing recent advancements in machine learning have been implemented to detect patterns of species-specific dolphin clicks (Frasier et al. 2017). Research on applying similar machine learning based data analysis may be useful for increasing the amount of acoustic data capable of being analyzed for signature whistles, improving estimates on abundance and habitat usage.

Conclusions

The Northern Migratory Coastal stock of bottlenose dolphins is listed as a strategic stock under the Marine Mammal Protection Act (Waring et al. 2014). With the proposal of the Maryland Wind Energy Area off Ocean City, MD, it is important to assess the potential impacts on these dolphins before construction takes place. Through acoustical analysis of bottlenose dolphin signature whistles, this study helps estimate the minimum number of dolphins vulnerable to construction noise and other activities within the wind energy area. This study demonstrates that it is possible to track individual bottlenose dolphins through their signature whistles. In the

majority of cases, individual dolphins were detected only once. However, there were instances where individuals were detected up to 79 days later. We estimate that a minimum of 174 dolphins occurred in our detection area and this could be used to help inform assessments of the potential exposure of bottlenose dolphins to wind farm construction noise and shipping traffic.

Acknowledgements

Thank you to Dr. Helen Bailey for advising this study, and to both her and Aimee Hoover for guidance, assistance, and inspiration throughout the course of this project. Additional thanks to everyone who assisted in the acoustic data collection, and to Dr. William Fletcher for technical support and introductions to softwares that were integral to conducting this study. Thank you to Dr. Mike Allen for coordinating and organizing this REU program, and to everyone else involved in maintaining and running this REU program. This study was supported by NSF grant OCE-1756244. The data collection was funded by the Maryland Department of Natural Resources, Maryland Energy Administration's Offshore Wind Development Fund and the U.S. Department of Interior's Bureau of Ocean Energy Management, Environmental Studies Program (Grant number 14-14-1916 BOEM/ BOEM Award # M14AC00018).

References

Buckstaff, K. C. 2004. Effects of Watercraft Noise on the Acoustic Behavior of Bottlenose Dolphins, *Tursiops truncatus*, in Sarasota Bay, Florida. Marine Mammal Science 20: 709–725. doi:10.1111/j.1748-7692.2004.tb01189.x

Caldwell, M. C., and D. K. Caldwell. 1965. Individualized Whistle Contours in Bottle-nosed Dolphins (*Tursiops truncatus*). Nature 207: 434.

Davis, G. E., M. F. Baumgartner, J. M. Bonnell, and others. 2017. Long-term passive acoustic recordings track the changing distribution of North Atlantic right whales (*Eubalaena glacialis)* from 2004 to 2014. Scientific Reports 7. doi:10.1038/s41598-017-13359-3

Deecke, V. B., and V. M. Janik. 2006. Automated categorization of bioacoustic signals: Avoiding perceptual pitfalls. The Journal of the Acoustical Society of America 119: 645–653. doi:10.1121/1.2139067

Esch, H. C., L. S. Sayigh, J. E. Blum, and R. S. Wells. 2009. Whistles as Potential Indicators of Stress in Bottlenose Dolphins (*Tursiops truncatus*). Journal of Mammalogy 90: 638–650. doi:10.1644/08-MAMM-A-069R.1

Frasier KE, Roch MA, Soldevilla MS, et al. Automated classification of dolphin echolocation click types from the Gulf of Mexico. Glotin H, editor. PLOS Computational Biology. 2017;13:e1005823.

Garrison, L. P., S. L. Swartz, A. Martinez, C. Burks, and J. Stamates. 2002. A Marine Mammal Assessment Survey of the Southeast US Continental Shelf: February–April 2002. 54.

Gridley, T., V. G. Cockcroft, E. R. Hawkins, M. L. Blewitt, T. Morisaka, and V. M. Janik. 2014. Signature whistles in free-ranging populations of Indo-Pacific bottlenose dolphins, *Tursiops aduncus*. Marine Mammal Science 30: 512–527. doi:10.1111/mms.12054

Heiler, J., Elwen, S.H., Kriesell, H.J. & Gridley, T. 2016 Changes in bottlenose dolphin whistle parameters related to vessel presence, surface behaviour and group composition. Animal Behaviour 117, 167–177.

Janik, V. M. 2009. Chapter 4 Acoustic Communication in Delphinids, p. 123–157. In Advances in the Study of Behavior. Elsevier.

Janik, V. M., S. L. King, L. S. Sayigh, and R. S. Wells. 2013. Identifying signature whistles from recordings of groups of unrestrained bottlenose dolphins (*Tursiops truncatus*). Marine Mammal Science 29: 109–122. doi:10.1111/j.1748-7692.2011.00549.x

Janik, V.M., Todt, D. & Dehnhardt, G. 1994. Signature whistle variations in a bottlenose dolphin *Tursiops truncatus*. Behavioral Ecology and Sociobiology 35: 243. https://doi-org.proxyau.wrlc.org/10.1007/BF00170704

Janik, V. M. 2000. Source levels and the estimated active space of bottlenose dolphin (*Tursiops truncatus)* whistles in the Moray Firth, Scotland. Journal of Comparative Physiology A 186: 673–680. doi:10.1007/s003590000120

Kishida, T., S. Kubota, Y. Shirayama, and H. Fukami. 2007. The olfactory receptor gene repertoires in secondary-adapted marine vertebrates: evidence for reduction of the functional proportions in cetaceans. Biology Letters 3: 428–430. doi:10.1098/rsbl.2007.0191

Quick, N. J., and V. M. Janik. 2012. Bottlenose dolphins exchange signature whistles when meeting at sea. Proceedings of the Royal Society B: Biological Sciences 279: 2539–2545. doi:10.1098/rspb.2011.2537

Rosel, P. E., L. Hansen, and A. A. Hohn. 2009. Restricted dispersal in a continuously distributed marine species: common bottlenose dolphins *Tursiops truncatus* in coastal waters of the western North Atlantic: FINE-SCALE POPULATION STRUCTURE IN TURSIOPS. Molecular Ecology 18: 5030–5045. doi:10.1111/j.1365-294X.2009.04413.x

Rumsey, F., and T. McCormick. 2010. Sound and Recording, 6th ed. Focal Press.

Sayigh, Peter L. Tyack, Randall S. Wells, and Michael D. Scott. 1990. Signature Whistles of Free-Ranging Bottlenose Dolphins *Tursiops truncatus*: Stability and Mother-Offspring Comparisons. Behavioral Ecology and Sociobiology 26: 247–260.

Sayigh, L. S., P. L. Tyack, R. S. Wells, A. R. Solow, M. D. Scott, and A. B. Irvine. 1999. Individual recognition in wild bottlenose dolphins: a field test using playback experiments. Animal Behaviour 57: 41–50. doi:10.1006/anbe.1998.0961

Sayigh, L., H. Carter Esch, R. Wells, and V. M. Janik. 2007. Facts about signature whistles of bottlenose dolphins, *Tursiops truncatus*.

Toth, J. L., A. A. Hohn, K. W. Able, and A. M. Gorgone. 2011. Defining bottlenose dolphin (*Tursiops truncatus*) stocks based on environmental, physical, and behavioral characteristics. Marine Mammal Science 28: 461–478. doi:10.1111/j.1748-7692.2011.00497.x

Waring GT, Josephson E, Maze-Foley K, Rosel, PE, editors. 2014. U.S. Atlantic and Gulf of Mexico Marine Mammal Stock Assessments—2013. NOAA Tech Memo NMFS NE p. 228; 464. Available from: National Marine Fisheries Service, 166 Water Street, Woods Hole, MA 02543-1026, or online at http://nefsc.noaa.gov/publications/

Zolman, E. S. 2002. Residence Patterns of Bottlenose Dolphins (*Tursiops Truncatus*) in the Stono River Estuary, Charleston County, South Carolina, U.S.A. Marine Mammal Science 18: 879–892. doi:10.1111/j.1748-7692.2002.tb01079.x

Tables and Figures

Table 1. The number of bottlenose dolphin signature whistles and unique signature whistle categories in comparison with deployment, length of deployment, and hours of acoustic data analyzed.

Deployment	*Summer 2016*	*Winter 2017*	*Summer 2017*	*Total*
Deployment Length (Days)	66	85	118	269
Data Analyzed (Hours)	88	86	135	309
No. of Signature Whistles Identified	168	150	80	398
No. of Signature Whistle Categories	77	55	42	174

Table 2. Time differences between earliest and latest identified signature whistles within categories where signature whistles of the same type occurred more than 24 hours apart.

Number of Days	*During Summer 2016*	*During Winter 2017*	*During Summer 2017*	*Total Reoccurrences*
1-20	3	4	1	8
21-40	0	3	0	3
41-60	0	1	0	1
61-80	0	2	0	2
Total per Deployment	3	10	1	14

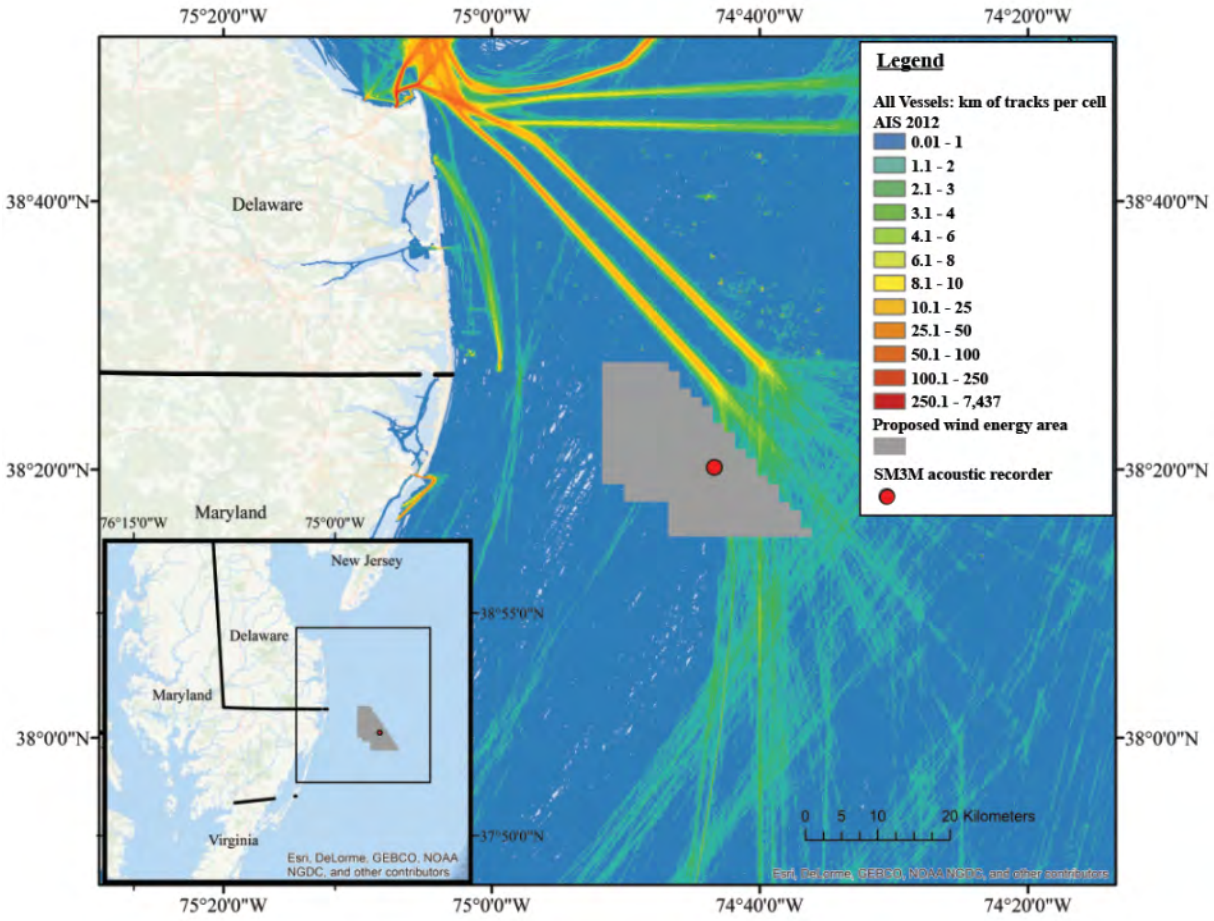

Figure 1. Map of the study area where signature whistles were recorded. Station A-5C is where the SM3M submersible was deployed. This map was created with ArcGIS® by Esri.

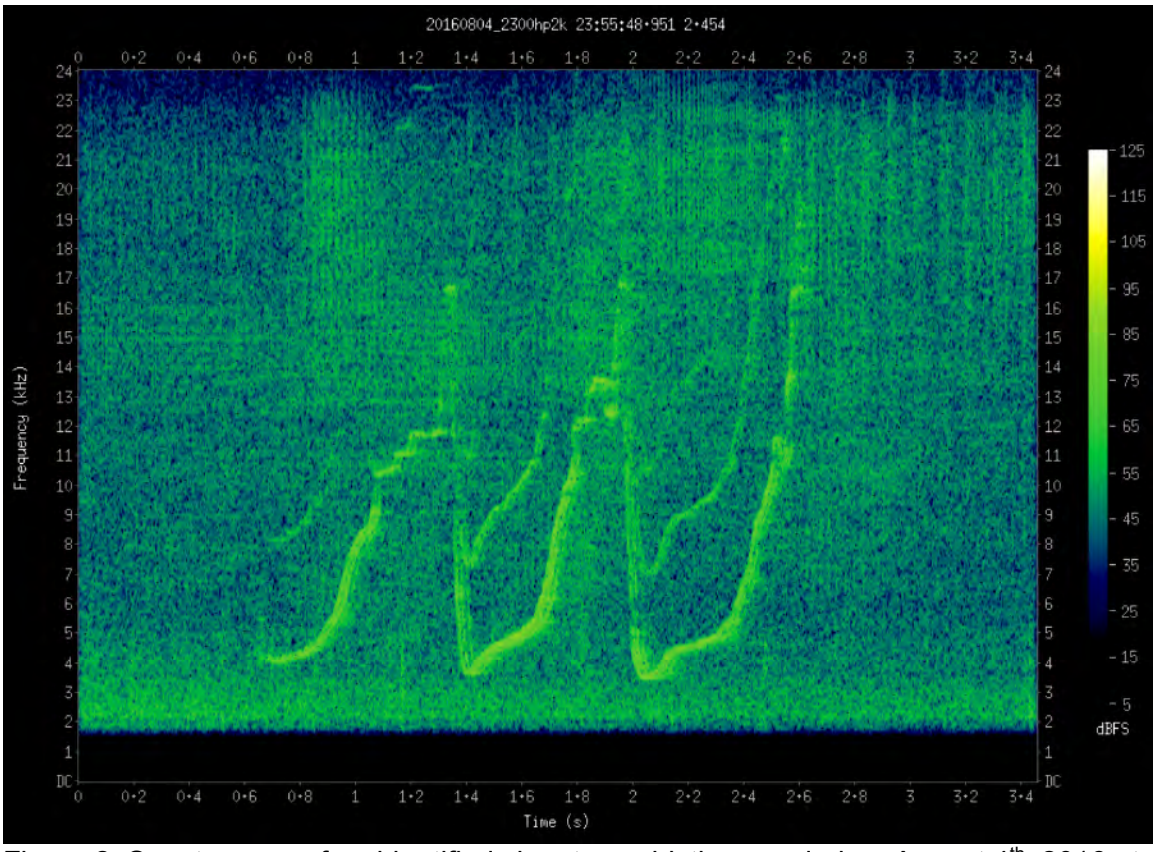

Figure 2. Spectrogram of an identified signature whistle recorded on August 4th, 2016 at 23:55:48 EST.

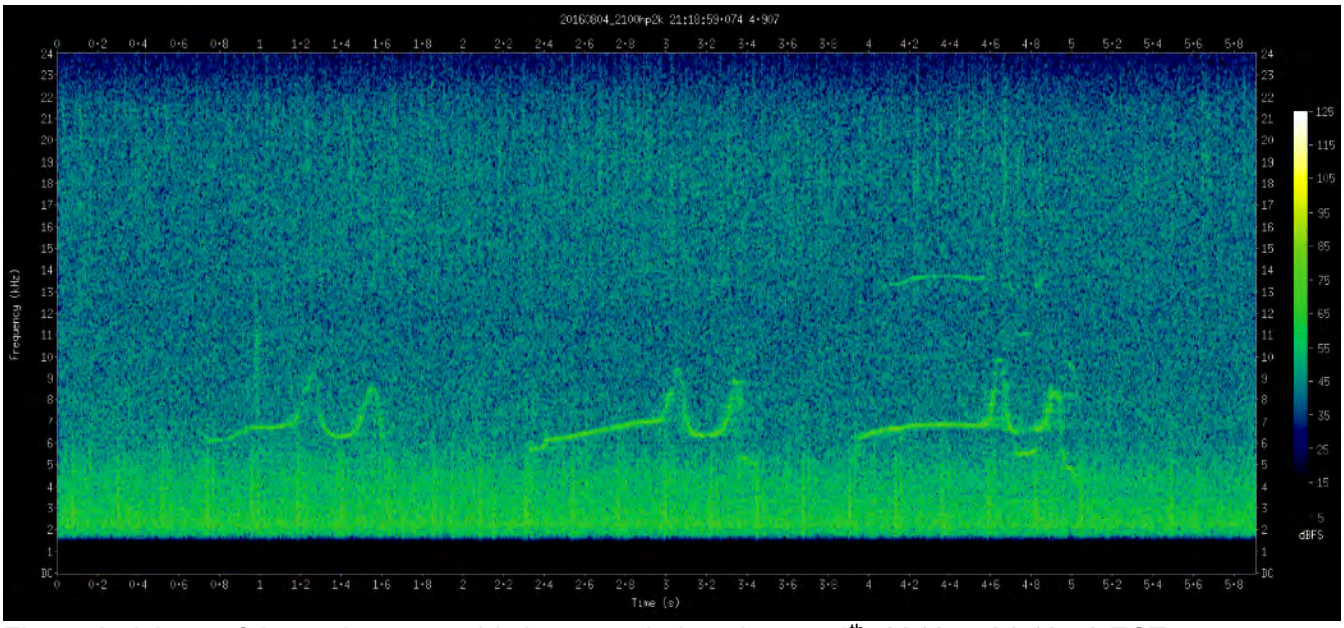

Figure 3. A bout of three signature whistles recorded on August 4th, 2016 at 21:18:59 EST.

Figure 4. Each numbered category depicts the contour of signature whistles that are contained within that category. Through categorization in ARTwarp and manual verification, 174 unique signature whistle categories were found. This diagram is based on images from in ARTwarp software.

(a)

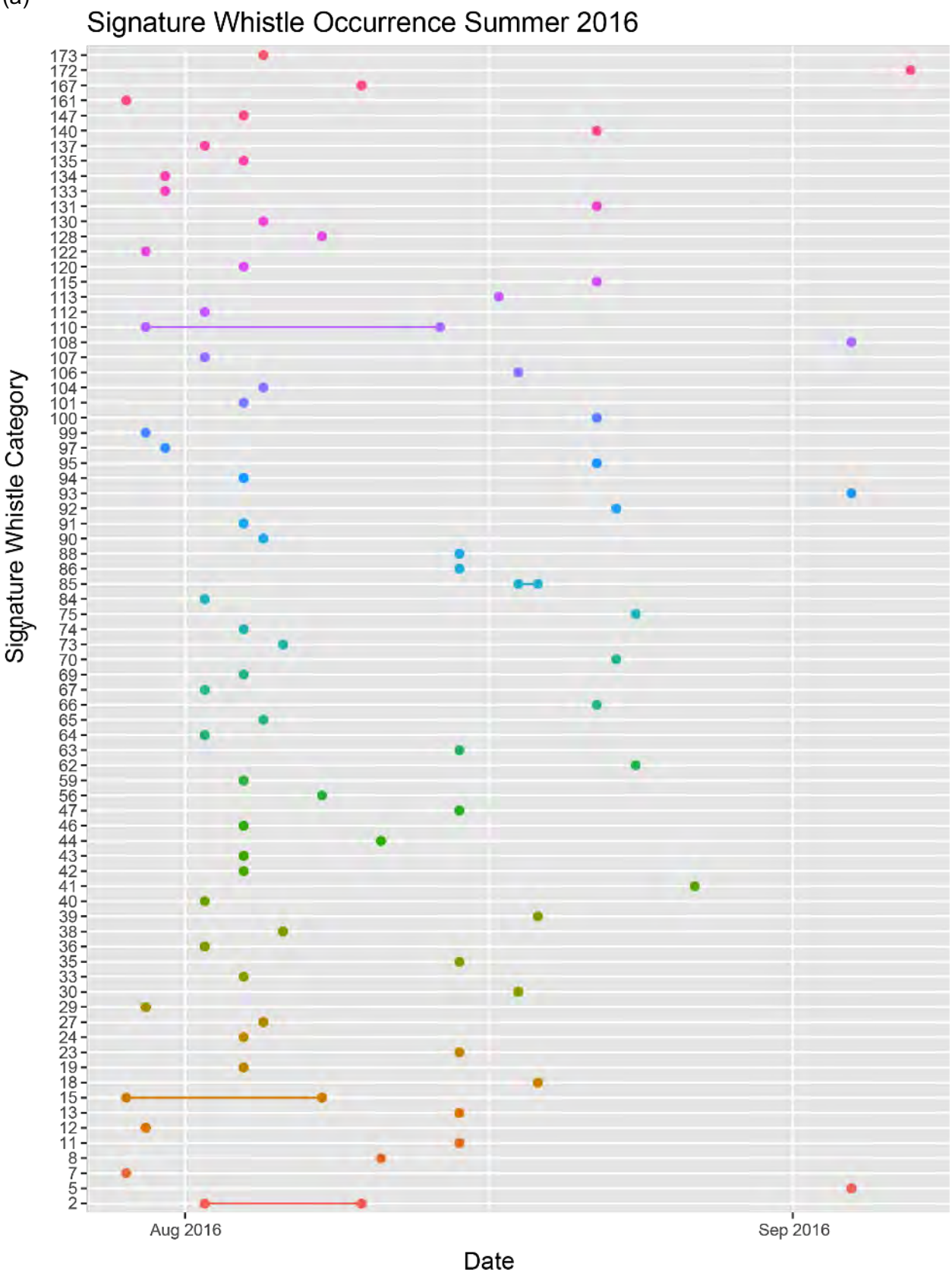
Signature Whistle Occurrence Summer 2016
Signature Whistle Category
173
172
167
161
147
140
137
135
134
133
131
130
128
122
120
115
113
112
110
108
107
106
104
101
100
99
97
95
94
93
92
91
90
88
86
85
84
75
74
73
70
69
67
66
65
64
63
62
59
56
47
46
44
43
42
41
40
39
38
36
35
33
30
29
27
24
23
19
18
15
13
12
11
8
7
5
2
Aug 2016
Sep 2016
Date

(b)

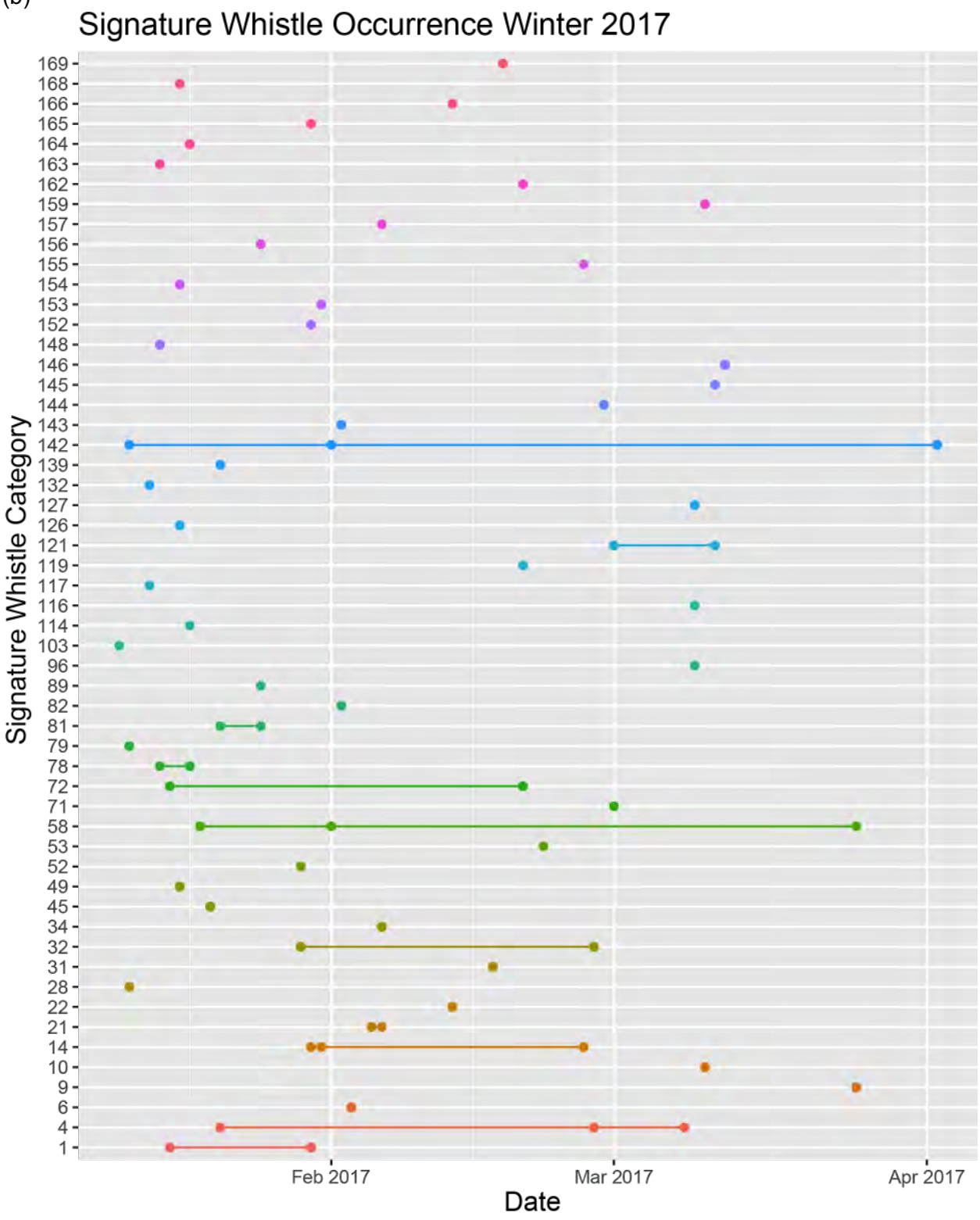
Signature Whistle Occurrence Winter 2017
Signature Whistle Category
169
168
166
165
164
163
162
159
157
156
155
154
153
152
148
146
145
144
143
142
139
132
127
126
121
119
117
116
114
103
96
89
82
81
79
78
72
71
58
53
52
49
45
34
32
31
28
22
21
14
10
9
6
4
1
Feb 2017
Mar 2017
Apr 2017
Date

(C)

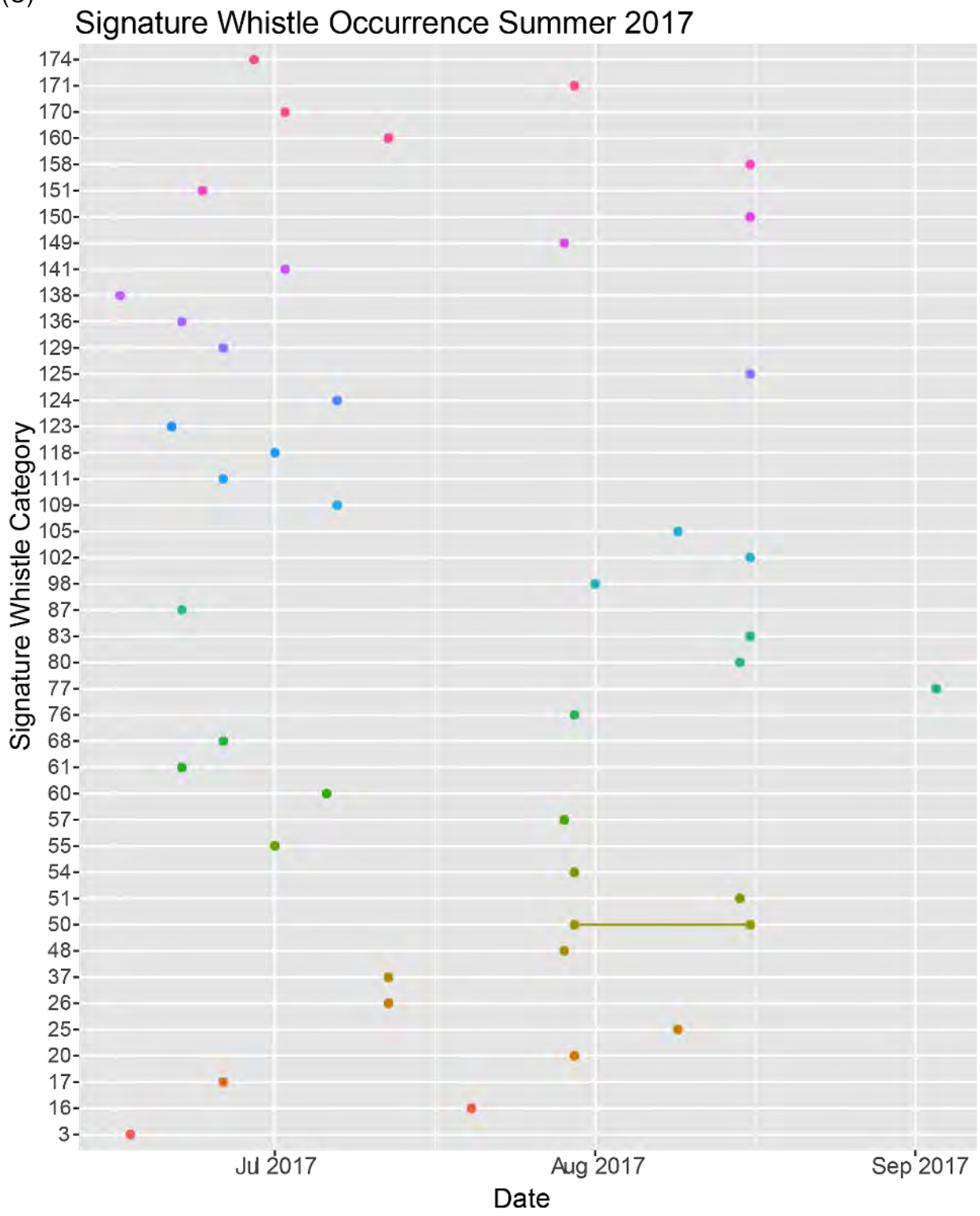

Figure 5. Timeline representation of signature whistle occurrences within categories. Each figure shows occurrence of dolphins within each deployment. Lines connecting dots indicate a dolphin revisiting our study site.

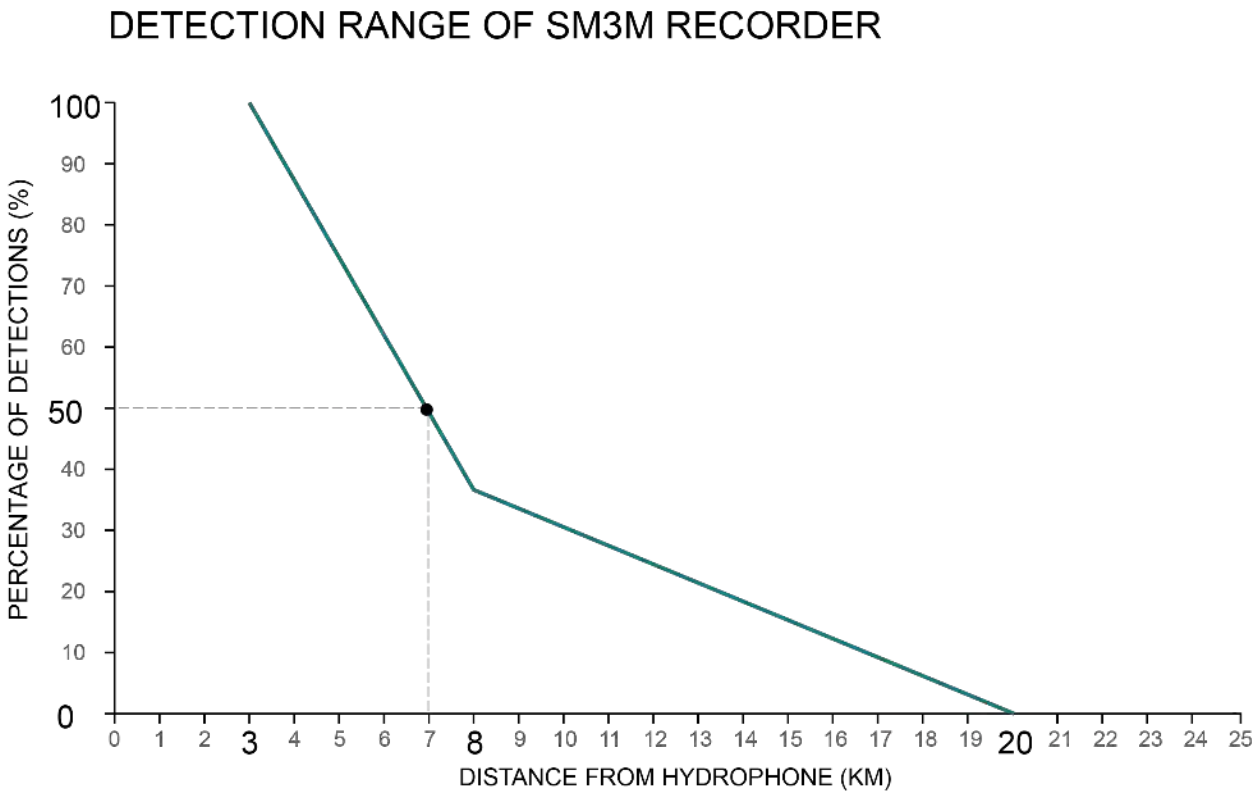

Figure 6. Percentage of whistles detected at additional sites 3km (100%), 8km (37%), and 20km (0%) from the acoustic recorder used in this study. A detection rate of 50% is estimated at a distance of approximately 7 km.

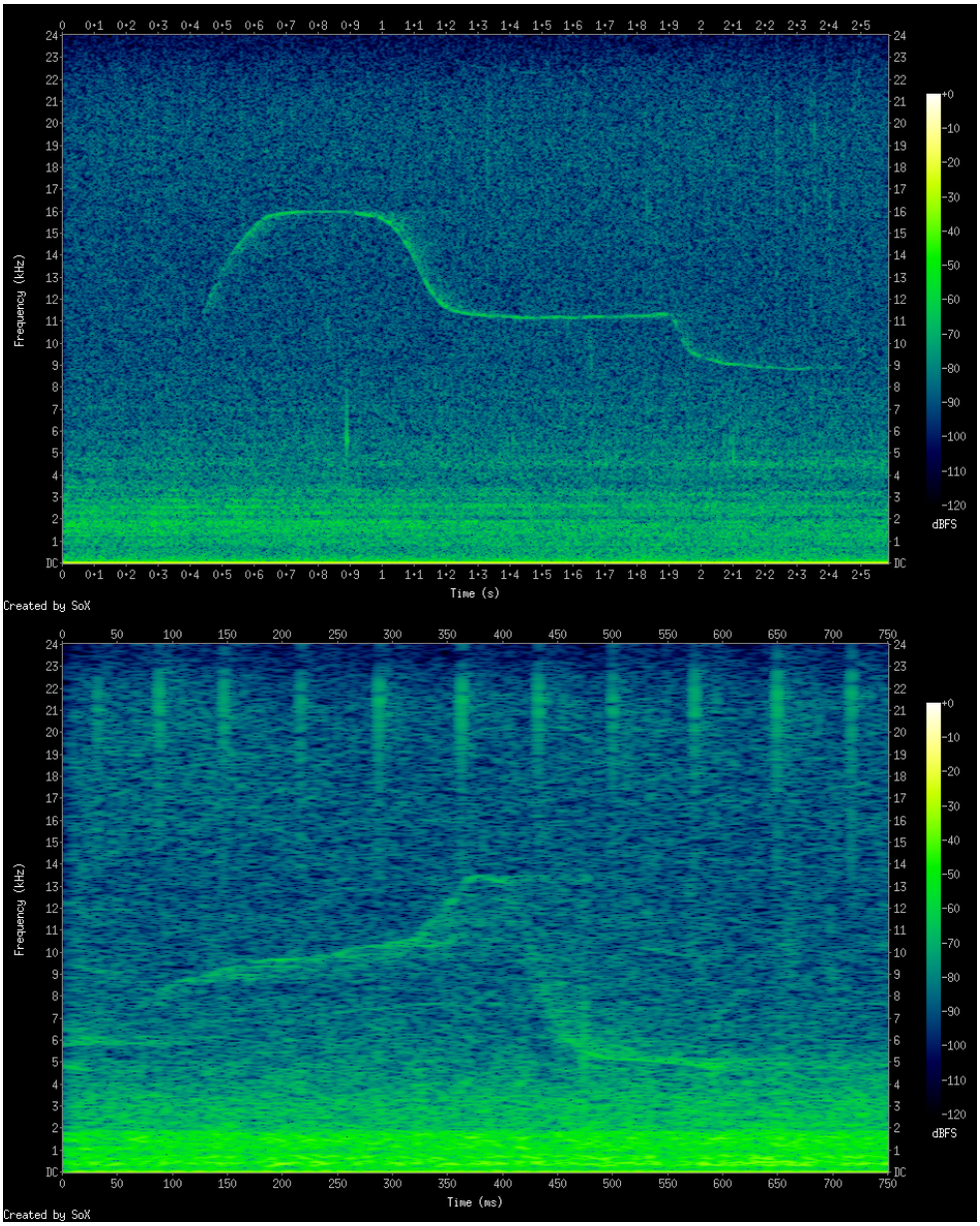

Figure 7. Comparison of ambient noise level associated with a signature whistle produced during winter (January–April, top panel) and summer (June–October, lower panel) 2017 deployments.

Viability of Epinephrine as an Inducer of Metamorphosis on the Oyster *Crassostrea virginica*

Justin Guider, REU Fellow
Maryland Sea Grant

Carys Mitchelmore, Professor
Chesapeake Biological Laboratory, University of Maryland Center for Environmental Science

Abstract

In the United States, oysters are induced to settle using either whole oyster shells or ground oyster shells ("cultch"). Settlement on cultch is used in aquaculture to provide single oysters for market. However, a common method used in European countries is to induce settlement using the hormone epinephrine. This study compared the settlement success of triploid *Crassostrea virginica* larvae of the Lola strain using cultch versus epinephrine as an inducer of metamorphosis and settlement in oysters. Specifically, the study was concerned with how epinephrine affected settlement success, as well and the short- and long-term growth of the oysters. To determine these effects, the larvae were raised for 8–13 days in a downwelling system, then the resulting spat raised for several weeks in an upwelling system. An additional treatment was also employed—the effects of using ambient, unfiltered water from the Patuxent River versus water filtered using a 5μm mesh screen during the settlement and metamorphosis phases of the oysters' life cycle. The effects of these treatments were examined in conjunction with the effects of the two inducers used to mimic a "good" versus a "poor" environmental condition (i.e. high and low food availability). In both treatments, exposure to epinephrine led to higher settlement success than cultch. Mortality was lower for the epinephrine-treated oysters than cultch, and growth in the first 8 days was similar for epinephrine and cultch oysters in the ambient treatment, but higher for the epinephrine oysters in the filtered treatment. Long-term growth was similar among all treatments and inducers. The filtered treatment led to lower settlement success and higher mortality than the ambient treatment in the first 8 days.

Introduction

Crassostrea virginica, the Eastern oyster, is a species native to the Chesapeake Bay. Prior to European colonization, *C. virginica* was abundant in the Bay, such that oyster beds once posed a navigational hazard for ships travelling in shallow waters (Newell 1988). However, beginning in the late 19th century, the oyster population in the Chesapeake Bay began to decline dramatically. The initial cause was the overharvesting of oysters, which were a popular commercial food item. Not only did the overharvesting lead directly to the depletion of oyster stocks, but the method in which oysters were harvested destroyed much of their habitat. Oysters form beds, or reefs, composed of many oysters stacked on top of one another. Larval oysters rely on chemical cues from beds to settle and metamorphose into juvenile spat, so the destruction of the beds by dredging reduced the oysters' ability to repopulate (Mackenzie 2007; Turner et al. 1994). Also, increased run-off and sediment into the water from various human

activities have reduced the oysters' capacity to settle and can smother oyster reefs. Water quality has also declined due to chemical pollutants such as excess nutrients (nitrogen and phosphorous) and an array of man-made chemicals. These and other impacts resulted in a steadily decreasing oyster stock up until the 1960s, when the protozoan parasite-caused diseases Dermo (*Perkinsus marinus*) and MSX (*Haplosporidium nelsoni)* compounded the population decrease. Due largely to these causes, *C. virginica* landings decreased almost 99% between 1890 and 2004 (Mackenzie 2007; Mann and Powell 2007).

This figure is especially alarming when one considers how important *C. virginica* was and is to the Bay's ecology and economy. *C. virginica* is an important keystone species and provides many ecosystem services. The destruction of oyster beds impacted the many species that rely on them for food and habitat. Many species find protection in the many nooks and crannies formed by oyster shells (Beck et al. 2011). Furthermore, oysters provide the ecosystem service of water filtration and nutrient recycling via pelagic/benthic coupling. *C. virginica* is a suspension feeder, filtering out organic and inorganic particulate matter from the water column. It does this very efficiently, such that prior to exploitation the oysters in the Bay could have filtered out between 23% and 41% of the daily carbon production in the Bay, whereas in 1988 that figure was only about 1%. The organic material that oysters don't ingest and absorb gets deposited in mucus-bound biodeposits and serves as food for benthic organisms, thus taking pelagic food to the benthic ecosystem. This can be in the form of faeces (i.e. leftover material after passing through the gut) or pseudofaeces. Due to less of the Bay being filtered and the increasing amount of nutrients, its food web has been restructured. Phytoplankton, most of which were once consumed by oysters, have become more abundant, contributing to the algal blooms and resulting anoxic zones that plague much of the Bay. The presence of more phytoplankton has resulted in a trophic cascade, leading to more zooplankton, which graze on phytoplankton, and thus more of their predators, such as ctenophores and jellyfish (Newell 1988).

Oysters were so fundamental to the Chesapeake Bay's ecology that their decline radically changed how the ecosystem functions. In addition to consuming phytoplankton, *C. virginica* also filters out nutrients, the excess of which (eutrophication) has been a huge problem for the Chesapeake Bay, exacerbating the problem of algal blooms and anoxic dead zones. In addition, oysters filter out inorganic particles, making the water of the Bay much clearer. The increasing turbidity in the Bay seen in the last century can be attributed in part to the decline in oyster stocks. This has had myriad ramifications, including the decline in seagrasses, which require ample sunlight (Beck et al. 2011).

Oyster restoration efforts in the Chesapeake Bay have been underway for decades. Restoration takes several forms, including provision of substrate like oyster shells and other 3D reef environments (including sunken ships, tires and man-made concrete reef structures (Feigenbaum et al. 1989). One strategy that is already practiced to an extent is seeding the Bay with hatchery-raised oysters. Hatcheries not only allow for the growth of oysters in controlled environments and away from predators, but also allow for genetic selection; for example, oysters that are more disease tolerant and/or can grow better at lower salinities. By raising disease-resistant strains of *C. virginica* it might be possible to decrease the prevalence of the diseases MSX and Dermo in the Chesapeake (Mann and Powell 2007). Oysters are raised in hatcheries from the larval stage until they are ready to survive in the wild, at which point they are taken out to the Bay and deposited to add to or make new oyster reefs (Brumbaugh et al. 2000). In addition to its importance to the Chesapeake Bay ecosystem, *C. virginica* is also a very important commercial fisheries species. However, in the Chesapeake Bay the oyster industry declined from a $60.1 million industry to a $4.3 million industry from 1980 to 2001, largely because of falling population numbers (National Research Council 2004). Instead of

harvesting oysters from the Bay, oyster aquaculture has expanded to fill this void, growing as an industry throughout the Bay and directly providing oysters for the shellfish market. Aquaculture is a good alternative to harvesting wild oysters, not least because shellfish aquaculture is a good alternative to other forms of aquaculture and terrestrial agriculture. Oyster aquaculture requires no addition of food or water; rather, oysters can subsist off of what is found in ambient water. Aquaculture requires single oysters for the shellfish market so the larvae is set on very small fragments of ground up oyster shell, known as cultch (roughly around 300 microns in size, about the same size as a competent larvae). Aquaculture may also be a positive for water quality by reducing nitrogen levels by removing nitrogen from the water column. As such, oyster aquaculture has relatively minor and potentially positive environmental impacts (Beck et al. 2011). A switch from wild harvests to aquaculture could revitalize the industry. Aquaculture could also be used to provide oysters for restoration too, removing the need for the oyster shells, a limited resource. However, *C. virginica* aquaculture runs into a bottleneck in the metamorphosis of larvae into juvenile spat as only around 5–25% of larvae settle onto shell or cultch.

As mentioned earlier, oysters require a suitable substrate to begin the process of metamorphosis, which in the wild comes from the presence of existing oyster shells; they attach to the shells in a process called settlement, and begin to metamorphose from larvae into juveniles, called spat (Joyce and Vogeler 2018). Current U.S. *C. virginica* aquaculture methods imitate wild conditions by providing larvae with cultch (Joyce and Vogeler 2018). However, this generally only results in less than 30% metamorphosis (Mesías-Gansbiller et al. 2013). Thus, the larvae to spat process represents a bottleneck in oyster aquaculture and reducing the magnitude of the bottleneck would greatly improve aquacultural yields. Much research has investigated the viability of using inducers to promote settlement and/or metamorphosis in bivalves. Among the substances used are L-3,4-dihydroxyphenylalanine (L-DOPA), gamma-Aminobutyric acid (GABA), 3-isobutyl-1-methylxanthine (IBMX), and jacaranone. Table 1 summarizes the effectiveness of these compounds on inducing settlement or metamorphosis on various bivalve species.

One chemical inducer that has yielded promising results is epinephrine, or adrenaline, a neurotransmitter that's involved in the process of metamorphosis. Epinephrine and the related neurotransmitter norepinephrine are part of a group of chemicals called catecholamines. In bivalves, these activate adrenergic receptor-mediated neural pathways that begin the process of metamorphosis. By artificially exposing competent bivalve larvae to epinephrine, metamorphosis can be induced (Bonar et al. 1990). Epinephrine has several characteristics that make it an excellent inducer. Exposure to epinephrine has increased metamorphosis rates of the Pacific oyster, *Crassostrea gigas*, up to over 90%, compared to sub-30% values for oyster larvae not exposed to an inducer (Coon et al. 1986; Nicolas et al 1998). Epinephrine also induces metamorphosis in a shorter time than the other common catecholamine, norepinephrine (Coon et al. 1986). Also, epinephrine has been shown not to increase mortality in bivalves even at long exposures, and oysters (*C. gigas*) grown form up to a year from larvae that were induced to metamorphose with epinephrine were not noticeably different from oysters grown by traditional methods (Coon et al. 1986; Mesías-Gansbiller et al. 2013). However, despite all these advantages, little investigation has been made into the possibility of using epinephrine to induce metamorphosis of *C. virginica* for commercial, restoration, or scientific purposes in the USA. Coon et al. did test the effects of epinephrine on oysters, but I could find no others, and their experiment used filtered seawater (1986). Our experiment will also use ambient seawater, which more realistically represents an aquacultural setting.

It should be noted that, in the wild, metamorphosis is preceded by settlement. Settlement is a reversible behavioral process that involves the larva swimming then “crawling” with its foot extended. If a substrate is insufficient, the larvae can resume swimming normally. Metamorphosis, on the other hand, is a morphogenetic process that involves irreversible changes. Normally, settlement and metamorphosis are serial processes, one following the other. However, whereas settlement is mediated by dopaminergic pathways, metamorphosis is mediated by adrenergic pathways, meaning that epinephrine induces metamorphosis without settlement (Bonar et al. 1990). Oysters grown this way are called “free” or “cultchless” (Coon et al. 1986; Nicolas et al. 1998). From a commercial aquaculture standpoint, growing cultchless oysters is advantageous because they have a better shape and uniformity, are easier to shuck and ship, and it is unnecessary to purchase expensive cultch material. Cultchless oysters are also easier to study in scientific experiments (Nicolas et al. 1998).

Despite all the advantages of inducing metamorphosis using epinephrine on bivalves, very little research has been done into the effects of epinephrine on *C. virginica*. As an important commercial species, as well as a vital part of the Chesapeake’s environment, improving the percent of larvae that metamorphose into adults could improve aquaculture yields and make it easier to repopulate the bay.

Materials and Methods

Our objective for this experiment was twofold. The first part was to compare the settlement successes of *C. virginica* larvae exposed to epinephrine to that of *C. virginica* larvae raised on cultch. The second part is to compare the longer-term survival and growth of *C. virginica* individuals exposed to epinephrine to those raised on cultch.

This experiment was performed at the Chesapeake Biological Laboratory (CBL) in Solomons, MD at the Cronin lab. The experiment used oyster larvae from four different sources. Source 1 provided diploid oyster larvae (strain Lola) and Sources 2–4 provided triploid larvae (2 and 4 were Lola strain and batch 3 Deby strain). Strains 3 and 4 were shipped to CBL on wet coffee filters and chilled by ice. Batch 1 and 2 arrived the same day and were held at ambient temperature. They all arrived within the same week, and each set of larvae was introduced to the downwelling tanks on the day it arrived. The epinephrine used was ordered from Sigma-Aldrich (Sigma-Aldrich E4250). All sources will remain confidential and results be presented only as “Source [1–4]” with no mention made of the hatchery that provided the larvae. The experiment consisted of two phases: the “downwelling” stage in which settlement occurred, followed by an “upwelling” stage to follow subsequent growth and mortality of the spat.

Phase ONE: Downwelling stage

The first phase of the experiment took place in four 12ft downwelling tanks (tanks A–D). The downwelling system was managed based on the methods used by Danci Johnston in her 2017 project “Advancing Settlement of Oyster Larvae *Crassostrea virginica* for Commercial Aquaculture.” Two of the four tanks were filled with running ambient water taken from the Patuxent river in front of CBL by the research pier; the other two were also be filled with running water from the Patuxent but filtered using a 5µm filter (see Fig. 1). Each tank contained ten individual silos. Each silo was comprised of two five-gallon buckets glued together with a 173 µm nylon mesh between them. The silos were coated with a very thin layer of Vaseline and labeled 1–40. Two silos in each tank contained larvae from Source 1, two contained oysters from Source 2, two contained oysters from Source 3, two contained oysters from Source 4

raised on cultch, and two contained oysters from Source 4 that were treated with epinephrine. The position of each silo within the tanks was randomly determined to avoid any potential bias.

When the larvae arrived from each hatchery source, they were removed from their respective shipping containers and allowed to come to room temperature if they were shipped on wet ice. The entire mass of larvae was weighed and based on the larval counts from the hatchery the approximate weight aliquot needed to provide eight replicates (or sixteen for Source 4) of around 100–150K of larvae per silo was estimated. Before larvae were added to the individual silos, one weighed subsample per source was used to determine the competency of the larvae by counting those in each larval stage (veliger and pediveliger). The total number of larvae in six other subsamples was counted under a microscope. Fifty larval size measurements each were taken by microscopy from five subsamples per source to determine the size distribution of the larvae. Two tablespoons of cultch were apportioned to each silo, except for the eight containing larvae that were exposed to epinephrine. Since the water used for the experiment came from a natural estuary, it had different properties throughout the day and throughout the course of the experiment. Temperature, pressure, dissolved oxygen, conductivity, and salinity of the water in the downwelling tanks were measured twice daily, in the morning and in the afternoon, using a YSI probe. Flow rates into each silo were also taken each day by holding a bag under each outflow for 30 seconds. The target flow rate was 1000 mL/min; any flow rate higher or lower than this target by more than 100 mL/min was adjusted. A chlorophyll sample was taken from each tank every day at noon. After the second day of experimentation, every silo was washed daily to remove waste produced by the oysters, ensuring the mesh screens did not become blocked. The times of the addition of the larvae to each of the silos and the exact weight of the aliquot added were noted.

Eight aliquots of larvae from Source 4 were transferred to 2L glass beakers filled with seawater. The epinephrine was dissolved in a 1M HCl solution and mixed with glass-distilled water in order to make a stock solution according to the procedure outlined by Coon et al. 1985. The larvae were allowed to acclimate for 15 minutes, as described in Coon et al. 1986. The stock solution was added to the glass beakers containing the *C. virginica* larvae in a 1:9 ratio, such that the oysters were exposed to a 10^{-4}M concentration of epinephrine. The larvae were only exposed to the epinephrine for four hours in order to avoid the possibility of the larvae experiencing low levels of dissolved oxygen. As shown in Table 2, two hours of exposure to epinephrine is enough to significantly increase metamorphosis rates in various bivalve species. After the four hours exposure, the larvae were removed, rinsed, and placed in their respective silos. After eight days the larvae were moved to the next phase, the upwelling stage. The cultch/larvae mixture was screened to determine how many larvae survived and the proportion that settled. This was done by passing the larvae through a series of mesh sieves containing large to small mesh sizes: 500µm, 355µm and 150µm. The material retained on each screen was placed in a coffee filter and the entire filter was weighed. The weight triplicates of a wet empty coffee filter were removed from the weight to provide the weight of the material only. The weight of the mass in each size fraction was recorded and then three aliquots were taken, their weight was recorded, and they were placed in 5µm filtered seawater in test tubes for larval counts and size measurements using a light microscope with a camera attachment. The oysters were placed in a circular well in order to count the number of individuals in each of the following categories: alive and settled (large), alive and settled (small), alive and free, dead and settled, and dead and free. The oysters that remained on the 355µm screen were returned to silos and kept in the ambient tanks of the downwelling system for an additional five days to allow for more to undergo settlement and metamorphosis. These groups that were retained for an additional five days before being moved on to the upwelling system were referred to as the “redos”.

Phase TWO: Upwelling stage

The second phase of the experiment involved transferring the oysters that had metamorphosed into spat and were larger than 500µm to upwelling tanks. A total of eight 12ft upwelling tanks, each of which can fit 10 large silos, were used in this experiment. Each silo from the downwelling phase was transferred to its own silo in the upwelling phase, with the exception of the redos, each of which was mixed with another redo silo from the same larval batch in order to conserve space. The upwelling silos used at the start of the experiment each had a 500µm mesh screen; after several weeks, the oysters were transferred to silos with 2mm screens. All of the upwelling tanks were filled with a continuous flow of ambient water from the Patuxent River. As with the previous phase, water quality measurements were taken twice daily, in the morning and afternoon, using a YSI probe. A chlorophyll sample was taken every day at noon. Each silo in the upwelling tanks was cleaned every day to remove waste.

After the oysters had been in the upwelling tanks for two weeks, the total wet weight and wet volume of the oysters was taken. Two weeks were allowed to elapse before the start of this procedure because of immense bryozoan growth that would have interfered with the measurements. The weight and number of oysters in three aliquots was taken from each silo each week. A fourth aliquot was frozen for later size analysis. Starting at week 3, a portion of the oysters in each silo was transferred to bags in the Patuxent, and no more measurements were performed on these oysters. For each batch, at whatever week <15% of the oysters were smaller than 2000µm (i.e. retained on the 2mm sieve, not the actual sizes), all the oysters above 2000µm in size were moved to an identical upwelling tank setup with the only difference being that the silos have 2000µm screens. Weight and volume measurements were taken each week.

Calculations

For each aliquot taken on day 0 (the day each batch of oysters came in), the number of larvae counted was divided by the aliquot weight to get the total number of larvae per gram. The hatcheries had each provided their own estimates of the number of larvae they had shipped, but we wanted to compare their numbers with our own. To do so, the average number of larvae per gram estimated from the aliquots was multiplied by the total weight of the larvae from each batch (minus an averaged filter weight). The resulting numbers were compared with the hatchery numbers using a percent increase calculation. The average estimated number of larvae per gram for each batch was multiplied by the weight of larvae added to each silo to get an estimated number of larvae per silo.

In order to calculate the percent of larvae that settled in each silo, the weight in each silo was divided by aliquot weights and that quotient was multiplied by the estimated number of oysters that had settled in each aliquot (scaled up from the aliquot counts). Averages were taken to get the average settlement success among the 500µm portions in both the ambient and filtered treatments. Mortality was calculated in a similar fraction, except instead of using the number of settled spat, the total number of oysters at the end of the downwelling phase was used, and percent decrease from the estimated initial number was calculated.

The program Infinity Capture was used to take the images at day 0 and day 8 of the downwelling phase. The program ImageJ was then used to measure the longest axis of each oyster in the images. All the lengths of the day 0 larvae and the lengths of the 500µm portion of the settled oysters at Day 8 were taken and used to calculate an average growth. The 500µm portion was focused on for all calculations because settlement was operationally defined as those oysters that were larger than 500µm.

An average increase in volume and weight were arrived at by calculating a percent increase using the total volume/weight from one week and the volume/weight carried over from the previous week. These values were averaged to get one for the oysters from the filtered treatment and one for those from the ambient treatment. A weight per 1000 oysters was calculated by dividing the aliquot weights by the number of oysters counted and multiplying by 1000.

Paired t-tests were performed to determine whether settlement and mortality differed in a statistically different way between settlement cues and treatments. An alpha of 0.05 was used for all tests.

Results

The hatchery estimates and our estimates for the number of larvae at the start of the experiment were similar for Source 3 and Source 4 (less than 6% difference), but quite different for Source 1 and Source 2 (see Table 1).

Settlement success (Fig. 4) was significantly higher for the oysters that were exposed to epinephrine than it was for those that were raised on cultch. In the ambient treatment, the difference was about 16.5%, with a p-value of 3.97E-07; in the filtered treatment, it was about 12.5%, with a p-value of 2.034E-05. Settlement success was overall higher in the ambient treatment than it was in the filtered treatment. The ambient epinephrine oysters had about 15.6% higher settlement success than the filtered epinephrine oysters, with a p-value of 7.55E-06. The ambient cultch oysters had about 11.6% higher settlement success than the filtered cultch oysters, with a p-value of 4.93E-05. Mortality (Fig. 5) was significantly lower among the epinephrine oysters than among the cultch oysters. In the ambient treatment, the difference was about 16.6%, with a p-value of 4.53E-07. In the filtered treatment, the difference was about 12.6%, with a p-value of 2.19E-05. Mortality was also significantly lower in the ambient treatment than in the filtered treatment. For the epinephrine oysters the difference was about 15.6%, with a p-value of 8.70E-06. For the cultch oysters the difference was about 11.6%, with a p-value of 5.57E-05. In the ambient treatment, growth during the ambient phase was similar when comparing the cultch and epinephrine oysters. In the filtered treatment, growth was slightly higher for the epinephrine oysters, though it has not yet been determined whether this difference is significant (Fig. 6).

The data for percent increase in volume and percent increase in weight showed a spread at Week 3 between the different combinations of treatments and inducers, with a smaller spread in Weeks 4 and 5. Weeks 4 and 5 show that growth in terms of both volume and weight is similar among treatments and inducers. Week 3 shows that the epinephrine oysters from the filtered treatment had the highest percent increase from the previous week in both volume and weight, followed by the cultch oysters from the filtered treatment (Fig. 7 & Fig. 8). The weight per 1000 oyster data show similar growth rates for all inducers and treatments (Fig. 9).

Discussion

The main goal of this project was to determine the viability of using epinephrine to induce settlement in Eastern oyster larvae compared to cultch. The results show that epinephrine is viable for several reasons: it leads to higher settlement success, lower initial mortality, and similar long-term growth. Moving on with this project, it is important that the mortality is calculated, and the sizes measured from the spat in the upwelling treatments, in order to

determine if epinephrine has an effect on these metrics. As shown in Table 1, Coon et al. found that the use of epinephrine led to a 60% settlement success for *C. virginica* larvae (1986). This is not far off from the value of about 54% arrived at in this study for the epinephrine oysters raised in ambient water. Interestingly, *Crassostrea gigas*, an oyster in the same genus as the Eastern oyster, was able to achieve a settlement success of over 90% when exposed to epinephrine (Coon et al. 1986, Nicolas et al.1998). This illustrates that even within the same genus, different species have different reactions to inducers and different settlement success under the same or similar conditions. This is why it is important to examine the effects of epinephrine on a species level.

It was interesting to find that the calculated counts diverged greatly from the calculated counts for Source 1 and Source 2, but were relatively close for Source 3 and Source 4 (Table 3). This shows the importance of using a consistent methodology to estimate total counts, especially considering how important those estimates were for so many of this project's calculations.

Source 4, the only source to which the epinephrine experiment applied, was a triploid Lola. Given that oyster strains are selected for their different properties, it would be a good future direction to repeat this experiment on other strains, both triploids and diploids. It is also important that statistical analyses are performed on the data from this study to determine which results are and are not statistically significant. Furthermore, a toxicology analysis could be done on the oysters that were exposed to epinephrine in order to determine whether the hormone persists in their tissues, which could have implications for the health of humans eating oysters that were induced to metamorphose by epinephrine.

Conclusion

Overall, epinephrine seems to be a viable way to induce settlement and metamorphosis of *C. virginica*. It led to higher settlement success in both treatments, as well as lower initial mortality and similar or higher initial growth. Given also that the longer-term growth of the epinephrine oysters was similar to that of the cultch oysters, it is reasonable to think that the use of epinephrine would help improve the efficiency of hatcheries and aquaculture efforts. The overall higher settlement success, higher growth, and lower mortality in the ambient treatment suggests that ambient water is a better option for raising oysters than filtered water. While the results of this study are promising, more analysis and gathering of data is required, and the steps taken here should be repeated with other strains of oysters, as well as with larvae from different sources.

Acknowledgements

I would like to thank my mentor, Dr. Carys Mitchelmore, for all her help and guidance this summer. I would like to extend my thanks to Dr. Tom Miller for additional assistance with my project and for the use of his lab. I would also like to thank Skyler Golt, for always being willing to help and to lend advice. In addition, I owe a debt of gratitude to Dr. Mike Allen and the Maryland Sea Grant for sponsoring my participation in the REU program, and well as to the National Science Foundation for funding my stay here. I also would like to thank MIPS and NSF grant OCE-1756244 for funding this research project.

References

Beck, M. W., R. D. Brumbaugh, L. Airoldi, and others. 2011. Oyster Reefs at Risk and Recommendations for Conservation, Restoration, and Management. Bioscience 61: 107–116. doi:10.1525/bio.2011.61.2.5

Bonar, D. B., S. L. Coon, M. Walch, R. M. Weiner, and W. Fitt. 1990. Control of oyster settlement and metamorphosis by endogenous and exogenous chemical cues. Bull. Mar. Sci. 46: 484–489.

Coon, S. L., D. B. Bonar, and R. M. Weiner. 1986. Chemical production of cultchless oyster spat using epinephrine and norepinephrine. Aquaculture 58: 255–262. doi:10.1016/0044-8486(86)90090-6

Coon, S. L., D. B. Bonar, and R. M. Weiner. 1985. Induction of settlement and metamorphosis of the pacific oyster, *Crassostrea gigas* (Thunberg), by L-DOPA and catecholamines. J. Exp. Mar. Bio. Ecol. 94: 211–221. doi:10.1016/0022-0981(85)90059-0

García-Lavandeira, M., A. Silva, M. Abad, A. J. Pazos, J. L. Sánchez, and M. Luz Pérez-Parallé. 2005. Effects of GABA and epinephrine on the settlement and metamorphosis of the larvae of four species of bivalve molluscs. J. Exp. Mar. Bio. Ecol. 316: 149–156. doi:10.1016/j.jembe.2004.10.011

Joyce, A., and S. Vogeler. 2018. Molluscan bivalve settlement and metamorphosis: Neuroendocrine inducers and morphogenetic responses. Aquaculture 487: 64–82. doi:10.1016/j.aquaculture.2018.01.002

Mackenzie, C. L. 2009. Causes underlying the historical decline in Eastern oyster (*Crassostrea virginica* Gmelin 1791) landings. J. Shellfish Res. 26: 927–938. doi:10.2983/0730-8000(2007)26[927:CUTHDI]2.0.CO;2

Mann, R., and E. N. Powell. 2007. Why oyster restoration goals in the Chesapeake Bay are not and probably cannot be achieved. J. Shellfish Res. 26: 905–917.

Mesías-Gansbiller, C., A. Silva, V. Maneiro, A. Pazos, J. L. Sánchez, and M. L. Pérez-Parallé. 2013. Effects of chemical cues on larval settlement of the flat oyster (*Ostrea edulis* L.): A hatchery approach. Aquaculture 376–379: 85–89. doi:10.1016/j.aquaculture.2012.11.022

National Research Council. 2004. Social and Economic Value of Oysters in the Chesapeake Bay, p. 100–119. In Nonnative Oysters in the Chesapeake Bay. The National Academies Press.

Newell, R. I. E. 1988. Ecological changes in Chesapeake Bay: Are they the result of overharvesting the American oyster, *Crassostrea virginica*. Understanding the Estuary: Advances in Chesapeake Bay Research. Chesapeake Research Consortium Publication. 536–546.

Nicolas, L., R. Robert, and L. Chevolot. 1998. Comparative effects of inducers on metamorphosis of the Japanese oyster *Crassostrea gigas* and the great scallop *Pecten maximus.* Biofouling 12: 189–203. doi:10.1080/08927019809378354

Turner, E. J., R. K. Zimmer-Faust, M. A. Palmer, M. Luckenbach, and N. D. Pentchef. 1994. Settlement of oyster (*Crassostrea virginica*) larvae: Effects of water flow and a water-soluble chemical cue. Limnol. Ocean. 39: 1579–1593.

Tables and Figures

Table 1. The maximum settlement success induced by various settlement cues on different species of bivalve.

Settlement Success of Various Bivalves Exposed to Settlement Cues

Reference	Species	Settlement Cue	Max settlement success
Nicolas et al. 1998	*Crassostrea gigas*	Epinephrine	~91%
		Jacaranone	Inhibited metamorphosis
		L-Dopa	<30%
		Control	~30%
	Pecten maximus	Epinephrine	~30%
		Jacaranone	~17%
		L-Dopa	~12%
		Control	~3%
Coon et al. 1986	*Crassostrea gigas*	Epinephrine	>90%
		Norepinephrine	~80%
		Control	<10%
	Crassostrea virginica	Epinephrine	~60%
		Control	<10%
Mesías-Gansbiller et al. 2013	*Ostrea edulis*	GABA	64.8%
		L-DOPA	~41%
		Epinephrine	~45%
		Norepinephrine	~40%
		IBMX	~40%
		Control	16.1%
Coon et al. 1985	*Crassostrea gigas*	L-DOPA	20-50%
		Epinephrine	>90%

		Norepinephrine	>80%
García-Lavandeira et al. 2005	*Mytilus galloprovincialis*	GABA	68%
		Epinephrine	63%
		Control	24%
	Venerupis pullastra	GABA	76%
		Epinephrine	75%
		Control	53%
	Ruditapes philippinarum	GABA	71%
		Epinephrine	78%
		Control	22%
	Ostrea edulis	GABA	57%
		Epinephrine	54%
		Control	16%

Table 2. Settlement success of various bivalves exposed to epi at different concentrations and for different lengths of time.

Reference	EPI dosing concentration	EPI dosing time	Time at which settlement was measured	Species	Approx. settlement success
Nicolas et al. 1998	0.1mg/L	24hrs	1 week	*C. gigas*	70%
	0.2mg/L				75%
	0.5mg/L				82%
	1mg/L				84%
	2mg/L				82%
	5mg/L				89%
	10mg/L				75%
	1mg/L	0hrs			29%
		2hrs			86%
		6hrs			87%
		12hrs			91%
		24hrs			86%
		48hrs			85%
	0.1mg/L	24hrs	1 & 2 weeks	*P. maximus*	2%
	0.2mg/L				1%
	0.5mg/L				3%
	1mg/L				5%
	2mg/L				16%
	5mg/L				25%
	10mg/L				33%
	1mg/L	0hrs			1%
		2hrs			3%

		6hrs			10%
		12hrs			8%
		24hrs			18%
		48hrs			13%
Coon et al. 1986	10^-6M	24-48hrs	24-48hrs	*C. gigas*	2%
	10^-5M				65%
	10^-4M				84%
	10^-3M				0%
	10^-6M			*C. virginica*	0%
	10^-5M				18%
	10^-4M				61%
	10^-3M				0%
	10^-4M	0min		*C. gigas*	3%
		5min			25%
		10min			60%
		20min			73%
		40min			83%
		60min			82%
		24hrs			91%
Coon et al. 1985	10^-6M	24-48hrs			0%
	10^-5M				50-80%
	10^-4M				>90%
	10^-3M				<10%
	10^-4M	5min			25%
		10min			60%
		20min			70%

		40min			83%
		60min			80%
		24hrs			90%

Table 3. Comparison of hatchery estimates of the total number of larvae at beginning of experiment compared to our estimates, calculated by scaling up aliquot counts.

Hatchery Estimates of No. of Larvae Vs. Our Estimates

	Hatchery Estimate of Total # Larvae	**Our Estimate of Total # Larvae**	**% Higher**
Source 1	1500000	2168341	44.56
Source 2	1500000	2725306	81.69
Source 3	1500000	1546606	3.11
Source 4	2500000	2645653	5.83

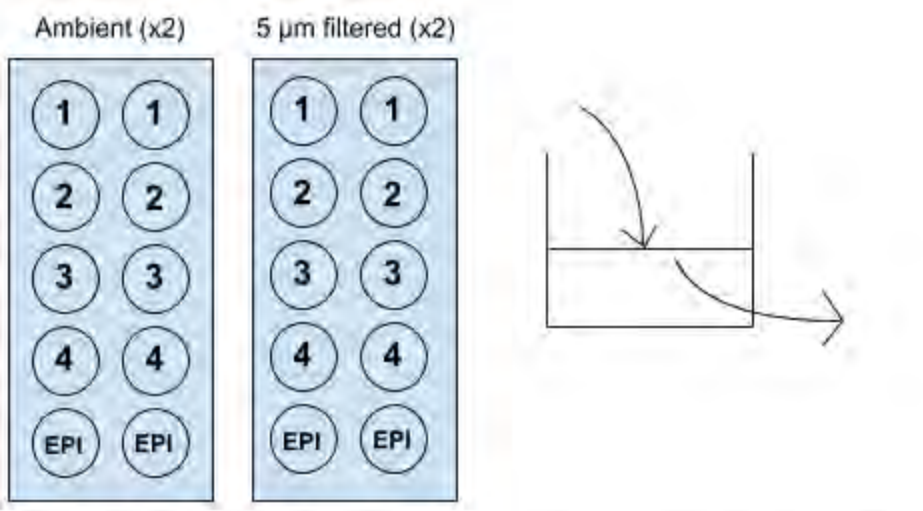

Figure 1. Setup of the downwelling tanks. The rectangles are tanks, and the circles are silos each with an aliquot of oysters from a single source. The number 1 represents oysters from source 1; 2 represents oysters from source 2; 3 represents oysters from source 3; and 4 represents oysters from source 4. EPI represents oysters from source 4 that have been treated with epinephrine for 2 hours. The schematic on the left represents an overhead view of the downwelling tanks; the schematic on the right represents a side view of one of the silos, with the arrows showing water flow.

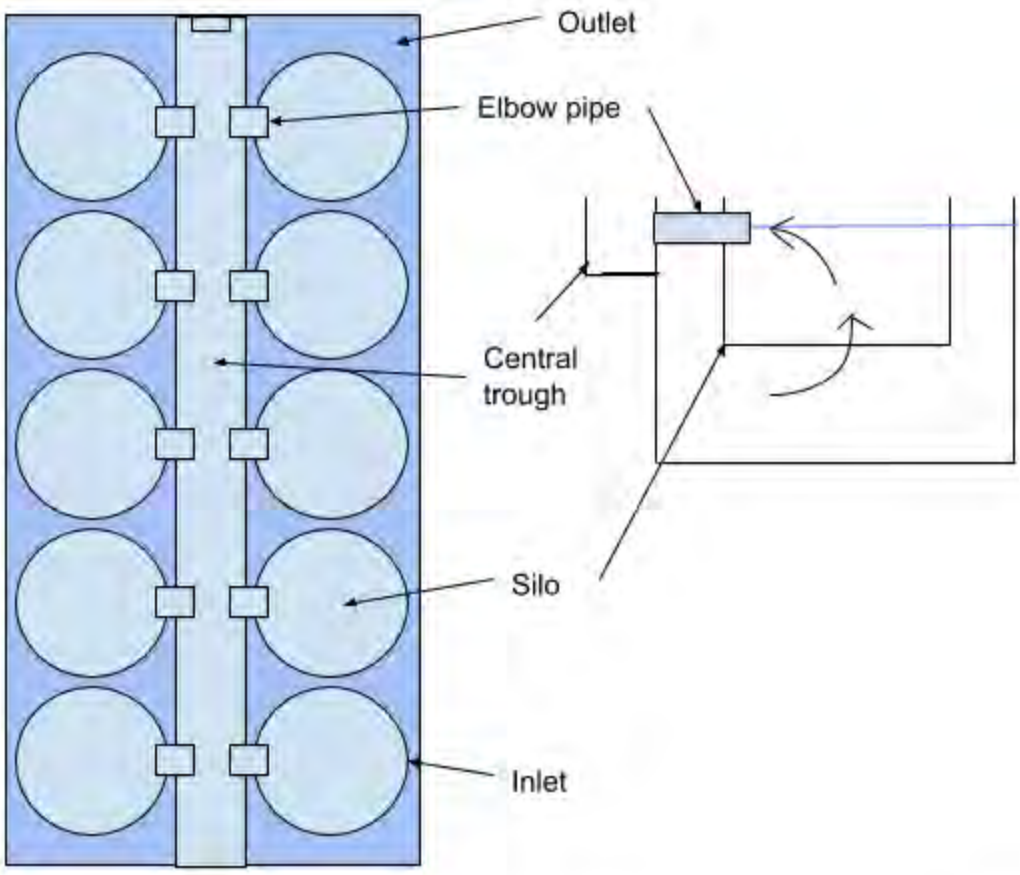

Figure 2. Setup of an upwelling tank. The schematic on the left shows an overhead view of the layout of an upwelling tank. The schematic on the right shows a cross-section, with arrows indicating water flow.

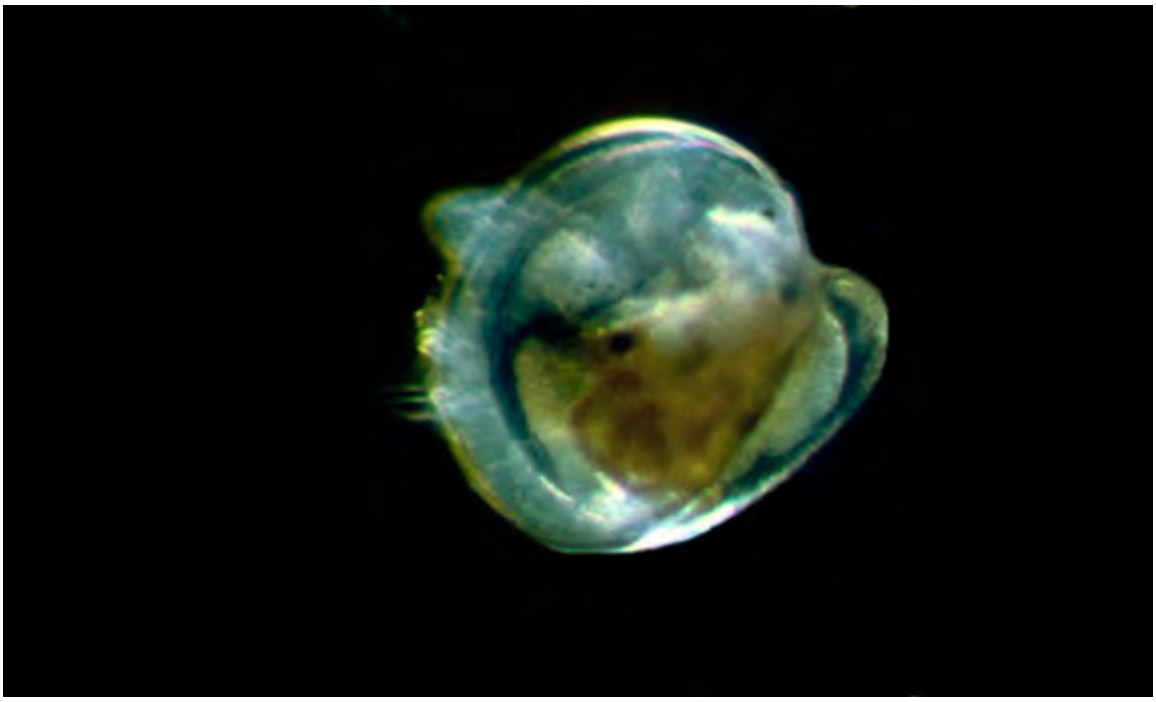

Figure 3. A competent oyster larva, with eyespot and searching foot. (From http://hatchery.hpl.umces.edu/facilities/follow-the-path-of-an-oyster/)

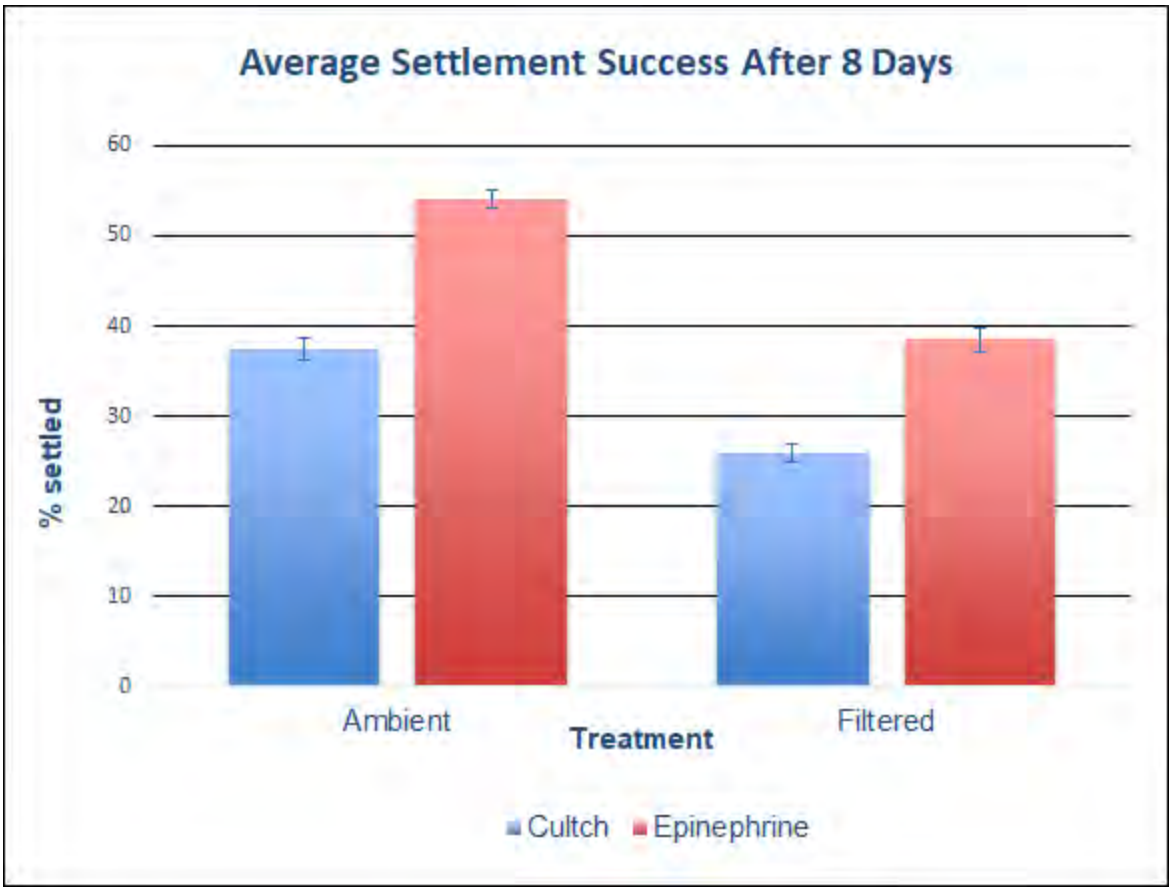

Figure 4. Average settlement success after 8 days for the 500µm portion of each silo. The blue bars represent the oysters raised on cultch; the red bars represent those exposed to epinephrine. Error bars represent standard error of the mean.

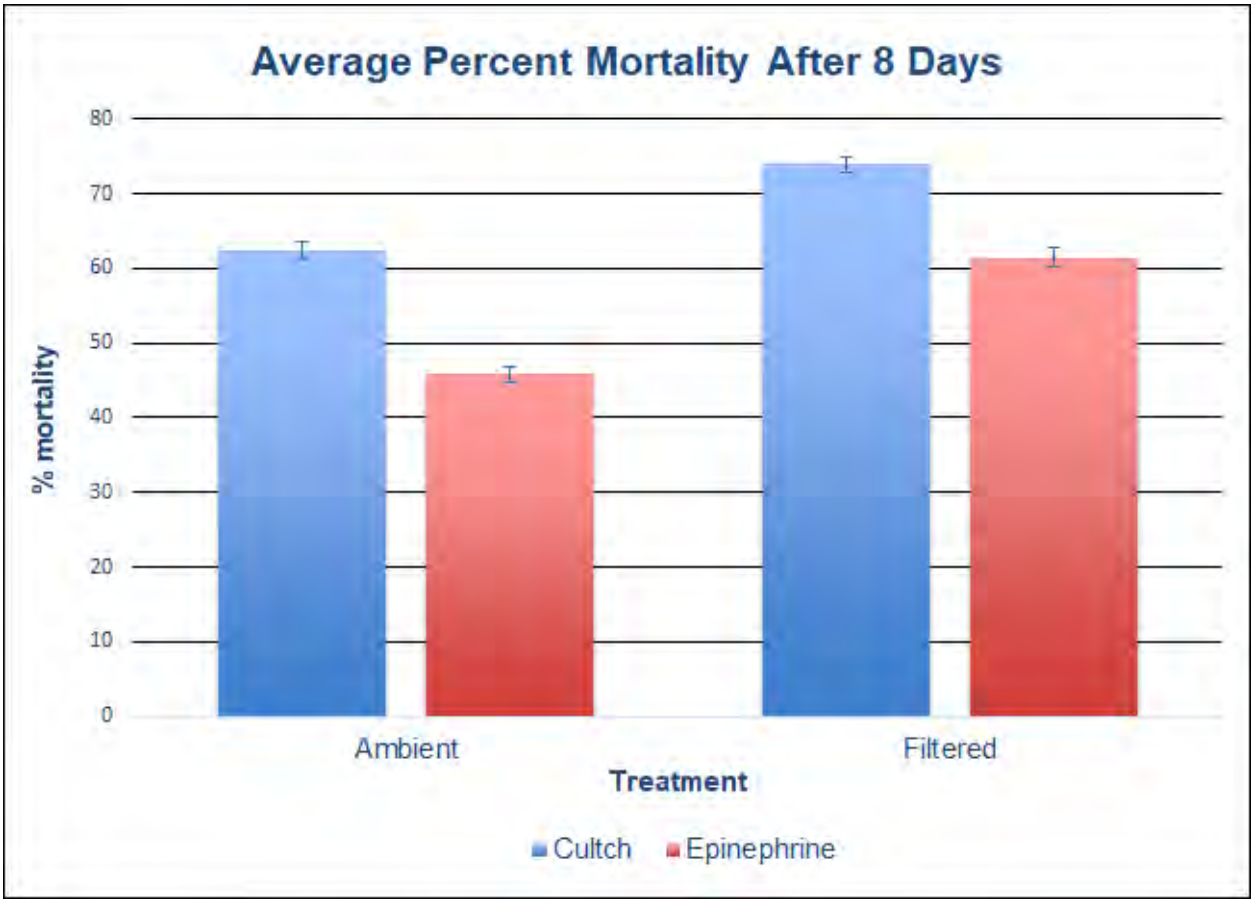

Figure 5. Average percent mortality after 8 days for the 500µm portion of each silo. The blue bars represent the oysters raised on cultch; the red bars represent those exposed to epinephrine. Error bars represent standard error of the mean.

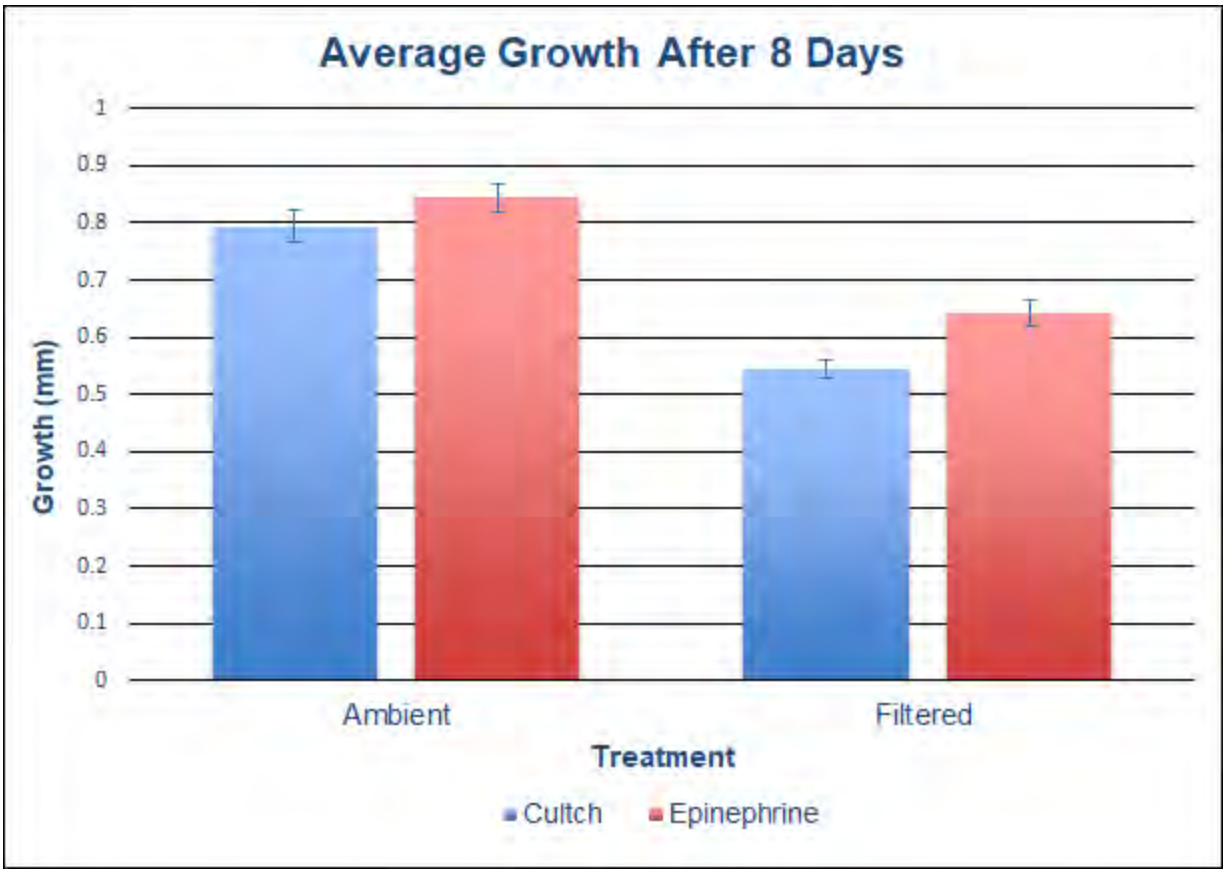

Figure 6. Average growth after 8 days for the 500µm portion of each silo. The blue bars represent the oysters raised on cultch; the red bars represent those exposed to epinephrine. Error bars represent standard error of the mean.

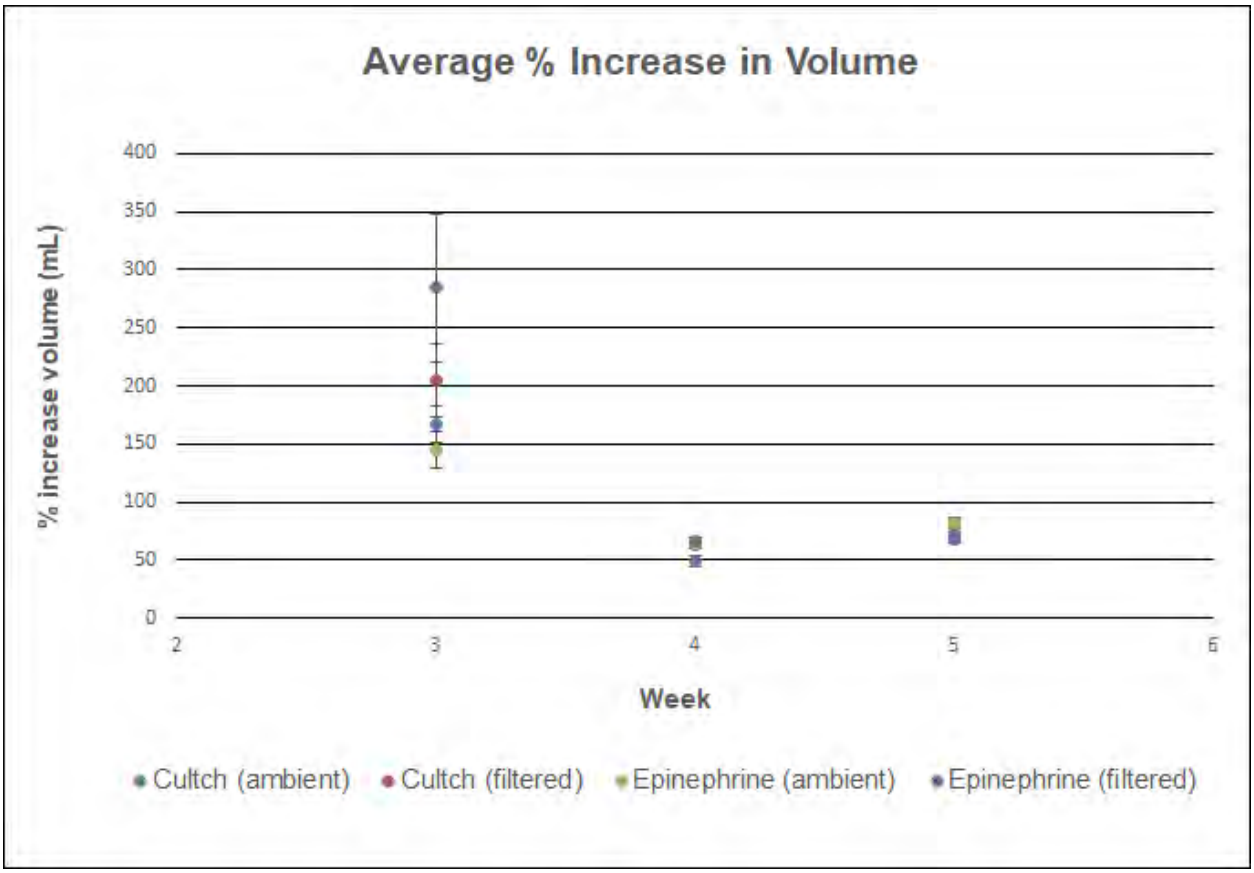

Figure 7. Average percent increase in volume from the previous week for weeks 3–5 (upwelling phase). Error bars represent standard error of the mean.

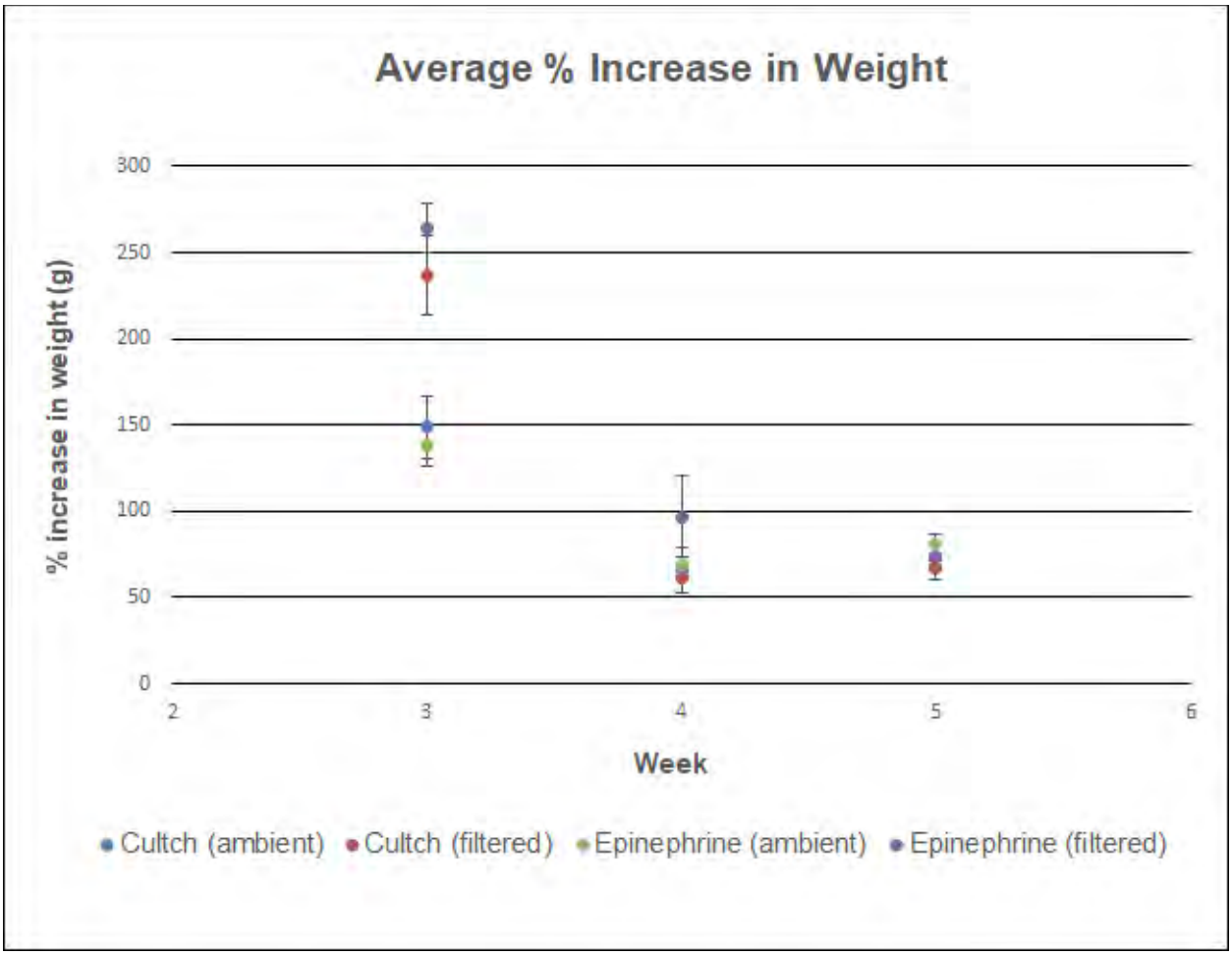

Figure 8. Average percent increase in weight from the previous week for weeks 3–5 (upwelling phase). Error bars represent standard error of the mean.

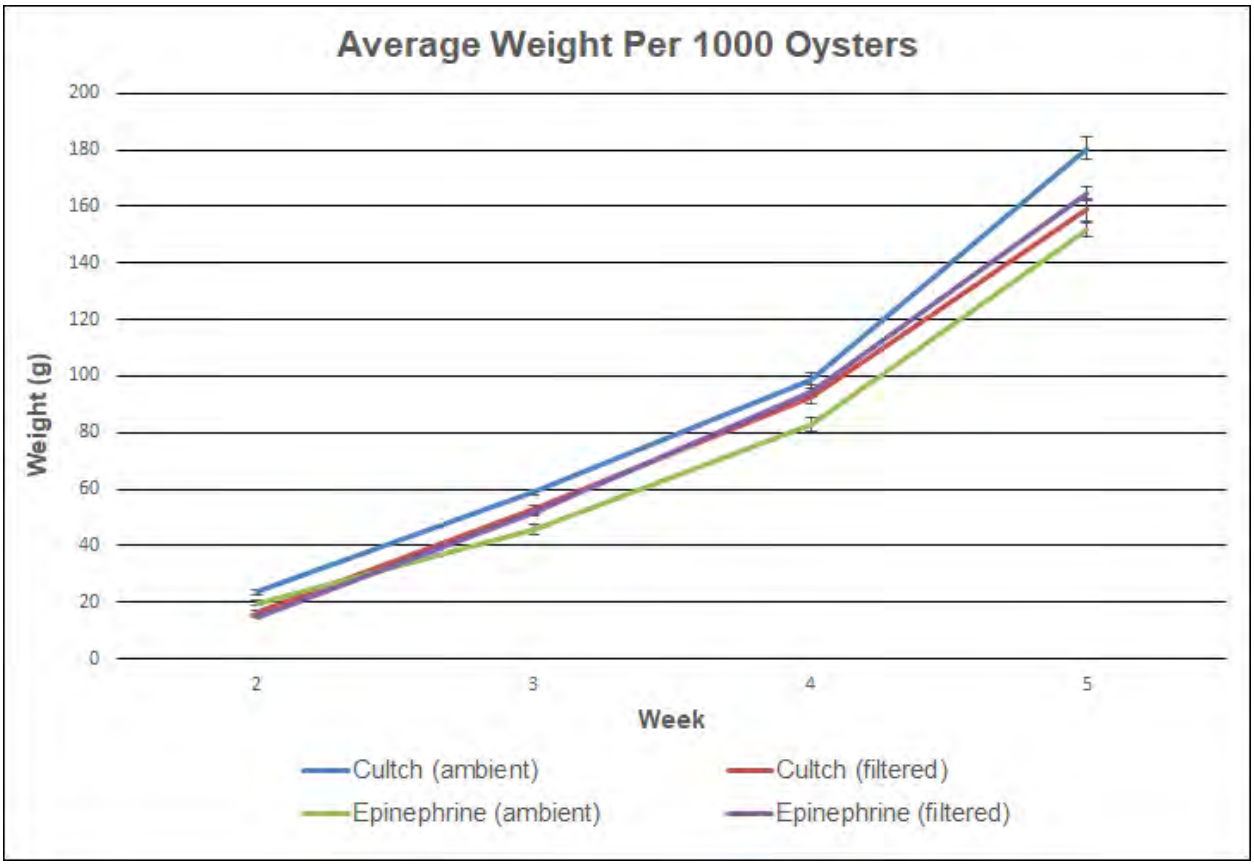

Figure 9. Average weight per 1000 oysters for weeks 2–5 (upwelling phase). Error bars represent standard error of the mean.

Quantifying energetics and scope for growth of different strains of the Eastern Oyster, *Crassostrea virginica*

Hannah Haskell, REU Fellow
Maryland Sea Grant

Thomas Miller, Professor and Director
Chesapeake Biological Laboratory, University of Maryland for Environmental Science

Abstract

Oyster aquaculture has found success in using a variety of oyster strains which have been developed to perform in specific environmental conditions. Strains differ in areas such as disease resistance, salinity tolerance, and growth rates. Although differences in growth rates among strains has been observed, the physiological cause of the growth differences remains unknown. The goal of this study was to investigate and begin to quantify the bioenergetic budget of oysters, specifically the relationships among environmental variables, respiration rate and growth. It was predicted that the faster-growing strain would have the lowest respiration rate and therefore more energy leftover to dedicate towards growth. This study utilized microrespirometry methods using Firesting O_2 fiber-optic oxygen probes to measure changes in oxygen concentration within the vials. Trials were run at various temperature and salinity combinations chosen to reflect the variation typical of the Chesapeake Bay. Changes in oxygen concentrations were converted to respiration rates and data was analyzed using response surface methodology. ANOVA results indicated that strain effects were not significant ($F=1.0122$). Some aspects of the results supported the hypothesis and other aspects were in conflict with the hypothesis such that an overall conclusion is not possible, and more work needs to be done in order to understand the bioenergetics of oysters.

Introduction

The Eastern Oyster, *Crassostrea virginica*, hereafter oyster, is commonly found along the east coast of North America and is a prominent component of the Chesapeake Bay ecosystem (National Research Council 2004). The oyster provides important ecosystem services within the Chesapeake Bay, including filtering of primary production leading to impacts on nutrient cycling, trophic services and food production for human consumption (Coen et al. 2007). Long-term declines in oyster in the Chesapeake Bay and in other coastal estuaries, resulting largely from overfishing and habitat decline, have compromised the provisioning of these services (Rothschild et al. 1994, Jackson et al. 2001). This has led to efforts in the Chesapeake Bay and elsewhere to undertake large scale ecosystem restoration (Coen et al. 2007) and to develop aquaculture (Maryland Sea Grant 2010).

Substantial work has been undertaken to develop strains of oysters that support successful aquaculture (e.g., Calvo et al. 2003). In the late 1970s, a graduate student at the University of

Maine's Darling Marine Center was the first to develop the triploid oyster (Hollier 2014). Since then, the use of triploid oysters has grown to dominate the aquaculture industry (Fincham 2010). Triploid oysters are typically sterile and are therefore able to dedicate more of their energy into growth rather than reproduction. This proves advantageous as these triploids are not only larger than the normal diploid oysters but can also be harvested in the summer months when native oysters are typically spawning (Hollier 2014). The aquaculture industry has taken the concept of an ideal oyster even further by now breeding different strains of triploids that are optimal at local environmental conditions.

Despite being initially selected for disease resistance, strains tend to vary from one another in other areas such as salinity tolerance and growth rates. Researchers at the Chesapeake Biological Laboratory are currently examining the production dynamics of oysters in aquaculture. Specifically, the project is working to determine settlement success, and subsequent growth and production for wild diploid oyster and two triploid strains known as lola and deby. As part of their studies, these researchers have demonstrated that there is a difference in growth rate among strains of oysters with lola appearing to grow at faster rate than deby and diploid (Mitchelmore et al. 2018, report). Figure 1 shows the difference in growth rates can be seen between strains even in only a two-week time interval. Although the differences in growth rate between strains is recognized, there has yet to be any substantial work done to try and determine the underlying physiological causes of these differences in growth. Knowledge of why certain strains grow faster than others can be used to forecast growth and meat yield of oysters under a range of future climate conditions. Such models have the potential to save time and money and help further advance the growing aquaculture industry.

Bioenergetics provide a useful foundation within which to understand growth differences (Wooton 1990, Kooijman 2000). Bioenergetics refers to an understanding of how the energy consumed by an individual is allocated among various biological processes such as metabolism and waste production (Figure 2). This pattern of allocation, often termed an "energy budget," can differ among individuals, genotypes, strains and species. Understanding the energy budget of an animal can help explain its growth, its reproductive strategy and ultimately its fitness (Kooijman 2000). Energy budgets often consider an individual's growth as an emergent property that results from the investment of any surplus energy once all vital processes (metabolism, digestion, respiration) have been provisioned (Wootton 1990). For instance, if an organism has just eaten a large meal it will need to allocate more of its energy into digestion and therefore less energy is available to be put towards other metabolic processes (Figure 2). Expressed mathematically, the energy budget can be represented as

$$\text{Growth} = \text{Consumption} - (\text{Respiration} + \text{Digestion} + \text{Fecal Production} + \text{Waste}) \quad (1)$$

This equation explicitly shows growth as an emergent process determined by the differences between consumption and metabolic costs. For many species, the costs of digestion, fecal production and nitrogenous waste are simple proportions of consumption. Thus, a simplified version would be expressed as

$$\text{Growth} = f(\text{Consumption}) - \text{Respiration} \quad (2)$$

where f(Consumption) is the proportion of consumption remaining after all metabolic costs other than respiration have been paid.

In this study the energetics of a wild diploid and two strains of triploid oysters, known as lola and deby, will be compared in order to determine how they differ in terms of energy distribution.

Hereafter the three different types of oysters will be referred to as three strains for the sake of simplicity. Considering an oyster's bioenergetics within an energy budget framework would suggest that differences in the growth between each of the three strains could result from differences in the energy consumed or in respiration rates. Given that the oysters are growing in the same environment, respiration rates of the three strains will be compared, assuming that feeding and other metabolic rates are fixed. With the knowledge that lola grows at a faster rate than deby or diploid, one might anticipate lola to have a lower respiration rate (i.e., less oxygen consumption) and therefore more available energy to dedicate to other metabolic processes such as growth.

Previous studies have found external factors such as temperature and salinity to have an effect on oyster respiration rates. When studying respiration in the subtidal flat oyster Dunphy et al.(2006) found that oysters held at 20°C had significantly higher oxygen consumption rates than those held at 10°C or 15°C. These results indicate a possible relationship between temperature and respiration rate. In a similar study looking at the effect of salinity on respiration rates in the eastern oyster, Casas et al. (2018) observed that during the summer, oxygen consumption was significantly greater at salinities of 15 and 25 compared to lower salinities. Based on the results of these studies, oxygen consumption will be measured as a function of temperature and salinity. This is to ensure that any differences in rates are a result of strain difference rather than external factors favoring one strain over the other.

The objective of the study is to compare the respiration rates of the three strains, lola, deby, and diploid with the overall goal of determining why the strains grow differently. Respiration rate was chosen to act as a proxy for metabolism efficiency which can then potentially be used to explain the apparent growth differences between the two strains. Each strain will be exposed to various levels of external factors (temperature and salinity) with the intent to eliminate the possibility of the observed respiration rates being a result of any of these factors rather than strain difference.

Hypothesis 1: Strain has no effect on respiration rate as a function of temperature and salinity conditions.

Hypothesis 2: Lola grows faster than deby and diploid oysters and will therefore exhibit a lower respiration rate than deby and diploid as a function of temperature and salinity conditions.

Materials and Methods

Oysters of each strain were raised in a commercial upwelling system in ambient water conditions. Oysters were sampled from upwelling tanks for use in respiration trials. Oysters used in the study were between 38–46 days old and varied in size from 10.1–617.4 mg dry weight. The study consisted of a replicated complete block experimental design in which the respiration rates of oysters from each strain were measured simultaneously in trials over a range of temperature and salinity conditions. Each trial included eight vials, six experimental vials containing oysters, and two blank vials that served as control. Each trial was replicated four times.

Microrespirometers were used to measure the respiration rates of the three oyster strains. Eight 25 mL capped vials were placed within a single temperature-controlled recirculating tank (Isotemp, Fisher Scientific Inc, Pittsburgh, PA). Each vial containing a three to five oysters, with the number adjusted to try to control the level of oxygen depletion, had a removable ring around it where the oxygen probes could be inserted, and a temperature sensor was inserted into a separate vial filled with water. Fiber-optic oxygen probes were used to measure O_2

concentration in the vials (FirestingO_2, Pyroscience, Aachen, Germany). The concentration of O_2 over time was then corrected into a respiration rate by comparing the experimental values to those of the control vials, this can be expressed as

$$\text{Respiration Rate} = \left[\left(\frac{mgO_{2final} - mgO_{2initial}}{time}\right) - \text{blank correction}\right] \times \frac{\text{vial volume}}{\text{oyster mass}} \quad (3)$$

Dimensional analysis indicated that respiration rates are expressed as mg O_2/g/s.

Trials were conducted over a range of temperatures and salinities. The chosen temperatures ranged from 16 to 28°C and salinity values ranged from 2 to 24 reflecting the possible variation of temperature and salinity conditions in the Chesapeake Bay. A series of trials involving each strain as well as blank controls were run for an hour at varying temperature and salinity combinations with the hopes that O_2 levels would not drop low enough to the point where they induce a stress response in the oysters. Past studies had found success by measuring O_2 levels for 30 minutes or until levels declined to 70% saturation (Dunphy et al. 2006). Once trials were complete, an initial wet weight of the oysters in each vial was recorded. Oysters were then put into a desiccation chamber followed by 48 hours in an oven to collect the overall tissue mass.

Results of all trials were combined into a single response surface analysis. This study was a three factor (strain, temperature, salinity) factorial experiment, in which strain is a fixed effect and temperature and salinity are random effects. Responses to each environmental variable were modeled as a quadratic second order model with interactions. Response surfaces were fit to the combined data using strain as a factor. Models that included or ignored strain effect were compared using ANOVA and a one-way F statistic was used to determine whether or not strain effect was significant. All models were fit in the rsm package within the R statistical environment.

Results

Figures 3 and 4 show the response of strains to a single factor. Figure 3 shows the respiration rate response to temperature and Figure 4 shows the response to salinity for each strain. Respiration rate response to temperature seemed to vary among strains with an overall trend of an increase in respiration rate as temperature increases. Lola appeared to have the greatest response to the changes in temperature (Figure 3). Respiration rate responses to changes in salinity were not as variable among strains, with each strain having a peak respiration rate around a salinity of 8.

Combined response surfaces for all three strains are shown in Figure 5. Each of the strains appear to have a peak respiration rate at an approximate salinity of 9. Peak respiration appears to occur at different temperatures for each strain with diploid having peak respiration around 24°C, lola's occurs at 28°C, and deby exhibits a peak respiration at 21°C (Figure 5). Referring to Figure 5, where the two blue lines intersect represents the typical salinity and temperature conditions of the Chesapeake Bay. In these specific conditions, the diploid strain has a respiration rate of approximately $6e^{-4}$ mg O2/g/s, lola's is around $7e^{-4}$ mg O2/g/s, and debys is approximately $3e^{-3}$ mg O2/g/s (Figure 5). An analysis of variance comparing models that included or ignored strain effect found strain effect not significant (F= 1.0122, Table 1).

Discussion

Respiration rate differences among strains were much more apparent in response to temperature than in salinity. Salinity does not appear to have a large effect on respiration rate among strains. Based upon our initial hypothesis, it was predicted that lola would have the lowest respiration out of the three strains and that would explain the apparent differences in growth as lola would have more energy leftover to dedicate towards growth. When looking at the temperature and salinity conditions typical of the Chesapeake Bay (where lines intersect in Figure 5) lola has a lower respiration rate than deby which supports our initial hypothesis as lola grows at a faster rate than deby. However, when comparing lola to diploid in these same conditions, diploid has the lower respiration rate out of the two which goes against our initial hypothesis. Although comparing lola to deby supports our hypothesis the fact that the same does not hold true when comparing lola and diploid indicates that a clear and direct relationship between respiration rate and growth does not appear to be present.

These results suggest that the foundation of our hypothesis—that growth is an emergent property of the difference between consumption and respiration—may not stand. Instead, it could be that respiration rate itself is a direct expression of consumption rates. Consumption in oysters is an active process (Casas et al. 2018). Thus, higher consumption rates would be supported by higher respiration rates. In this way, a higher measured respiration rate would be reflective of a higher growth rate. Determination of this possible pattern would require measurement of consumption rates, possibly through isotopically labelled food.

Moving forward it would be beneficial to repeat the experiment as described while also adding an additional element by raising oysters in ambient conditions as well as in a range of salinities and temperatures. The experiment reported here involves the measurement of respiration rate over a range of temperature and salinities. But the temperatures and salinities were applied acutely – that is they differed from the conditions in which the oysters were reared. Measuring respiration rates throughout the ranges of temperatures and salinities would allow for the measurement of chronic responses in addition to the acute responses. This would be beneficial as it gives us insight on not only how temperature and salinity immediately effect the energetics of oysters but also how oysters might respond to changing environmental conditions from a long-term perspective. When incorporating this long-term aspect into the experimental design another factor that might be worth accounting for would be respiration responses to changes in pH levels. Ocean acidity will likely change significantly within the years to come and understanding how that will impact the energetic processes of oysters would be beneficial for both aquaculture and wild population restoration.

Additionally, it might prove worthwhile to control for oxygen depletion within the trials. Analyzing our data and excluding any vials where oxygen concentration was depleted by more than 70% appeared to notably alter our response surfaces, especially for the lola strain. If oxygen depletion was specifically controlled for from the start, then it would reduce the possibility of respiration responses being a stress response as a result of low available oxygen concentrations and provide a more accurate representation of respiration rate for each of the strains.

Another possible direction to move towards would be to investigate other areas of the energetic budget and tease out any possible relationships that might explain the apparent growth differences better than respiration efficiency. For instance, look into whether or not respiration indicates anything about feeding rates among the strains and whether feeding rate appears to have a stronger correlation with growth rates. The bioenergetic budget of oysters is not well

understood and the scope for work within this area is substantial. If more knowledge could be gained within this field then it would provide many practical implications in both the aquaculture industry as well as ecosystem restoration. Understanding how oysters allocate their energy and how that differs between various strains would prove useful in developing models to help predict the potential growth and meat yield of oysters within a variety of environmental conditions. This has the potential to save oyster farmers significant amounts of time and money and help further the development and success of oyster aquaculture. Additionally, understanding how different salinity, temperature, and acidity conditions effect oyster bioenergetics would provide insight into how oysters might be affected as their natural environmental conditions change with time.

Conclusion

In conclusion, there were aspects of the results that supported the hypothesis and there were other aspects that were in conflict with the hypothesis such that an overall conclusion is not possible and clearly more work needs to be done in order to understand the bioenergetics of oysters in aquaculture systems and out in the wild as well.

Acknowledgements

Special thanks to Dr. Tom Miller for all of the support and guidance throughout the course of the summer. I would also like to extend my gratitude to Dr. Carys Mitchelmore for everything she has taught me over the past few months and to Skyler Golt for being there to help with anything and everything along the way. Thank you to Dr. Mike Allen, Maryland Sea Grant, and the National Science Foundation for making this REU program both possible and worthwhile. This study was supported by NSF grant OCE-1756244.

References

Casas, S. M., R. Lavaud, M. K. LaPeyre, L. A. Comeau, R. Filgueira, and J. F. LaPeyre. 2018. Quantifying salinity and season effects on eastern oyster clearance and oxygen consumption rates. Marine Biology 165: 1–13. doi:10.1007/s00227-018-3351-x

Coen, L., R. D Brumbaugh, D. Bushek, R. Grizzle, M. Luckenbach, M. H Posey, S. P Powers, and S. G. Tolley. 2007. As we see it. A broader view of ecosystem services related to oyster restoration.

Dunphy, B., R. M.G. Wells, and A. Jeffs. 2006. Oxygen consumption and enzyme activity of the subtidal flat oyster (*Ostrea chilensis*) and intertidal Pacific oyster (*Crassostrea gigas*): Responses to temperature and starvation.

Fincham, M. W. 2010. Trials & Errors & Triploids Odyssey of an Oyster Inventor. Chesapeake Quarterly, June

Hollier, D. 2014. Tasty Mutants: The Invention of the Modern Oyster. The Atlantic, September 29

Jackson, J. B. C., M. X. Kirby, W. H. Berger, and others. 2001. Historical Overfishing and the Recent Collapse of Coastal Ecosystems. Science 293: 629. doi:10.1126/science.1059199

Maryland Sea Grant. 2010. A Future for Oyster Farming? Chesapeake Quarterly, June

National Research Council. 2004. Nonnative Oysters in the Chesapeake Bay, The National Academies Press.

Ragone Calvo, L. M., G. W. Calvo, and E. M. Burreson. 2003. Dual disease resistance in a selectively bred eastern oyster, Crassostrea virginica, strain tested in Chesapeake Bay. Aquaculture 220: 69–87. doi:10.1016/S0044-8486(02)00399-X

Rothschild, B., J. Ault, G. Philippe, and M. Herald. 1994. Decline of the Chesapeake Bay oyster population: a century of habitat destruction and overfishing.

Wootton, R. J. 1990. Ecology of Teleost Fishes, Chapman & Hall.

Figures and Tables

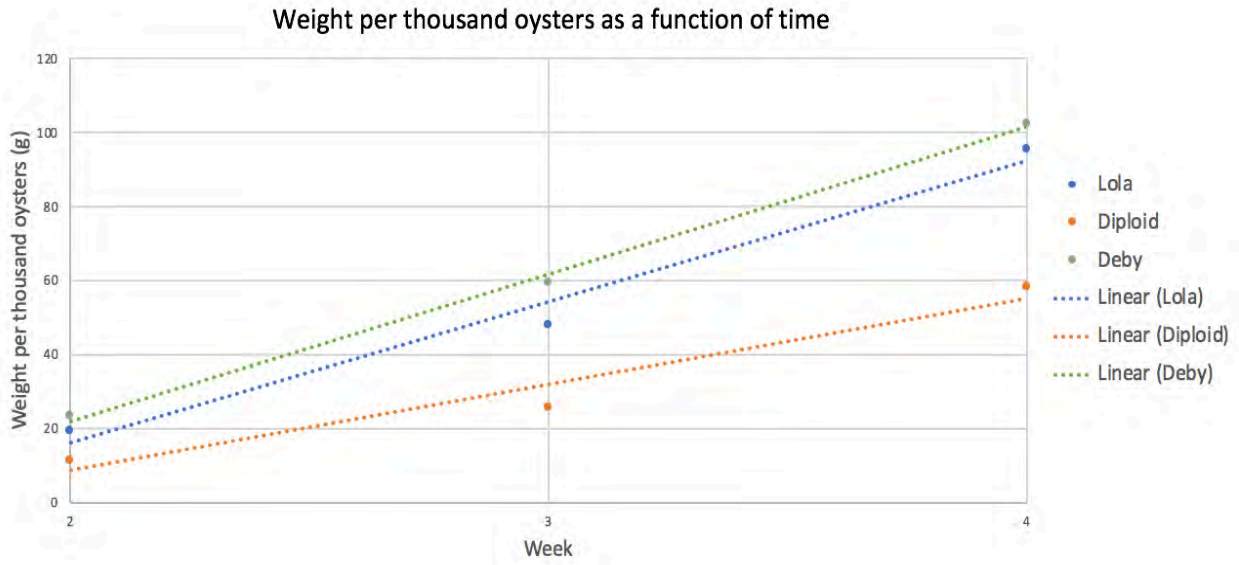

Figure 1. Differences in growth among strains over a two-week time period.

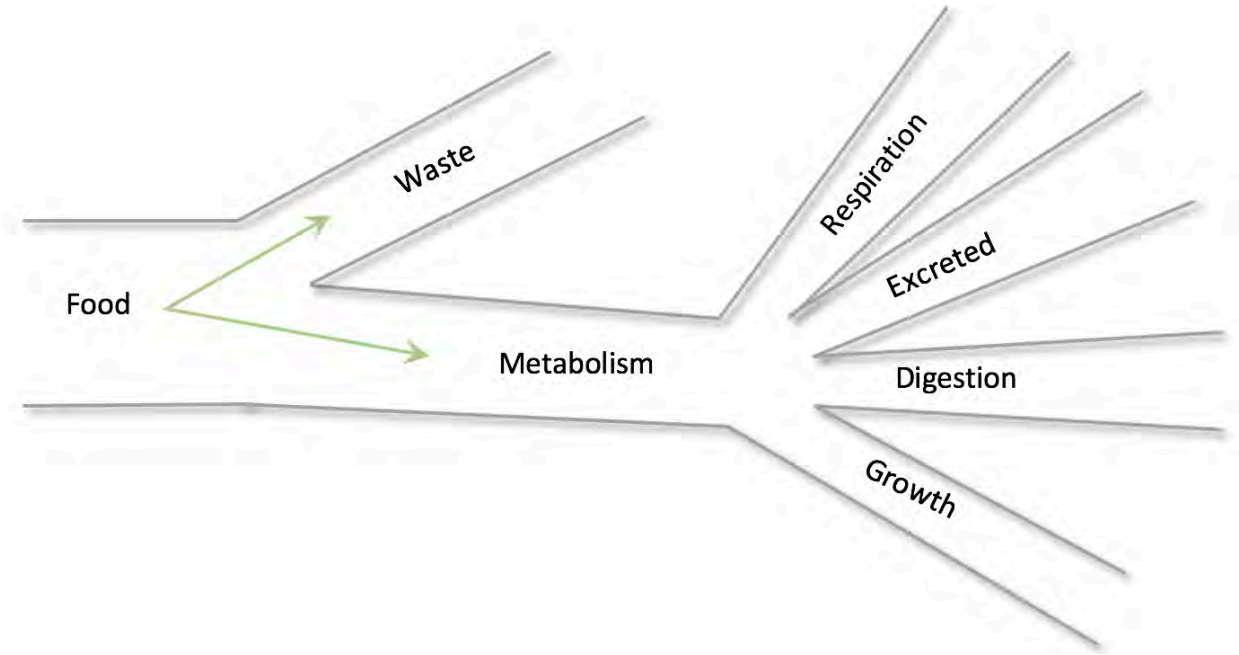

Figure 2. Bioenergetics schematic.

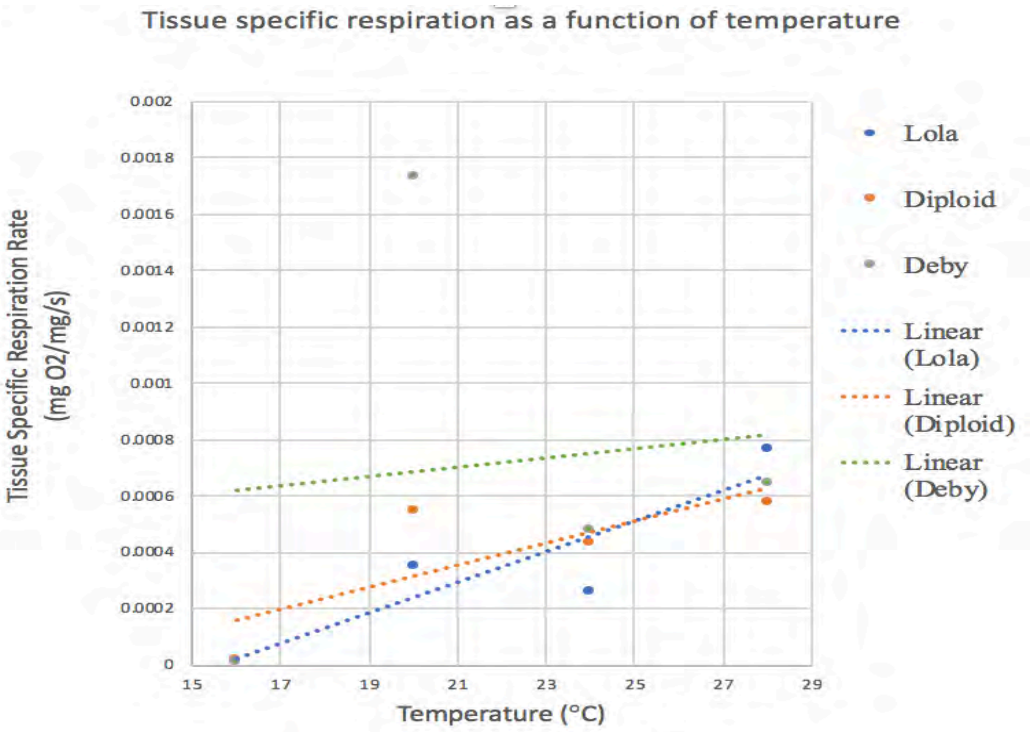

Figure 3. Tissue specific respiration rate as a response to temperature.

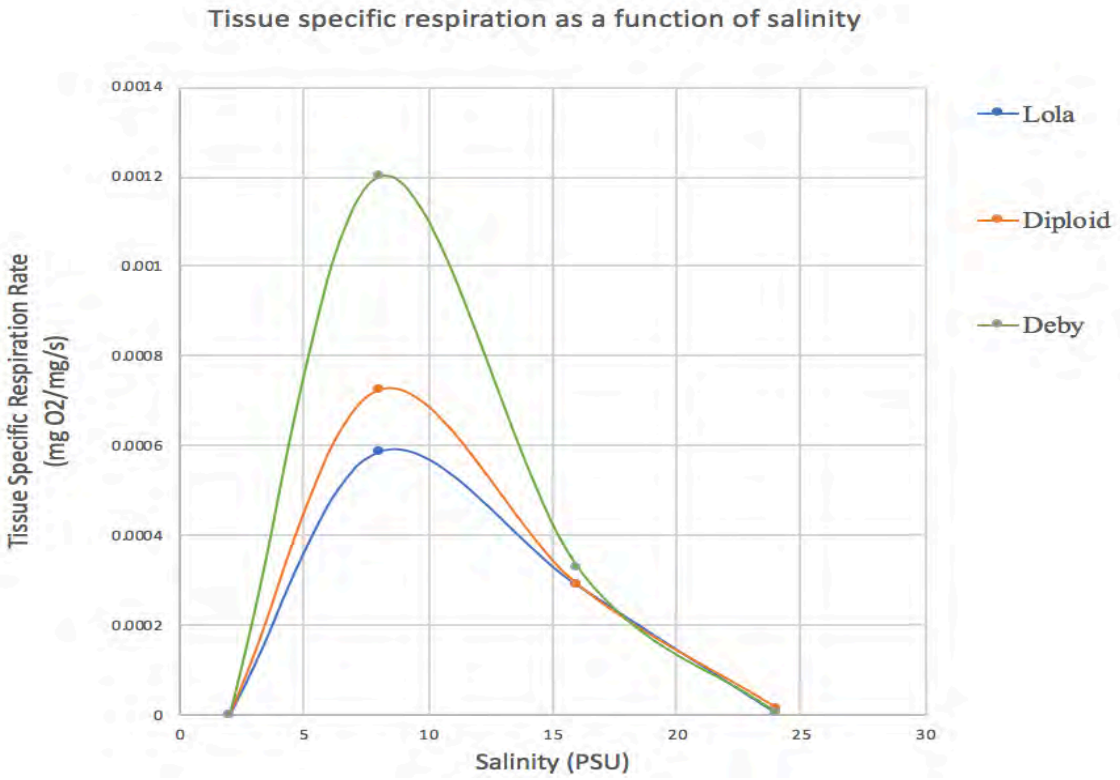

Figure 4. Tissue specific respiration rate as a response to salinity.

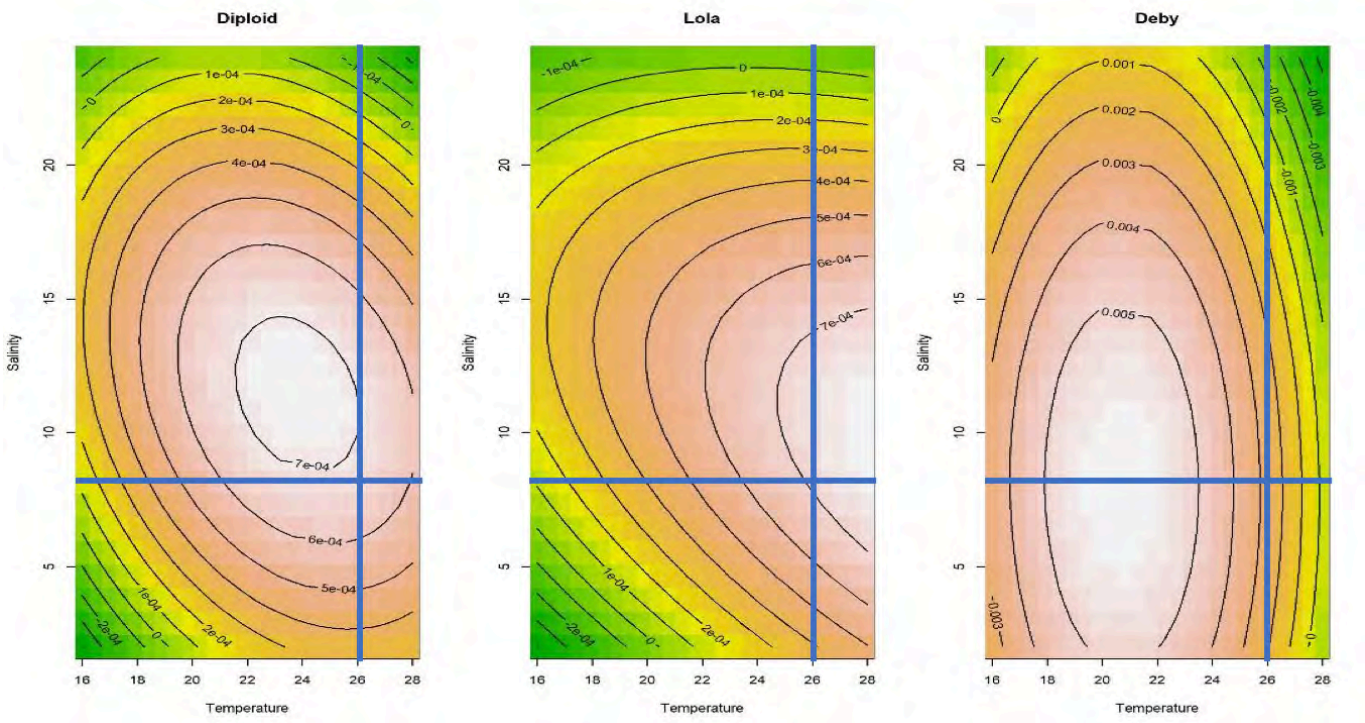

Figure 5. Response surface analysis results, intersection of the two blue lines represents environmental conditions typical of the Chesapeake Bay.

Table 1. Results from AVOVA

Analysis of Variance Table

	Res.Df	RSS	Df	Sum of Sq	F	Pr(>F)
1	186	0.0055044				
2	181	0.0053546	5	0.00014972	1.0122	0.4119

Greenhouse gas release from permafrost soil incubations under aerobic and anaerobic conditions at relevant soil temperatures

Lillian Henderson, REU Fellow
Maryland Sea Grant

Laura Lapham, Associate Professor
Chesapeake Biological Laboratory, University of Maryland Center for Environmental Science

Abstract

Studies have shown that thawing permafrost has the potential to release significant amounts of greenhouse gases directly to the atmosphere. Yet, some areas of the world with continuous permafrost-containing mineral soils have not been characterized and need to be constrained to gain a global picture of the potential impact of thawing permafrost on global warming. In this study we report on recent cores drilled from terrestrial permafrost, as well as permafrost underlying shallow marine waters, in Tuktoyaktuk Island, Northwest Territories, Canada. Material was subsampled from ~1 m increments and measured for concentrations of dissolved methane. Methane concentrations ranged from 0.03 to 0.13 mg CH_4 per kg soil, with a peak in concentration at 2 m, just below the active layer. These concentrations are similar to other mineral soil permafrost cores. Material from the active layer and 2.8 m below the surface was incubated for ~6 weeks under aerobic and anaerobic conditions at -20°C, -5°C, and +15°C to quantify the amount of methane and carbon dioxide being released from microbial activity. These biotic treatments were compared to killed controls to determine if any abiotic processes may be contributing to methane and carbon dioxide release. Under anaerobic conditions, methane concentrations increased over time at all temperatures compared to the killed controls, suggesting microbial production. In addition, methane concentrations increased faster under warmer conditions, but we did measure appreciable amounts of methane in the -20°C treatment. This paper reports on both the aerobic and anaerobic incubation results within the broader context of the downcore characterization work. It will also discuss how the results fit into the larger framework of permafrost incubation experiments.

Introduction

Air temperatures are rising globally, but even more so in the Arctic, with regional warming over the past 30 years of about 1°C per decade there (Christensen et al. 2013). Global climate models suggest that this amplified warming in the Arctic will continue (Christensen et al. 2013). Therefore, the Arctic is more susceptible to climate changes than any other place on the planet. The Arctic stores the largest amount of carbon, contained within permafrost. Permafrost is defined as soils that remain at or below 0°C for two or more consecutive years (Romanovsky et al. 2017), or perennially frozen ground. Ground sitting above the permafrost which freezes and thaws seasonally is known as the active layer. Approximately 1,330–1,580 Pg of organic carbon is currently stored in permafrost in the Arctic and sub-Arctic regions due to accumulation and

freezing of plant and animal remains over thousands of years (Schuur et al. 2015). This estimate does not include the potential for about 400 Pg of carbon stored in other deep permafrost sediments or the unquantified aquatic permafrost carbon (Schuur et al. 2015). Key metrics for permafrost conditions are the active layer thickness (ALT) and permafrost temperature, and prior research shows that both are increasing (Romanovsky et al. 2017). This is significant because with a thicker active layer, more organic carbon is available for microbial processing.

Studies have shown that within the permafrost active layer, microbes remineralize the organic matter and produce carbon dioxide (under aerobic conditions) or methane and some carbon dioxide (under anaerobic conditions) (Treat et al. 2015). Furthermore, new studies suggest that permafrost may also release nitrous oxide, a potent greenhouse gas (Yang et al. 2018). Both methane and carbon dioxide are also powerful greenhouse gases, and estimates using the RCP 8.5 emissions scenario suggest that thawing permafrost stocks may release between 50 and 250 GtC to the atmosphere in the form of CO_2 or CH_4 over the coming century (Stocker et al. 2013). Additionally, rising permafrost temperatures can cause permafrost to eventually thaw and allow microbes to decompose that carbon (Schuur et al. 2015). There is much uncertainty about to what extent these additional greenhouse gases may accelerate rising air temperatures due to uncertainties about the size of the permafrost carbon pool and projections for regional changes in precipitation (Schuur et al. 2015).

The intensity of emissions during permafrost thaw and active layer expansion depends on many factors, including a variety of landscape factors, soil properties, and environmental conditions (Treat et al. 2015). To investigate these factors, researchers conduct incubation tests with permafrost material from the active layer and just below it, within the surface regions of the permafrost. Such incubations take place in the laboratory under different conditions (such as changes in temperature) using material from various environments, including different biomes (tundra versus boreal), different landscape positions, varying soil types (organic or mineral) and either continuous or discontinuous permafrost zones (Treat et al. 2015). In comparing aerobic and anaerobic incubation experiments carried out worldwide, it was found that cumulative carbon emissions over a one year time frame from anaerobic soils are on average about 80% lower than those from aerobic soils (Schuur et al. 2015). However, specialized microbes called methanogens produce methane as well as carbon dioxide in anaerobic environments, and its added potency can partially offset the decreased overall decomposition and emission rate (Schuur et al. 2015).

Prior anaerobic incubations have been conducted on permafrost samples from a variety of different sites throughout the Arctic with a variety of soil types, landscapes, and environmental conditions (Treat et al. 2015). These studies revealed that production of methane generally decreased with depth, production was higher from active layer soils than from the permafrost, and substrate and the decomposability of soil organic matter are important controls on production of methane and carbon dioxide (Treat et al. 2015). Few anaerobic incubations extended more than six months in duration, and most are conducted at temperatures far above the mean annual air temperature of the region from which the cores originate (Treat et al. 2015). For example, 15°C is a very common incubation temperature, even for cores from areas with mean annual air temperatures as low as -12°C (Treat et al. 2015). This may not represent a realistic amount of warming in the short-term future, which may produce rates of production in the incubation greater than we are likely to see in nature.

Furthermore, the type of permafrost zone can influence how incubation results are implemented into global models. Discontinuous permafrost means that the permafrost does not extend over

the entire region, with areas of permafrost interspersed with areas lacking permafrost (Stocker et al. 2013). Continuous permafrost thus has greater potential for the release of greenhouse gases if the same amount of both continuous and discontinuous permafrost were to thaw. This is an important factor when estimating rates of greenhouse gas release from specific regions.

Methanogenesis, or the production of methane, has been found to be more sensitive to temperature than aerobic respiration (Yvon-Durocher et al. 2014). One study that conducted anaerobic incubations at lower temperatures, such as -2, 4, and 8°C, found significant carbon dioxide production at all temperatures over the course of the incubation. Significant methane production was also seen at 4 and 8°C, with increasing concentrations of both methane and carbon dioxide with increasing temperature (Chowdhury et al. 2015). However, methane production began much more slowly than the release of carbon dioxide, and production of both gases was greater from soils with higher organic carbon content (Chowdhury et al. 2015).

In this study, an incubation has been conducted using cores from a new area that has never been studied in this way. Permafrost cores were collected from the Tuktoyaktuk, NWT region of the Mackenzie River Delta (see Figure 1). Most anaerobic incubations have been focused in regions of discontinuous permafrost and/or boreal forest biome with mostly organic soil (Chowdhury et al. 2015). Our region, however, is in a continuous permafrost zone and tundra biome with mineral soil. This unique environment has seen very little study in terms of permafrost incubations. Additionally, many incubations conducted from other regions were observed for less than 30 days. Our experiments for this study were observed for 5–6 weeks, but will set the stage for future similar incubations on longer timescales. Incubations were conducted at temperatures of -20°C, -5°C, and +15°C. These three temperatures span most of the seasonal variability (Figure 2). Furthermore, the intermediate temperature choice, -5°C, is closer to the mean annual air temperature in the region, -10°C (http://climate.weather.gc.ca/climate_normals/, last accessed 6/14/18), which provided a more realistic temperature increase this region could encounter in the near future. Climate models suggest that the Arctic may be about 4°C warmer during the period 2081–2100 compared to the period 1986–2005 based on a modest emissions scenario (RCP4.5) and may be about eight degrees warmer during the same period based on the “business as usual” emissions scenario (RCP8.5) (Collins et al. 2013). This range of projected changes thus encompasses the -5°C temperature condition. Furthermore, these incubations were conducted using sediments from both the active layer (under aerobic and anaerobic conditions) and the deeper permafrost (under only anaerobic conditions). The data we have collected will help to not only answer questions about how sediments from this region may respond to warming temperatures in the near future but also about the potential for warming on a multi-century timescale.

The main question we sought to answer through this study was if the rates of methane and carbon dioxide production from these cores are consistent with other permafrost studies. The objective was to carry out laboratory incubations at different temperatures under aerobic and anaerobic conditions from within different depths of a permafrost core and measure for methane and carbon dioxide production. We hypothesized that CH_4 and CO_2 production rates would be higher at higher temperatures across both aerobic and anaerobic environments but that at -5°C, we would observe production at a rate that is significant. Additionally, we hypothesized that there would be greater CH_4 and CO_2 production from anaerobic sediments in the active layer than from the permafrost.

Materials and methods

Permafrost core collection

Permafrost cores were collected from Tuktoyaktuk, NWT at four locations (reference map below, Figure 1) on 24–28 March 2018. Air temperatures vary between about -30 and 15°C on average throughout the year (see Figure 2), but were less than -20°C during core collection. Cores were collected by Midnight Sun Drilling. The upper one meter was drilled with an auger to get through rocky material. The bottom 7.6 meters (~25 feet) of permafrost samples were collected by CRREL coring. In the field, for 4 days, 10 cm whole round cores were sawed off as the material was drilled and stored in plastic bags at in situ air temperatures. The sections were then transferred to the Aurora Research Institute in a -20°C freezer. The samples were then taken by hand onto the plane stored at -20°C using Chronos Advance 4 L shipping containers which maintain contents at -20°C. The sample containers were at -5°C upon returning to CBL, at which time all samples were transferred to a -20°C freezer within one week of sample collection.

Methane characterization of full core

After core collection, a small subsample from each sample depth was taken for preliminary analyses. Downcore methane concentrations were measured by drilling each sample depth with a hole saw to obtain ~3 cm long, 1.5 cm outer diameter subcores (~6 grams of material). These subcores were then placed into pre-weighed 20 mL glass serum vials and capped with black butyl rubber stoppers and aluminum caps. Vials were weighed after permafrost was added and were then flushed with nitrogen gas for 3 minutes. Analysis of concentrations occurred by injecting an aliquote of the headspace into a gas chromatograph with a flame ionization detector (GC-FID).

Anaerobic incubation of 9'3" depth interval

On 30 May 2018, the 9'3" depth interval was taken out of the freezer and processed using the same method stated above. Approximately 37 vials were prepared; 18 were used for the anaerobic permafrost incubation. Once the vials flushed, 3 mL of 1M potassium hydroxide (KOH) was injected into half of the vials to kill any microbial life. These vials were referred to as the killed control. Permafrost incubations were conducted at three temperatures: -20, -5 and 15°C. During the incubation, vials were stored upside down in a small tub of water at their respective temperatures to prevent gases from escaping. Our -5°C freezer actually malfunctioned around week 3.5/4 and reached temperatures of ~0°C . It fluctuated between -5° and 0°C for the rest of the incubation.

At the end of this incubation (six weeks), headspace was removed from the vial using a plastic syringe and displacing headspace with brine solution, ~20 mL volume. This volume was injected into a Picarro Small Sample Isotope Module (SSIM) coupled to a cavity ring down spectrometer to measure $\delta^{13}C$. Standards of between 20 and 80 ppm CH_4 were used to calibrate the instrument and determine an instrumental offset in $d^{13}C$ values.

Aerobic and anaerobic incubations in active layer

Subsamples of soil were also collected from two to four feet augered material. Because this depth interval was augered, the samples were small broken pieces rather than taken as a whole core. Samples were handpicked from the bags and placed into 20 mL glass serum vials. Some

ice crystals had formed on the surface of the material post-sampling and this material was scraped off (see Figure 3). Vials were capped and sealed in the same way as before. This experiment was only conducted at 15°C but with four possible treatments: anaerobic (flushed with nitrogen), aerobic (not flushed), slurried (water added), and killed (basified as stated above).

Measurement of methane and carbon dioxide concentrations

All incubations were subsampled for methane and carbon dioxide once a week. Once the vials were capped, 6 mL of N_2 were added to the headspace from the initial (time 0) so that 6 mL of the diluted sample could be collected as an aliquote and injected into a gas chromatograph with a flame ionization detector (SRI, GC-FID) to measure methane and a thermal conductivity detector (TCD) for carbon dioxide. Some samples were analyzed with duplicate injections to verify analytical precision of 3%. The conditions for our sample runs can be found in Table 1. Sample areas were compared to certified standards (Airgas, 30 ppm CH_4, 2000 ppm CO_2) and converted to ppmv in the headspace.

Dissolved methane concentrations in the permafrost pore-waters were calculated by applying ideal gas law to convert ppmv to uM using equations from Magen et al., 2014. Then, using the porosity and the weight of each sample, this was converted to units of mgC/gram dry weight. This was plotted against time, fit with a linear regression, and used to calculate a rate of methane release. (Figure 13)

Tips and tricks for the continuation of this experiment:

- Turn the GC on about 1.5–2 hours before use if you'll be needing the TCD. It takes a while to warm up.
- Dilute with 6 mL N_2 to take a headspace subsample.
- Files to use for temperature and event settings:
    - Temperature: MeasureO2CH4CO2_loop.tem
    - Event: Measure O2CH4CO2_loop.evt
    - Make sure to select these for both the FID and the TCD.

Results

Methane characterization of full core

Methane concentrations in the core ranged from 0.03 to 0.13 mg CH_4 per kg soil, with a peak in concentration at 2 m, just below the active layer (Figure 4).

Anaerobic incubation of 9'3" depth interval

Under anaerobic conditions, methane concentrations increased over time at all temperatures compared to the killed controls. In addition, methane concentrations increased faster under warmer conditions, but we did measure appreciable amounts of methane in the -20°C treatment (Figure 5). Carbon dioxide release was also higher from the experimental groups than from the corresponding killed controls (Figure 6). Furthermore, when analyzing the headspaces for stable isotopes ($\delta^{13}C$) we found a value of about -68‰ for the experimental group at -5°C,-66‰ for the experimental group at 15°C, and -73.5‰ for the killed controls at both these temperatures (Figure 9). Finally, the -5°C freezer problem mentioned above didn't seem to impact the slope of the methane or carbon dioxide releases significantly.

Aerobic and anaerobic incubations in active layer

Methane release from the anaerobic treatment experimental groups in the active layer was much higher than from the corresponding killed controls (Figure 7). Carbon dioxide release from active layer soils was higher under aerobic conditions than anaerobic, but both experimental groups were higher than the killed controls (Figure 8). For the most part, we had very little issues with variability between triplicates. However, from the aerobic killed control triplicates we observed two vials with similar headspace concentrations of methane and one with headspace concentrations far above anything else we observed under this treatment, including the experimental group. Figure 10 shows this discrepancy. When averaged, this discrepancy pulls the average of the killed control above that of the experimental group but with very large error bars (Figure 11). Without the outlier, the killed control and the experiment are similar in magnitude and rate of methane emission (Figure 12). Outlier status should be statistically determined in the future.

Discussion

Methane concentrations in our cores are similar to or slightly below those found in other mineral soil permafrost cores (Rasmussen et al. 1993; Brouchkov and Fukuda 2002). Our data from both the active layer and 9'3'' depth anaerobic incubations suggest microbial production of methane, as the experimental groups released more methane than the killed controls. Our $\delta^{13}C$ measurements confirm microbial production for the -5°C and +15°C 9'3'' depth experiments compared to the killed controls (Figure 9). The data also show that methane and carbon dioxide releases both increase under warmer conditions, aligning with our initial hypothesis. This implies that as global temperatures rise, more permafrost carbon will be released into the atmosphere in the form of methane and carbon dioxide.

Our aerobic active layer incubation, however, showed no production of methane compared to the killed control, regardless of the inclusion of an outlier, suggesting a lack of microbial production. This supports what we were expecting, as methanogenesis is an anaerobic process, and oxygen is toxic to methanogens. In a broader context, this suggests that if thawing permafrost sediments remain oxygenated throughout their thaw, methane will not be directly released to the atmosphere. This could reduce the magnitude of the greenhouse effect derived from this source. However, our active layer incubations also reveal that carbon dioxide release is higher under aerobic conditions than anaerobic conditions. This could partially offset the reduction of the greenhouse effect from the lack of methane.

The main objective of this study was to investigate if permafrost soils from Tuktoyaktuk, NWT, Canada would release methane and carbon dioxide in amounts similar to other mineral soil regions. We found a rate of 0.0001 mgC-CH_4/gram dry weight/day released from the 9'3'' depth soils incubated under anaerobic conditions at 15°C. This is comparable to rates obtained from other mineral soil incubations under these conditions of between $1.2x10^{-6}$ and $2.4x10^{-4}$ mgC-CH_4/gdw/day (Lee et al. 2012).

Also notable is the rate we found from the killed control soils at the same conditions as stated above. A rate of $3x10^{-5}$ mgC-CH_4/gdw/day was found to be released from these soils, which is still within the range given in Lee et al. 2012. This could be the result of outgassing, which is the process we intended to control for. However, this could also suggest that the base did not kill all the methanogens present and may have just suppressed methane production instead of stopping it. Microbial analysis would have to occur to verify either way.

The anaerobic active layer incubation exhibited a rate of methane release of $6x10^{-6}$ mgC-CH_4/gdw/day at 15°C. This is about two orders of magnitude less than the release from the deeper permafrost soils under the same conditions. This is likely due to the active layer soils' makeup: they are more rocky and sandy than the underlying permafrost. Analysis of total organic carbon content (TOC) could also help to resolve this question.

This data could be used to refine global models and could contribute to the knowledge base on permafrost as a whole. Incubation studies are useful for quantifying the potential of permafrost soils to release greenhouse gases with rising temperatures (Schuur et al. 2015). Since the region and soil type where our cores are from is unstudied in terms of incubations, this data will be useful to help refine model projections and will leave us with a better understanding of the region's permafrost.

Conclusions

Our hypothesis that warmer conditions would cause greater production of methane and carbon dioxide is suggested to be correct based on the data. However, we predicted that more methane would be released from the active layer sediments than from the deeper permafrost soils, yet the opposite is suggested by the data, likely due to the rocky and sandy nature of the active layer sediments. We also found no methane production from active layer sediments under aerobic conditions, but more carbon dioxide under aerobic than anaerobic conditions. This excess carbon dioxide would likely offset the effects of reduced methane output if oxygenated thaw was sustained over a long period of time.

Acknowledgements

First, I'd like to thank my mentor Dr. Laura Lapham for all of her guidance on this research project this summer. I would like to thank Maryland Sea Grant for giving me the opportunity to conduct independent research this summer. I would also like to thank Hadley McIntosh and Cedric Magen for their support and guidance in the laboratory, and the Geological Survey of Canada for making the collection of these cores possible. This study was supported by NSF grant OCE-1756244.

References

Brouchkov, A., and M. Fukuda. 2002. Preliminary measurements on methane content in permafrost, Central Yakutia, and some experimental data. Permafr. Periglac. Process. 13: 187–197. doi:10.1002/ppp.422

Chowdhury, T. R., E. M. Herndon, T. J. Phelps, D. A. Elias, B. Gu, L. Liang, S. D. Wullschleger, and D. E. Graham. 2015. Stoichiometry and temperature sensitivity of methanogenesis and CO2 production from saturated polygonal tundra in Barrow, Alaska. Glob. Change Biol. 722–737. doi:10.1111/gcb.12762

Christensen, J. H., Krishna Kumar, E. Aldrian, and others. 2013. Climate Phenomena and their Relevance for Future Regional Climate Change, p. 1217–1308. *In* Climate Change 2013: The Physical Science Basis. Contribution of Working Group I to the Fifth Assessment Report of the Intergovernmental Panel on Climate Change. Cambridge University Press.

Collins, M., R. Knutti, J. Arblaster, and others. 2013. Long-term Climate Change: Projections, Commitments and Irreversibility, p. 1029–1136. *In* Climate Change 2013: The Physical Science Basis. Contribution of Working Group I to the Fifth Assessment Report of the Intergovernmental Panel on Climate Change. Cambridge University Press.

Lee, H., E. A. G. Schuur, K. S. Inglett, M. Lavoie, and J. P. Chanton. 2012. The rate of permafrost carbon release under aerobic and anaerobic conditions and its potential effects on climate. Glob. Change Biol. 18: 515–527. doi:10.1111/j.1365-2486.2011.02519.x

Magen, C., L. L. Lapham, J. W. Pohlman, K. Marshall, S. Bosman, M. Casso, and J. P. Chanton. 2014. A simple headspace equilibration method for measuring dissolved methane. Limnol. Oceanogr. Methods 12: 637–650. doi:10.4319/lom.2014.12.637

Rasmussen, R. A., M. A. K. Khalil, and F. Moraes. 1993. Permafrost methane content: 1. Experimental data from sites in northern Alaska. Chemosphere 26: 591–594.

Romanovsky, V. E., S. L. Smith, K. Isaksen, and N. I. Shiklomanov. 2017. Terrestrial Permafrost. Artic Rep. Card 2017.

Schuur, E. A. G., A. D. McGuire, and C. Schadel. 2015. Climate change and the permafrost carbon feedback. Nature 520: 171–179. doi:10.1038/nature14338

Stocker, T. F., D. Qin, G.-K. Plattner, and others, eds. 2013. IPCC, 2013: Summary for Policymakers, p. 1–30. *In* Climate Change 2013: The Physical Science Basis. Contribution of Working Group I to the Fifth Assessment Report of the Intergovernmental Panel on Climate Change. Cambridge University Press.

Treat, C. C., S. M. Natali, J. Ernakovich, C. M. Iversen, and A. D. McGuire. 2015. A pan-Arctic synthesis of CH4 and CO2 production from anoxic soil incubations. Glob. Change Biol. 2787–2803. doi:10.1111/gcb.12875

Yang, G., Y. Peng, M. Marushchak, and others. 2018. Magnitude and pathways of increased nitrous oxide emissions from uplands following permafrost thaw. Environ. Sci. Technol.

Yvon-Durocher, G., A. P. Allen, D. Bastviken, R. Conrad, C. Gudasz, A. St-Pierre, N. Thanh-Duc, and P. A. del Giorgio. 2014. Methane fluxes show consistent temperature dependence across microbial to ecosystem scales. Nature 507: 488–491. doi:10.1038/nature13164

Figures and tables

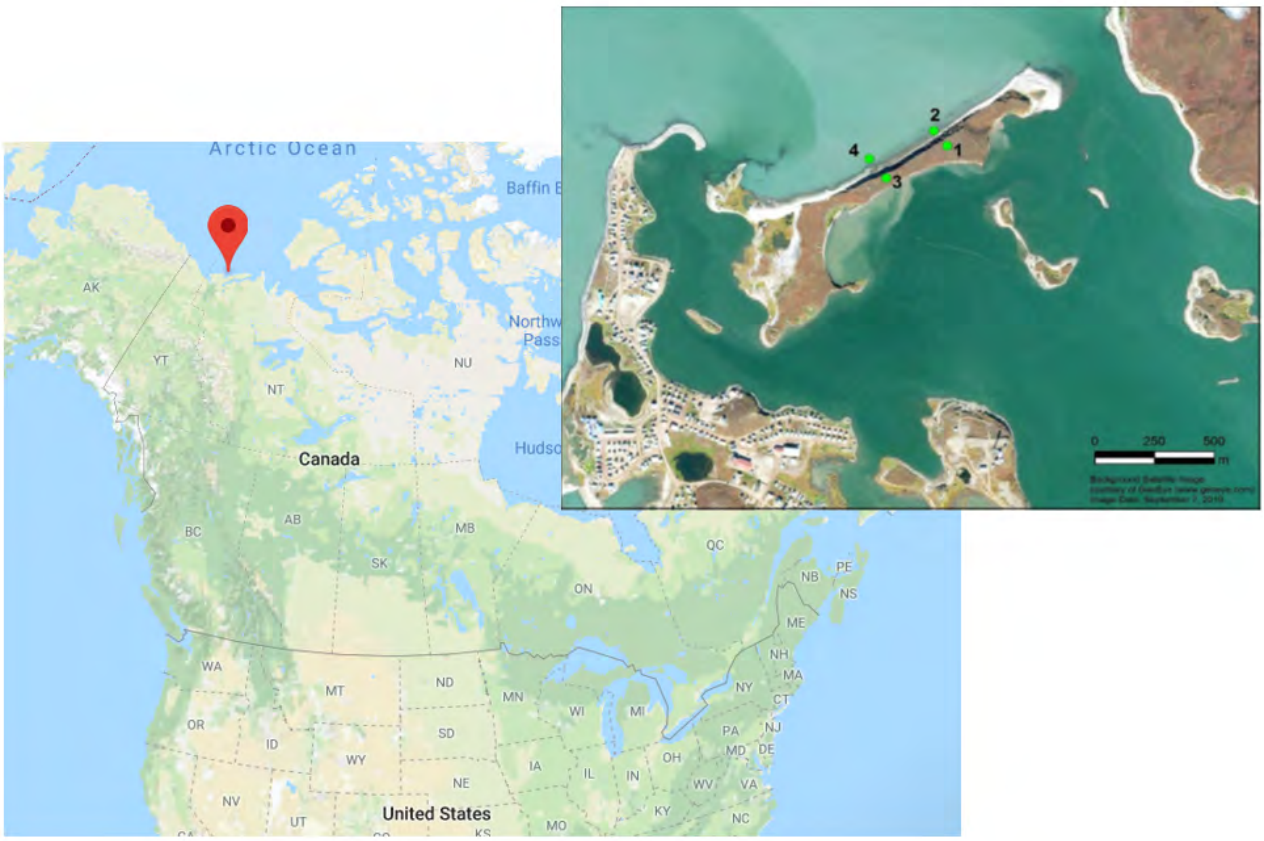

Figure 1. Red marker depicts Tuktoyaktuk, NWT, Canada. Map taken from Google Maps. Inset shows an up-close map of our studied region, taken from the Tuktoyaktuk Island permafrost drilling field report. Our core was from station 3.

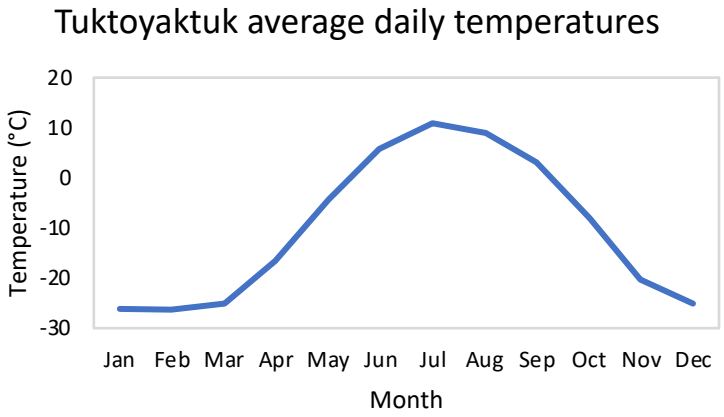

Figure 2. Canadian climate normals from 1971-2000. Data courtesy of http://climate.weather.gc.ca/climate_normals/results_e.html?searchType=stnProv&lstProvince=&txtCentralLatMin=0&txtCentralLatSec=0&txtCentralLongMin=0&txtCentralLongSec=0&stnID=1699&dispBack=0, last accessed 6/14/18.

Figure 3. Active layer sediment subsampling, showing ice crystals.

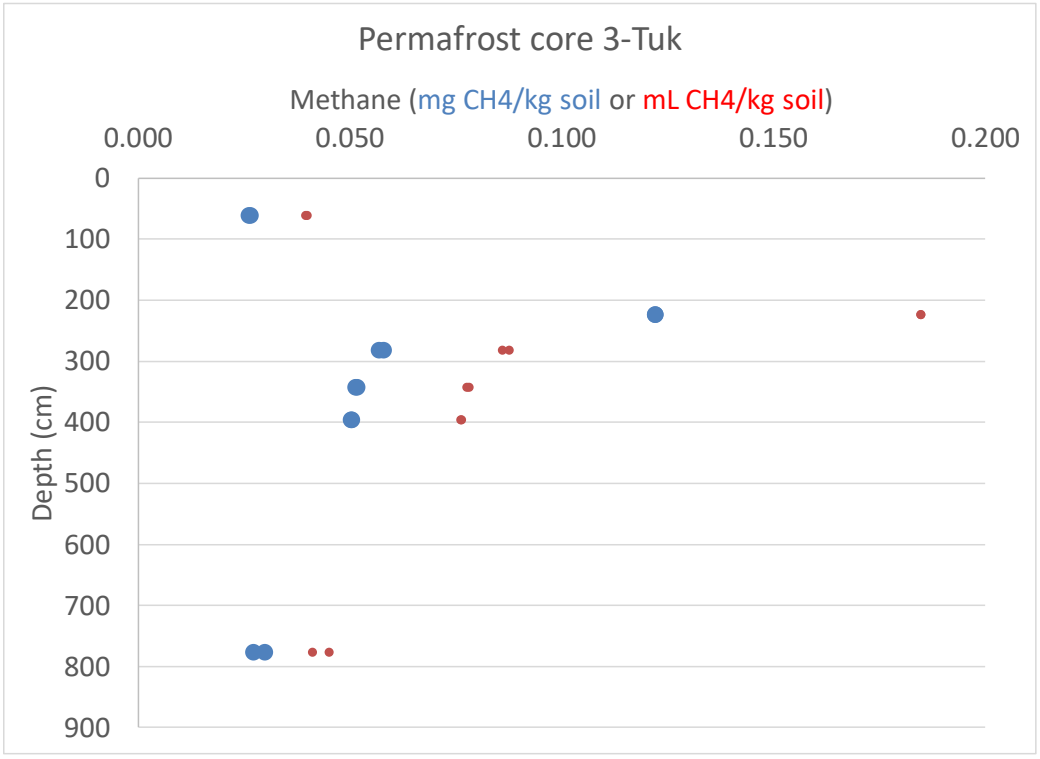

Figure 4. Methane characterization of the whole core. Shows the range of methane concentrations present.

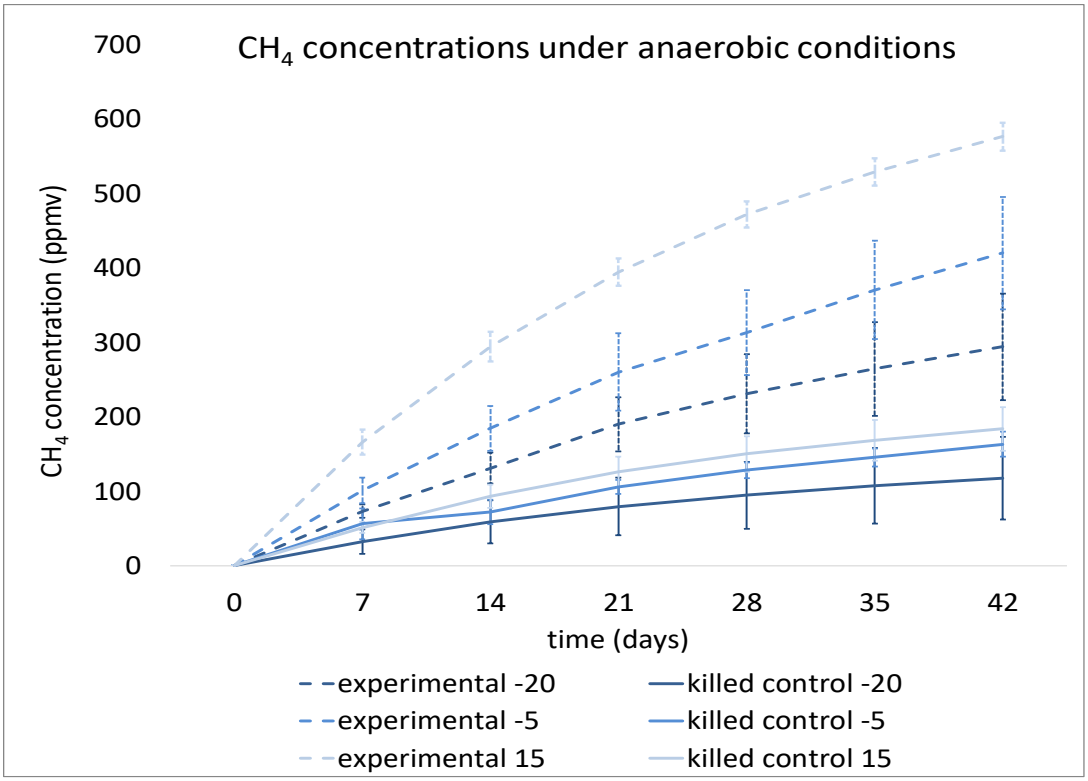

Figure 5. 9'3" depth anaerobic incubation results. Experimental groups show methane release above that of the killed controls.

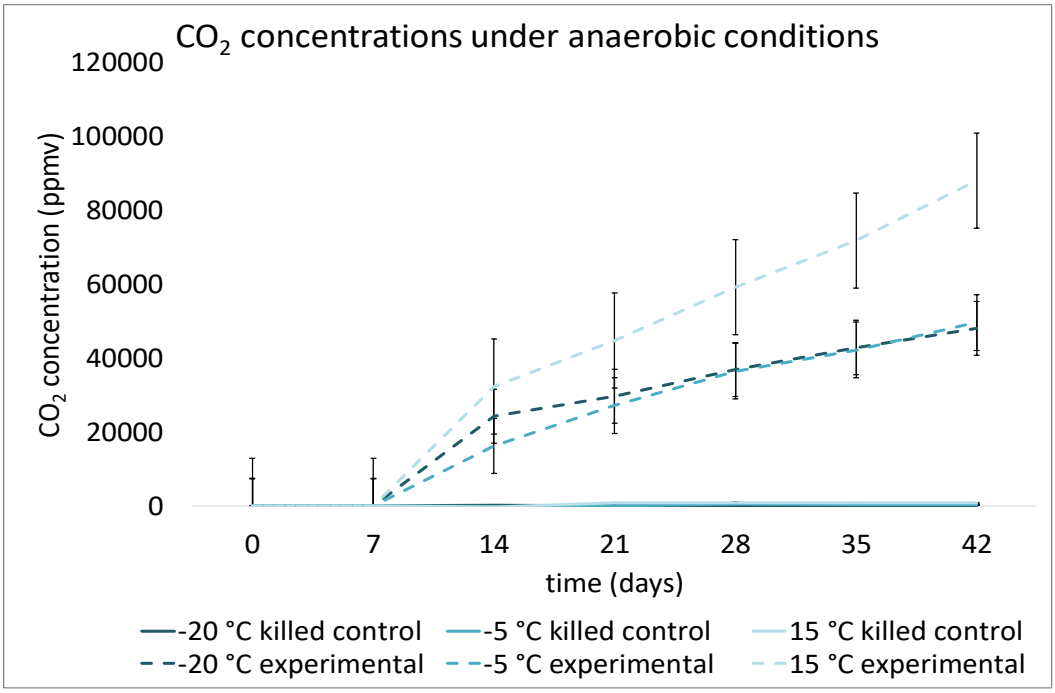

Figure 6. 9'3'' depth anaerobic incubation: carbon dioxide concentrations.

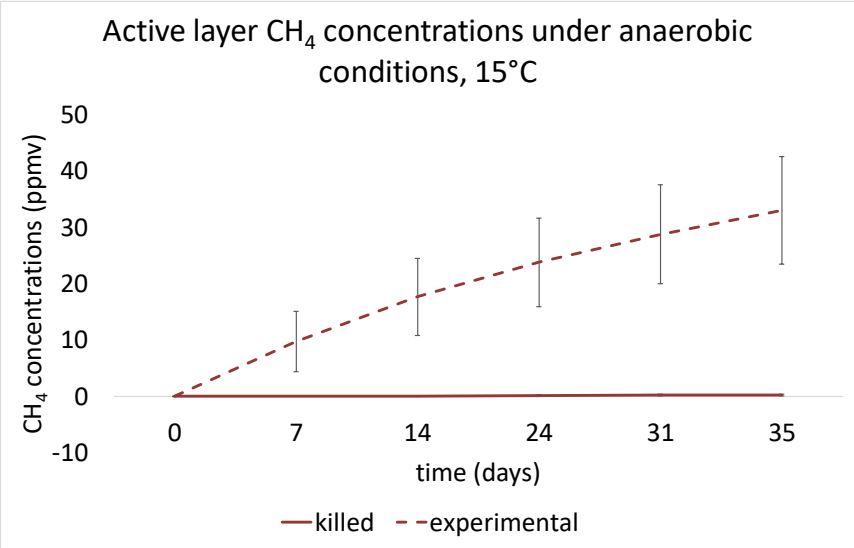

Figure 7. Active layer methane concentrations. The experimental shows an increase over the killed control, suggesting microbial production.

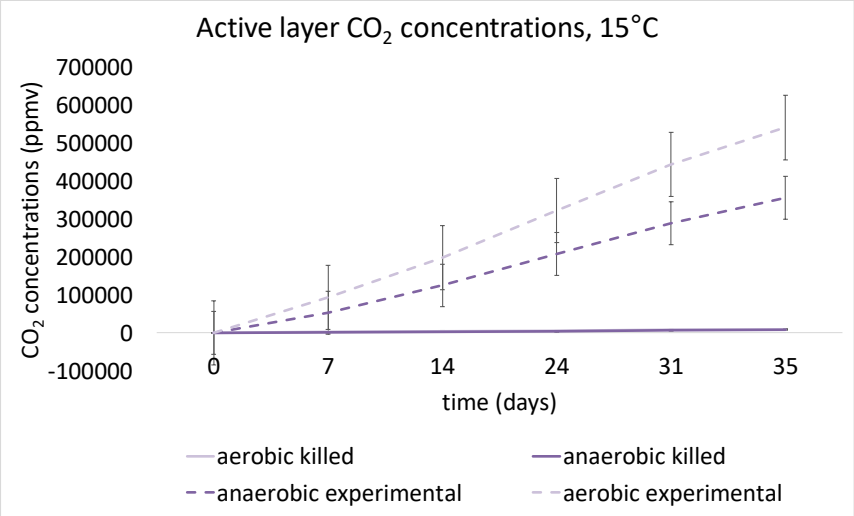

Figure 8. Active layer carbon dioxide concentrations. Anaerobic and aerobic experiments show increases over the killed control, with a larger increase present in the aerobic experiment.

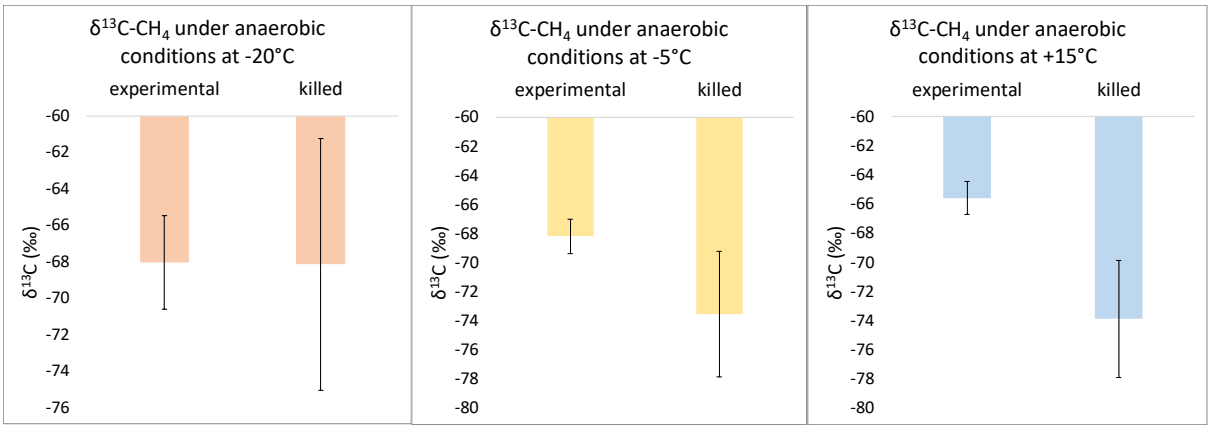

Figure 9. Stable isotope values for 9'3" depth incubations.

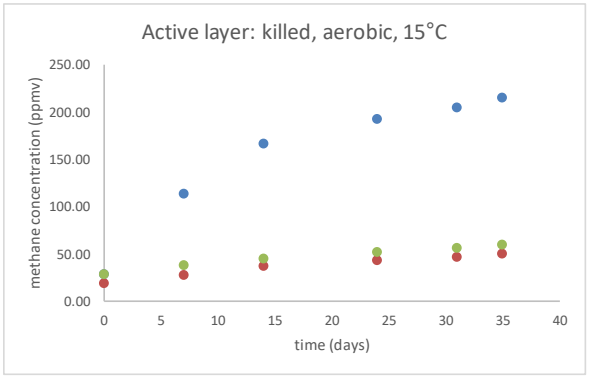

Figure 10. Showing variability in the samples. Each color represents a different vial (triplicates).

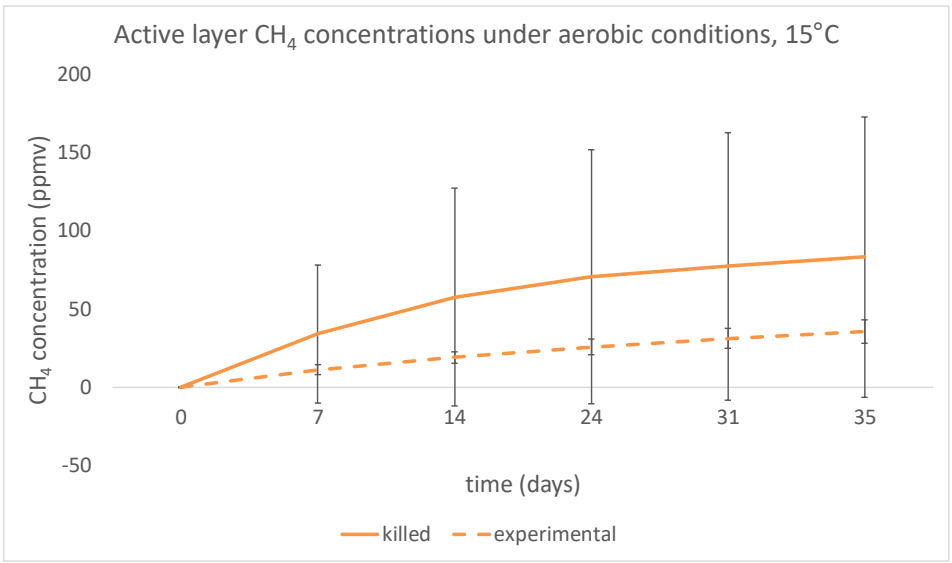

Figure 11. Showing active layer methane concentrations averaged within triplicates with the huge variability shown in the figure above.

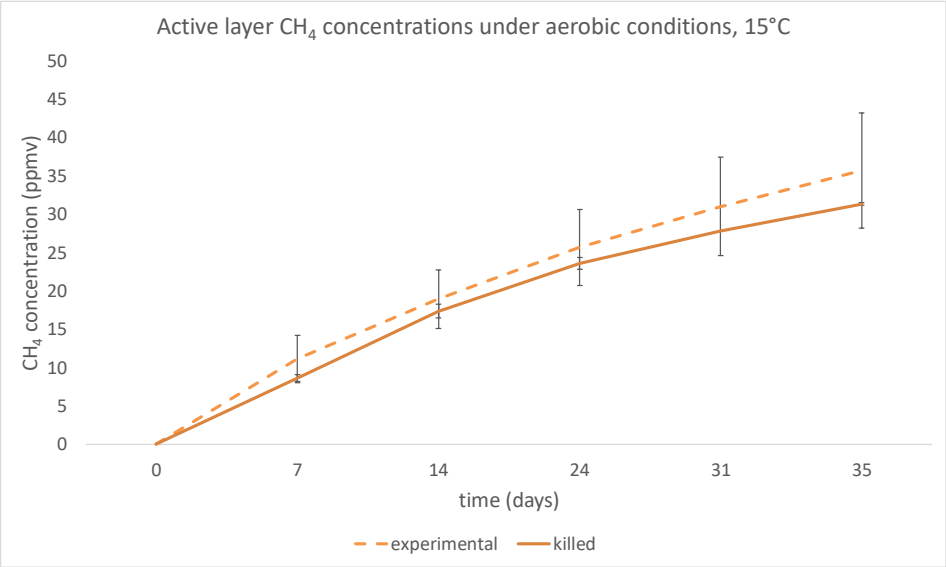

Figure 12. Shows the same as Figure 11 but with the outlier removed. There is no difference between the experimental and killed control.

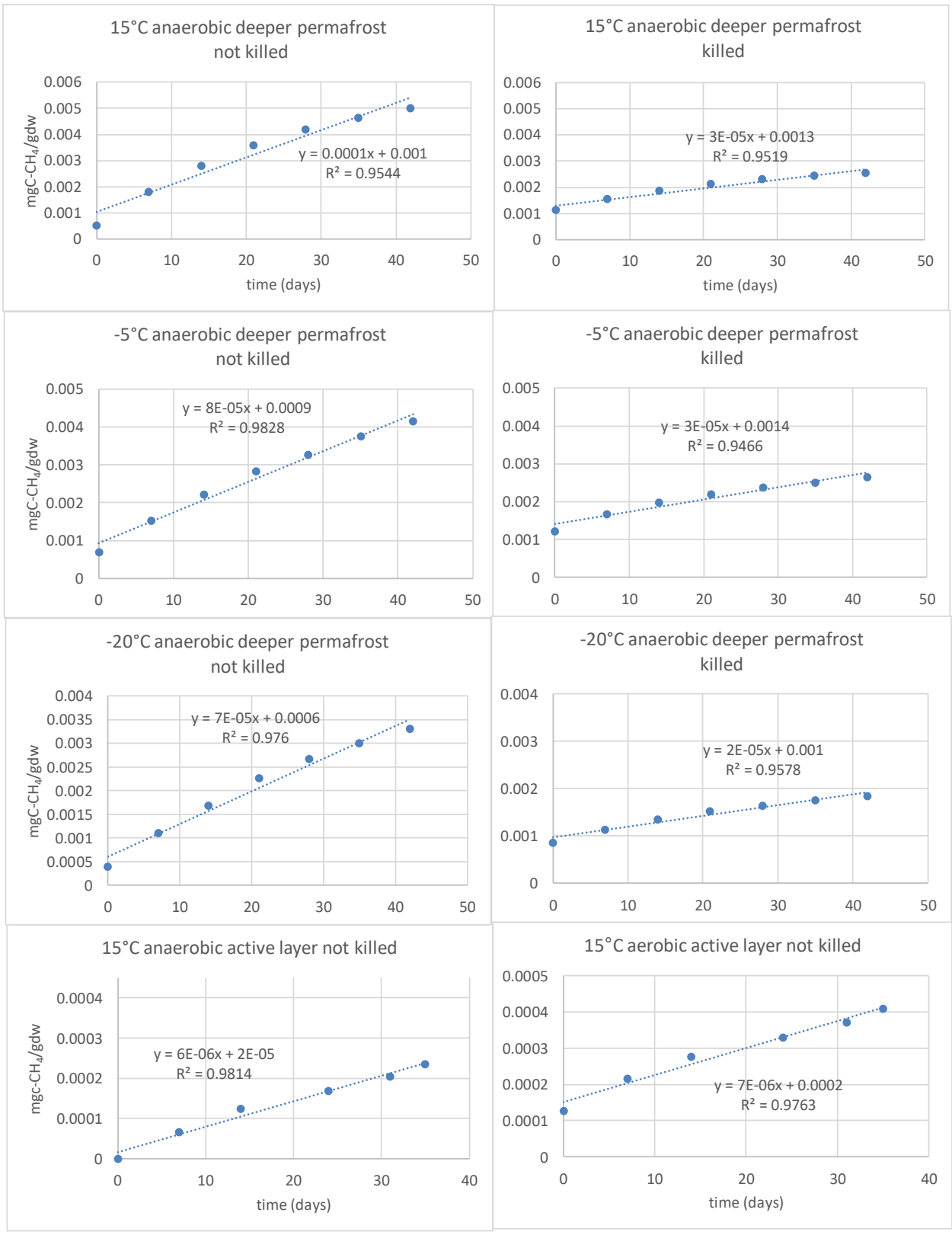

Figure 13. Plots showing method of determining methane release rate. All x axes are showing time in days, y axes are showing methane concentrations in mgC/grams dry weight.

Table 1. Conditions for analyzing samples for methane and CO_2 on the GC-FID.

He flow	**H2 flow**	**air flow**	**loop**
20 mL/min	25 mL/min	250 mL/min	4 mL
oven temperature (°C)			
35 °C for 6 minutes and then ramp up to 85 °C for remaining 4			

Sargassum as an Important Source of Methylmercury in Aquatic Systems

Kenna D. Leonzo, REU Fellow
Maryland Sea Grant

Andrew Heyes, Associate Research Professor
Chesapeake Biological Laboratory, University of Maryland Center for Environmental Science

Abstract

Sargassum is a pelagic macroalgae that accumulates in the warm Mid-Atlantic providing shelter, food, and a breeding ground to over 60 marine species. *Sargassum* can export about 43% of its production both as particulate organic carbon (POC) and dissolved organic carbon (DOC). It is also known to sequester heavy metals, such as mercury. Due to its vast coverage and high activity, *Sargassum* mats seem like an ideal place for production of methylmercury (MeHg), the only mercury to bioaccumulate in fish and humans. After analysis of the values of MeHg, T-Hg, and optical properties present inside and outside *Sargassum* mats in the Gulf Stream and in Puerto Rico, a connection between the quantity of dissolved organic matter (DOM) present and T-Hg being methylated can be made. DOM can act as a mercury carrier and is released the most when *Sargassum* degrades. *Sargassum* does contain mercury (3.92 ng/g wet wt) and methylmercury (0.011 ng g wet wt). We found that *Sargassum* beds release Hg (2.62 ng/L) and MeHg (1.03 ng/L) into the ocean water, concentrations much higher than the Hg (0.67 ng/L) and MeHg (0.02 ng/L) seen in the open ocean. The more DOM present correlates with the more MeHg produced. High methylation is often observed when the *Sargassum* is stressed, such as in coves, where microbial activity changes as DOM export from the *Sargassum* increases. In the waters of the Laguna Grande, Puerto Rico, a lagoon impacted by a *Sargassum* invasion, the input of fresh DOM from *Sargassum* resulted in low oxygen conditions and Hg and MeHg concentrations in waters outside *Sargassum* mats ranging from 0.02 to 0.7 and 0.02 to 0.4 ng/L, respectively. This suggests *Sargassum* can have significant local impacts on water quality. Laboratory simulations of these low oxygen conditions yielded concentrations of 6.43 ng/L T-Hg and 4.47 ng/L MeHg. Further research can be done to look at the type of bacteria responsible for methylation in *Sargassum* mats as well as where the MeHg attaches itself on the DOM.

Introduction

Sargassum mats are a prime nursery habitat for a diversity of large fish. *Sargassum* is a tropical plant; therefore, it prefers warmer oceans, allowing it to bloom in the tropical North Atlantic. It is a pelagic macroalgae, meaning it inhabits the upper layers of the open sea providing shelter and a food source to a wide variety of marine species (crabs, birds, fish, turtles, whales, shrimp) (Fig.1). Not only is *Sargassum* edible but it is also harvested to feed livestock. Its reproduction is asexual, making them spawn in ridiculous numbers while currents, winds, and storms help disperse *Sargassum* throughout the world's oceans (S. Franks et al. 2016). Previous research shows a seasonal pattern in which *Sargassum* is said to originate northwest of the Gulf of

Mexico in the spring and flow northward into the Atlantic, depending on the Florida current (Fig.2) (L. Casazza and Ross 2008; Gower and King 2011). *Sargassum* habitats appear to be important as the majority of fish collected (96%) from the Gulf of Mexico and off the southeastern Unites States are juveniles (L. Casazza and Ross 2008). The role of *Sargassum* in oceanic carbon cycle is only recently being addressed (Powers pers comm 2018).

Methylmercury is known to be a neurotoxin, meaning it is poisonous and destructive to nerve tissues (Clarkson Thomas William 1990). Major human epidemics linked to methylmercury consumption have occurred, such as the fatal and nonfatal neurological diseases that were caused by methylmercury exposure from consumption of seafood in Minamata and fresh-water fish in Niigata in the 1950s and 1960s in Japan (Tollefson and Cordle 1986). Methylmercury (CH_3Hg) has a very long half-life, averaging at approximately two years in fish. It is distributed throughout the tissues and then discharged from binding sites very slowly (Tollefson and Cordle 1986). CH_3Hg is the only Mercury (Hg) species to biomagnify in aquatic food webs as it enters the food chain and is stored and accumulated in these tissues of aquatic organisms (Schartup et al. 2015). Biomagnification is particularly a problem since larger fish contain more CH_3Hg and is typically the type of fish humans like to eat. CH_3Hg directly effects the central nervous system of higher organisms (Clarkson Thomas William 1990). Identifying sources of CH_3Hg^+ to oceanic fish has been a challenge and are even more difficult to quantify.

Microbial mercury production is the main driver associated with methylmercury pollution as mercury is converted into methylmercury by the presence of methylating anaerobic bacteria. These bacteria can include those such as methanogens and sulfate-reducing bacteria (SRB) (Schartup et al. 2015). SRB use sulfate as their terminal electron acceptor, creating sulfide in the process. They also require a carbon source, such as the supply of dissolved organic carbon (DOC). High methylation is often observed in surface sediments where microbial activity is greatest due to the input of fresh organic matter. Therefore, systems with high levels of organic matter production may show signs of extremely high rates of methylmercury production (Benoit et al. 2002). Mercury methylation appears to be an anaerobic process, but the primary site of methylation is often at the anoxic interface. In the water column methylation has only been detected under anoxic conditions in lakes. This agrees with the idea that methylation is mediated by anaerobic bacteria (Eckley and Hintelmann 2006).

Sargassum can export about 43% of its production both as particulate organic carbon (POC) and dissolved organic carbon (DOC). Research shows that the CO_2 that has been sequestered over centuries is drifting to the deep seafloor as evidence of fresh *Sargassum* was found in the guts of abyssal isopods. This carbon is then locked away from exchange with the atmosphere making *Sargassum* an identifiable carbon sink. (Krause-Jensen and Duarte 2016). Global drivers such as eutrophication and climate change can lead to a growing macroalgal harvest influencing the sequestration of carbon in aquatic systems.

Macroalgae have also been shown to sequester metals, including Hg (Esmaeili et al. 2015). It is known that dissolved organic matter (DOM) may “enhance the activity of methylating microbes in oligotrophic ecosystems by providing a substrate for bacterial activity, while under eutrophic conditions, impacts on binding to Hg^{II} may be more important” and results of this research show that “DOM composition has a large impact on reactivity of Hg and biological uptake of MeHg” (Schartup et al. 2015). Since it is known that the macroalgae releases DOC, a link between the release of DOM, a possible mercury carrier, and the methylation of mercury on the *Sargassum* can be made. It is possible that on the surface of *Sargassum* or within the *Sargassum* itself, low oxygen conditions exist allowing anaerobic bacteria to live and methylate Hg.

Due to its vast coverage and high activity, *Sargassum* mats appear to be an ideal place for the methylation of mercury in the ocean, where sites for Hg methylation are scarce. While there are many factors that can influence methylation of mercury, the supply and availability of mercury, the availability of nutrients and anaerobic environment are the key parameters.

The goal of this study is to determine if *Sargassum* mats are an important source or a "hotspot" of methylmercury (CH_3Hg) in the ocean ecosystem. To achieve this goal, a series of objectives/questions are asked:

- Does open ocean *Sargassum* contain mercury and methylmercury?
- Are these concentrations significant such as to be a relative source to the food web?
- Do *Sargassum* beds release CH_3Hg into the ocean water?
- Given CH_3Hg is associated with dissolved organic matter (DOM), is the CH_3Hg associated with a type of DOM that provides clues to the source of methylmercury production within the *Sargassum* bed?

Methods and Materials

Description of Sampling Sites and Experimental Design

This study design is "opportunistic" in nature. This study was conducted at two sample sites in the North/Mid-Atlantic. Samples were collected in early June 2018 from Laguna Grande, Puerto Rico on the north side of the beach as well as in the lagoon itself. Water samples were collected inside and outside floating patches of *Sargassum*, and *Sargassum* was collected in conjunction with the water samples. Water samples are filtered in the field and the dissolved fraction acidified and particulate fraction frozen. Samples were taken in the same spot on different days to monitor the changes of methylmercury produced after the *Sargassum* starts to degrade. Further sampling was performed on a trip to the Gulf Stream in early July of 2018, at a location east of Savannah, Georgia. Here, surface water and *Sargassum* were collected for a static incubation experiment. *Sargassum* and open ocean water was placed in four 2 L Teflon bottles. Four other Teflon bottles received just open ocean water. The bottles were kept in the sunlight immersed in water to simulate normal irradiance. Teflon allows most light wave lengths to pass through. The bottles were subsampled at 0, 23, 48, 72, 120, and 240 hours and 100 to 200 ml of water removed for the determination of Hg, MeHg, and DOC concentrations and DOM characterization. After seven days, we placed the bottles in the dark and sampled after three days. The subsampling resulted in a concentration effect, but we wanted to simulate increased density that occurs in near-shore environments.

Analysis of Mercury and Methylmercury and Characterization of DOM

In general, Mercury and CH_3Hg were analyzed using EPA methods 1631 and 1630. Filtered water was distilled (Horvat et al. 1993) prior to aqueous phase ethylation and atomic fluorescence detection using a Tekran 2700. For T-Hg analysis, filtered water is digested with BrCl prior to SnCl reduction and atomic fluorescence detection using a Tekran 2600.

For the particulate fraction of the water samples and *Sargassum* tissue, we use the method of Taylor et al. (2008). Briefly, MeHg in tissue and on particulate fractions (filter samples) are placed in quartz vials where they were acidified with 10 ml of 4 M HNO_3. A subsample is then analyzed for MeHg and the remaining sample further acidified and digested using a microwave prior to analysis for T-Hg. Analysis of the Hg species will be done as above.

An examination of the Dissolved Organic Matter (DOM) in the water samples was done by characterizing the DOMs optical properties to relate these characteristics to the source water. The characterization will be done by studying excitation emission spectra (Horiba Aqualog). DOC was determined by the Total Organic Carbon Analyzer (TOC-V).

Results

The Puerto Rico sampling consisted of sampling in and around *Sargassum* mats in various locations. Samples inside the mats contained much higher MeHg concentrations (1.03 ng/L) than just outside of the mats (0.02 ng/L). T-Hg concentrations were also higher inside the mat (2.67 ng/L). DOM was incredibly high inside the mats as well (21.80 vs 1.02 mg/L) suggesting there is a direct correlation between the more DOM present influencing more methylmercury present. It was found that the sites with higher concentrations of TOC, TDN and absorbance also contained higher amounts of methylmercury. By analyzing the optical properties from the Horiba Aqualog, Figure 6 shows a correlation between the amount of methylmercury produced at each site with the amount of DOM present. DOM was much higher inside the *Sargassum* patch than just outside the *Sargassum* patch but even more so in the 24-hour leach sample.

Sargassum filter samples (particulate fraction) produced methylmercury concentrations too low to be significant. It is important to point out, however, that both Lagoon Shore samples showed high amounts of T-Hg at 14.15 ng/L but still contained low methylmercury concentrations at 0.19 ng/L. An interesting sample came from an ad hoc study where *Sargassum* was held in a bottle for a 24-hour leaching experiment. The sample was taken indoors and started to degrade. This sample gave off a sulfur compound smell and contained the highest MeHg concentration, highest TOC, highest TDN, and highest absorbance value.

We used the results from the Puerto Rico leaching experiment to develop the Georgia Gulf Stream experiment. The *Sargassum* was placed in Teflon bottles in a water bath outside in direct sunlight every day to simulate a natural habitat once it was transported from the Gulf Stream to the laboratory (shown in Figure 8). Methylmercury concentrations were very small (0.01-0.02 ng/L) (Table 1) to begin with and over time was decreasing in the seawater while staying relatively stagnant in the *Sargassum* water. However, once brought inside at 120 hours, the methylmercury concentration increased rapidly over the following days in the *Sargassum* samples and decreased in the seawater samples. T-Hg also followed this same trend in which it increased in the *Sargassum* samples and decreased in the seawater samples.

Discussion

Understanding the mechanisms of how methylation occurs on or in *Sargassum* environments is crucial, as *Sargassum* may be an important site of Hg methylation and transfer to the food web. Based on our results, the open ocean *Sargassum* tissue samples did not contain significant amounts of MeHg (the highest being 0.19 ng/g wet wt), and therefore the focus shifted to the water samples taken in conjunction with the tissue samples, where we found high concentrations of MeHg in the dissolved phase. CDOM values outside the *Sargassum* patches were low (2.7 1/m) using absorbance (254) versus what is found inside the *Sargassum* patches (91.8 1/m). There is a correlation between DOC and MeHg concentration, which suggests a link with Hg methylation and DOC export from the *Sargassum*. The sample incubated in Puerto Rico further solidified this linkage with much more total mercury and methylated Hg appearing with increased DOC concentrations. This supports the idea that DOM is at least a Hg and MeHg carrier.

The Hg, MeHg and DOM linkage was further investigated using the *Sargassum* samples brought back from the Gulf Stream. First, in the seawater-only samples, a decrease in methylmercury concentrations from 0.03 to 0.01 ng/L is most likely due to the photochemical degradation of methylmercury to elemental mercury, as it was placed in direct sunlight between 0 and 96 hours. Second, in the *Sargassum* we also saw a rapid increase in T-Hg concentrations from 0.05 to 1.4 ng/L after 23 hours, but then only increasing slightly up until 72 hours. *Sargassum* MeHg concentrations stayed stagnant around 0.1 ng/L up until 72 hours. We hypothesize that the *Sargassum* can still be "happy" and healthy although it has moved locations in the previous weeks from its natural habitat to a sample bottle. Since the *Sargassum* can still photosynthesize, it created enough oxygen limiting anoxia and therefore methylation was not occurring. There is also a possibility that since there is no sulfide smell coming from the *Sargassum*, there is no evidence of sulfate-reducing bacteria. To expedite this process, *Sargassum* was brought inside at 120 hours. As a result of being stressed and no longer receiving sunlight, DOM is released into the waters and MeHg increased drastically over the next few days. This backs up our initial hypothesis that DOC can act as a mercury carrier. The DOC analysis and characterization is yet to be completed on these samples.

Since we now know DOM plays a major role in the amount of total mercury being methylated, further research can be done to explore the ways Hg and MeHg is attached to the *Sargassum*. We also need to explore the productivity in the open ocean verses MeHg values found on shores since the degrading of the *Sargassum* also plays a role in releasing this DOM and MeHg. Bacteria do play an important role in acting as methylators, however, there are ways that methylation can happen abiotically. Perhaps working with microbiologists and performing further analysis on what kind of bacteria is present in the *Sargassum* or completely getting rid of bacteria present to see what results could be an area of future study.

The extent of *Sargassum* blooms are only recently becoming known, as is their importance to the food web. We can expect that warming in the North Atlantic due to climate change would cause an increase in *Sargassum* numbers as the macroalgae favors a warmer ocean. Excessive beaching is already a problem in many areas where *Sargassum* in prevalent, costing millions of dollars on cleanup. *Sargassum* provides a floating habitat for a variety of ecosystems in what is otherwise a nutrient-poor environment. *Sargassum* already poses a health and environmental risk as it collects floating debris, but the aquatic food web present in the mats might also be at risk to a high MeHg exposure which can eventually impact both the ecosystem and human consumers. Regulation of Hg pollution requires researchers to predict the relationship between mercury and methylmercury among ecosystems, which is being studied and almost understood completely. Therefore, controlling mercury contamination is crucial and knowing the bioavailability in the environment is necessary if we are to make efforts in remediating the production of methylmercury.

Conclusion

Based on our findings, it is safe to consider *Sargassum* mats as source of methylmercury in aquatic systems under some conditions. MeHg is found inside *Sargassum* mats in concentrations that are very high compared to what is normally found out in the open sea, where mats become dense. These concentrations are found just outside of the *Sargassum* suggesting it is released along with DOM into the surrounding waters. When *Sargassum* is outside and receiving sunlight, it likely does not methylate unless it starts to die off. However, as soon as it does start to degrade, especially when placed in an area with no sunlight, methylation increases rapidly.

Acknowledgements

I would like to thank Dr. Andrew Heyes for his mentorship and support throughout this project.
Special thanks to Leanne Powers for assistance and sample collecting.
This study was supported by NSF grant OCE-1756244.

References

Benoit, J. M., C. C. Gilmour, A. Heyes, R. P. Mason, and C. L. Miller. 2002. Geochemical and Biological Controls over Methylmercury Production and Degradation in Aquatic Ecosystems, p. 262–297. *In* Biogeochemistry of Environmentally Important Trace Elements. American Chemical Society.

Clarkson Thomas William. 1990. Human health risks from methylmercury in fish. Environmental Toxicology and Chemistry 9: 957–961. doi:10.1002/etc.5620090713

Eckley, C., and H. Hintelmann. 2006. Determination of Mercury Methylation Potentials in the Water Column of Lakes Across Canada,.

Esmaeili, A., B. Saremnia, and M. Kalantari. 2015. Removal of mercury(II) from aqueous solutions by biosorption on the biomass of *Sargassum glaucescens* and *Gracilaria corticata*. Arabian Journal of Chemistry 8: 506–511. doi:10.1016/j.arabjc.2012.01.008

Gower, J., and S. King. 2011. Distribution of floating *Sargassum* in the Gulf of Mexico and the Atlantic Ocean mapped using MERIS,.

Horvat, M., L. Liang, and N. S. Bloom. 1993. Comparison of distillation with other current isolation methods for the determination of methyl mercury compounds in low level environmental samples: Part II. Water. Analytica Chimica Acta 282: 153–168. doi:10.1016/0003-2670(93)80364-Q

Krause-Jensen, D., and C. Duarte. 2016. Substantial role of macroalgae in marine carbon sequestration,.

L. Casazza, T., and S. Ross. 2008. Fishes associated with pelagic *Sargassum* and open water lacking *Sargassum* in the Gulf Stream off North Carolina,.

S. Franks, J., D. Johnson, and D. Ko. 2016. Pelagic *Sargassum* in the Tropical North Atlantic,.

Schartup, A. T., U. Ndu, P. H. Balcom, R. P. Mason, and E. M. Sunderland. 2015. Contrasting Effects of Marine and Terrestrially Derived Dissolved Organic Matter on Mercury Speciation and Bioavailability in Seawater. Environ. Sci. Technol. 49: 5965–5972. doi:10.1021/es506274x

Taylor, V. F., B. P. Jackson, and C. Y. Chen. 2008. Mercury speciation and total trace element determination of low-biomass biological samples. Analytical and Bioanalytical Chemistry 392: 1283–1290. doi:10.1007/s00216-008-2403-3

Tollefson, L., and F. Cordle. 1986. Methylmercury in Fish: A Review of Residue Levels, Fish Consumption and Regulatory Action in the United States,.

Figures and Tables

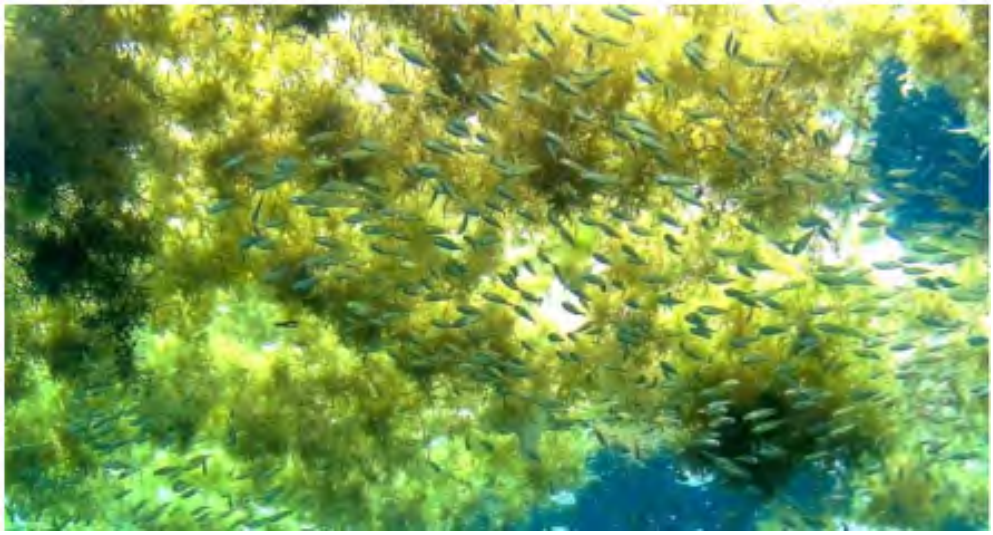

Figure 1. *Sargassum* as a habitat for many species in the Gulf Stream. Source: Doyle, E. and J. Franks. 2015. *Sargassum* Fact Sheet. Gulf and Caribbean Fisheries Institute.

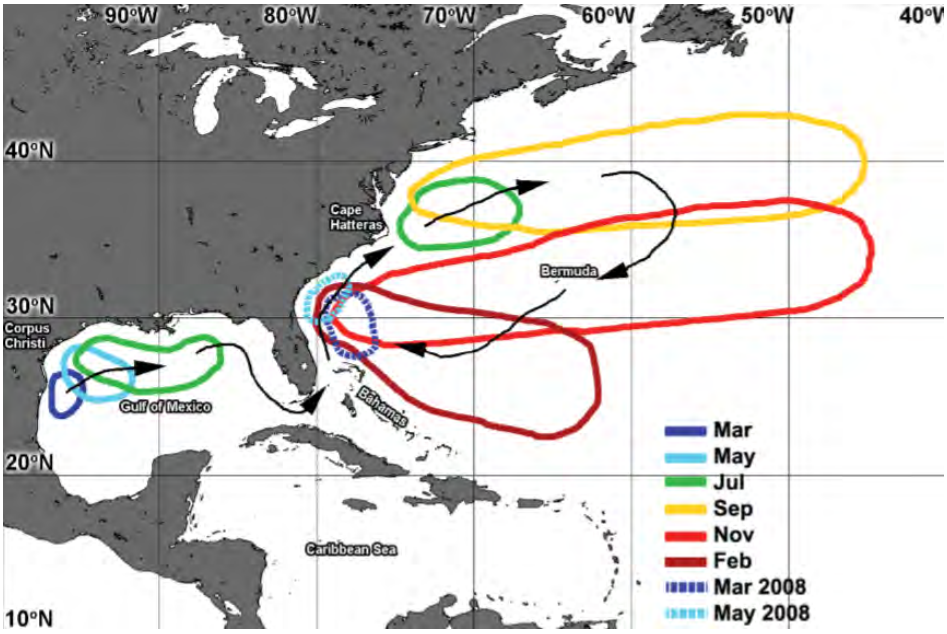

Figure 2. Average spatial distribution and movement of *Sargassum* in March, May, July, September, November, and February using satellite imagery from the European Space Agency (ESA) Medium Resolution Imaging Spectrometer (MERIS) optical sensor. Source: (Gower and King 2011)

Figure 3. Sample site 1: North side of beach in Fajardo, Puerto Rico where Laguna Grande lies. Source: Google Maps


Figure 4. *Sargassum* in Laguna Grande, Fajardo, Puerto Rico; Source: Mike Allen

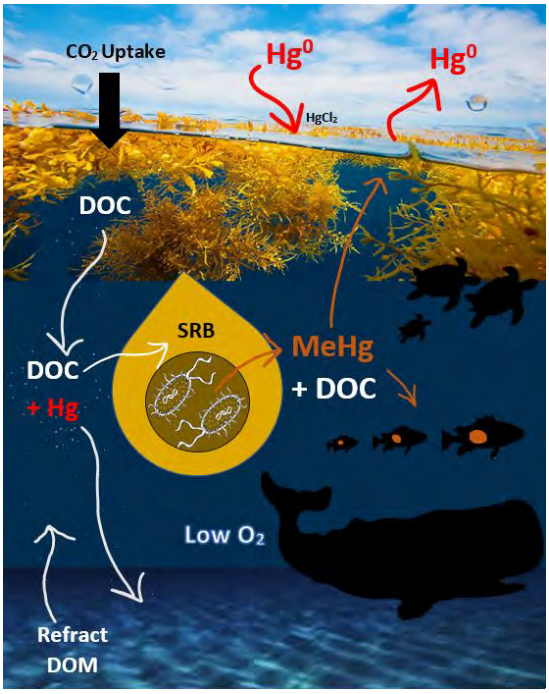

Figure 5. Mercury Methylation in *Sargassum* Diagram. Source: Kenna Leonzo

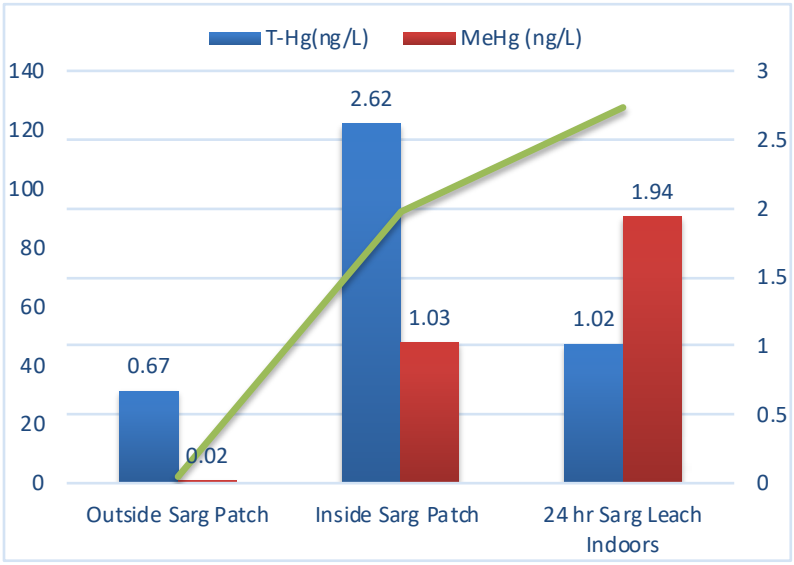

Figure 6. A comparison of total Hg and MeHg and DOC just outside of a *Sargassum* patch, inside a *Sargassum* patch, as well as a similar sample being brought inside for 24 hours. DOC is much higher inside the *Sargassum* patch which can be correlated with the amount of T-Hg being methylated but even higher once a sample is brought inside.

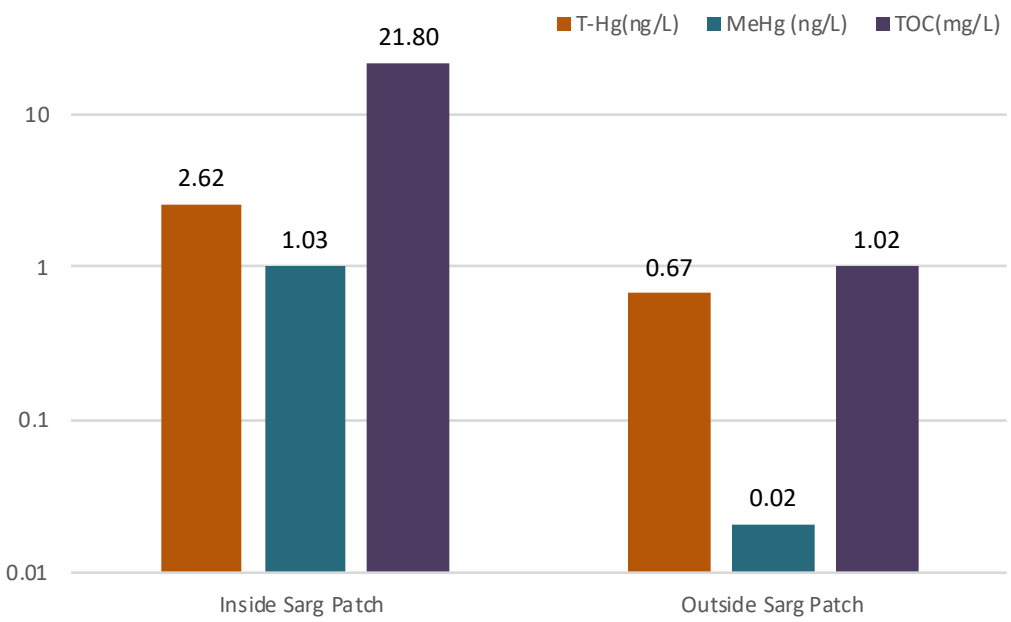

Figure 7. Puerto Rico samples inside verses outside *Sargassum* mats.

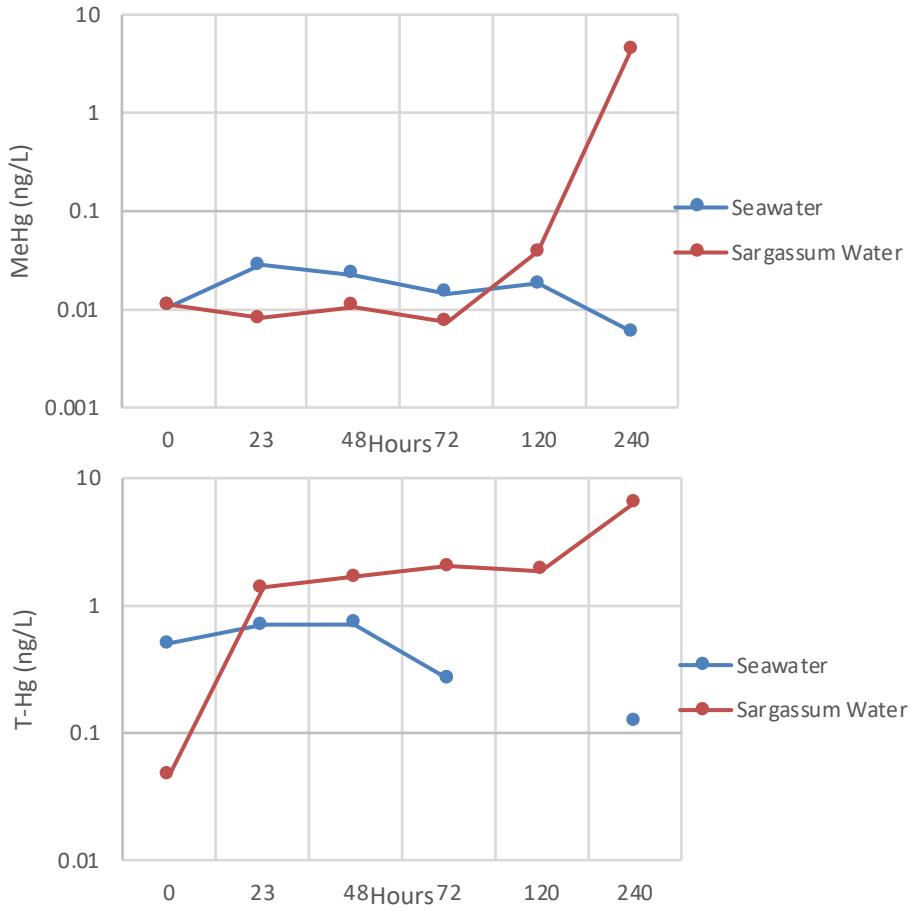

Figure 8. Gulf Stream time experiment in which *Sargassum* water and seawater close to the *Sargassum* mat is left outside for 120 hours where it was then brought inside for a couple of days.

Table 1. Values in correspondent with Figure 8 data.

	TIME (HOUR)	T-HG (NG/L)	MEHG (NG/L)
SEAWATER	0.000	0.499	0.011
	23.000	0.695	0.028
	48.000	0.709	0.023
	72.000	0.264	0.014
	120.000	N/A	0.018
	240.000	0.124	0.006
***SARGASSUM* WATER**	0.000	0.046	0.011
	23.000	1.386	0.008
	48.000	1.663	0.011
	72.000	2.032	0.007
	120.000	1.867	0.038
	240.000	6.431	4.470

Photochemical ammonium production from dissolved organic matter in anthropogenic, freshwater, and estuarine sources

Shirley Ma, REU Fellow
Maryland Sea Grant

Michael Gonsior, Associate Professor
Chesapeake Biological Laboratory, University of Maryland Center for Environmental Science

Leanne Powers, Assistant Research Scientist
Chesapeake Biological Laboratory, University of Maryland Center for Environmental Science

Abstract

We examined photo-ammonium production from dissolved organic matter (DOM) in three different sites. Photoproduced ammonium has been found to be an important source of nutrients in nitrogen-limited waters, but this process is not well understood. In this study, samples were taken from St. Mary's Lake and the Patuxent River in Maryland and three different landfill leachates in Florida—active, closed reverse osmosis brine (brine), and closed landfill leachate. These samples were chosen to reflect a range of conditions to allow us to compare photoammonification across different sites. All samples were filtered through glass microfiber filters (Whatman GF/F) and solid phase extraction was done on all samples. Photo-degradation experiments were conducted on both filtered samples and extracts. Fluorescence excitation emission matrices (EEMs) were collected every twenty minutes on an Aqualog fluorometer and irradiation lasted either twenty or twenty-eight hours for all samples. Significant ammonium photo-production was observed in brine landfill leachate solid phase extract and St. Mary's Lake filtered sample and solid phase extract. Significant ammonium loss was observed in active and closed landfill leachate, which may have been due to outgassing of ammonia during the experiment. Photoammonifcation rates were strongly correlated with total dissolved nitrogen (TDN) concentrations. Samples with higher TDN tended to have higher rates of photo-ammonium loss. Parallel factor analysis (PARAFAC) was used to analyze EEM data. This is the first time that photoammonification has been studied in any of these sites.

Introduction

Dissolved organic matter (DOM) plays an important role in aquatic ecosystems as well as the global carbon cycle (Aarnos et al. 2012; Hansell et al. 2009). DOM is one of the largest exchangeable reservoirs of organic material on Earth with an estimated 620 gigatons of DOM in the world's oceans alone (Hansell et al. 2009). DOM can originate from both natural and anthropogenic sources and is defined as any organic matter that passes through glass fiber filters with a nominal pore size of 0.7 µm (Hansell 2015).

DOM contains a colored or chromophoric portion, which is referred to as chromophoric dissolved organic matter (CDOM). Because CDOM absorbs light in the UV and visible regions, it can limit the amount of light available for photosynthesis, but it can also absorb harmful UVA and UVB radiation that would otherwise harm marine life (Nelson and Siegel 2013). Absorbing light can degrade the chromophores and result in the production of a new stable product or reactive species (Hansell 2015). Therefore, photochemical reactions are an important pathway for altering DOM composition.

A fraction of CDOM also exhibits fluorescence and is known as fluorescent DOM (FDOM). Most of the DOM in our waters is uncharacterized, thus optical properties such as fluorescence offer a convenient way to study and track DOM. FDOM excitation emission matrices (EEMs) are typically characterized by protein-like and humic-like fluorescence (Coble 2007). Protein-like fluorescence gets its name from its similarity to three fluorescent amino acids in proteins: tryptophan, tyrosine, and phenylalanine. When dissolved in water, these amino acids have fluorescence maxima at Ex. 275/Em. 350 nm, Ex. 275/Em. 300 nm, and Ex. 255/Em. <300 nm, respectively (Hansell 2015). Humic-like fluorescence is so named because similar fluorescence was first found in soil organic matter and XAD extracts. Humic-like fluorescence has a broad emission spectrum from 400–600 nm (Hansell 2015).

Photo-degradation of DOM depends on its composition and a variety of factors including location, depth, pH, salinity, and season (Koopmans and Bronk 2002; Timko et al. 2015a; Timko et al. 2015b). This photo-degradation process can lead to the production of new species including ammonium, nitrites, nitrates, carbon dioxide, carbon monoxide, and methane.

Photo-production of ammonium is not well understood and the mechanisms for this process remain to be further explored. Photoammonifcation has been found to increase with increasing salinity and decreasing pH separately (Aarnos et al. 2012; Wang et al. 2000). This process has also been correlated with pH, CDOM and NH_3 concentrations, light exposure history of DOM, and DOC:DON ratios (Jeff et al. 2012). Photoammonification rates typically range from 10^{-6}–10^{-9} Mh^{-1} (Hansell 2015).

A study by Jeff et al. (2012) found significant ammonium photo-production in seven out of sixteen freshwater lakes in Saskatchewan, Canada. By combining results from other studies, Jeff et al. (2012) found that DON concentration and pH can be used to predict photoammonification rates. Koopmans and Bronk (2002) found significant ammonium photoproduction in four out of five of their estuarine samples and two out of thirteen groundwater samples. Furthermore, ammonium concentrations decreased significantly in five out of thirteen of their groundwater samples.

While the causes for ammonium photoproduction and loss are unclear, areas where ammonium is photo-produced often benefit from this new source of nitrogen. Vähätalo and Järvinen (2007) found that photoproduction of bioavailable N can sustain background productivity of plankton in nitrogen limited surface waters. The importance of this photoproduced N ranges from a few percent to greater than fifty percent of the bioavailable N, depending on other nitrogen fluxes (Hansell 2015). Photo-degradation of DOM can stimulate bacterial and plankton growth, with impacts on food web dynamics and community structure.

To gain a better understanding of ammonium photoproduction, we studied DOM from landfill leachate in Florida, St. Mary's Lake in Maryland, and the Patuxent River. By looking at DOM from anthropogenic, freshwater, and estuarine sources, we hoped to obtain a better understanding of what controls this photo-process. The objectives of this study were to quantify

photoproduction of ammonium from DOM in three different sites and understand the DOM photo-degradation kinetics.

Materials and Methods

Study Locations

Landfill leachate samples were collected by Nicole Robey on May 22, 2018 in Florida. Active landfill leachate was obtained from New River Landfill Cell 6. New River Landfill is a publicly owned and operated facility in Union County, 35 miles north of Alachua County. Closed landfill leachate and closed reverse osmosis (RO) brine leachate were both collected from Alachua County Southwest Landfill. The active landfill leachate was a very dark brown liquid darker than the other two leachates. Both the brine and closed landfill leachates were a lighter yellowish brown with the brine being a little darker than the closed. This difference in color can also be seen in these samples' initial absorbance spectra (Figure 1).

Surface water from St. Mary's Lake in St. Mary's River State Park in Callaway, Maryland was collected on July 17, 2018. St. Mary's Lake is a manmade freshwater lake approximately 250 acres that is a popular spot for fishing. Water was collected to the left of the boat ramp at 38°15'08.9"N 76°32'29.5"W with two 2 L glass bottles. Lake water was clear yellow.

Surface water from the mouth of the Patuxent River was collected at the end of the research pier at Chesapeake Biological Lab on July 25, 2018 shortly after high tide. Water was collected using a 2 L glass bottle and the bottle and cap were rinsed three times in the bay water before collecting the sample. The river water was very clear.

Sample Preparation

All water samples were vacuum filtered through 0.7 µm glass microfiber filters (Whatman GF/F) and stored at 4°C. Solid phase extraction was done on a portion of all the filtered samples to isolate the DOM. Varying volumes were extracted depending on the sample's dissolved organic carbon (DOC) concentration. 1g PPL cartridges were used for all samples and were first activated with 5 mL of methanol followed by 5 mL of 0.1% formic acid. Water samples were acidified to pH 2 using concentrated HCl. After all the sample had been filtered through the cartridge, the cartridge was washed with 15 mL of 0.1% formic acid and allowed to dry for half an hour. After drying the cartridges, 8-10 mL of methanol were used to elute the DOM, and the solid phase extract was stored in a freezer. The mass of the sample that ran through the cartridges was recorded for dilution calculations.

Photo degradation experiments were done on both the filtered samples and solid phase extracts for all locations. All filtered landfill leachate samples were diluted by 40X. Water from St. Mary's Lake and Chesapeake Bay were not diluted. Solid phase extract samples were prepared by drying 1 mL of the extract in methanol and re-dissolving the DOM in 50 mL of Milli-Q water. Patuxent River extracts were prepared by drying 5 mL of the extract in methanol and re-dissolving the DOM in 50 mL of Milli-Q water.

Experimental Design

A custom designed photo-degradation system was used to irradiate samples while monitoring sample absorbance and fluorescence (Figure 2) (Gonsior 2017). This system can measure photo kinetic data of DOM, changes in apparent fluorescent quantum yields, and time-resolved

photo-metabolite formation (Gonsior 2017). In this system, samples flow from a temperature and pH-controlled water bath to the Aqualog fluorometer. The Aqualog records fluorescence measurements every twenty minutes for a total of 60 excitation emission matrices (EEMs) for each photo-degradation experiment. From the Aqualog, samples move to a solar simulator that mimics the intensity of one solar sun at 45° at solar noon in summer, and back to the water bath (Gonsior 2017).

Photo-degradation experiments were done in duplicates with filtered water and solid phase extract samples for every site. All experiments except two lasted twenty hours with an integration time of 0.4 seconds. Experiments with the Patuxent River water lasted twenty-six hours because the integration time on the Aqualog was increased to three seconds to allow for adequate fluorescence yields. Fluorescence was normalized to a 1 ppm quinine sulfate standard for all experiments. The pH was maintained around 8 for the duration of each experiment to prevent pH from affecting fluorescence or photo-degradation kinetics of our samples (Timko et al. 2015a).

Twenty-two mL of each sample were run through the photo-degradation system and the leftover, non-irradiated sample was frozen. At the end of each run, the irradiated sample was removed and frozen for further analysis. In between experiments, the system was cleaned with 22 mL of isopropanol and then rinsed four times with 22 mL of Milli-Q water. The pH probe was placed in a beaker with Milli-Q water and the pH control was shut off after each experiment. The pH probe was placed in storage solution over the weekends and calibrated about once a week.

Data Analysis

Before and after samples from each photo-degradation experiment were sent to Nutrient Analytical Services Laboratory (NASL) at Chesapeake Biological Laboratory for ammonium, nitrite, and nitrate analysis. Initial DOC and TDN concentrations were measured with a Shimadzu TOC analyzer. Excitation emission matrices were analyzed using parallel factor analysis (PARAFAC). Photo-kinetic data from each sample were analyzed in MATLAB.

Results

Water chemistry

The studied sites covered a range of dissolved organic carbon (DOC) and total dissolved nitrogen (TDN) concentrations (Table 1). The majority of the samples had nitrite and nitrate levels below detection limits, therefore, total organic nitrogen (TON) was calculated by subtracting the initial ammonium concentration from that samples' TDN. Solid phase extraction efficiencies were calculated using DOC concentrations of the filtered samples and extracts and ranged from 65-94%.

Photoammonification

Ammonium concentrations increased significantly in the brine landfill leachate solid phase extract, St. Mary's Lake, and Patuxent River solid phase extract samples (Table 2). This corresponds to 1.47–42.04% increase in TDN and a 22–320% increase in ambient ammonium concentration. With an average production of 0.147 mg N/L and an ambient ammonium concentration of 0 mg N/L, our results suggest that photoproduced ammonium can provide a significant source of ammonium in St. Mary's Lake in the summer. Ammonium concentrations decreased significantly in the active and closed landfill leachate samples. This loss corresponds

to a 10.26–11.12% decrease in TDN and a 12.84–13.47% decrease in ambient ammonium concentration. All other samples had insignificant changes in ammonium concentrations. One replicate of the brine landfill leachate increased in ammonium concentration by about 3.824 mg/L while the other replicate decreased in ammonium concentration by 3.072 mg/L. Additionally, one replicate of the closed solid phase extract had no change in ammonium concentration while the second sample had an increase of 0.016 mg/L of ammonium.

Photoammonification rates ranged from -212.475 µg/L*h to 18.8 µg/L*h (Table 3).
The rate of photoammonification in St. Mary's Lake fell within the range of rates found in other bodies of freshwater. The Patuxent River did not have significant ammonium photoproduction and its rate was lower than those of other estuarine studies. A strong relationship was found between photoammonification rates and TDN concentrations (Figure 3). As TDN concentrations increased, the rate of ammonium loss also increased. Moderate relationships were found between photoammonifaction rates and TON concentrations (R^2=0.441), initial absorbance at 300 nm (R^2=0.42), final absorbance at 300 nm (R^2=0.4344), and initial absorbance at 300 nm normalized to DOC concentration (R^2=0.4229).

Nitrite/Nitrate Production

The majority of the samples had nitrite/nitrate levels below the method detection limit and/or method reporting limit at NASL. The method detection limit for nitrite/nitrate analysis was 0.0057 mg N/L. Samples that had detectable levels of nitrite and nitrate were Patuxent River water before and after irradiation and irradiated brine landfill leachate. Nitrite and nitrate levels for these samples were 0.0380 mg N/L, 0.0359 mg N/L, and 0.2001 mg N/L respectively.

PARAFAC analysis

A four component PARAFAC model was created from EEMs collected from all the photo-degradation experiments (Figure 4). Components one and two are characterized by humic-like fluorescence and component three is dominated by protein-like fluorescence. The PARAFAC model was uploaded onto OpenFluor, an online library of fluorescence from organic compounds in the environment to compare our components with those from other studies (Figure 5). The first three components in our model had matches from fifteen other models and the fourth component did not have any matches. The fluorescence maximum of the first component showed a clear difference in degradation over time for landfill leachate and natural water samples (Figure 6). For the second component, all the samples degraded relatively similarly over time (Figure 7). In the third component, the active landfill leachate and active solid phase extract show different degradation trends over time (Figure 8). For the fourth component, the fluorescence maximum of the active landfill leachate behaved differently from its solid phase extract again (Figure 9). The rest of the landfill leachate samples all degrade similarly over time and the natural water samples are also similar.

Relative apparent quantum yields

Relative apparent quantum yields (AQY) were plotted over excitation wavelength for each sample (Figure 10). Relative AQYs were obtained by normalizing the integrated fluorescence to the sample absorbance. Aside from the Patuxent River samples, all solid phase extracts had higher relative AQYs than their whole water sample. Relative AQYs tended to decrease over time, with a few exceptions. The active landfill leachate had a few large spikes in relative AQY towards the end of the experiment while the active extract decreased in relative AQY over time. Both the closed and brine whole water samples and extracts behaved similarly and decreased

in relative AQY over time. The relative AQY of the whole water sample from St. Mary's Lake decreased over time while the extract had two increases in relative AQY towards the end of the experiment. The Patuxent River whole water sample's relative AQY increased during the experiment and the extract's relative AQY decreased over time with one spike towards the end of the experiment.

Mini electrodialysis (ED) system

An ElectroPrep Electrophoresis Dialysis system from Harvard Apparatus was used this summer to explore the possibility of desalting samples through ED and comparing the results to solid phase extraction. Both closed and brine landfill leachate were successfully desalted at 200V and 90–160 min and 135 minutes respectively. Salinity was measured using a refractometer. Ten mmol of formate buffer was used for all experiments and 500 MW cellulose acetate membranes. The range in times it took to desalt the same sample may have been related to the number of times the buffer and membranes were reused. A desalted sample of the closed landfill leachate was also run on the photo-degradation system for 20 hours with DOC and TDN measurements taken before irradiation. After accounting for dilutions, DOC in the desalted sample was 552 ± 4 mg/L. In the filtered closed leachate DOC was 538.4 ± 8 mg/L and in the closed solid phase extract DOC was 482 ± 5.5 ± mg/L. TDN in the desalted sample before irradiation was 357.6 ± 2 mg/L. TDN in the filtered closed leachate was 1048.4 mg/L and in the solid phase extract it was 39.5 ± 0.9 mg/L. After irradiation, ammonium concentration decreased by 0.438 mg/L, corresponding to a rate of -21.9 µg/L*h. In the filtered closed landfill leachate sample, ammonium concentrations decreased by -3.0305 mg/L*h, corresponding to a rate of -151.525 µg/L*h. In the closed extract, ammonium concentrations increased by 0.008 mg/L, corresponding to a rate of 0.4 µg/L*h, which was not significant.

Landfill leachate isotopic analysis

Landfill leachate from all three treatments were measured for delta13C-extractable DOC and delta15N-extractable DON in triplicates using Thermo Scientific IRMS Delta Uplus Coupled to Elemental Analysis Costech ECS 4010. Solid phase extracts of each sample were pipetted into smooth wall tin capsules and dried at 45°C. Replicates were very consistent and d13C-DOC values averaged -22.50 ± 1.68‰, -25.13 ± 0.23‰, and -25.73 ± 0.23‰ for active, brine, and closed landfill leachate respectively. In the same order, d15N-DON values averaged 3.43 ± 0.12‰, 4.2 ± 0‰, and 4.3 ± 0.1‰. This analysis was done on a semi-consistent pool (non-volatile) of a semi-consistent pool (extractable by PPL-SPE), making these results hard to interpret. While little is known about d13C-DOC in wastewater and d15N-DON in general, these values are consistent with the few existing measurements done using other methods looking at a larger pool (Griffith et al. 2009).

Discussion

Rates of photoammonification were studied in three different sites and the samples that had significant ammonium photoproduction were brine landfill leachate solid phase extract, St. Mary's Lake whole water and extracts, and Patuxent River solid phase extract. Consistent with the observed trend, these samples all had TDN concentrations on the lower end from 0.41–2.41 mg N/L. This is somewhat in contrast to a previous study that found DON to be an important predictor in photoammonification, with higher DON concentrations correlating with greater photoammonification rates (Jeff et al. 2012).

The active landfill leachate and closed landfill leachate both had significant loss of ammonium after irradiation. These samples all had high TDN concentrations ranging from 26.21 mg N/L to 38.20 mg N/L. A similar trend was observed in another study that found that groundwater samples with higher ambient ammonium concentrations lost more ammonium after irradiation (Koopmans and Bronk 2002). This photochemically mediated loss of ammonium could be due to a variety of factors including ammonium oxidation, but no increases were observed in nitrite and nitrate concentrations. The two samples that did increase in nitrite and nitrate concentrations did not have significant changes in ammonium concentrations. Ammonium may have been volatilized as ammonia as a result of hydroxide produced during the photooxidation of DOM (Stumm and Morgan 2012). Ammonium loss could also have been due to the photochemical incorporation of ammonia into DOM (Koopmans and Bronk 2002).

Significant ammonium photoproduction and loss was found in five samples including filtered samples and solid phase extracts. Filtered water and solid phase extracts from the same sample had different photoammonification rates and optics behavior. Solid phase extraction isolates and concentrates the DOM and in this process the sample was acidified to pH 2 and DOM recovery was not 100%. The effects of changing the pH on sample composition are unknown (Hansell 2015). It is possible that the lost DOM or other removed compounds play an important role in the photo-loss or production of ammonium. Bushaw et al. (1996) also studied photoammonification rates in a boreal pond and looked at both filtered water and the fulvic acid fraction of DOM isolated by hydrophobic resin and found a difference in photoammonification rates.

Differences in fluorescence and relative AQY curves were observed in whole water samples and solid phase extracts. The active landfill leachate whole water sample and extract behaved differently in the third and fourth components of the PARAFAC model and had different relative AQY curves. In comparison, both the brine and closed leachate whole water samples and extracts behaved similarly in terms of fluorescence and relative AQYs. This difference could have been due the differences in d13C-DOC and d15-DON values between the active and both brine and closed leachates. The brine and closed leachates had similar d13C-DOC, d15-DON, DOC, and TDN concentrations, all of which may have impacted fluorescence and relative AQYs. St. Mary's Lake and the Patuxent River both behaved differently in the third component of the PARAFAC model and had different relative AQYs for the whole water samples and extracts.

Our PARAFAC model had fifteen matches on OpenFluor. Component one matched five models with samples from the Florida Keys, US, Canadian Archipelago and coastal Beaufort Sea surface, San Francisco Bay, Florida coastal Everglades, and drinking water treatment plants in Australia (Murphy et al. 2013; Shutova et al. 2014; Walker et al. 2009; Yamashita et al. 2013; Yamashita et al. 2010). Component two had nine matches on OpenFluor. These studies had samples from the Temperate Northern Atlantic, Baltic Sea, and Kattegat, Neuse River Estuary, North Carolina, San Francisco Bay, Shark Bay, Australia, and Zambezi River and Kafue River in Africa (Cawley et al. 2012; Lambert et al. 2016; Murphy et al. 2013; Osburn et al. 2012; Osburn et al. 2016; Osburn and Stedmon 2011; Stedmon et al. 2007a; Stedmon et al. 2007b). Many of these studies were conducted in the Baltic Sea and the Neuse River Estuary, North Carolina. Component three had two matches and these samples came from five ecosystem groups of the Great Lakes and another study that sampled from the Temperate Northern Atlantic, Baltic Sea, and Kattegat and included sites downstream of a wastewater treatment plant (Williams et al. 2016). Component four did not match any model in the database. This component was very different between the landfill leachates and the natural water samples, which were essentially unchanged during the experiment.

In this study, we also examined the time-resolved photochemistry of these components and found differences in fluorescence behavior among the samples. Ammonium concentrations were measured before and after irradiation while changes in fluorescence in the DOM pool were measured every twenty minutes. Measuring ammonium concentrations at different time points could allow us to link photoproduction with changes in optical properties. Therefore, future studies should seek to determine if there is a relationship between photo ammonium production or loss and DOM fluorescence.

Conclusions

To the best of our knowledge, this was the first study on photoammonification in these three locations. Both filtered water samples and solid-phase extracts were examined in this study and our data indicate that solid-phase extraction may not be representative of DOM behavior in its environment. Differences were found in photoammonification, fluorescence, and relative AQYs between whole water and extracts. Three out of four components in our PARAFAC model had at least two matches on OpenFluor with samples from a range of locations. Future work should include studying the relationship between ammonium photoproduction and optical properties. This would allow us to determine if photoammonification can be predicted by DOM fluorescence.

Acknowledgements

I would like to thank my mentor, Dr. Michael Gonsior, and Dr. Leanne Powers for their tremendous mentorship and guidance this summer. I would also like to thank Katie Martin for helping me in the lab and NASL for analyzing my samples. Thank you to Maryland Sea Grant and the National Science Foundation for providing me the opportunity and funding to conduct research at Chesapeake Biological Laboratory this summer. This study was supported by NSF grant OCE-1756244.

References

Aarnos, H., P. Ylöstalo, and A. V. Vähätalo. 2012. Seasonal phototransformation of dissolved organic matter to ammonium, dissolved inorganic carbon, and labile substrates supporting bacterial biomass across the Baltic Sea. Journal of Geophysical Research: Biogeosciences 117.

Bushaw, K. L. and others 1996. Photochemical release of biologically available nitrogen from aquatic dissolved organic matter. Nature 381**:** 404.

Cawley, K. M., Y. Ding, J. Fourqurean, and R. Jaffé. 2012. Characterising the sources and fate of dissolved organic matter in Shark Bay, Australia: a preliminary study using optical properties and stable carbon isotopes. Marine and Freshwater Research 63**:** 1098–1107.

Coble, P. G. 2007. Marine optical biogeochemistry: the chemistry of ocean color. Chemical reviews 107**:** 402–418.

Gonsior, M. 2017. Time-resolved photodegradation of natural colored dissolved organic matter (CDOM) and contaminants in fresh- and marine waters using a custom-designed photodegradation system. Feature Article Masao Horiba Awards.

Griffith, D. R., R. T. Barnes, and P. A. Raymond. 2009. Inputs of fossil carbon from wastewater treatment plants to US rivers and oceans. Environmental Science & Technology 43: 5647–5651.

Hansell, D. A. 2015. Biogeochemistry of Marine Dissolved Organic Matter, Second ed. Elsevier Science.

Hansell, D. A., C. A. Carlson, D. J. Repeta, and R. Schlitzer. 2009. Dissolved organic matter in the ocean: A controversy stimulates new insights. Oceanography 22: 202–211.

Jeff, S., K. Hunter, D. Vandergucht, and J. Hudson. 2012. Photochemical mineralization of dissolved organic nitrogen to ammonia in prairie lakes. Hydrobiologia 693: 71–80.

Koopmans, D. J., and D. A. Bronk. 2002. Photochemical production of dissolved inorganic nitrogen and primary amines from dissolved organic nitrogen in waters of two estuaries and adjacent surficial groundwaters. Aquatic Microbial Ecology 26: 295–304.

Lambert, T. and others 2016. Along-stream transport and transformation of dissolved organic matter in a large tropical river. Biogeosciences 13: 2727–2741.

Murphy, K. R., C. A. Stedmon, D. Graeber, and R. Bro. 2013. Fluorescence spectroscopy and multi-way techniques. PARAFAC. Analytical Methods 5: 6557–6566.

Nelson, N. B., and D. A. Siegel. 2013. The global distribution and dynamics of chromophoric dissolved organic matter. Annual Review of Marine Science 5: 447–476.

Osburn, C. L., L. T. Handsel, M. P. Mikan, H. W. Paerl, and M. T. Montgomery. 2012. Fluorescence tracking of dissolved and particulate organic matter quality in a river-dominated estuary. Environmental science & technology 46: 8628–8636.

Osburn, C. L., L. T. Handsel, B. L. Peierls, and H. W. Paerl. 2016. Predicting sources of dissolved organic nitrogen to an estuary from an agro-urban coastal watershed. Environmental science & technology 50: 8473–8484.

Osburn, C. L., and C. A. Stedmon. 2011. Linking the chemical and optical properties of dissolved organic matter in the Baltic–North Sea transition zone to differentiate three allochthonous inputs. Marine Chemistry 126: 281–294.

Shutova, Y., A. Baker, J. Bridgeman, and R. K. Henderson. 2014. Spectroscopic characterisation of dissolved organic matter changes in drinking water treatment: from PARAFAC analysis to online monitoring wavelengths. Water research 54: 159–169.

Stedmon, C. A., S. Markager, L. Tranvik, L. Kronberg, T. Slätis, and W. Martinsen. 2007a. Photochemical production of ammonium and transformation of dissolved organic matter in the Baltic Sea. Marine Chemistry 104: 227–240.

Stedmon, C. A., D. N. Thomas, M. Granskog, H. Kaartokallio, S. Papadimitriou, and H. Kuosa. 2007b. Characteristics of dissolved organic matter in Baltic coastal sea ice: allochthonous or autochthonous origins? Environmental science & technology 41: 7273–7279.

Stumm, W., and J. J. Morgan. 2012. Aquatic chemistry: chemical equilibria and rates in natural waters. John Wiley & Sons.

Timko, S. A., M. Gonsior, and W. J. Cooper. 2015a. Influence of pH on fluorescent dissolved organic matter photo-degradation. Water research 85: 266–274.

Timko, S. A. and others 2015b. Depth-dependent photodegradation of marine dissolved organic matter. Frontiers in Marine Science 2: 66.

Vähätalo, A. V., and M. Järvinen. 2007. Photochemically produced bioavailable nitrogen from biologically recalcitrant dissolved organic matter stimulates production of a nitrogen-limited microbial food web in the Baltic Sea. Limnology and oceanography 52: 132–143.

Walker, S. A., R. M. Amon, C. Stedmon, S. Duan, and P. Louchouarn. 2009. The use of PARAFAC modeling to trace terrestrial dissolved organic matter and fingerprint water masses in coastal Canadian Arctic surface waters. Journal of Geophysical Research: Biogeosciences 114.

Wang, W., M. A. Tarr, T. S. Bianchi, and E. Engelhaupt. 2000. Ammonium photoproduction from aquatic humic and colloidal matter. Aquatic Geochemistry 6: 275–292.

Williams, C. J. and others 2016. Human activities cause distinct dissolved organic matter composition across freshwater ecosystems. Global change biology 22: 613–626.

Yamashita, Y., J. N. Boyer, and R. Jaffé. 2013. Evaluating the distribution of terrestrial dissolved organic matter in a complex coastal ecosystem using fluorescence spectroscopy. Continental shelf research 66: 136–144.

Yamashita, Y., L. J. Scinto, N. Maie, and R. Jaffé. 2010. Dissolved organic matter characteristics across a subtropical wetland's landscape: application of optical properties in the assessment of environmental dynamics. Ecosystems 13: 1006–1019.

Figures and Tables

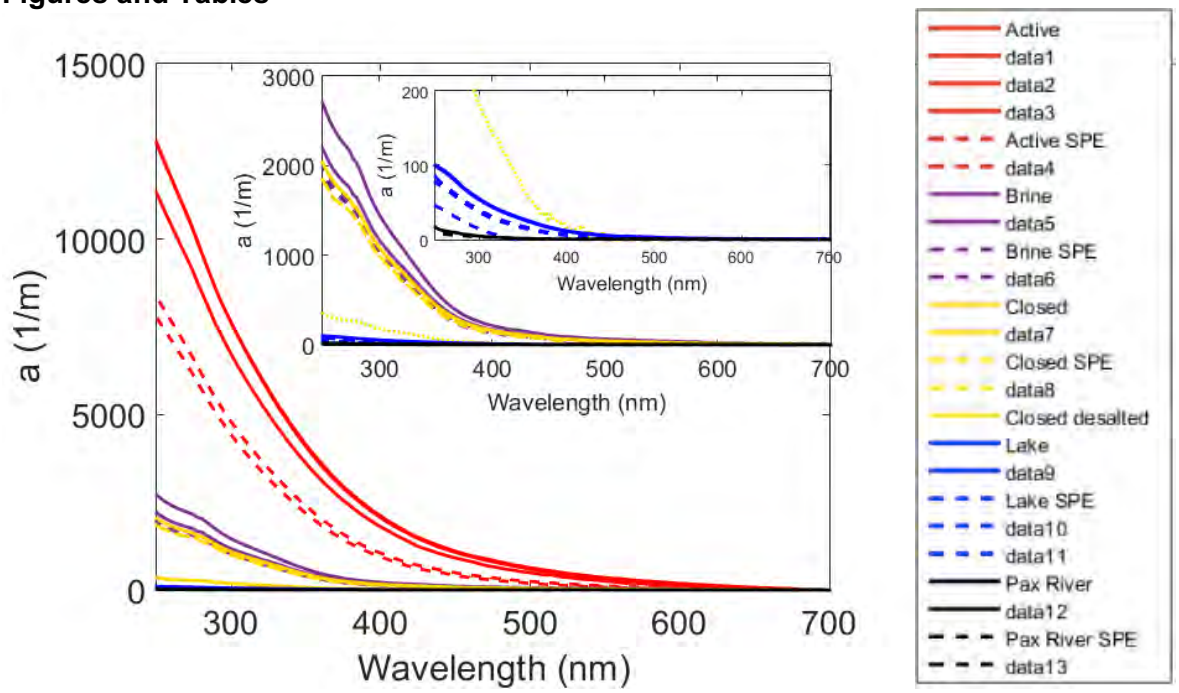

Figure 1. Initial absorbances of each sample plotted over wavelength. Solid lines represent whole water samples and dotted lines represent solid-phase extracts. Red is active leachate, purple is brine leachate, yellow is closed leachate, blue is St. Mary's Lake, and black is Patuxent River.

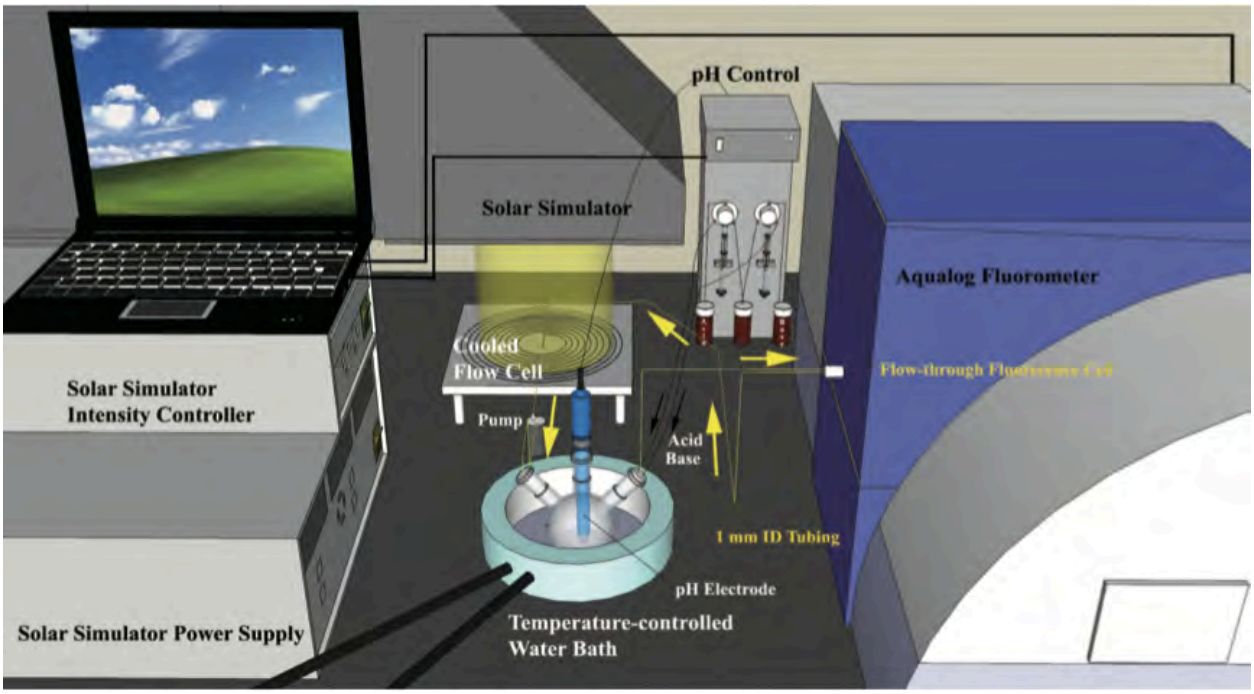

Figure 2. Custom-designed photo-degradation system used in this study (Gonsior 2017).

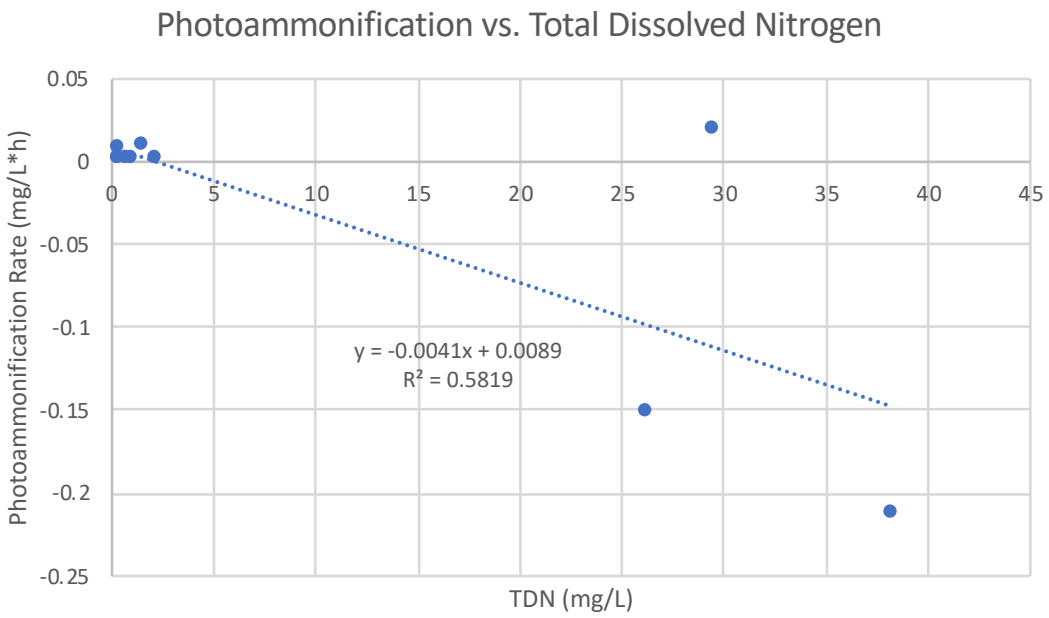

Figure 3. Photoammonification rate graphed over TDN concentrations. Photo-ammonium loss tends to increase as TDN increases.

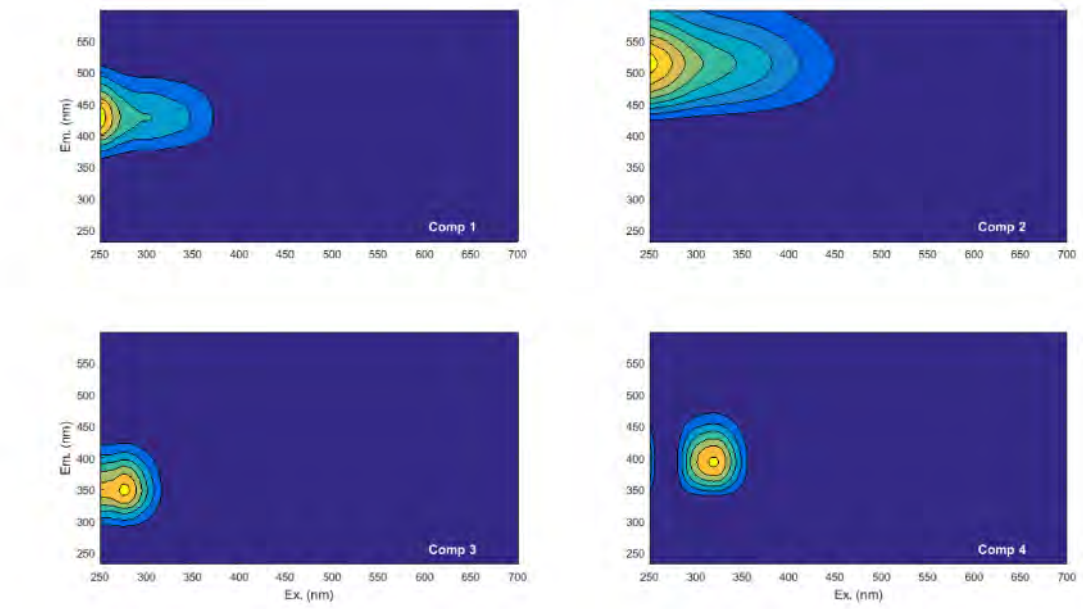

Figure 4. Four component PARAFAC model compiled from EEMs from all the photo-degradation experiments.

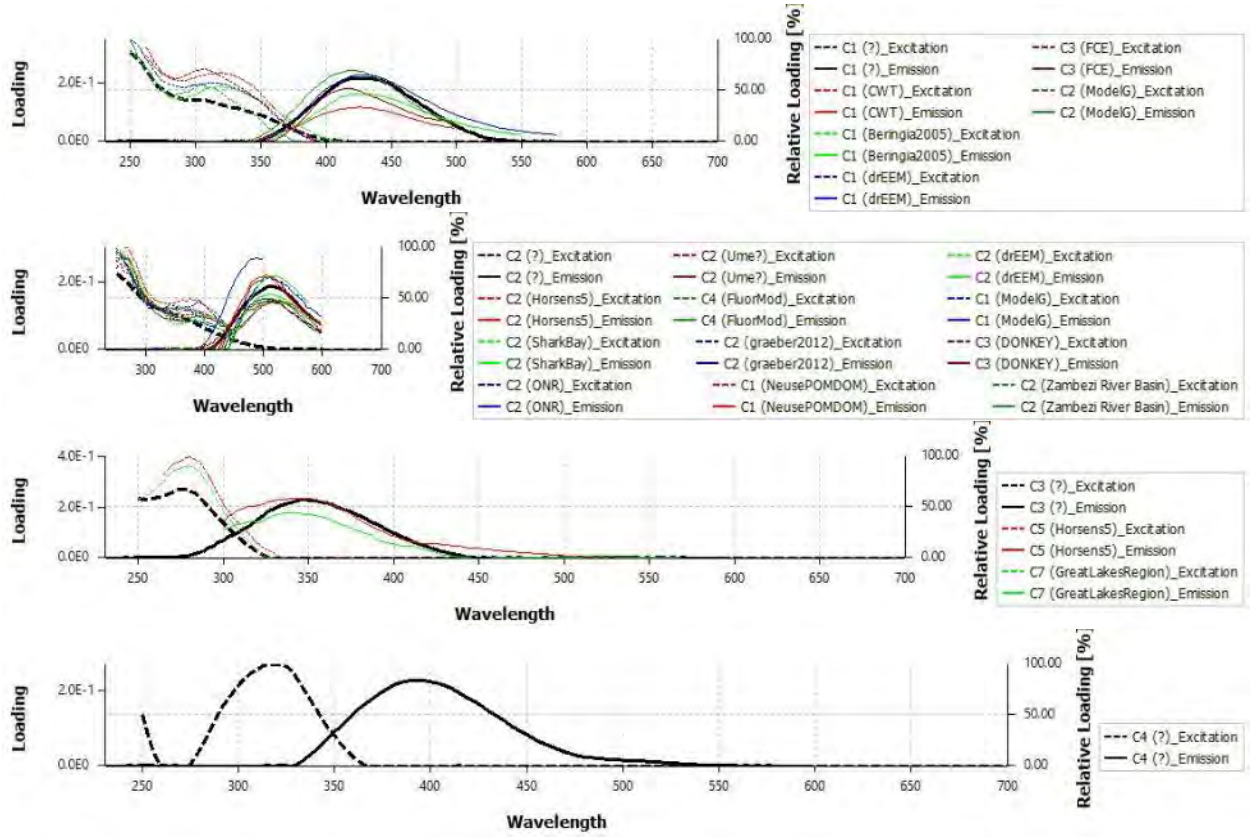

Figure 5. OpenFluor results

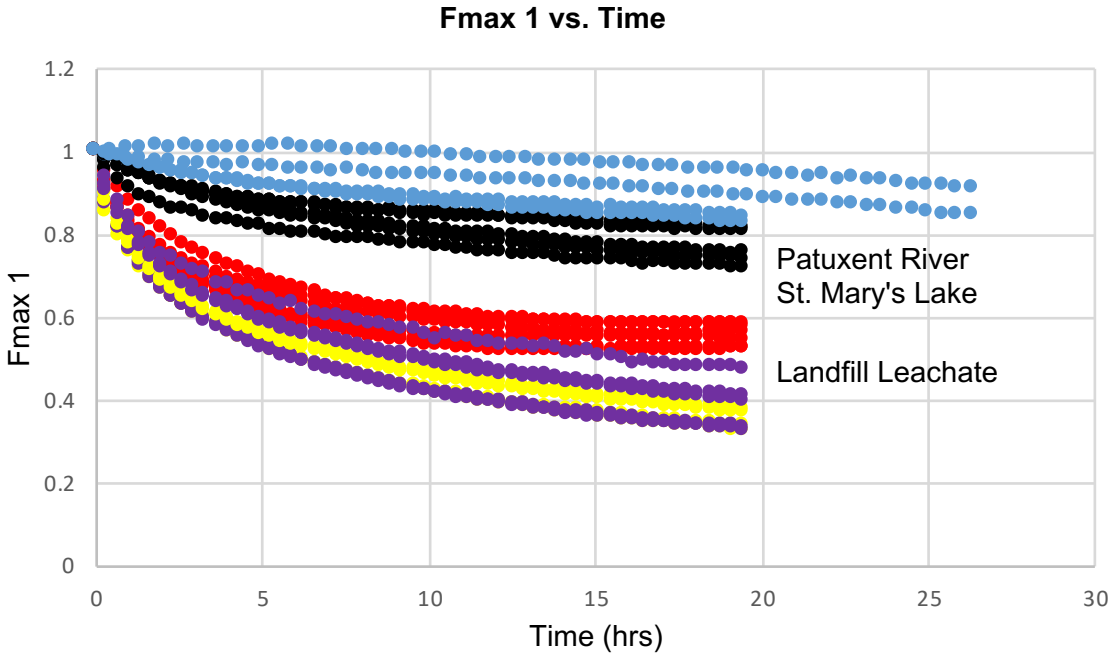

Figure 6. Fluorescence maximum of component one for each sample graphed over time.

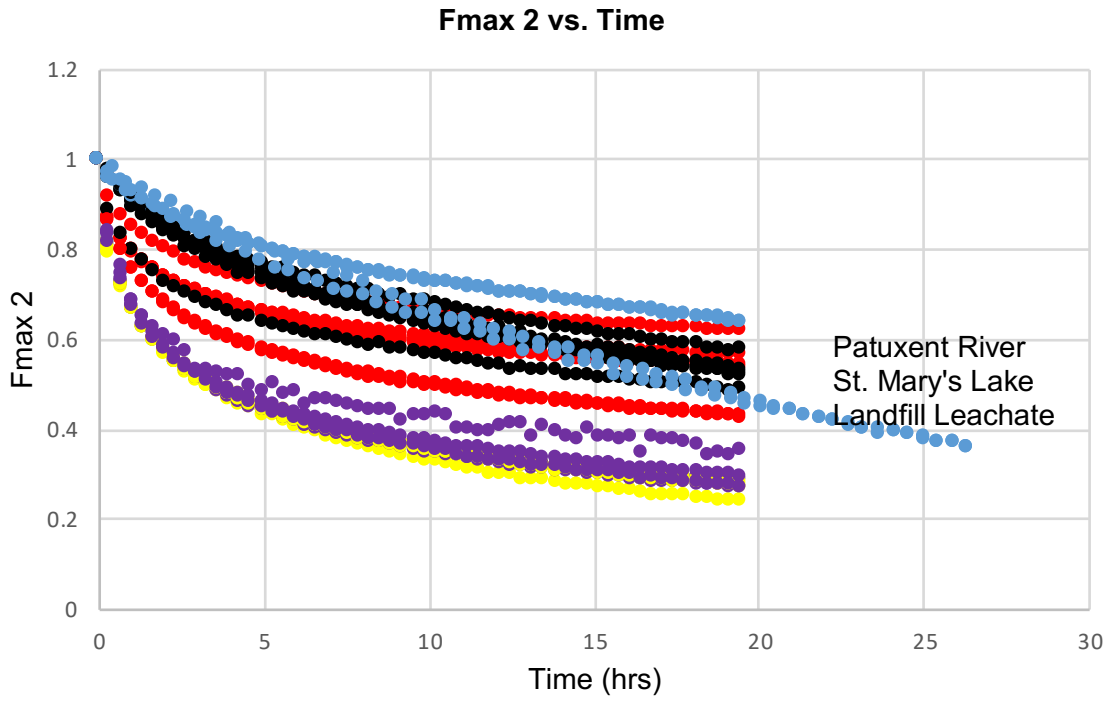

Figure 7. Fluorescence maximum of component two for each sample graphed over time.

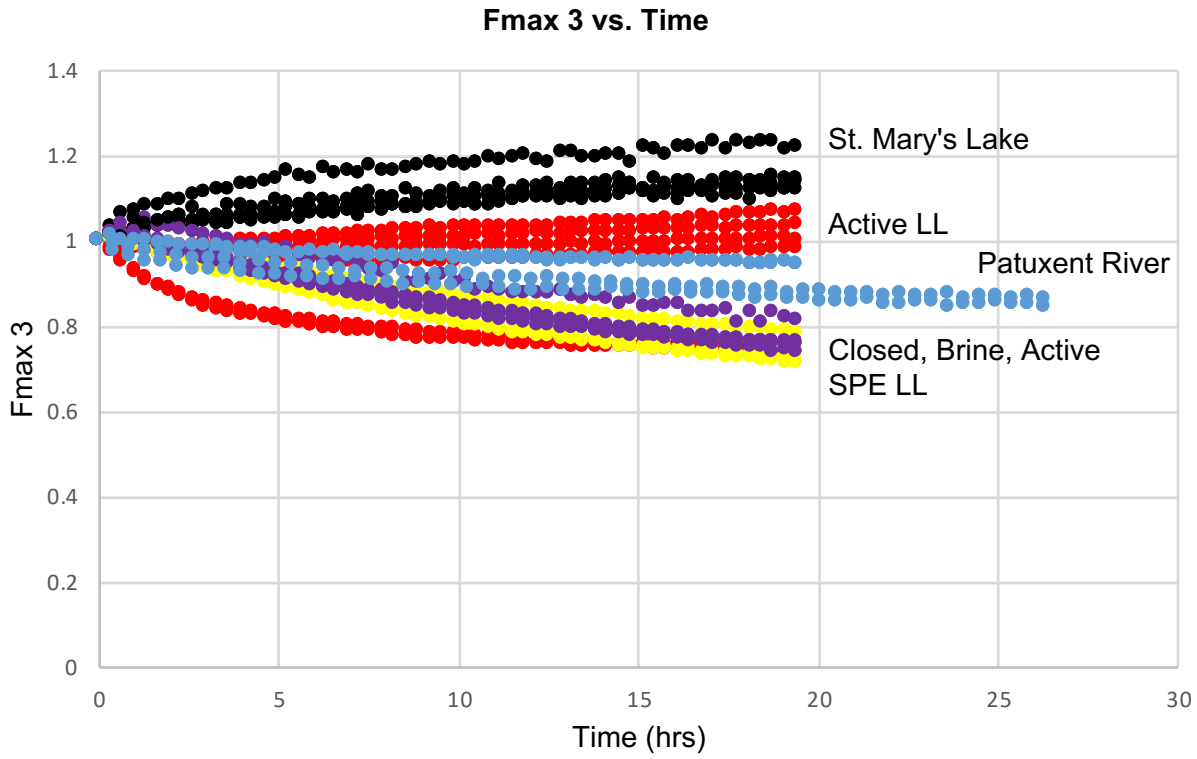

Figure 8. Fluorescence maximum of component three for each sample graphed over time.

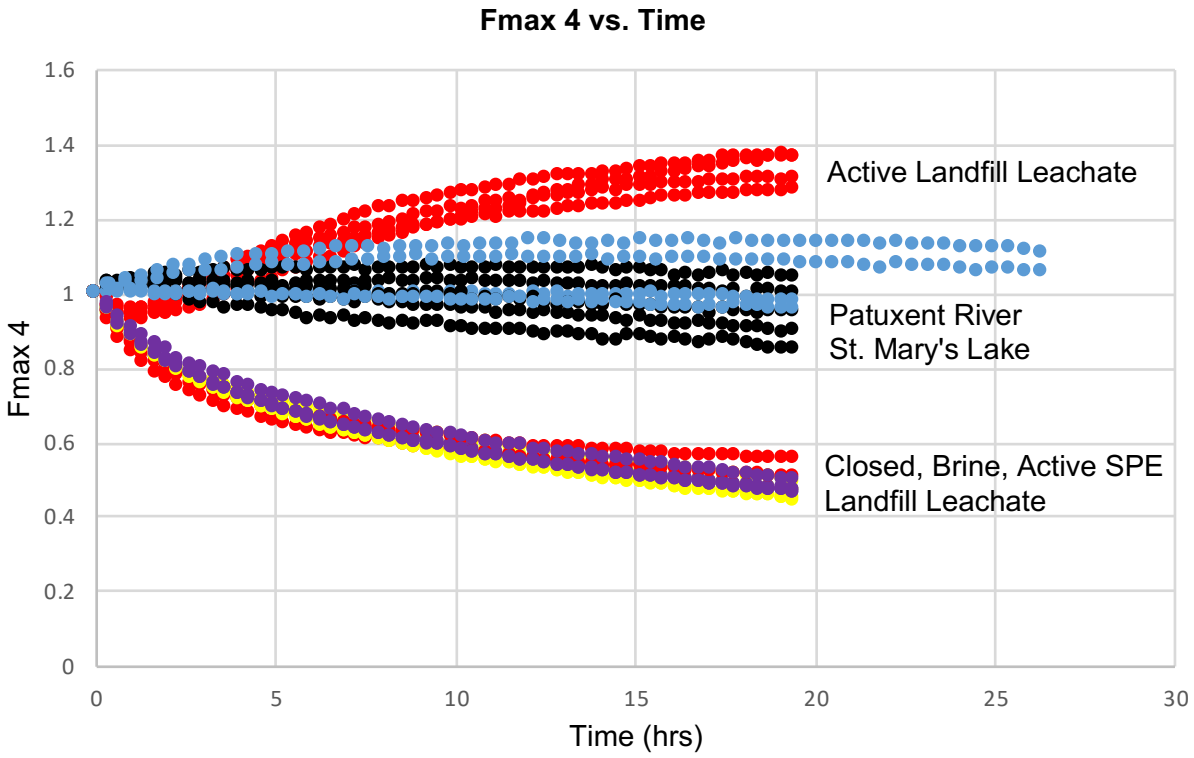

Figure 9a. Fluorescence maximum of component four for each sample graphed over time.

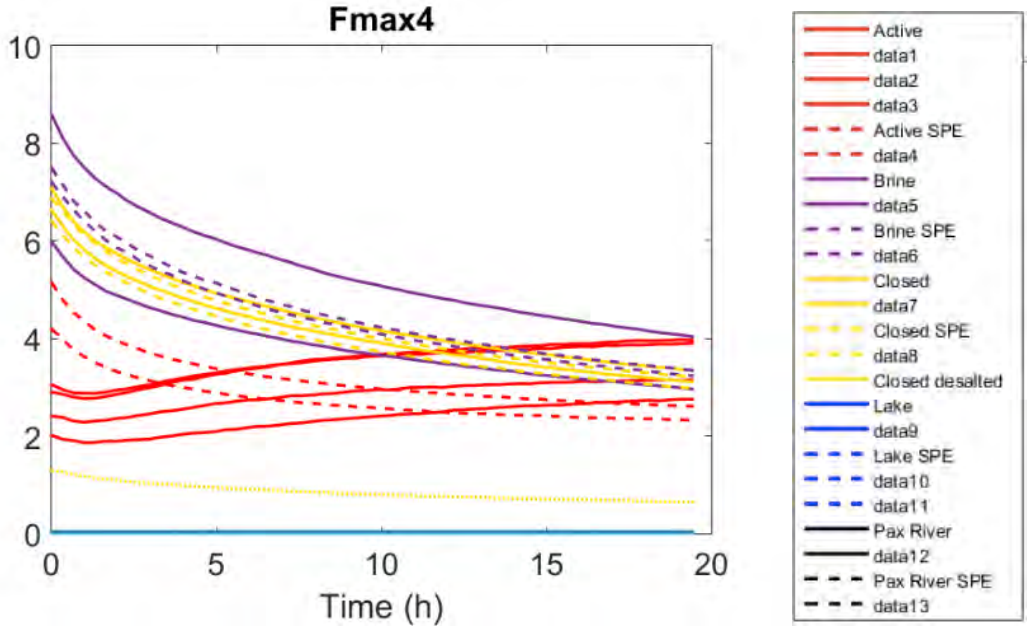

Figure 9b. Fluorescence maximum of component four for each sample graphed over time. Solid lines represent whole water samples and dotted lines represent solid phase extracts. Red is active leachate, purple is brine leachate, yellow is closed leachate, blue is St. Mary's Lake, and black is Patuxent River.

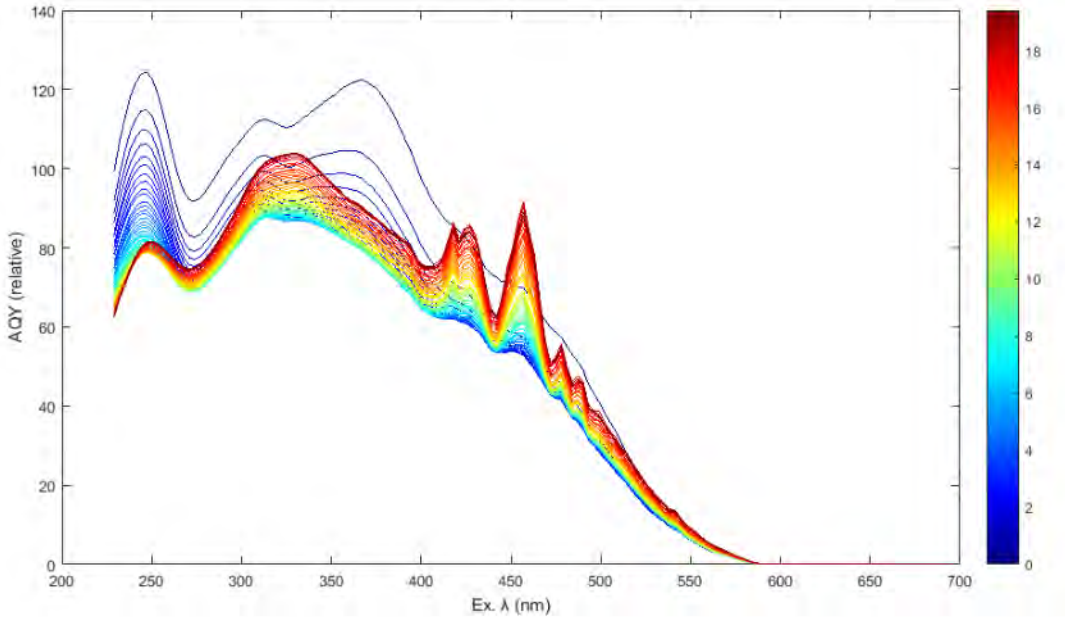

Figure 10a. Active Landfill Leachate

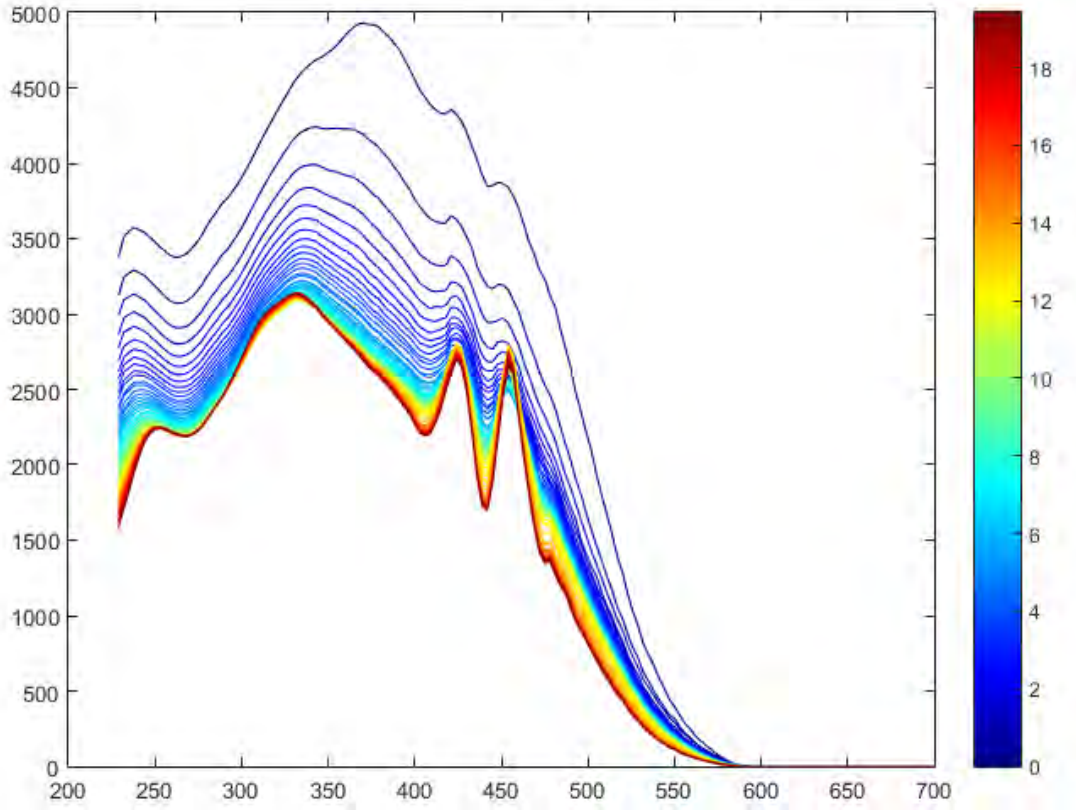

Figure 10b. Active SPE

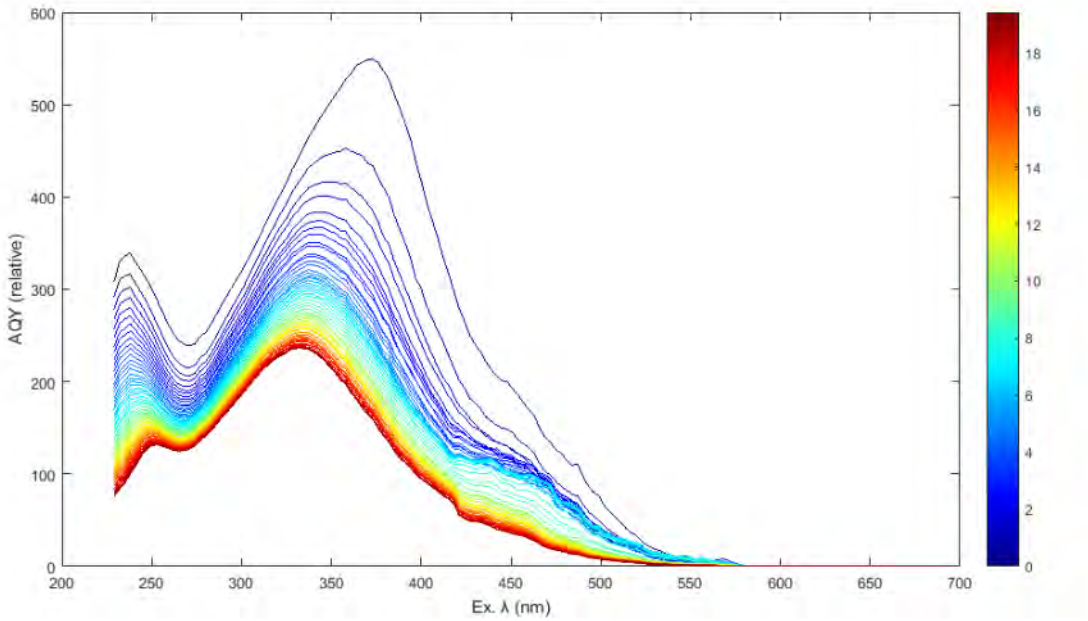

Figure 10c. Brine Landfill Leachate

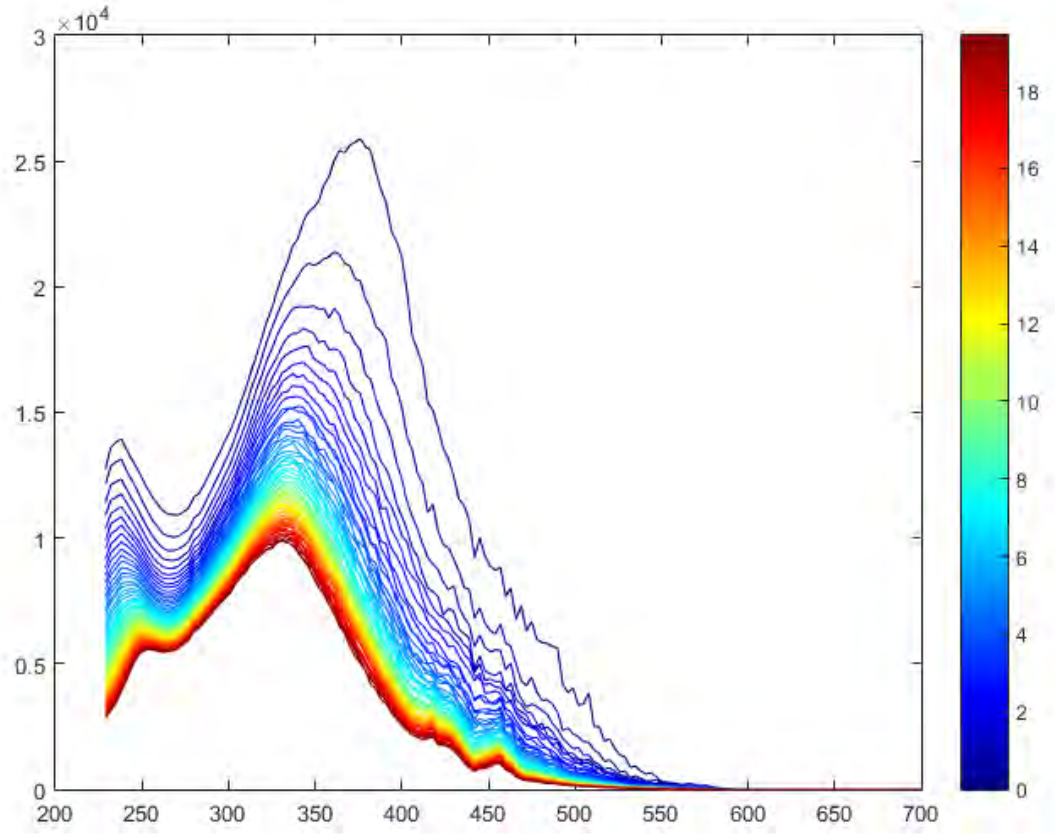

Figure 10d. Brine SPE

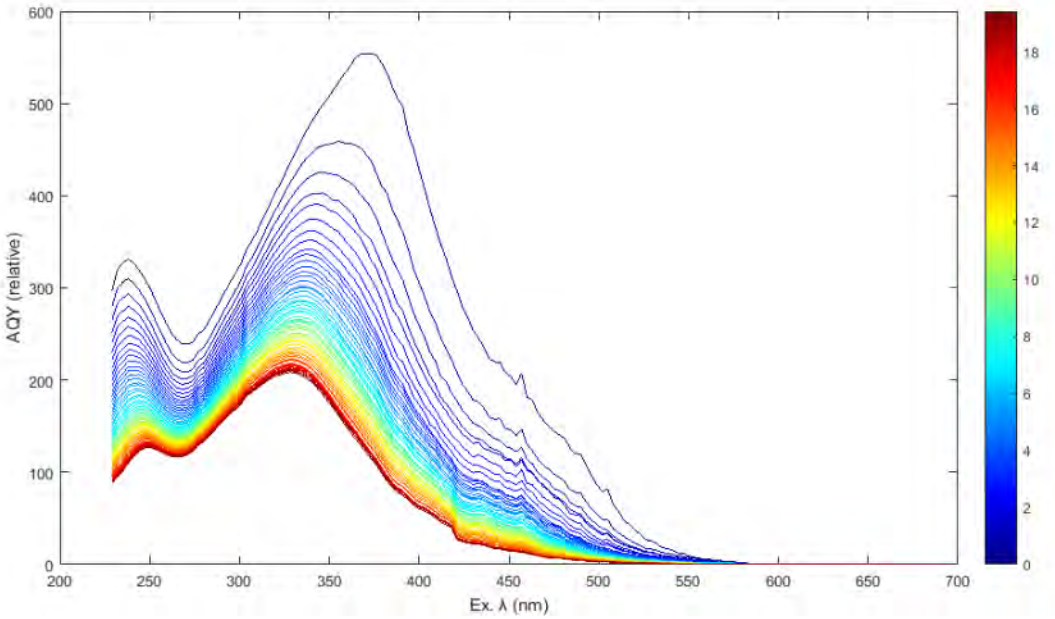

Figure 10e. Closed Landfill Leachate

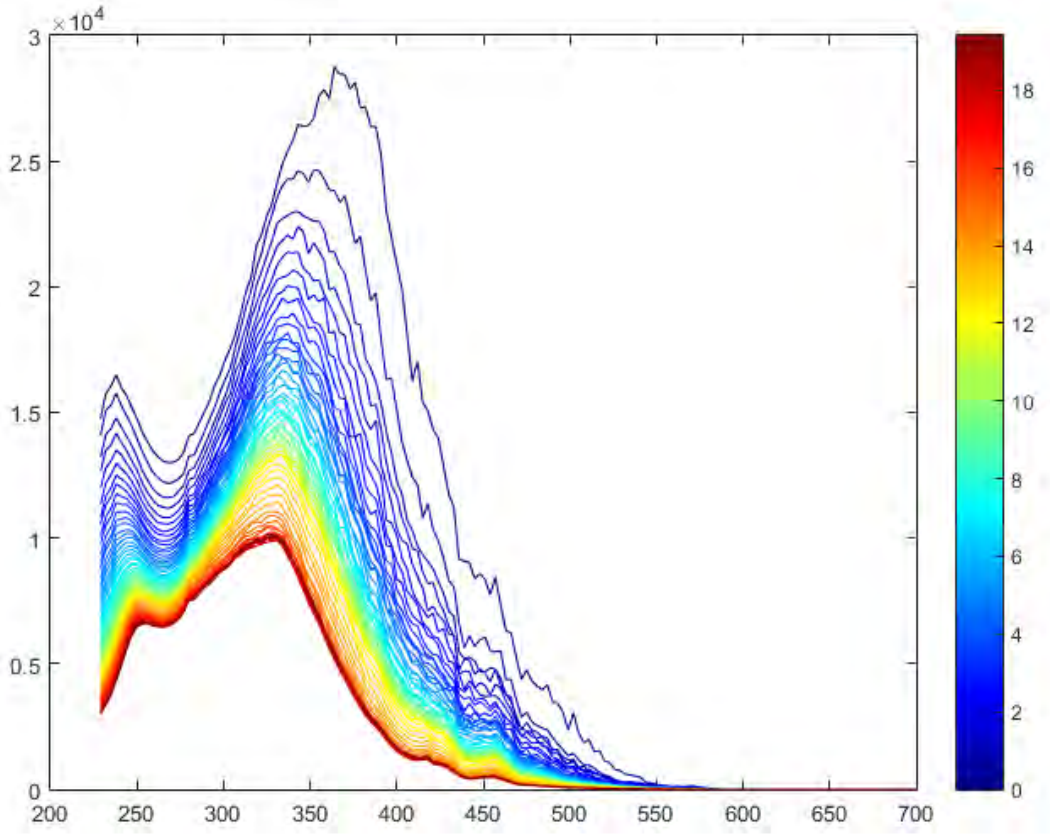

Figure 10f. Closed SPE

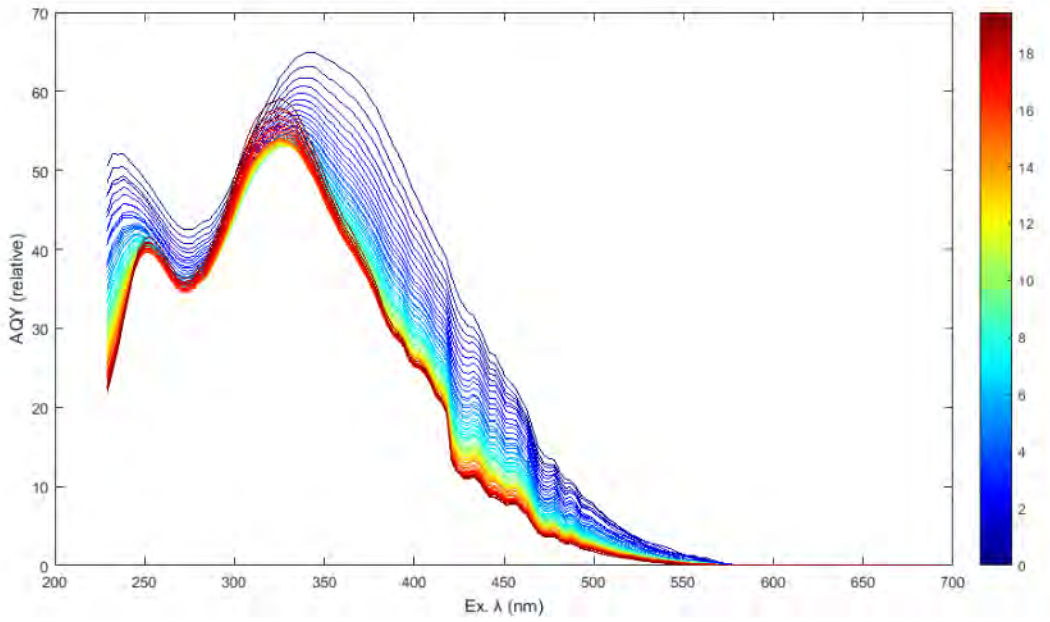

Figure 10g. St. Mary's Lake

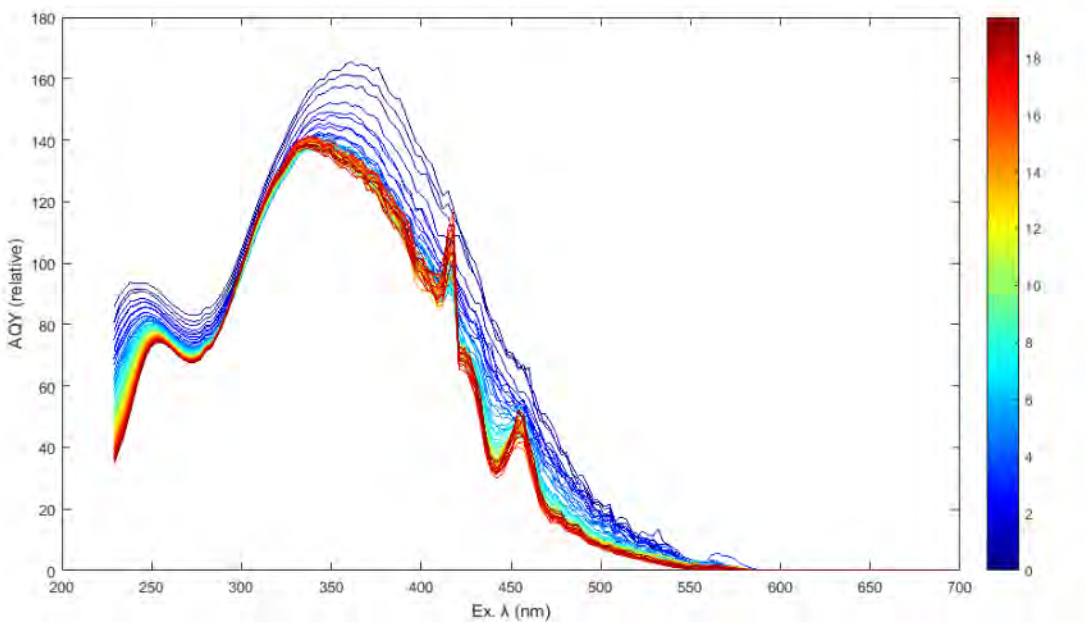

Figure 10h. St. Mary's Lake SPE

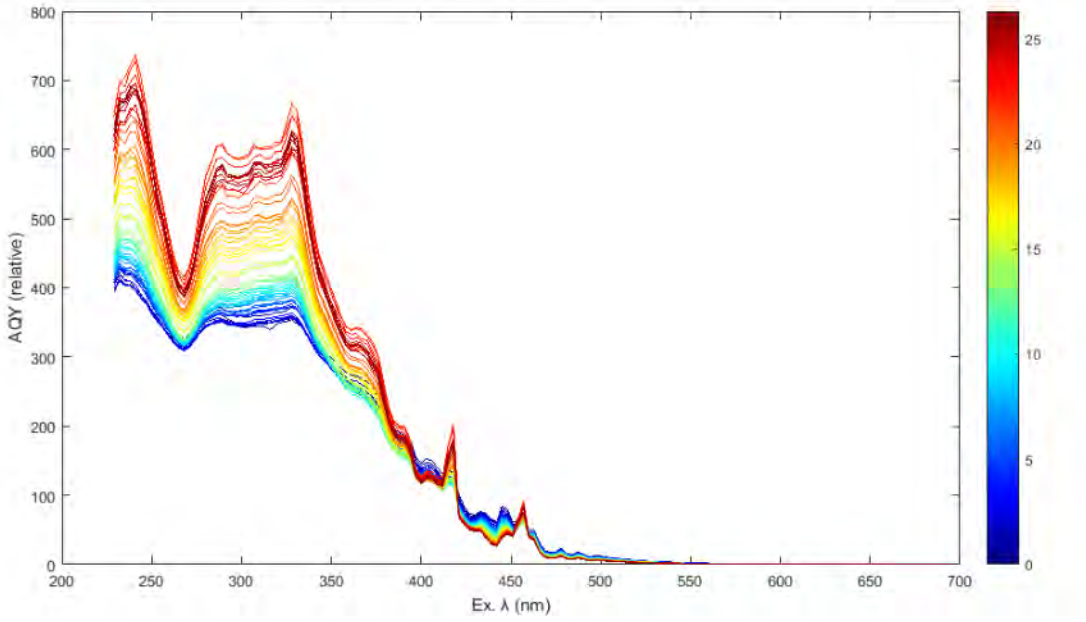

Figure 10i. Patuxent River

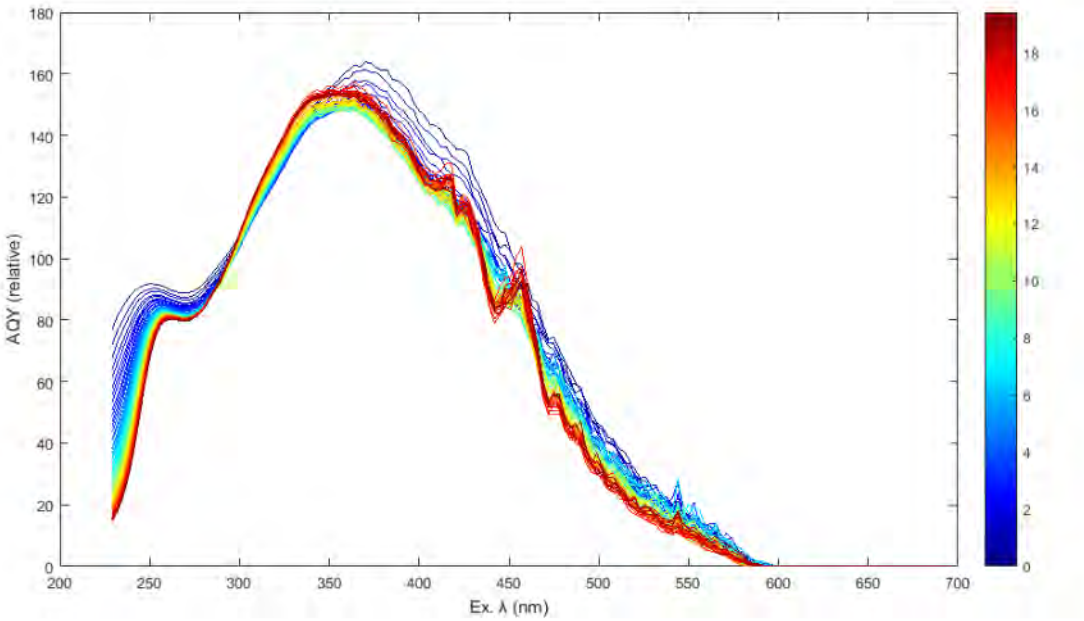

Figure 10j. Patuxent River SPE

Figure 10a-j. Relative apparent quantum yields (AQY) graphed over excitation wavelengths for all samples. Color bars indicate time in hours.

Table 1. Chemical and optical characteristics of the samples: salinity, dissolved organic carbon (DOC), total dissolved nitrogen (TDN), total organic nitrogen (TON), absorbance before ($a300_1$) and after ($a300_2$) irradiation, and ammonium production and loss rates, and DOC:DON ratios. Landfill Leachate (LL), Solid Phase Extract (SPE)

Sample	Dilution Factor	Salinity (ppt)	DOC (mg/L)	TDN (mg/L)	TON (mg/L)	$a300_1$ (m^{-1})	$a300_2$ (m^{-1})	$a300_1$:DOC	NH_4 rate (mg/L*h)	DOC:DON
Active LL	40	0	26.10	38.20	5.10	7606.75	5929.55	291.45	-0.2125	5.12
Active SPE	31.25	0	25.70	1.55	1.29	4595.65	3451.15	178.81	0.0163	19.98
Brine LL	40	12	16.39	29.54	4.74	1314.80	1133.15	80.22	0.0188	3.46
Brine SPE	41.67	0	12.84	1.01	0.85	1044.20	703.10	81.30	0.0018	15.16
Closed LL	40	10	13.46	26.21	3.71	1090.50	875.29	80.99	-0.1515	3.63
Closed SPE	50	0	9.66	0.79	0.65	991.58	690.08	102.60	0.0004	14.78
Lake	1	0	10.85	0.35	0.35	54.15	37.45	4.99	0.0073	31.13
Lake SPE	0.8676	0	11.80	0.32	0.32	25.50	18.83	2.16	0.0013	37.44
Patuxent River	1	10	3.33	0.41	0.27	4.73	0.00	1.42	0.0004	12.16
Patuxent River SPE	0.05282	0	40.68	2.14	2.13	4.06	3.40	0.10	0.0016	19.07

Table 2. Average photo-ammonium production and loss and photo-ammonification rates. Numbers in bold indicate significant production/loss or rate.

Sample	Photo-ammonium loss/production (mg/L)	Standard Deviation (mg/L)	Photo-ammonification Rate (µg/L*h)	Standard Deviation (µg/L*h)
Active Landfill Leachate (LL)	**-4.2495**	0.7902	**-212.475**	39.508
Active LL Solid Phase Extract (SPE)	0.1925	0.2019	9.625	10.096
Brine LL	0.376	4.695	18.8	234.73
Brine LL SPE	**0.0365**	0.0035	**1.825**	0.177
Closed LL	**-3.0305**	1.2948	**-151.525**	64.738
Closed LL SPE	0.008	0.008	0.4	0.412
St. Mary's Lake	**0.1465**	0.1252	**7.325**	6.258
St. Mary's Lake SPE	**0.0255**	0.0134	**1.275**	0.672
Patuxent River	0.011	0.016	0.432	0.776
Patuxent River SPE	**0.0315**	0.0123	**1.575**	0.617

Table 3. Photoammonification rates compared to studies in similar locations. Asterisks indicate significant photoproduction/loss.

System	Photoammonification Rate (µM h^{-1})	Study
Anthropogenic		
Active Landfill Leachate	-11.78 µM h^{-1}*	Current
Brine Landfill Leachate	1.04 µM h^{-1}	Current
Closed Landfill Leachate	-8.40 µM h^{-1}*	Current
Freshwater		
St. Mary's Lake	0.41 µM h^{-1}*	Current
16 Lakes from Saskatchewan, Canada (mean)	0.01 µM h^{-1}*	Jeff et al. (2012)
Pond in coniferous woodland	0.04-0.97 µM h^{-1}*	Grzybowski (2002)
Satilla River	0.09 µM h^{-1}*	Gao and Zepp (1998)
Estuary		
Patuxent River	0.0011 µM h^{-1}	Current
Skidaway River Estuary	0.050 µM h^{-1}*	Bushaw et al. (1996)
Orinoco River Estuary	0.015 µM h^{-1}*	Morell and Corredor (2001)

Extracting Microplastics in Archived Sediment Samples from Baltimore Harbor

Katherine Mitchell, REU Fellow
Maryland Sea Grant

Johan Schijf, Associate Professor
Chesapeake Biological Laboratory, University of Maryland Center for Environmental Science

Abstract

Microplastic pollution has become a major concern in today's environmentally aware society. It is now a worldwide problem that has been documented extensively in scientific journal articles and also in the mainstream media. The long-term goal of our study is to analyze different sediment samples taken from Baltimore Harbor to determine the type and amount of microplastics found. Sediments collected in the 1970s and 1980s will be used along with modern samples to determine the extent of microplastic pollution over the years. This paper focuses on developing the best method to extract microplastic particles from the sediments. The samples were first disaggregated using a Calgon solution with a rotary shaker and sonicator. Next, the larger particles were removed using 500 and 106 µm mesh sieves. Dissolved organic matter was removed by adding hydrogen peroxide. Zinc chloride solution was then used in a density separation device to separate the microplastics from the sediment through flotation and filtration. The method was applied to four samples in order to test and, if possible, optimize each individual step.

Introduction

Microplastic (MP) pollution is an emerging environmental concern of modern society and a relatively new area of research. It occurs in any surface or deep-water system on Earth. The use of plastics has now become a necessity for most people; as a result, plastic production has increased exponentially since the early 1950s and reached 322 million tonnes in 2015 (http://www.fao.org, 01 August 2018).

Microplastics can vary in shape, color, and size; ranging from 1 nm to 5 mm and thus are mostly undetectable to the naked eye. Microplastics can be categorized into two groups, primary and secondary MPs. Primary microplastics are small and consist of microbeads, capsules, fibers, and pellets. This type of pollution is often found in cosmetics and personal care products (National Oceanic and Atmospheric Administration 2018). However, the majority referred to as secondary microplastics, consists of larger pieces that have broken down into smaller pieces (Hanvey et al. 2017). The origin of the latter includes bags, bottle caps, pellets, disposable cutlery, and takeaway food packaging (Hanvey et al. 2017).

Contamination of the environment from microplastics may be harmful to marine organisms (Van Cauwenberghe and Janssen 2014). Understanding the interaction between marine organisms

and microplastics is essential when completing environmental risk assessments (Potthoff et al. 2017). Since microplastics are so small, a wide range of animals are able to ingest them through filter or detritus feedings (Galloway et al. 2017). Microplastics have been found in the stomachs of turtles, fish, and bivalves (Wilcox et al. 2015; Schuyler et al. 2016) The eastern oyster, *Crassostrea virginica,* is an important organism to the estuary system of the Chesapeake Bay. This species has suffered from a large population decline due to habitat loss, over-harvesting, and disease outbreak (Wilberg et al. 2011). The rapid growth of oyster aquaculture has made up for some of the declines. The aquaculture industry is itself a source of microplastics and cultured oysters may be exposed to more or different microplastics than natural ones. Plastic cages, floats, and buoys that are exposed to air and UV light can become embrittled and fragment forming microplastics (www.fao.org, 01 August 2018). Since oysters are consumed by humans, there is a direct connection to the general public who should be more aware of and concerned about the microplastic issue and how it could affect them.

My project focused on extracting microplastics from archived sediment samples which were collected in the 1970s and 1980s (Yonkos et al. 2017). The samples were collected along the Patapsco River into Baltimore Harbor and from the Rhode and Ware Rivers (Sinex and Helz 1982). They were originally collected and used for a study of trace metals in the sediments of Chesapeake Bay. The sediment cores were sliced into 2 cm sections and dried in an oven soon after collection and have been stored ever since. My project mainly involved the development of a method for extracting microplastics from the archived sediment samples from Baltimore Harbor.

Investigating microplastics in archived and modern sediment is part of a larger two-year project. In addition to the sediment section of the project, an analysis of microplastics in Chesapeake Bay surface water and analysis of microplastics in Chesapeake Bay oysters will be performed as well. The analysis of microplastics in the surface water will relate to land use patterns and point/non-point sources of introduction, testing in different water depths, in sediment at various proximities to oyster production, and in oysters grown on-bottom and at the water surface (Yonkos et al. 2017). Mature oysters will be collected from various reefs and the retention of microplastics in oysters from different sources will be compared by measuring abundances before and after depuration in the lab (Yonkos et al. 2017).

The ultimate goal of this study is to present the first comprehensive report of microplastics within the Chesapeake Bay (Yonkos et al. 2017). Microplastics will be identified and classified into categories based on specific characteristics which will help determine the primary source of pollution. The number of pieces of plastic found in each sediment sample will be enumerated through visual counting verified by Micro-Raman spectroscopy. Micro-Raman spectroscopy is able to identify plastic particles as small as 5 μm and categorize them into types of plastic based on unique scattered-light spectra.

It is expected that there will be more microplastics in the modern sediment samples than in the archived samples. The current rapid growth in plastic production is extraordinary, surpassing most other man-made materials (Geyer et al. 2017). In addition, we expect that the composition of microplastics will differ when comparing the archived sediment samples with the modern samples. The microplastic composition can change and will indicate the type of plastics available from that time period and the manufacturing practices (Yonkos et al. 2017).

Plastic is a manufactured product and does not occur naturally, so anywhere we find it in nature is directly due to human pollution. Zooplankton are able to ingest plastic and are a common prey

of krill, shrimp, and small fish (Devriese et al. 2015). This shows how something so small can result in biomagnification in the food web.

Filter feeders such as mussels and oysters have been studied and are reported to ingest microplastics (Van Cauwenberghe et al. 2015; Green 2016). Microplastics have also been found in the guts of fish, turtles, and other larger animals (Taylor et al. 2016). People can eventually be affected by consuming fish, mussels, and oysters. In a broader context, plastics can entangle species such as turtles and birds and cause severe injuries.

There are many companies and non-government organizations that have put forth more research and funding towards understanding more about microplastics. This is still a new field of study, but many scientists want to learn more about the effects of these harmful plastics and seek solutions for mitigating the pollution entering the ocean. Scientists, consumers, and the general public have become much more aware of the effect of microplastics in our waters and environments. Supporting efforts of these organizations and partnerships is vital to the restoration of the food web and the health of the ocean.

Materials and Methods

Disaggregation

Disaggregation is used to break down the sediment, so it can be sieved in the next step. This process was required to be performed on the archived samples that were oven dried which produces hard clumps of sediments. Freshly collected sediments can be sieved without this step. The sediment clump is completely submerged in a solution of surfactant or a water softener like Calgon (sodium hexametaphosphate) which promotes the dispersion of charged clay particle. Disaggregation is further stimulated by a combination of continuous shaking and repeated sonication, over a period of days to weeks. In my project, the Calgon solution was chosen as the reagent and its concentration, the duration of shaking, and the frequency of sonication were all optimized.

Sieving

Once the sediment sample was completely disaggregated, it was passed through two brass or stainless-steel sieves with a minimal amount of Milli-Q water, using a small squirt bottle. Before each use, the sieves were gently cleaned under flowing water with a metal wire brush and then air-dried. A 500 µm mesh (No. 35) sieve was used to remove small rocks, shell fragments, and plant matter such as roots. The remaining sediment was passed through a 106 µm mesh (No. 140) sieve. Each size fraction (>500 µm, 106–500 µm, and <106 µm) was collected in a separate glass bowl or metal tray and then transferred to a lidded glass jar with additional Milli-Q water. Supernatant water was siphoned off after settling of the solids, but not retained for the purpose of this study.

Oxidizing Organic Matter

Oxidizing OM is commonly used to clean microplastic particles from biofouling material which makes it hard to distinguish under a microscope (Zobkov and Esiukova 2017). Sediment from the <106 µm fraction of Core A, Pax 1 box 3, and 2–12 sample was used for testing 2% and 20% of H_2O_2 and Milli Q water as the procedural blank. From the three sediment samples, three aliquoted sub-samples were taken and put in glass cups. Each of the three sub-samples

contained either 20 mL of Milli Q water, 20 mL of 2% H_2O_2, or 20mL of 20% H_2O_2. The samples reacted with the solution at room temperature for 24 hours with a Petri dish cover placed on top to avoid any contamination and to keep the sample from foaming over the top.

Flotation Device

The flotation device (Fig. 3), or Sediment Microplastic Isolation (SMI) unit, was used to separate the plastics from the sediment by means of their different densities using a 1.5 g cm^{-3} zinc chloride solution (Coppock et al. 2017). All the fractions from the four samples that resulted from the sieving process were put in the SMI unit for separation. The sediment was put in the bottom of the device followed by the zinc chloride solution. The SMI unit was placed on a magnetic stir plate with a stirring bar placed inside which was turned on for an hour, then turned off for another hour at which time the valve was closed. The top and bottom portions were then filtered in the next step.

The unit was cleaned after each use with Milli-Q water then air dried. This prevented any residual water that would dilute the zinc chloride solution if the separator was used immediately after washing.

Filtering

All the fractions processed through the SMI unit were put through a vacuum filtration apparatus to separate fine particulate matter and microplastics from the zinc chloride solution (Zobkov and Esiukova 2018). To filter the top of SMI unit, a glass fiber filter with a pore size of 0.70 µm was positioned on a glass funnel with a glass frit support (Fig. 4). The glass fiber filter was removed from the filtration device and placed in a glass Petri dish to dry, then examined under a microscope to identify matter from the top section of the SMI unit. To filter the bottom of the SMI unit, a ceramic funnel and a rubber stopper were pushed into the reservoir flask to ensure no leakage (Fig. 5). A large 90 mm glass fiber filter was placed inside the funnel and the sediment was deposited onto the filter and placed in a glass Petri dish to dry.

Detecting and Quantifying Microplastics

The Zeiss Stemi-2000 C (optical microscope) was used to detect and visually count the microplastics and other fine particulate matter. The fiber filter from the filtering step was dried and then placed under the microscope.

Results and Discussion

Disaggregation

Core A 78–80 cm and Core B 78–80 cm were both disaggregated, however, the process was slightly different. A solution was initially made using 5 g of Calgon dissolved in 1 L of Milli Q water. This solution filled 70 mL of a graduated cylinder which was then poured into the Core B 78–80 cm jar. Core A 78–80 cm jar was filled with 70 mL of Milli Q water (Fig.1). Both samples were put in the shaker and sonicator for a week to ensure identical processes were conducted on both samples. Core A and B both remained in the sonicator for a total of 14 thirty-minute cycles.

After the third cycle, more of the original Calgon solution (5g/ 1 L Milli Q water) was added to Core B so the total volume in the jar was 90 mL. A similar proportion of 0.45g of Calgon was dissolved in 20 mL of Milli Q water for Core A to achieve the total volume of 90 mL in the jar.

After the addition of the Calgon solution to the jars, both were returned back to the sonicator for 11 more thirty-minute cycles and then placed back on the shaker throughout the span of a week. Sonication was confirmed to be successful for the first three cycles of 30 minutes. Further sonication did not show any additional changes. This is most likely because loose sediment in the solution absorbs more and more of the sound energy and it becomes less effective. By using both the shaker and sonicator it showed to efficiently work and break apart the large clumps. The sediment looked to be completely broken apart (Fig. 2), so the next step of the sieving process was started.

Core #140 78–80 cm was the only sample using the increased Calgon solution (10 g/ L in Milli-Q water) and never fully disaggregated. This archived sediment sample is from Virginia and we assume it is composed differently than the Baltimore Harbor samples. This was the final sample in which we would go through all the steps of the method with the improved changes. Unfortunately, since it has taken more than twice as long as expected to separate the sediment apart we could not continue with this sample any further. We are confident that the increased Calgon solution will disaggregate the archived Baltimore Harbor samples within two weeks.

Both Pax 1 box 3 and 2-12 samples were kept in the freezer soon after collection and then put in the refrigerator for two to three days, so the sediment could thaw and be processed. These sediment samples were completely broken apart after being removed from the refrigerator, so the disaggregation step was not necessary, which made the following processes go much faster. Sample 2-12 of a modern core and Pax 1 box 3 from the Patuxent River were processed while Core A and B were on the shaker.

Sieving

Sieving allows microplastics to be divided into three (or more) size fractions and to be counted separately in the corresponding size fractions of sediment. It may also increase the efficiency of the subsequent density separation step, by preventing very small microplastic particles from becoming trapped among larger sediment grains. Different sediment samples can have very different distributions among the size fractions, which can also have different compositions. The two archived Baltimore Harbor samples used in my study (from 78–80 cm below the sediment surface) were gray in color and the >500 µm fraction was small and consisted mostly of shell fragments. The recently collected Patuxent River samples (2–12 cm below the surface) were black with a larger >500 µm fraction, consisting mostly of plant matter. The <106 µm fraction was by far the largest part of the archived samples and is probably made up of fine clay minerals. This fraction was a smaller part of the Patuxent River sediments and appeared to contain a lot of organic matter; a larger part of these samples was contained in the 106–500 µm fraction. The largest size fraction of each sample was directly separated from the solution by vacuum filtration. The two smaller size fractions were individually transferred to the flotation step, preceded if necessary by digestion of the organic matter. Since no water should be introduced into the SMI device, it was siphoned off first. In this project, the water was discarded to save time, but it should be filtered and counted in the final protocol as it may contain microplastics. Care should be taken to reduce the amount of water used in this step as much as possible, but otherwise, no major problems were encountered. This step is one of the most laborious of the procedure since only one or two 100 g sediment samples can be completely processed per day by a single person.

Oxidizing Organic Matter

In the sediment samples, organic matter (OM) was present and hydrogen peroxide (H_2O_2) was found to be successful in removing OM (Sanchez-Nieva et al. 2017). The sediment samples were used to establish the most efficient concentration of H_2O_2 for digesting organic matter without dissolving microplastics. OM in the sample jars could be a variety of fine particulate organic matter and hydrogen peroxide dissolves the organic matter from the sediment.

This step tested different concentrations of H_2O_2 with 2% and 20% along with a procedural blank that consisted of Milli-Q water. There were nine sub-samples in total given that there were three samples (Core A, Pax 1 box 3, and 2-12) and three concentrations. Modern samples, Pax 1 box 3 and 2-12, reacted more quickly and bubbled to the top of the Petri dish while Core A took longer for any sort of bubbling. This bubbling reaction indicated that there was a large amount of organic matter in the modern samples. With additional time and testing, a suitable concentration of H_2O_2 will be determined by other scientists. We found color differences between each sample after 24 hours and the 20% concentration reacted faster and foamed more than the others.

Flotation Device

Zinc chloride is a high-density salt solution of 1.5 g cm $^{-3}$ which was deemed an effective and relatively inexpensive flotation medium (Coppock et al. 2017). The density of zinc chloride can vary depending on the amount of salt dissolved in the solution. All the fractions from the four samples that resulted from the sieving process were put in the SMI unit for separation. The sediment was put in the bottom of the device followed by the zinc chloride solution. The SMI unit was placed on a magnetic stir plate with a stirring bar placed inside which was turned on for an hour, then turned off for another hour at which time the valve was closed. The device has a ball valve that can be closed to seal off the sediment in the bottom from the microplastics in the top of the device so the microplastics on the top can be poured off without sediment contaminating it.

Three fractions from the sieving step were processed in the density separator each day. The unit was cleaned after each use with Milli-Q water then air dried. This prevented any residual water that would dilute the zinc chloride solution if the separator was used immediately after washing.

Filtering

It was observed that the fiber filter from the top portion of the SMI unit contained some microplastics (Fig. 6) as well as clay, minerals, and sponge spicules. The bottom portion of the SMI unit was filtered mainly to recover all the zinc chloride solution so it could be reused.

It was observed that the glass fiber filters for the top and bottom portions risked getting clogged, which sometimes slowed the filtration process from 30 minutes up to 90 minutes. The liquid in the funnel for either filter always needed to be completely filtered before adding more solution.

Detecting and Quantifying Microplastics

The optical microscope's main purpose is to obtain a general idea of what is on each filter, but it is not able to identify every piece of microplastics because of their small size (Fig. 6) Two additional steps can be taken to further detect and identify the types of microplastics.

The fluorescent microscope uses a Red Nile stain which adsorbs onto plastic surfaces and fluoresces when exposed to different color filters of a light source (Maes et al. 2017). Different color filters reveal various plastics based on specific composition characteristics. The Micro-Raman spectroscopy is a light scattering technique where monochromatic light is directed toward a sample, and the reflected light is color-shifted by the size and type of the molecular bonds within the sample (Maes et al. 2017). The Raman allows for identification of microplastics. When light is directed towards the sample a light of different color is reflected back and the spectral range is shown for that particle. This spectroscopy has an option to automatically scan which is very beneficial since the fluorescent microscope can only show a zoomed-in view of a small section of the filter and the sample needs to be moved manually. The Micro-Raman spectroscopy is a slow and expensive process and will be used by other scientists who will continue this project.

Anticipated Benefits

This study will determine if MP pollution has increased from the 70s and 80s to the present day in the Patapsco River into Baltimore Harbor and from the Rhode and Ware Rivers. This will allow us to determine the size and type of MPs in the different sediment samples and more importantly how it has changed over the years. Additionally, we will be able to identify which type of microplastics were used 50 years ago and also compare the result to today's microplastic pollution and analyze the changes. This information will be combined with a much larger study of the Chesapeake Bay area to determine the prime location of microplastic within the water column, the amount oysters retain within their tissue after a three-day depuration, and the actual range of microplastics to which oysters are likely to be exposed (Yonkos et al. 2017). This study will provide the most comprehensive study to date of MP pollution in the Chesapeake Bay Area.

Conclusions and Further Research

It became evident halfway through the project that there would be insufficient time to complete the comparison of samples between the old and new sediments. The focus of the project shifted to developing the method to separate the microplastics from the sediments. Based on the results and discussion, the following three steps still need to be examined further to obtain consistent results: disaggregation, oxidizing organic matter, and detection and quantifying of microplastics. The disaggregation method is almost complete, but an archived Baltimore Harbor sample needs to go through this step with the increased Calgon solution to determine if the solution is successful in breaking apart the sediment. In addition, a revised timeline for this project needs to be developed prior to it being undertaken in the future. The original hypothesis was not able to be proven this summer, however, future researchers on the broader project will use the method developed this summer to test the hypothesis.

Acknowledgments

I would like to thank Maryland Sea Grant for giving me the chance to conduct research with the University of Maryland Center for Environmental Science at Chesapeake Biological Laboratory. My most sincere and deepest appreciation to my fabulous mentor Dr. Johan Schijf for his guidance and support throughout this project. I would also like to thank Dr. Hali Kilbourne for allowing me to use her lab and some of her equipment. In addition, I would also like to thank Dr. Carys Mitchelmore and Dr. Andrew Heyes for lending some of their equipment. The Maryland Sea Grant REU program is supported by the National Science Foundation. This study was funded by NSF grant OCE-1756244.

References

Coppock, R. L., M. Cole, P. K. Lindeque, A. M. Queirós, and T. S. Galloway. 2017. A small-scale, portable method for extracting microplastics from marine sediments. Environmental Pollution 230: 829–837.

Devriese, L. I., M. D. van der Meulen, T. Maes, K. Bekaert, I. Paul-Pont, L. Frère, J. Robbens, and A. D. Vethaak. 2015. Microplastic contamination in brown shrimp (Crangon crangon, Linnaeus 1758) from coastal waters of the Southern North Sea and Channel area. Marine Pollution Bulletin 98: 179–187. doi:10.1016/j.marpolbul.2015.06.051

Galloway, T. S., M. Cole, and C. Lewis. 2017. Interactions of microplastic debris throughout the marine ecosystem. Nat. Ecol. Evol. 1: UNSP 0116. doi:10.1038/s41559-017-0116

Geyer, R., J. R. Jambeck, and K. L. Law. 2017. Production, use, and fate of all plastics ever made. Science Advances 3: e1700782. doi:10.1126/sciadv.1700782

Green, D. S. 2016. Effects of microplastics on European flat oysters, Ostrea edulis and their associated benthic communities. Environmental Pollution 216: 95–103. doi:10.1016/j.envpol.2016.05.043

Hanvey, J. S., P. J. Lewis, J. L. Lavers, N. D. Crosbie, K. Pozo, and B. O. Clarke. 2017. A review of analytical techniques for quantifying microplastics in sediments. Anal. Methods 9: 1369–1383. doi:10.1039/c6ay02707e

Maes, T., R. Jessop, N. Wellner, K. Haupt, and A. G. Mayes. 2017. A rapid-screening approach to detect and quantify microplastics based on fluorescent tagging with Nile Red. Scientific Reports 7: 44501. doi:10.1038/srep44501

National Oceanic and Atmospheric Administration. 2018. What are microplastics?

Potthoff, A., K. Oelschlaegel, M. Schmitt-Jansen, C. D. Rummel, and D. Kuehnel. 2017. From the sea to the laboratory: Characterization of microplastic as prerequisite for the assessment of ecotoxicological impact. Integr. Environ. Assess. Manag. 13: 500–504. doi:10.1002/ieam.1902

Sanchez-Nieva, J., J. Antonio Perales, J. Maria Gonzalez-Leal, and E. Rojo-Nieto. 2017. A new analytical technique for the extraction and quantification of microplastics in marine sediments focused on easy implementation and repeatability. Anal. Methods 9: 6371–6378. doi:10.1039/c7ay01800b

Schuyler, Q. A., C. Wilcox, K. A. Townsend, K. R. Wedemeyer-Strombel, G. Balazs, E. van Sebille, and B. D. Hardesty. 2016. Risk analysis reveals global hotspots for marine debris ingestion by sea turtles. Glob. Change Biol. 22: 567–576. doi:10.1111/gcb.13078

Sinex, S. A., and G. R. Helz. 1982. Entrapment of zinc and other trace elements in a rapidly flushed industrialized harbor. Environ. Sci. Technol. 16: 820–825. doi:10.1021/es00105a018

Taylor, M. L., C. Gwinnett, L. F. Robinson, and L. C. Woodall. 2016. Plastic microfibre ingestion by deep-sea organisms. Scientific Reports 6: 33997. doi:10.1038/srep33997

Thompson, R. C., S. H. Swan, C. J. Moore, and F. S. vom Saal. 2009. Introduction: Our Plastic Age. Philosophical Transactions: Biological Sciences 364: 1973–1976.

Van Cauwenberghe, L., M. Claessens, M. B. Vandegehuchte, and C. R. Janssen. 2015. Microplastics are taken up by mussels (*Mytilus edulis*) and lugworms (*Arenicola marina*) living in natural habitats. Environmental Pollution 199: 10–17. doi:10.1016/j.envpol.2015.01.008

Van Cauwenberghe, L., and C. R. Janssen. 2014. Microplastics in bivalves cultured for human consumption. Environmental Pollution 193: 65–70. doi:10.1016/j.envpol.2014.06.010

Wilberg, M. J., M. E. Livings, J. S. Barkman, B. T. Morris, and J. M. Robinson. 2011. Overfishing, disease, habitat loss, and potential extirpation of oysters in upper Chesapeake Bay. Marine Ecology Progress Series 436: 131–144.

Wilcox, C., E. V. Sebille, and B. D. Hardesty. 2015. Threat of plastic pollution to seabirds is global, pervasive, and increasing. PNAS 112: 11899–11904. doi:10.1073/pnas.1502108112

Yonkos, L., C. Mitchelmore, and J. Schijf. 2017. Abundance and Variety of Microplastics in Surface Waters, Sediments, and Oysters: Relationship to Point-Sources and Land Use Practices. Maryland Sea Grant.

Zobkov, M. B., and E. E. Esiukova. 2018. Microplastics in a Marine Environment: Review of Methods for Sampling, Processing, and Analyzing Microplastics in Water, Bottom Sediments, and Coastal Deposits. Oceanology 58: 137–143. doi:10.1134/S0001437017060169

Zobkov, M., and E. Esiukova. 2017. Microplastics in Baltic bottom sediments: Quantification procedures and first results. Marine Pollution Bulletin 114: 724–732. doi:10.1016/j.marpolbul.2016.10.060

Figures

Figure 1. Shown above are Core A and B sediment samples collected at a depth of 78–80 cm from Baltimore Harbor prior to performing the disaggregation process using the rotary shaker and sonicator device.

Figure 2. Shown in the image Core A and B sediment samples after the disaggregation process was performed using the rotary shaker and sonicator and found to be successful.

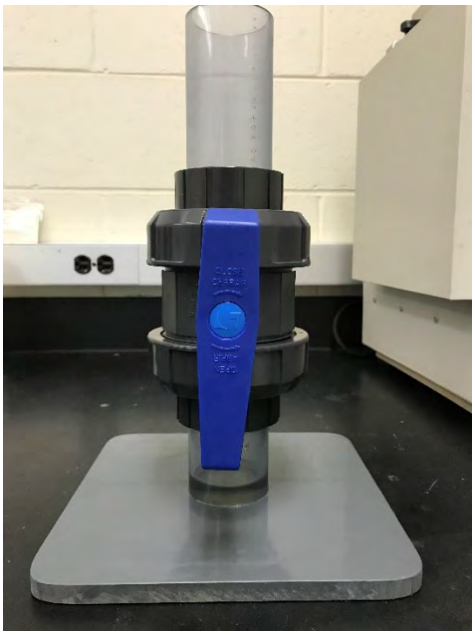

Figure 3. Sediment-Microplastic Isolation (SMI) unit is used to separate the plastics from the sediment by means of their densities using a zinc chloride solution.

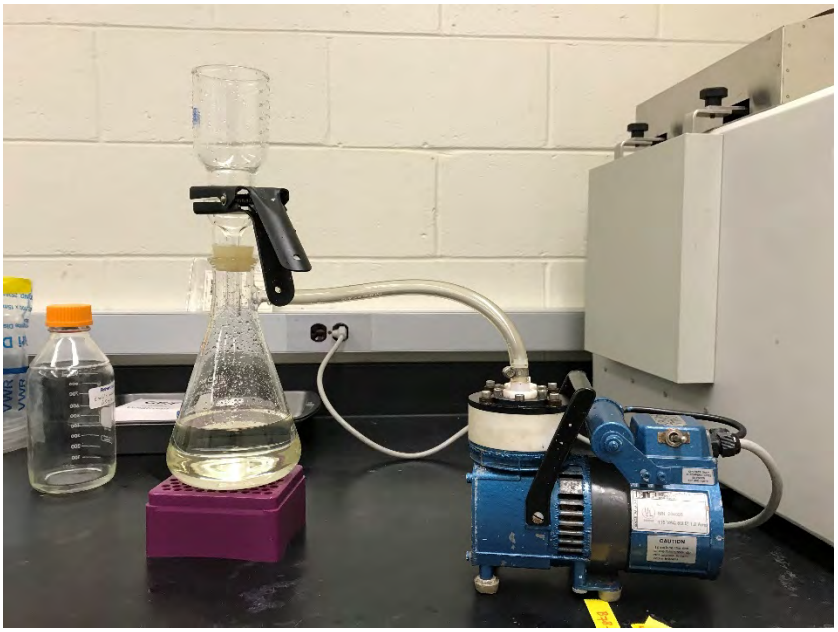

Figure 4. The setup for filtering the top portion of the SMI unit includes a glass frit support base with a rubber stopper attached and a funnel placed on top of the base with a spring clamp holding the two pieces together.

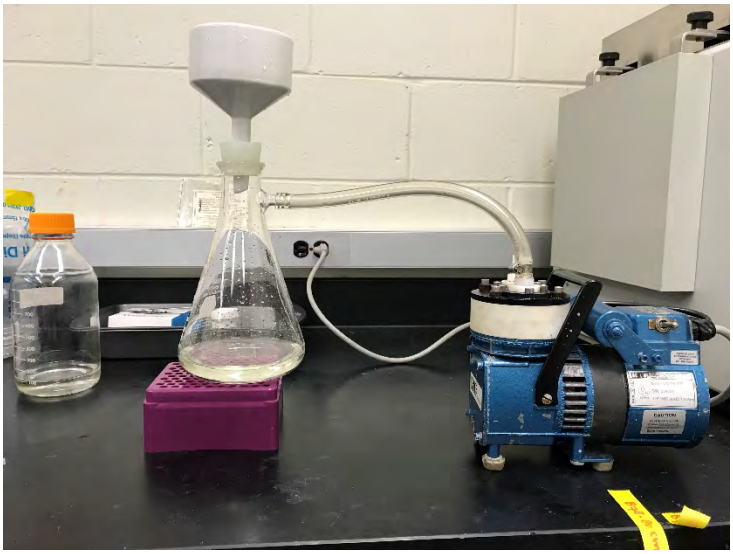

Figure 5. The setup for filtering the bottom portion of the SMI unit includes a ceramic funnel with a rubber stopper attached and a reservoir flask to retain $ZnCl_2$ solution.

Figure 6. The small filter from the top portion of the SMI unit shows a blue and white pattern synthetic fiber.

Impacts of Oxygen Depletion on Phosphorus Cycling in Rock Creek, an Aerated Tidal Tributary of the Patapsco River

Curtis Szewczyk, REU Fellow
Maryland Sea Grant

Jeremy Testa, Assistant Professor
Chesapeake Biological Laboratory, University of Maryland Center for Environmental Science

Abstract

Anne Arundel County, Maryland, operates a destratification system used to mitigate the effects of eutrophication-driven oxygen depletion in a small tidal tributary called Rock Creek. The system provided the opportunity for ecosystem-scale experimentation of manipulated oxygen levels by turning the system on or off, effectively inducing hypoxia and anoxia. Eutrophication can lead to overall declines in dissolved oxygen concentrations via the elevated consumption of oxygen during the decomposition of organic matter. There are known impacts of these oxygen reductions on phosphorus cycling by increasing the flux of phosphate from sediment into the water column. To determine the severity or duration of hypoxia needed to induce phosphate accumulation in the water column, both model simulations and field observations were used to quantify changes in phosphate fluxes from sediments and associated water column increases. Model predictions indicate that phosphate flux is sensitive to exposure to low oxygen, primarily severe hypoxia (0.5 mg/L). Model results paired with observed field data suggest that within 3–7 days of hypoxic conditions, a large signal of phosphate increase (500–900%) is experienced, likely due to elevated sediment-water flux. Future studies should include a focus on system recovery to increased phosphate flux resulting from hypoxia.

Introduction

Eutrophication, the excessive and typically anthropogenic elevation of organic matter in a body of water, has been associated with elevated phytoplankton biomass (including harmful algal blooms; Anderson et al. 2002), increased oxygen (O_2) consumption (Howarth et al. 2011), the accumulation of sulfide in bottom waters, low pH waters (Cai et al. 2017), and loss of benthic communities (Diaz and Rosenberg 2008; Levin et al. 2009). According to Kemp et al. (2005), eutrophication has played a significant role in the history of the Chesapeake Bay's sedimentation, biological communities, and cycling of key nutrients like nitrogen and phosphorus. Studies in Chesapeake tributaries, such as the Choptank and Patuxent tributaries, have also experienced nutrient input (primarily nitrogen and phosphorus) increases two- to five-fold during 1970–2004 due to a variety of anthropogenic influences including sewage discharge, application of fertilizer, atmospheric deposition, and land use changes (Fisher et al. 2006). Recent studies have analyzed the impacts of restoration efforts on the Chesapeake Bay estuary from eutrophication, and noted that reductions in nutrient loading have shown improvements on

the water quality of the system in many regions of the estuary (Boynton et al. 2014; Testa et al. 2018; Zhang et al. 2018).

A well-documented consequence of eutrophication in the Chesapeake Bay is a decline in dissolved oxygen (DO) concentrations within the estuarine environment (Diaz and Rosenberg 2008). Extreme decreases in DO levels can lead to hypoxic (O_2 < 2–3 mg/L) or anoxic (no oxygen) portions of the water column. Hypoxia within estuaries can result from high respiration rates associated with surface runoff among other aforementioned anthropogenic activities (Levin et al. 2009), river discharge (Lee et al. 2013), and stratification as a result of wind-induced stress (Scully et al. 2005; Lee et al. 2013). Key biogeochemical processes are impacted by the reduced availability of DO, such as those within the nitrogen and phosphorus cycles (Testa and Kemp 2012). Nitrogen and phosphorus are key nutrients to estuarine and marine ecosystems because of their capacity to act as limiting factors on the growth of primary producers like phytoplankton. For nitrogen, limited O_2 availability can inhibit coupled nitrification-denitrification and shift the system towards dissimilatory nitrate reduction to ammonium (DNRA), leading to reductions in N_2 production (and thus N removal from the system) and the accumulation of ammonium (NH_4^+) (McCarthy et al. 2008; Testa and Kemp 2012). Similarly, reduced O_2 concentrations can lead sorbed inorganic phosphate to be released from their metal oxide-hydroxide particles (Testa and Kemp 2012). The coastal benthos, like invertebrate macrofauna, can be affected by hypoxic/anoxic conditions that will ultimately cause physiological stress (Levin et al. 2009; Testa and Kemp 2012), and prevent them from being able to provide ecosystem services associated with the regulation of water quality. A major concern of these altered biogeochemical processes is the excessive efflux of NH_4^+ and PO_4^{3-} to the overlying water column, thus creating a feedback loop that allows for further organic production and oxygen depletion (Testa and Kemp 2012).

A local system that exemplifies the effects of eutrophication and its associated decline in oxygen availability is a small tidal tributary of the Patapsco River in Anne Arundel County, Maryland known as Rock Creek. Historically, Rock Creek was characterized by poor water quality due to the elevated availability of nutrients and reduced DO levels, but to counter these conditions, an aeration system was introduced in 1988 to eliminate stratification from the water column and thus prevent deoxygenation (Harris et al. 2015). The presence of the aeration system provides an opportunity to perform comparative ecosystem experimentation on the effects of oxygen on this eutrophic tributary system. These experiments can be completed through observing the environmental response of the tributary to turning the aerators on and off. Usage of a controllable, ecosystem-scale experiment on hypoxic/anoxic conditions is rare, and thus Rock Creek provides a unique opportunity for investigations into oxygen's effects on biogeochemistry. This project incorporated past sampling efforts in Rock Creek with new attention to phosphorus flux and oxygen input to the inner region of the creek during experimental deoxygenation (aerator system shut off).

Increasing knowledge on the dynamics and features of phosphorus cycling in systems of the Chesapeake Bay undergoing hypoxia/anoxia is vital in understanding the sensitivity of biogeochemical processes to reductions in oxygen. Based on literature, we expected phosphate fluxes to increase under experimental deoxygenation, however our aim was to try and determine how the severity and duration of hypoxic conditions impact the magnitude of sediment-water fluxes. Lastly, following the analysis of data, we hoped to address whether the aeration system was successful in mitigating the negative effects that are caused by eutrophication within Rock Creek.

Materials/Methods

Site Description

The study was conducted in Rock Creek, located in Pasadena, Maryland. The creek is a tidal sub-tributary to the Patapsco River, a watershed that drains into the northern portion of the Chesapeake Bay southeast of Baltimore (see Fig. 1). Approximately 80% of land use in Rock Creek is attributed to residential and urban development, with the additional 20% accounted for by forested land (Harris et al. 2015). Over time, the tributary system has experienced poor water quality paired with low oxygen levels. In October 1988, the Anne Arundel County Department of Public Works built an aeration system, consisting of 830 m of aeration pipes and 138 diffusers, to alleviate low DO levels and complaints of hydrogen sulfide odor. A site map is included in (Fig. 2) depicting Rock Creek along with five full sampling stations, two vertical profile stations, and a continuous monitoring station. The sampling stations, which included bottom and surface water collection, vertical profiling, and nutrient filtration, run along a transect from the upstream aeration zone within Rock Creek through the mouth of the creek and into the Patapsco River.

General Model Description and Simulations

On multiple instances in the past decade, the Sediment Flux Model (SFM; Di Toro 2001) has been calibrated and validated for the region encompassed by the Chesapeake Bay (Brady et al. 2013; Testa et al. 2013). The model structure includes three layers: (1) the overlying water, (2) an aerobic sediment layer near the sediment-water boundary, and (3) an anaerobic bottom layer (total sediment depth (10 cm) – depth of aerobic layer). The model accounts for two sources of phosphorus (organic matter deposition and phosphate-sorbed sediment deposition), simulates diagenesis, represents dissolution of metal oxyhydroxides and the release of sorbed phosphates from limited oxygen availability, and transports dissolved and particulate P forms via diffusion and mixing (Conley et al. 2002; Testa et al. 2013). The phosphorus portion of the model is summarized in Figure 3. For this study, SFM was calibrated to observed Rock Creek conditions in 2012 (Harris et al. 2015), at which point, the levels of available DO in the overlying water were altered to moderate hypoxia (1.5 mg/L) or severe hypoxia (0.5 mg/L). The two hypoxic conditions of differing severity were both simulated at varying durations (1, 3, 7, and 14 days). For each simulation, the output was parsed specifically for the sediment-water flux of phosphate over the course of a two-week period. Quantifying the net results of phosphate fluxes from all simulations on the same two-week time period makes them comparable. For comparisons based on the foundation of the experimental oxygen levels, each simulation was tested against a model run using untampered oxygen levels from 2012. After testing each experimental simulation to the aforementioned control run, a percent change in phosphate flux was computed. To provide the ability to compare trends, the same efforts were done with ammonium flux.

Experimental Study Design

We executed an ecosystem experiment that involved measuring observed conditions through the course of a week-long period of deoxygenation while the aerators were turned off. The baseline conditions were gathered on July 10, 2018. The aeration system was shut down on the morning of July 11, 2018 at 7:30 AM, and our sampling stations were measured on the 11th (a few hours after aeration system was shut down), 13th, 15th, and 17th. Field efforts for this study included a continuous monitoring station for basic chemical and physical valuables, and an ADCP to measure current velocity at one station, along with vertical profiles and water sample

grabs across a spatial gradient of Rock Creek, from the aeration zone into the Patapsco River (see Fig. 2).

Continuous Monitoring Station

For this study, a continuous monitoring station was set up at a dock in Rock Creek (see Fig. 2) just outside of the aeration zone and was used for the bottom deployment of a YSI EXO2 multi-parameter sonde along with a Nortek Aquadopp acoustic Doppler current profiler (ADCP). The sonde measured DO, conductivity, salinity, temperature, turbidity, chlorophyll-a, and pH on a 15-minute interval. Post-calibration measurements were made prior to removing the instrument from the water on July 20th. On the other hand, the ADCP was used to measure current velocity throughout the project. At the surface, a suite of HOBO onset data loggers was used to track DO, conductivity, salinity, temperature, and water depth. These devices were deployed to compare vertical profile water conditions to the continual measurements, along with tracking the stated conditions on a more consistent basis. Prior to traveling to the field, using AquaPro software, the ADCP was set for 2-minute burst measurements, on a 15-minute time interval, with an up-facing shallow water deployment. The ADCP sensor unit was then attached to a premade rigging platform (see Fig. 4). On the initial day of sampling, prior to going on the water, the ADCP was deployed at the dock in Rock Creek. Following the experimental phase of deoxygenation, the ADCP was retrieved and brought back to the laboratory for cleaning and data downloading. From there, the data was retrieved and converted from binary to a readable format. Following the retrieval and conversion of the Aquadopp data, the files were imported to MATLAB_R2015a for velocity analysis.

Vertical Profiles

For each day in the field, a vertical profile was taken of the water column using a calibrated YSI EXO2 multi-parameter sonde at any of the five stations that samples were gathered for that given day. Additionally, if time permitted on field days, stations A and B were used for additional water column profiling, but no water sample collections were completed. The following parameters were measured: Sample depth (m), Temp (°C), Dissolved O_2 (%), Dissolved O_2 (mg/L), Spec Cond (mgS/cm), Salinity (PSU), pH, FNU, CHL (µg/L). These values were recorded on data sheets in the field for each day of sampling at 0.5m increments. To accompany the vertical profiles, Secchi disk depth, Li-Cor light meter readings with LI-190 deck and LI-192 underwater quantum sensors, and meteorological conditions were recorded at each sampling station as well.

Water Sample Grabs

Prior to leaving for the field, a large cooler was loaded with ice and 2 L containers were placed within the cooler for each station (surface and bottom each). These were accompanied by 500 mL dark bottles used for chlorophyll measurements. Within the field, at each station and depth, the appropriate containers were sample rinsed and then filled with water from a submersible water pump. For bottom water, the pump was lowered to the sediment surface and then slightly lifted off the bottom. For surface water collection, the pump was lowered approximately half a meter below the surface of the water.

Nutrient Filtering

Following the collection of water samples, the filtration for nutrients was completed back at the lab, rather than within the field. The samples were kept in the cooler until ready for the filtering

process to begin at the lab. All filtering was processed through Whatman GF/F filter pads using either vacuum or syringe filtration methods. Water samples were filtered using both dissolved and particulate nutrients including orthophosphate (PO_4), total dissolved phosphorus (TDP), and particulate phosphorus (PP). After the filtration process was completed, PO_4 and TDP filtrate samples, along with PP Whatman GF/F filter pads, were taken to the Nutrient Analytical Services laboratory (NASL) at Chesapeake Biological Laboratory for analysis. At NASL, both TDP and PO_4 were analyzed using EPA method 365.1, whereas PP was analyzed using EPA method 365.1, ASPILA. It is important to also note that due to time constraints, only stations 1, 2, and 7 had full sampling (vertical profiles, water grabs, and nutrient filtration) completed on all days of work in the field.

Results

Model Simulations

Table 1 displays the different simulation runs of varying low-oxygen durations and severity performed for this project. To display different sensitivities to low oxygen exposure, the simulated percent change in overall flux for the two-week experimental period was calculated against the observed 2012 conditions, without any oxygen manipulation inputs, for both ammonium and phosphate (Figs. 1, 5). Phosphate fluxes were elevated at all simulation runs of both moderate hypoxia (1.5 mg/L) and severe hypoxia (0.5 mg/L). It was determined that phosphate flux is a much more sensitive system to reductions in oxygen levels than that of ammonium. The results show that with our fourteen days of severe hypoxia phosphate had an 856% increase in flux, whereas ammonium only showed approximately a 30% increase.

$$\frac{(Total\ Experimental\ Flux)-(Total\ Observed\ Flux)}{(Total\ Observed\ Flux)} \times 100\ \% = \%\ PO4\ Flux\ Change \quad (1)$$

Continuous Monitoring Sonde Data

After collection of the EXO2 sonde from the field, a time series was generated to display the bottom water oxygen levels over the course of the experiment (Fig. 6). The general trend supports that as the aerators were turned off, the bottom water dissolved oxygen values decreased over the week. However, there was a spike in oxygen values early on in the deoxygenation that at this time is unexplained. This increase in dissolved oxygen levels occurred between 2:00 and 22:00 on July 12 and consisted of concentrations consistently above 3.0 mg/L while upwards to 8.8 mg/L. It appeared as though the conditions within the water column stayed mostly hypoxic (<2 mg/L) from the night of July 13 until the aerators came back on with multiple instances of extended anoxia.

ADCP Deployment

Following the collection of the ADCP, the data was analyzed within MATLAB. The North/South velocity measurements were pulled and used to calculate an oxygen flux time-series (Fig. 7). ADCP data was categorized by velocities of either north, east, or vertical; Northern velocity was selected because it was the main axis of water movement within Rock Creek (Fig. 8). Equation 2 was utilized for our oxygen flux calculation by multiplying the bottom water velocities, averaged over the bottom 0.5 m of the water column, and bottom water dissolved oxygen concentrations from the continuous monitoring station sonde. The trend shows a substantial landward influx of oxygenated water towards the aerator zone in Rock Creek. It also appears as though the influx lines up with the oxygenation event that was seen at the dock and in the

profiles at stations 7 and 2 when lined up upon the same time series. In the surface waters, the southward velocities were more substantial than at the bottom, upwards of 0.05 m/s, when compared to bottom water, and this is likely due to the fact that surface waters do not have friction against the sediment (Fig. 8).

$$\left[DO\ Concentration\ \left(\frac{mg}{L}\right)\right] * \left[North\ Velocity\ \left(\frac{m}{s}\right)\right] = O_2\ Flux\ \left(\frac{g}{m^2-s}\right) \quad (2)$$

Water Chemistry and Profiles

The initial day of field work was conducted on July 10, 2018, while the aerators were on, and consisted of bottom and surface water collection, vertical profiling, and nutrient filtering for water at each station. Throughout the course of the experimental deoxygenation phase, field efforts were repeated, and Figure 9 displays initial profiling compared to final profiling of stations 1, 2, and 7. The figure indicates that for each station, dissolved oxygen concentrations throughout the water column tend to decrease more rapidly over depth after seven days of no aeration as compared to aerated conditions. It appears that for all stations, our vertical profile data shows no hypoxia within surface waters for the entirety of sampling. To further view dissolved oxygen trends, Figure 10 was generated to visualize the bottom water DO concentration time series trend for each of the three stations. It appears that station 1 DO concentrations steadily decreased over the seven days, however, that is not the case for stations 2 and 7 where increases were experienced around July 13, 2018. For stations 1 and 2, near-anoxic conditions were experienced after seven days, with their final and lowest concentrations at 0.13 mg/L and 0.14 mg/L respectively. Following the analysis done by NASL, phosphate concentrations were gathered and plotted against these bottom water DO trends for the three highlighted stations (Fig. 11). It appears that station 1 had the highest magnitude of phosphate increase, following an exponential increase over the seven days. Station 2 seemed to mimic the same pattern as station 1 but in a delayed fashion, and station 7 showed no large increase in phosphate levels, as the concentrations stayed an order of magnitude less than those experienced in both stations 1 and 2.

Discussion

Oxygen Trends

The overall trend in bottom water concentrations of dissolved oxygen was surprising due to the presence of an extended oxygenation event, but otherwise expected because of the system's eventual decline into both hypoxic and even anoxic conditions. As displayed in Figure 6, there was the heavy spike in oxygen levels that was not foreseen that occurred two days after the aerators were turned off and lasted for nearly 24 hours. Due to previous work done at Rock Creek, we expected a sudden decline over the deoxygenation phase from saturated water down to anoxic conditions because oxygen levels dropped to near anoxia within 11–24 hours in both 2012 (Harris et al. 2015) and unpublished 2016 data. The increase experienced on July 12 seemed to be sudden, and following this oxygenation event the dissolved oxygen levels did fall towards anoxia. The true cause of the oxygen spike is unknown at this time, and could have resulted from (1) extreme algal blooming that led to higher rates of photosynthesis and oxygen production, (2) a circulation event that brought about oxygenated water as a result of the aerators being turned off, or (3) some external driver, like a weather event leading to more oxygenated water.

An examination of each station's bottom water concentrations throughout the sampling period reveals a spatially varying response to the aeration system being off. It appears that both stations 2 and 7 were consistent to the trend established from our continuous monitoring station, because there was a period of elevated oxygen concentrations while the aerators were off, experienced between the 11th and 13th of July. On the other hand, station 1 does not seem to respond to this oxygenation event, but rather responds as we anticipated with a gradual decline in oxygen levels throughout deoxygenation down to anoxic levels. The calculated oxygen flux performed with data at the dock just seaward of the aeration zone indicates a large oxygen influx during these first days of the experiment (Fig. 7). Due to the manner that the ADCP parses out its velocity data, we had to select a directional velocity to focus on and we selected north velocity, therefore negative measurements indicate southward flow, or flow towards the inner reaches of Rock Creek. The time series plotted on the x-axis of Figure 7 is the same as the continuous monitoring data from Figure 6, and there appears to be a coordinated influx of oxygenated water that lines up with our increase in bottom water DO on July 12. Station 1, unlike both stations 2 and 7, does not show a response to the oxygenation. This could provide support for a southward influx because of its upstream location in Rock Creek—the station may not have experienced exposure to this oxygenated water. Clearly, an event led to heavily oxygenated water from the Patapsco River down into Rock Creek on July 12.

Along with allowing oxygenation for the system, a main reason for establishing the aerator system was for destratification purposes. It is clear that while the aerators were on there was more consistency in the DO concentrations as you moved along the depth of the water column, indicating vertically well-mixed conditions (Fig. 9). The aforementioned consistency was especially evident in stations 1 and 2, but station 7 already showed signs of some slight stratification. I believe station 7 likely shows this even with aeration on because it is outside the aeration zone and closer to the mouth of Rock Creek (Fig. 2). After a week of deoxygenation with the aerators being turned off, however, all stations show a large vertical gradient between surface concentrations and that of their bottom water with DO declines associated with deeper water. It appears as though without the aeration system, an oxycline forms over the shallow depths of Rock Creek, indicating that the aeration system is imperative in destratification because it forces vertical mixing from the rising air displacing the above water out and downwards, creating this almost convective type of mixing.

Phosphate Concentrations

It appears that there is a positive relationship between hypoxic conditions and the magnitude of increase in phosphate concentrations (Fig. 11). Our ability to make that general statement is upheld by the presence of three distinct bottom water DO trends between stations 1, 2, and 7. As previously mentioned, I hypothesized that all stations would show just a gradual decline in oxygen levels, however, the way the different stations responded to the experimental period varied and provided different oxygen conditions to analyze. For example, station 1 had the lowest oxygen concentrations out of the three stations, and it also experienced a longer duration of consistent severe hypoxia. It is for those reasons that station 1 also experienced the highest magnitude of increase in phosphate concentrations (Fig. 11a), consistent with model simulations. The trend seems to show a signal at which phosphate exponentially grew to higher concentrations along with the worsening of oxygen concentrations. A similar pattern was observed in station 2's data because like station 1, it ends in anoxic conditions (Fig. 11b). The difference between the stations is the severity of hypoxia because the signal response for station 2 is delayed in comparison to station 1, not allowing it to reach the same magnitude of increase in terms of phosphate concentrations. I believe this is attributed to the response on July 13 to increased oxygen levels that was not experienced at station 1. On the other hand,

station 7 was of interest because it told a very different story in terms of the change in phosphate concentrations. Upon analyzing the data, station 7 had final phosphate concentrations an order of magnitude less than the other stations, but it also did not have high durations or severity of hypoxic conditions (Fig. 11c), so this should be expected of the station. When comparing the phosphate trend to that of oxygen, however, you still see the inverse relationship between them persists, thus the relationship is present but there wasn't a signal response that resulted in heavy magnitudes of phosphate level increases.

We compared expected phosphate increases resulting from the model predictions of sediment-water flux to our actual observed measurements. In order to do this, there had to be a station that was relatively close to the stable oxygen levels maintained by our model runs, and station 1 was the only one available for this comparison. Station 1 had at least three days of oxygen values within the severe hypoxia zone, thus that simulation and station was used for comparison purposes. Table 2 shows the comparison of our computed, predictive phosphate increase for three days of severe hypoxia (0.5 mg/L) and the observed change experienced at station 1 at Rock Creek. The relatively similar values indicate that the model was an appropriate source of estimates and that our observed phosphate increase was likely a result of phosphate flux from the sediments into the overlying water column. Prior studies have also demonstrated large phosphate fluxes in Rock Creek following the aerators being turned off (Harris et al. 2012). Lastly, the amount of TDP that was accounted for by phosphate at the end of sampling for both stations 1 and 2 were 82%, and in comparison to initial percentages (station 1 = 34%, station 2 = 21%), that is a vast increase which is consistent with the concept that sediment-water phosphate flux was the dominate driver of phosphorus cycling through the experimental deoxygenation.

Conclusion

Eutrophication is an issue that has plagued the Chesapeake Bay area for some time, however, efforts to mitigate the negative effects of eutrophic conditions have recently shown promise. Our results indicate that not only is Rock Creek successful in mitigating the effects of stratification, but also severe eutrophication-driven hypoxia and the many associated consequences linked to those conditions. We were successful in manipulating oxygen levels within Rock Creek on an ecosystem scale for experimentation, with the exception of a natural oxygenation event. Both our model and observed results indicate higher levels of phosphate flux from sediments into the overlying water column. These paired results between the model and field suggest that within 3-7 days of hypoxic conditions, an expected signaled increase in phosphate flux is expected. Again, this project was a part of a larger study that may be able to better address responses to deoxygenation. In terms of future work, I believe that broadening the sampling efforts to include a recovery period would be of importance. Adding a recovery phase, following the aeration system being turned back on, would allow us to flip our project objective and analyze rather how long the system would take to recover from hypoxic durations. The additional analysis would further our understanding on the overall cycling of phosphorus with special attention on the interaction between the sediment-water boundary.

Acknowledgements

I would like to give a huge thanks to Dr. Jeremy Testa for being an incredible mentor throughout this summer and providing guidance through the development and implementation of this project. Along with Jeremy, I would like to thank Dr. Lora Harris for her partnership and help in the Rock Creek study. All members of both the Testa and Harris labs were imperative in the preparation and completion of the field efforts done at Rock Creek and deserve my thanks,

primarily Casey Sperling Hodgkins for her tremendous help this summer. Other collaborating members that I'd like to acknowledge are Drs. Laura Lapham and Andrew Heyes. Thanks to Mike Allen and all those involved in the funding and acceptance into the REU Program through Maryland Sea Grant and National Science Foundation. Lastly, I would like to thank the University of Maryland Center for Environmental Science Chesapeake Biological Laboratory for hosting me this summer. This study was supported by NSF grant OCE-1756244.

References

Anderson, D. M., P. M. Glibert, and J. M. Burkholder. 2002. Harmful algal blooms and eutrophication: Nutrient sources, composition, and consequences. Estuaries. 25: 704–726. doi:10.1007/BF02804901

Boynton, W. R., C. L. S. Hodgkins, C. A. O'Leary, E. M. Bailey, A. R. Bayard, and L. A. Wainger. 2014. Multi-decade Responses of a Tidal Creek System to Nutrient Load Reductions: Mattawoman Creek, Maryland USA. Estuaries and Coasts. 37: 111–127. doi:10.1007/s12237-013-9690-4

Brady, D. C., J. M. Testa, D. M. Di Toro, W. R. Boynton, and W. M. Kemp. 2013. Sediment flux modeling: Calibration and application for coastal systems. Estuarine, Coastal and Shelf Science. 117: 107–124. doi:10.1016/j.ecss.2012.11.003

Cai, W.-J., W.-J. Huang, G. W. Luther, and others. 2017. Redox reactions and weak buffering capacity lead to acidification in the Chesapeake Bay. Nature Communications. 8. doi:10.1038/s41467-017-00417-7

Diaz, R. J., and R. Rosenberg. 2008. Spreading Dead Zones and Consequences for Marine Ecosystems. Science. 321: 926–929. doi:10.1126/science.1156401

Di Toro, D.M., 2001. Sediment flux modeling, 116 pages. Wiley-Interscience, New York.

Fisher, T. R., J. I. D. Hagy, W. R. Boynton, and M. R. Williams. 2006. Cultural eutrophication in the Choptank and Patuxent estuaries of Chesapeake Bay. Limnology and Oceanography. 51: 435–447. doi:10.4319/lo.2006.51.1_part_2.0435

Harris, L. A., C. L. S. Hodgkins, M. C. Day, D. Austin, J. M. Testa, W. Boynton, L. Van Der Tak, and N. W. Chen. 2015. Optimizing recovery of eutrophic estuaries: Impact of destratification and re-aeration on nutrient and dissolved oxygen dynamics. Ecological Engineering. 75: 470–483. doi:10.1016/j.ecoleng.2014.11.028

Howarth, R., F. Chan, D. J. Conley, J. Garnier, S. C. Doney, R. Marino, and G. Billen. 2011. Coupled biogeochemical cycles: eutrophication and hypoxia in temperate estuaries and coastal marine ecosystems. Frontiers in Ecology and the Environment. 9: 18–26. doi:10.1890/100008

Kemp, W. M., W. R. Boynton, J. E. Adolf, and others. 2005. Eutrophication of Chesapeake Bay: historical trends and ecological interactions. Marine Ecology Progress Series. 303: 1–29.

Lee, Y. J., W. R. Boynton, M. Li, and Y. Li. 2013. Role of Late Winter–Spring Wind Influencing Summer Hypoxia in Chesapeake Bay. Estuaries and Coasts. 36: 683–696. doi:10.1007/s12237-013-9592-5

Levin, L. A., W. Ekau, A. J. Gooday, and others. 2009. Effects of natural and human-induced hypoxia on coastal benthos. Biogeosciences. 6: 2063–2098. doi:10.5194/bg-6-2063-2009

McCarthy, M. J., K. S. McNeal, J. W. Morse, and W. S. Gardner. 2008. Bottom-water Hypoxia Effects on Sediment–Water Interface Nitrogen Transformations in a Seasonally Hypoxic,

Shallow Bay (Corpus Christi Bay, TX, USA). Estuaries and Coasts. 31: 521–531. doi:10.1007/s12237-008-9041-z

Scully, M. E., C. Friedrichs, and J. Brubaker. 2005. Control of estuarine stratification and mixing by wind-induced straining of the estuarine density field. Estuaries. 28: 321–326. doi:10.1007/BF02693915

Testa, J. M., and W. M. Kemp. 2012. Hypoxia-induced shifts in nitrogen and phosphorus cycling in Chesapeake Bay. Limnology and Oceanography. 57: 835–850. doi:10.4319/lo.2012.57.3.0835

Testa, J. M., D. C. Brady, D. M. Di Toro, W. R. Boynton, J. C. Cornwell, and W. M. Kemp. 2013. Sediment flux modeling: Simulating nitrogen, phosphorus, and silica cycles. Estuarine, Coastal and Shelf Science. 131: 245–263. doi:10.1016/j.ecss.2013.06.014

Testa, J. M., W. M. Kemp, and W. R. Boynton. 2018. Season-specific trends and linkages of nitrogen and oxygen cycles in Chesapeake Bay: Linked oxygen and nitrogen trends. Limnology and Oceanography. doi:10.1002/lno.10823

Zhang, Q., R. R. Murphy, R. Tian, M. K. Forsyth, E. M. Trentacoste, J. Keisman, and P. J. Tango. 2018. Chesapeake Bay's water quality condition has been recovering: Insights from a multimetric indicator assessment of thirty years of tidal monitoring data. Science of The Total Environment. 637–638: 1617–1625. doi:10.1016/j.scitotenv.2018.05.025

Figures and Tables

Figure 1. Site location of Rock Creek depicted by the red arrow. This was generated using Google Earth.

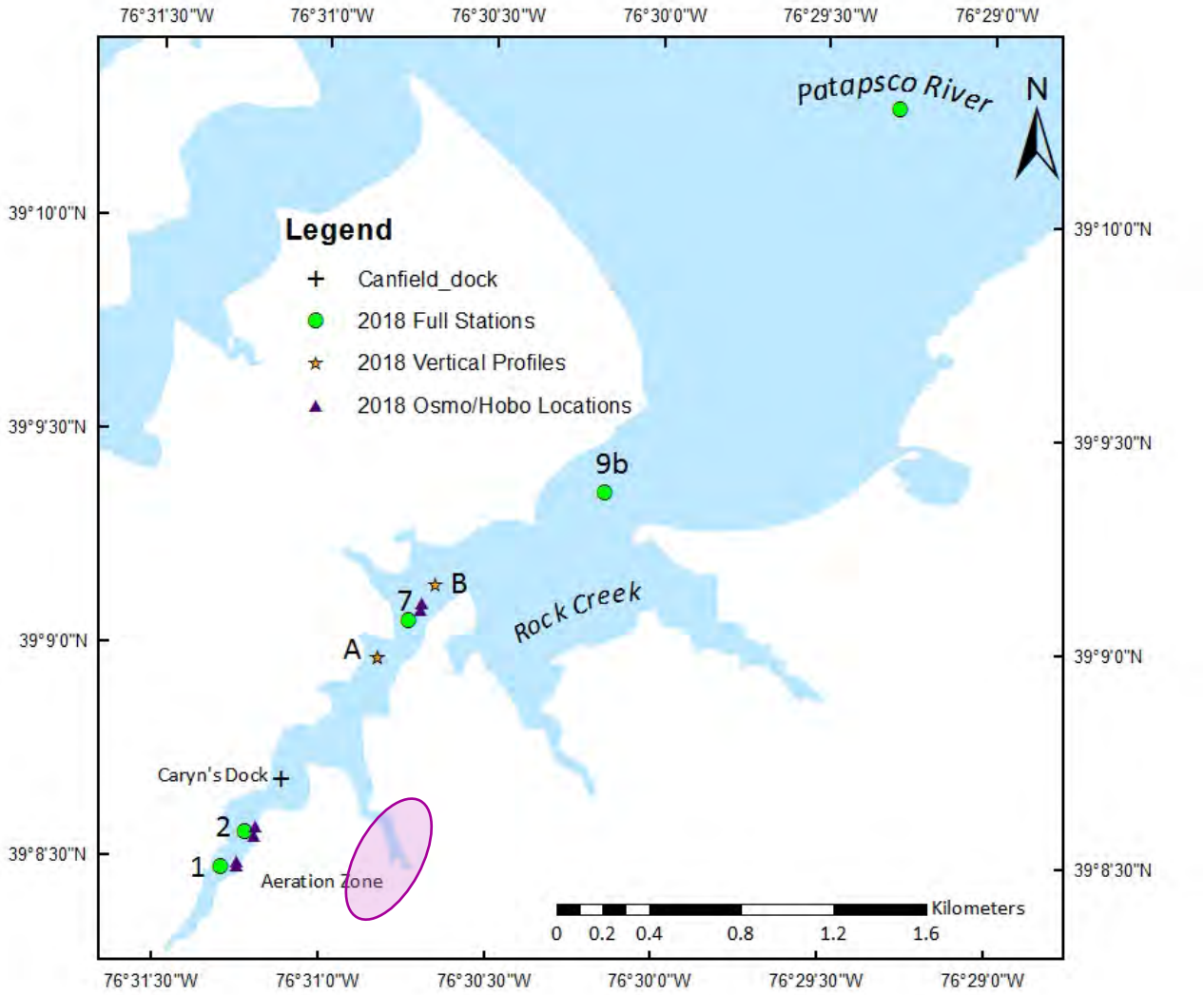

Figure 2. Map depicting site location along with points of interest. Green circles represent the full sampling locations, sites A and B represented by gold stars are additional vertical profile locations, and the black cross represents the continuous monitoring station at Caryn's Dock. Additionally, the aeration zone was shaded pink to visually display the spatial scale encompassed by the aerators. Lastly, OsmoSamplers and Hobo's are designated by the purple triangles.

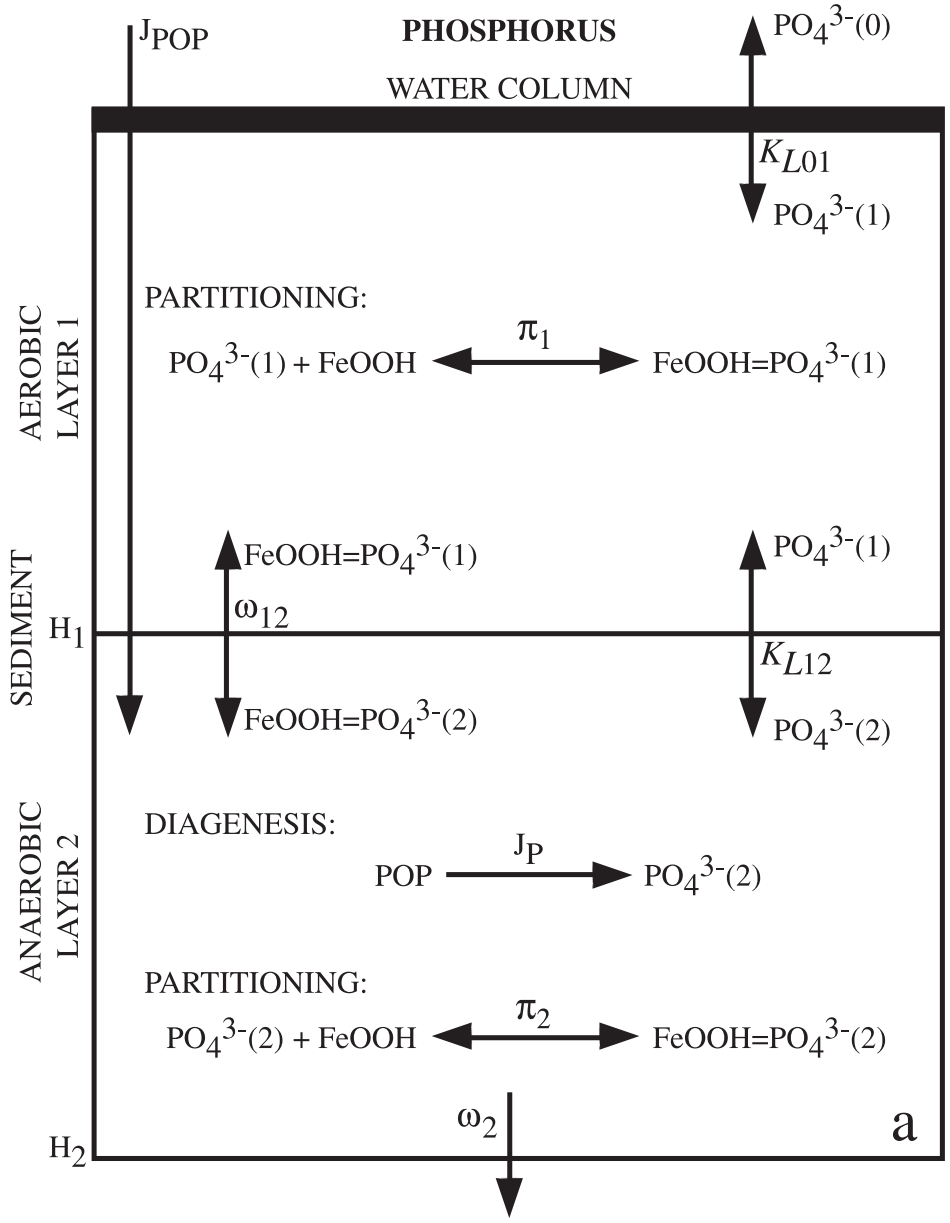

Figure 3. Schematic representation of the phosphorus cycle as completed in the Sediment Flux Model. Originally published by Testa et al. (2013).

Figure 4: Rigging setup for ADCP and EXO2 sonde deployment. ADCP was set for a deployment while looking up in shallow water, therefore, this platform setup was necessary.

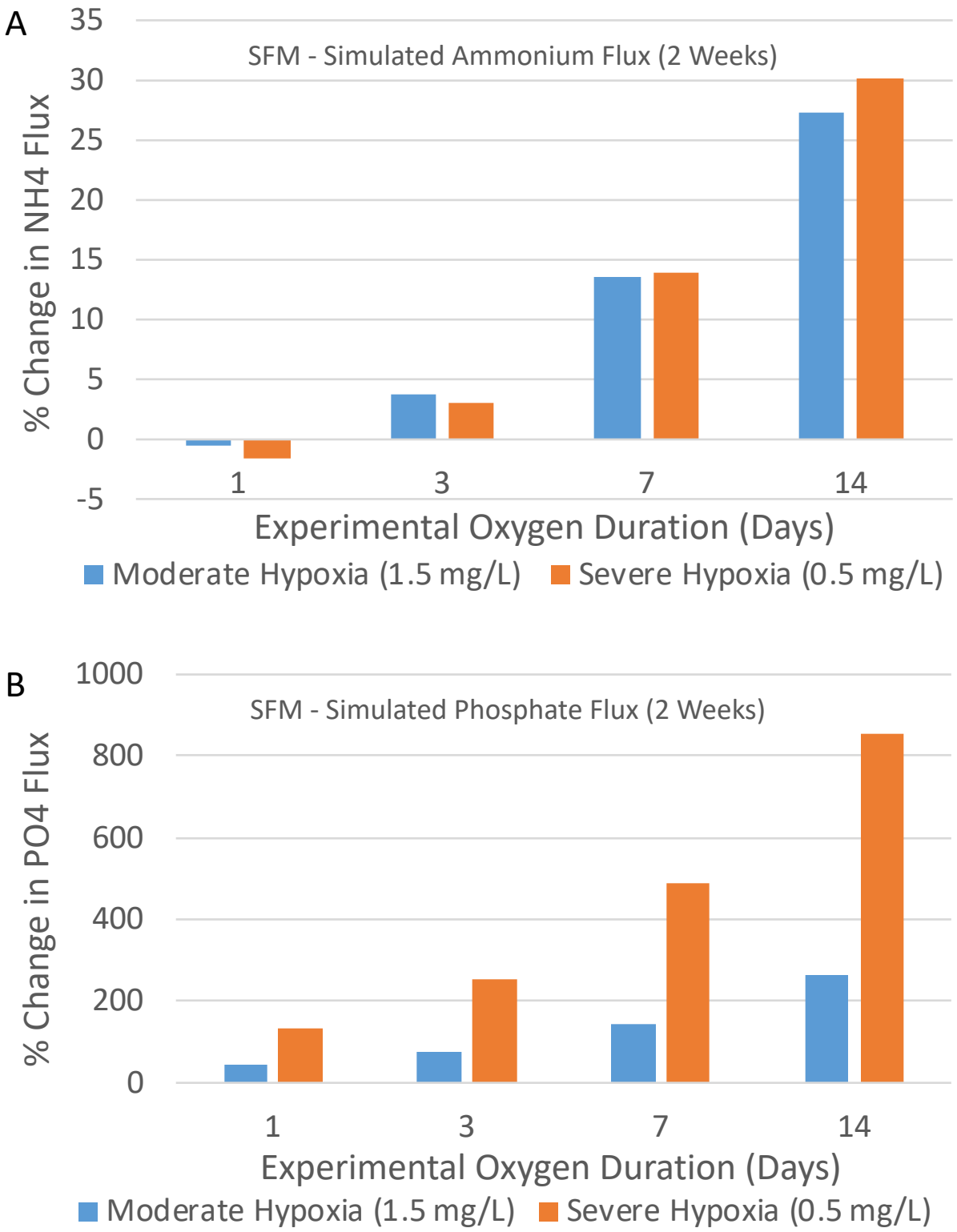

Figure 5. The simulated percent change in flux over the course of experimental two weeks from the Sediment Flux Model for A) Ammonium and B) Phosphate. The experimental two weeks

consisted of changing durations of either moderate hypoxia (1.5 mg/L) or severe hypoxia (0.5 mg/L), and the total flux for the period was computed against untampered conditions.

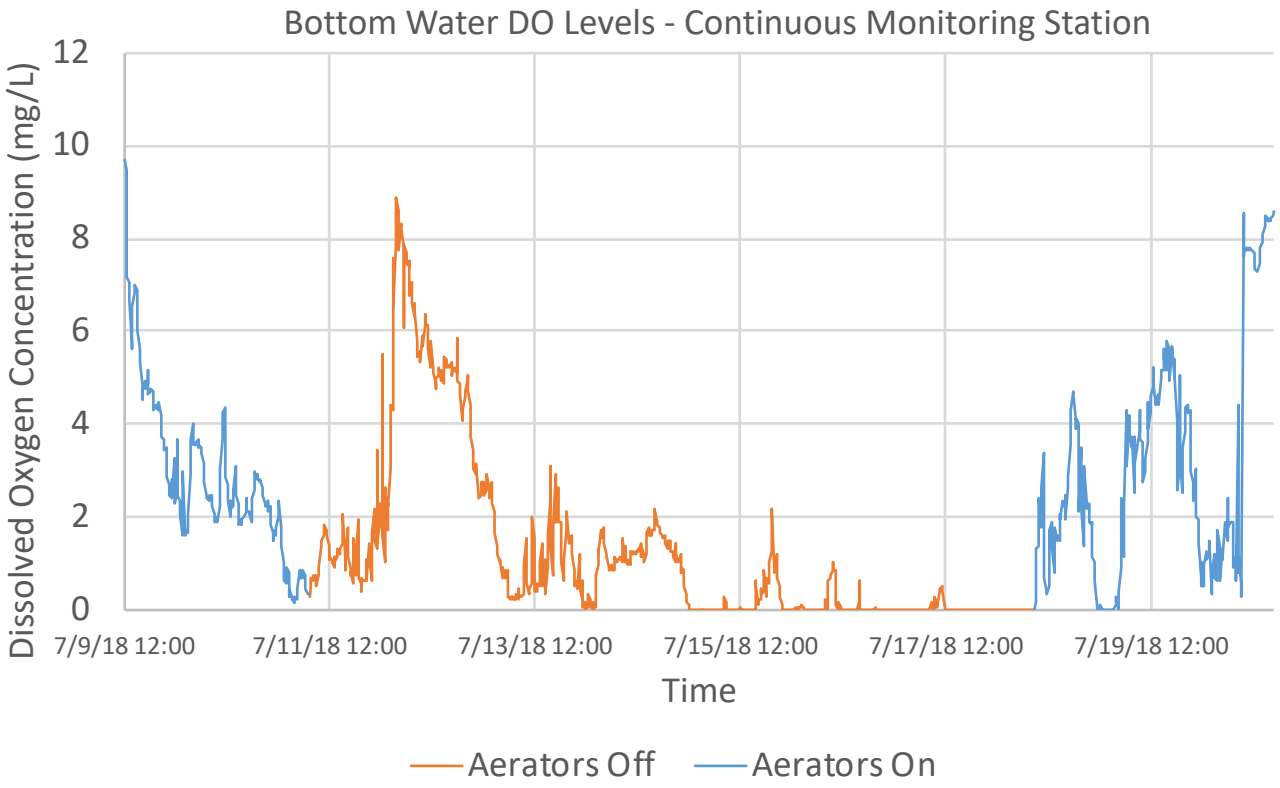

Figure 6. A time series displaying the bottom water dissolved oxygen levels (mg/L) from the YSI EXO2 multi-parameter sonde located at the continuous monitoring station at Caryn's Dock. The phase labeled as aerators off is the experimental phase of the project, while the aerators on series include data preceding and following the experimental phase.

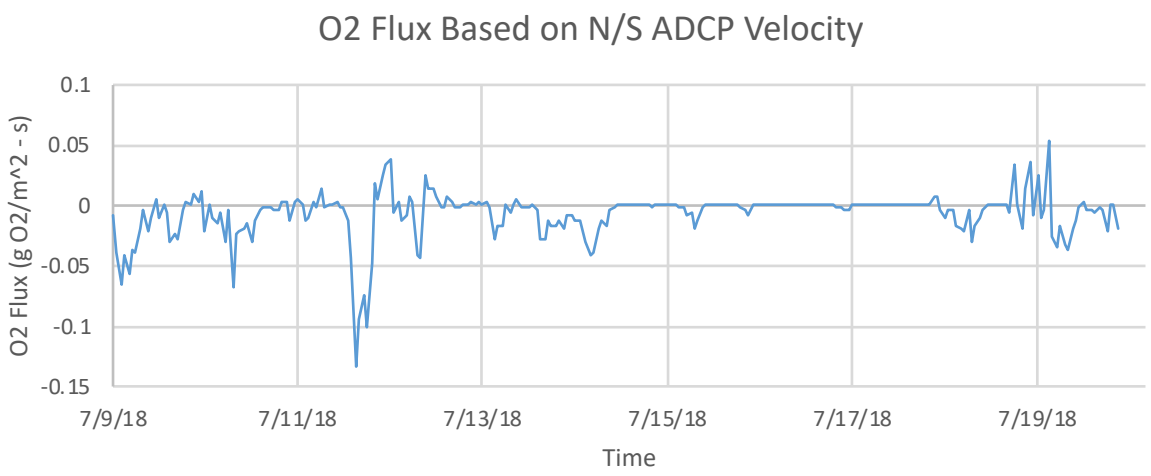

Figure 7. The above figure displays the O2 flux output of multiplying the N/S velocity for bottom water from ADCP to the bottom water DO from continuous monitoring station. Negative numbers represent flux moving south, towards the upstream portion of Rock Creek.

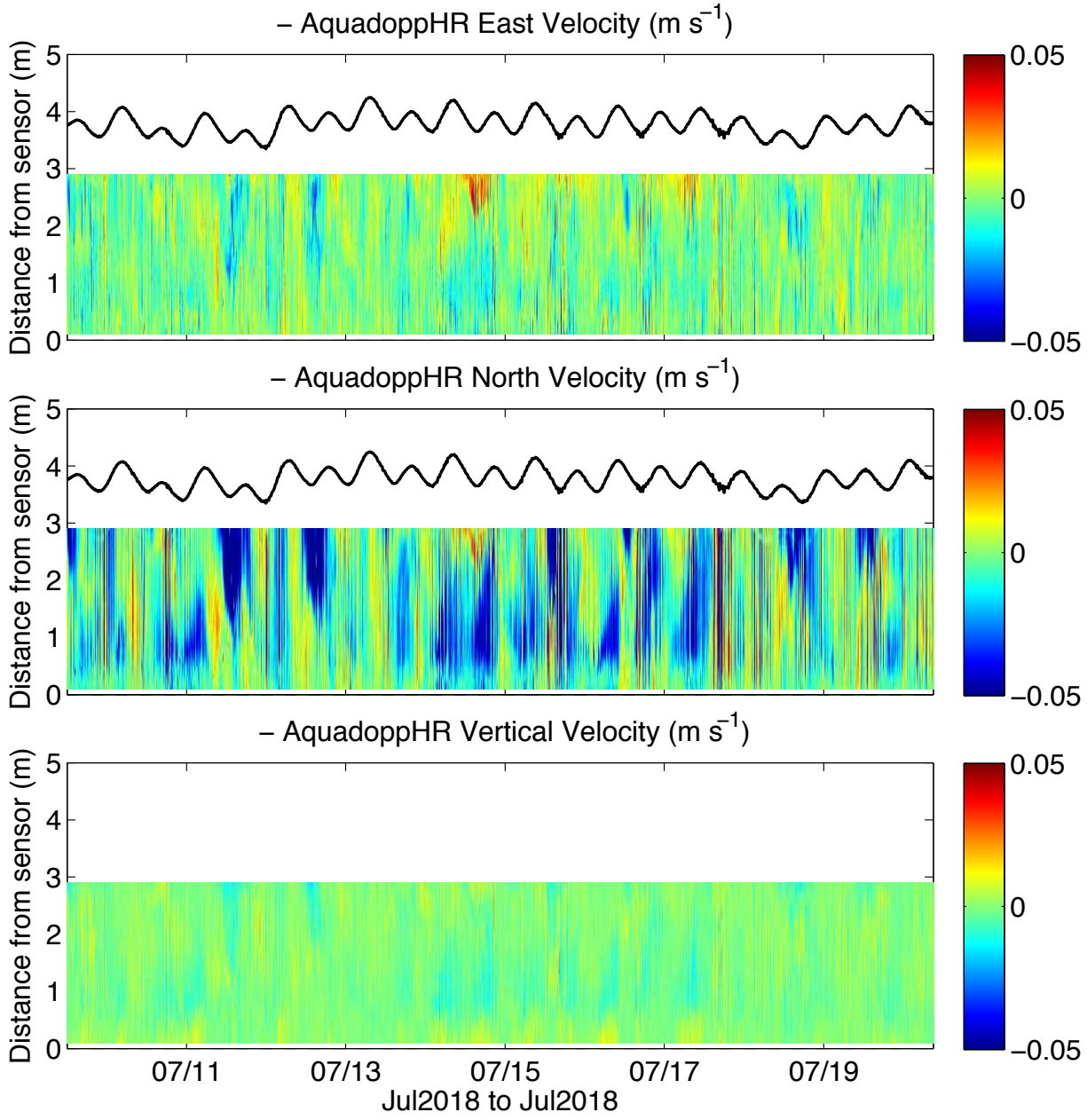

Figure 8. ADCP Velocity measurements through the course of the sampling based on ENU (East-North-Up) coordinate system. Color scale indicates magnitude of velocity for the contour plots.

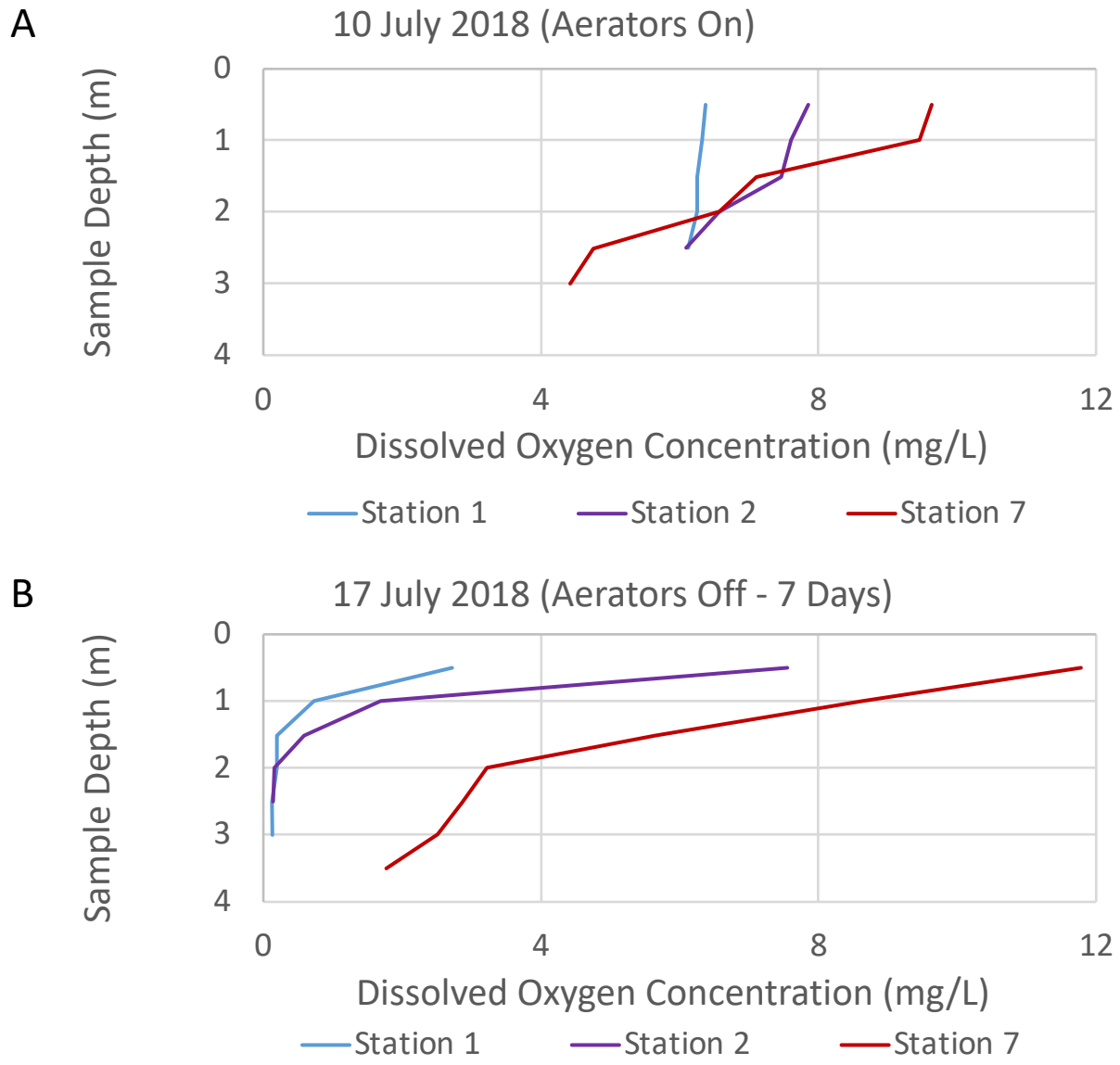

Figure 9. Vertical profiles of A) initial conditions on 7/10/18 and B) final sampling conditions on July 17, 2018, were compared to illustrate dissolved oxygen concentrations throughout the water column at stations 1, 2, and 7.

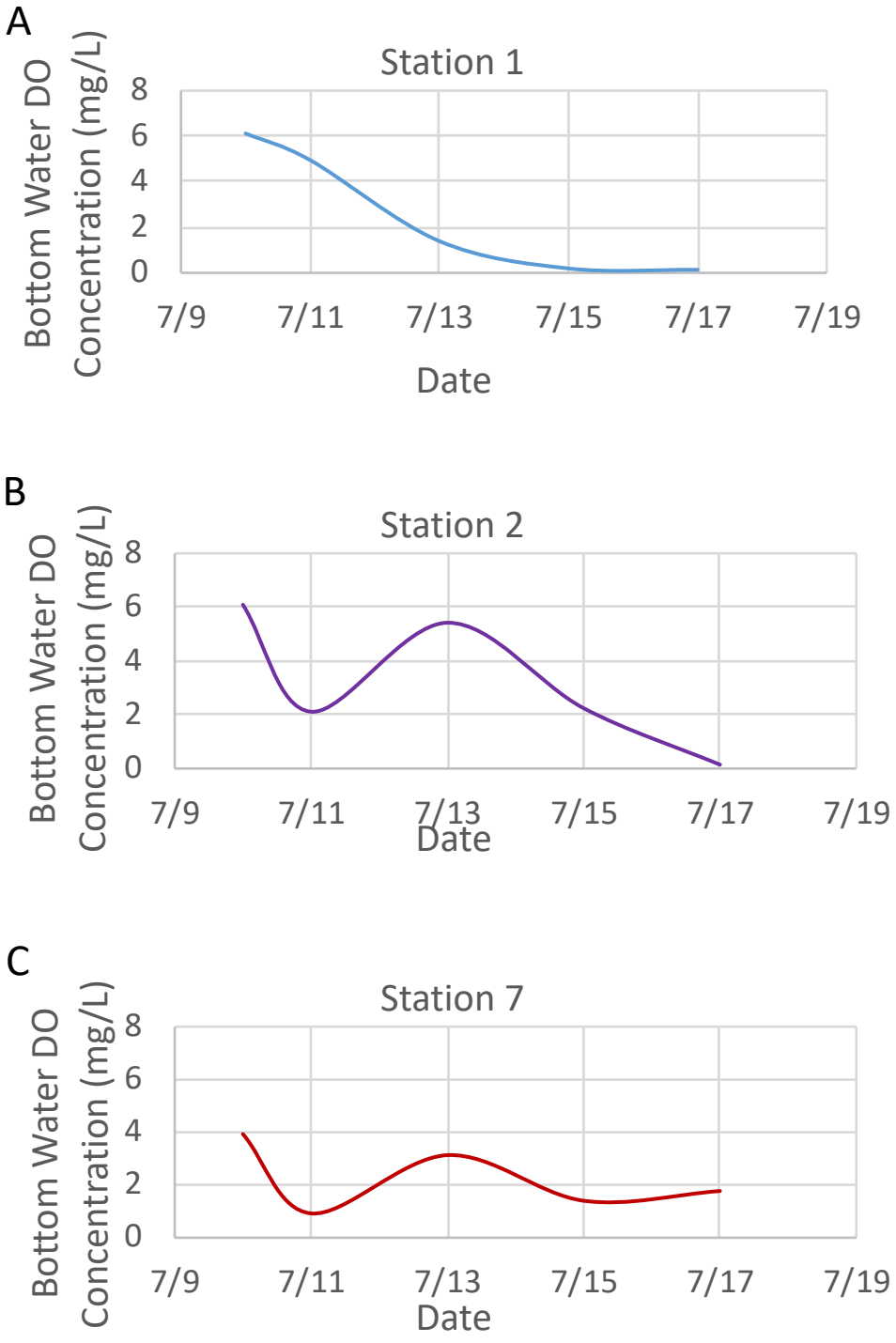

Figure 10. Bottom water DO concentrations from the YSI EXO2 used for vertical profiles at each station during field efforts plotted against time of the project. The trends are displayed within the figure as A) Station 1, B) Station 2, and C) Station 7.

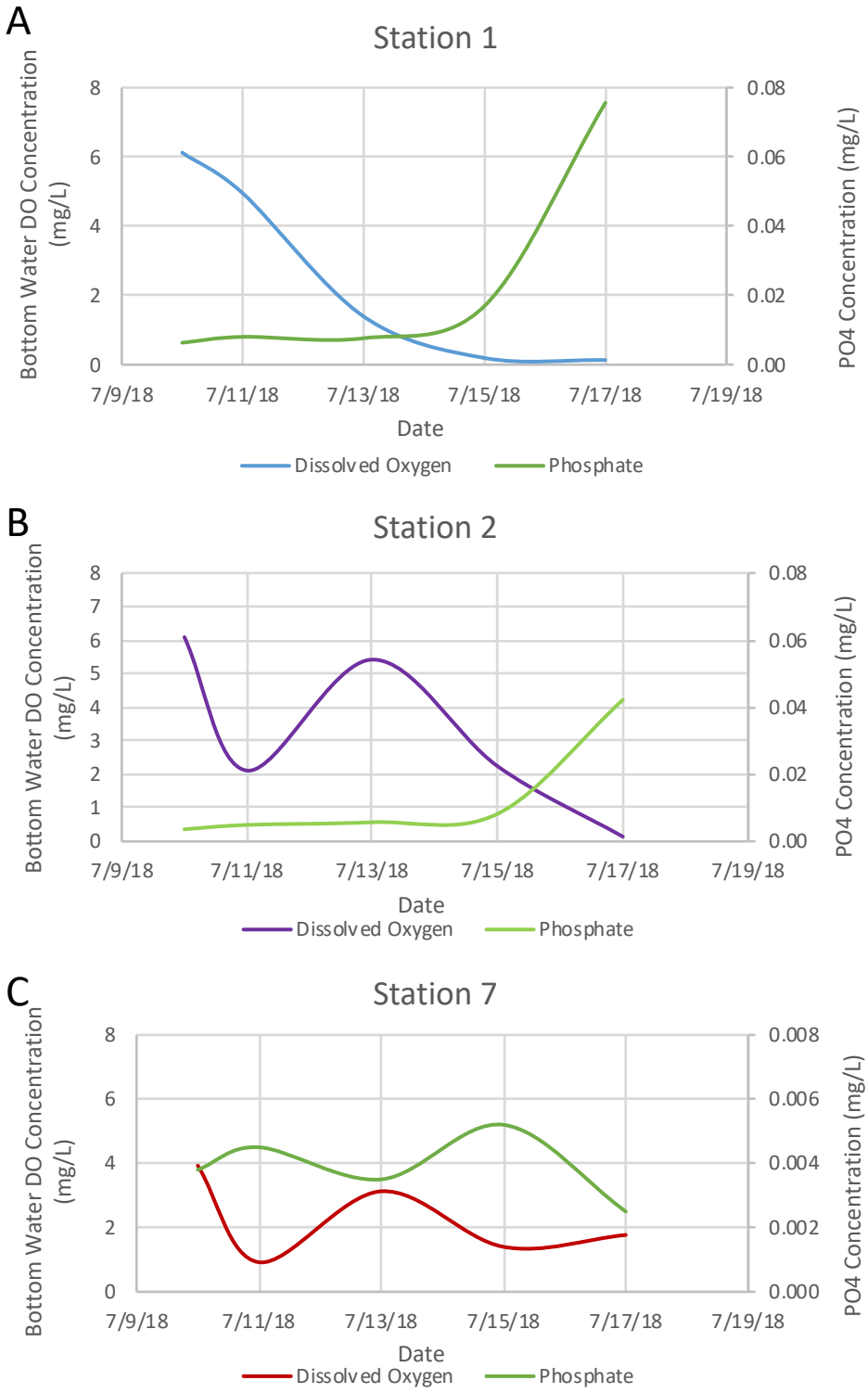

Figure 11. Bottom water DO concentrations from the YSI EXO 2 used for vertical profiles at each station during field efforts and the phosphate concentrations from our filtrate samples provided to NASL plotted against time. The trends are displayed within the figure as A) Station 1, B) Station 2, and C) Station 7.

Table 1. All model simulation trials ran for this project.

Sediment Flux Model Simulation Trials				
Moderate Hypoxia (1.5 mg/L)	1-Day	3-Days	7-Days	14-Days
Severe Hypoxia (0.5 mg/L)	1-Day	3-Days	7-Days	14-Days

Table 2. Comparison of model simulation (3-days severe hypoxia) to observed station 1 bottom water for phosphate concentrations. Computed model simulation phosphate increase was done by dividing the overall modeled phosphate flux from a week-long period over an assumed well-mixed 3 m water column (similar to depths in Rock Creek). Observed difference was calculated by subtracting the final concentration by the initial concentration.

PO4 Model Prediction (3 Days – Severe Hypoxia (0.5 mg/L)	Observed PO4 Concentration Difference – Rock Creek Station 1 Bottom Water
0.0814 mg/L	0.0693 mg/L

University of Maryland
Center for Environmental Science
Horn Point Laboratory

Inducing Mixotrophy in the Dinoflagellate *Heterocapsa rotundata*

Alexius Dingle, REU Fellow
Maryland Sea Grant

Emily Brownlee, Postdoctoral Researcher
Horn Point Laboratory, University of Maryland Center for Environmental Science

Sairah Malkin, Assistant Professor
Horn Point Laboratory, University of Maryland Center for Environmental Science

Abstract

Mixotrophy is a nutrient acquisition method that combines photosynthesis and heterotrophy. Although mixotrophy is known to be prevalent throughout aquatic microbial ecosystems, mixotrophy has been poorly represented in current marine food web models. The ability to quantify carbon and nutrient acquisition associated with mixotrophy would be a major step forward in the attempt to better understand the behavior. *Heterocapsa rotundata* is a dinoflagellate species indigenous to the Chesapeake Bay that has been confirmed to exhibit mixotrophy and begins to graze on bacteria when light levels are low. *Heterocapsa rotundata* is a prominent species in Chesapeake Bay during the winter season. The objective of this study was to measure mixotrophic grazing in a culture of *Heterocapsa rotundata* isolated from the Choptank River, across a gradient of light levels. To measure ingestion rates, *H. rotundata* were allowed to feed on fluorescent microspheres for a brief incubation period. Ingestion rates were calculated as the rate of fluorescent beads engulfed by *H. rotundata*, as observed using fluorescence microscopy. The study demonstrated a significant negative relationship between light level and ingestion in indigenous *Heterocapsa rotundata.*

Introduction

Mixotrophy describes a metabolic lifestyle in which microorganisms acquire carbon, nutrients, and energy through both photosynthesis and ingestion, and has been proven to be a means of survival for many aquatic microbes (Stoecker et al. 2017). It has been traditionally thought that microorganisms can fall into one of two fundamental trophic categories, either heterotrophy in which organisms ingest food or photoautotrophy in which organisms employ photosynthesis to harness energy from sunlight to meet their energetic and nutritional requirements. Heterotrophs obtain carbon and nutrients from the consumption of other organisms while photoautotrophs use light energy to perform photosynthesis, in which energy is a byproduct and nutrients are assembled by the organism itself. Mixotrophic organisms can use both fundamental lifestyles, combining photosynthesis with ingestion. Mixotrophy grants capable marine microbes a metabolic upper hand (Stoecker et al. 2017), and it is becoming increasingly apparent that there are a considerable number of aquatic protists that are mixotrophic (Worden et al. 2015). Most ecosystem models that predict trophic transfer in aquatic microbial food webs currently do not

explicitly incorporate mixotrophy. The true breadth of the ecological impact of this behavior is poorly understood because the basis for prey selection, feeding rates, and alternate strategies are not well known (Worden et al. 2015). To better quantify the role of mixotrophy in carbon, nutrient, and energy transfer through aquatic ecosystems, we require novel tools.

There have been several methods developed to identify and quantify mixotrophy in marine microbes. The most widely used method is to quantify through microscopy the photopigments left behind from consumed photosynthetic food sources or food vacuoles within the organism of interest. Recently, genetic approaches have additionally been applied. Transcriptomes of two mixotrophic marine planktonic ciliates and their algal food source (i.e. their prey) were sequenced in the attempt to find genes indicative of a mixotrophic lifestyle (Santoferrara et al. 2014). While both methods enable a quantification of mixotrophy, neither provide a quantification of the carbon and nutrient contribution of different food sources (Flynn et al. 2013). Tracer studies, on the other hand, can be used to quantify carbon and nitrogen transfer. In one study, stable isotope probing (SIP) was used to identify sources of carbon in a mixotrophic Chrysophyte (Terrado et al. 2017). SIP is commonly used in microbial ecology and allows for specific functional groups of organisms that incorporate particular substrates to be identified without cultivation (Neufeld et al. 2007). In another study, cell sorting coupled with radioisotope tracer additions were used to measure mixotrophy in natural systems (Hartmann et al. 2012). These methods have been beneficial for studying samples in a moderate quantity but are not sufficiently efficient (in terms of direct expense and effort) for high-throughput experiments in natural samples.

This research will expand upon the methods used to induce heterotrophic behavior in phytoplankton based upon previous mixotrophy experiments (Millette et al. 2017). *Heterocapsa rotundata* is a dinoflagellate that has been confirmed to exhibit a mixotrophic lifestyle and is abundant in the Chesapeake Bay, with peak abundance observed around March (Johnson 2015; Millette et al. 2017). It has been hypothesized that their growth in the winter is partially enabled by their ability to graze on bacteria. *Heterocapsa rotundata* will be cultured under controlled conditions to induce varying levels of mixotrophic behavior. Growth rates and chlorophyll concentrations will be measured. Fluorescent beads, or microspheres, will then be added to the cultures with the expectation that *Heterocapsa rotundata* will feed on the beads indiscriminately. Preserved samples will then be looked at under a fluorescent microscope to determine bead grazing rates.

Materials and Methods

Media and Cultures

Culture media was prepared by enriching filtered (0.2 µm) Choptank River water using an L1 Medium Kit (Bigelow Laboratory for Ocean Sciences, Boothbay, ME). Salinity was adjusted to 16 by adding Instant Ocean Sea Salt (Spectrum Brands, Madison, WI). Cultures were transferred through 2 rounds of media as follows. Media was sterilized by autoclaving for 45 minutes. 25 ml of media was subsequently added to 10 culture tubes and autoclaved for 25 minutes. Media was then cooled to 14°C in Percival incubator. Once cooled, 5 ml of culture was added to each tube. Cultures were grown to a density of approximately $2x10^5$ cells/ml upon transfer to 16 experimental bottles. 90 ml of media was transferred to 16 bottles. The bottles containing the media were then autoclaved for approximately 30 minutes and allowed to cool to 14°C. 10 ml of culture was added to each bottle. Cell counts were conducted throughout the 48-hour period at $T_{0,}$ $T_{24,}$ and T_{48} using a flow cytometer (BD Accuri™ C6 Plus; BD Biosciences, San Jose, CA).

H. rotundata growth rates were averaged for each treatment and calculated with the following equation: μ is growth rate, $(H.\ rotundata)_f$ is the final abundance of *H. rotundata*, $(H.\ rotundata)_i$ is the initial abundance of *H. rotundata* and T_f and T_i are the final and initial sampling times in hours (Terrado et al. 2017).

$$\mu = (\ln[H.\ rotundata_f] - \ln[H.\ rotundata_i])/ (T_f - T_i) \quad (1)$$

Inducing Heterotrophy

Heterocapsa rotundata cultures were subjected to different static light levels for a period of 48 hours. To achieve the different light levels, neutral density mesh filters were used to cover the bottles. Using a cosine PAR detector, light levels were measured inside each bottle, and reported in Table 1.

Absorbance Spectra

Absorbance spectra of the culture replicates were measured at T_0 and T_{24}. Absorbance spectra (500-750 nm) of cultures were measured at each light treatment at T_0 and T_{24}. 20-22.5 mL subsamples were filtered onto a 25 mm GF/F glass microfiber filter and absorbance was measured using a DigiLab Hitachi U3310 Spectrophotometer (Digilab, Inc., Hopkinton, MA), in scanning mode, using a blank filter as a reference. A DI rinsed filter was used as a blank. After the initial measurement, each filter was exposed to 5 ml of 10% bleach for 5 minutes and absorbance was re-measured on the spectrophotometer. The bleached values represent absorbance unrelated to photopigments and were subtracted from the initial values.

Bead Grazing and Filtering

After the 48-hour acclimation period, 125 µl of fluorescent microspheres were added to the remaining 12 bottles at a density of 4.54×10^5 beads/ml. The bottles were incubated for 30 minutes, then 50 ml samples were taken from each bottle. Samples were preserved in amber bottles with 25 µl of alkaline lugols, 2.5 ml of paraformaldehyde, and 50 µl of sodium thiosulfate. This formulation was used to prevent egestion of microspheres (Millette et al. 2017). Samples were filtered onto 3 µm Millipore filters with a Millipore apparatus. The filters were then mounted on a slide with mounting fluid and covered with a glass cover.

Fluorescent Microscopy and Counting

To visualize and count the fluorescent microspheres that had been ingested by *Heterocapsa rotundata,* a Zeiss Model Axio Imager M1 Upright Fluorescence Microscope (Carl Zeiss Microscopy Ltd, Jena, Germany) was used on the 100x objective with immersion oil. Beads were counted, and pictures were taken using the DAPI filter (Fig. 4). Ingested beads were tallied amongst 100 cells at random. *Heterocapsa rotundata* ingestion rates were calculated using the following equation, with *r* corresponding to ingestion rate:

$$r = (\text{beads counted})/100 \quad \text{cells/incubation time} \quad (2)$$

Results

Heterocapsa rotundata Growth Rates, Chlorophyll Concentrations, and Ingestion Rates

The growth rate of the *Heterocapsa rotundata* cultures that were subjected to the no mesh treatment continued to increase over the 48-hour period. The growth rates of the 2 mesh and 4 mesh treatments showed a decline in the algal populations from the 24 to 48-hour period depicted in Fig. 1.

Absorbance spectra data revealed that the cultures exposed to the lowest irradiance had the highest chlorophyll concentrations, while the cultures exposed to the highest irradiance had the lowest chlorophyll levels depicted in Fig. 2.

In the *Heterocapsa rotundata* culture, ingestion rates declined as a function of irradiance (Figure 3). Cultures subjected to the 4-mesh treatment revealed the highest bead ingestion rates of approximately 0.6 beads/cell/hour, while the cultures that had no mesh (full light) exhibited the lowest bead ingestion rates, at a little less than 0.2 beads/hour. The logarithmic curve showing the trend amongst the data is $y = -0.203\ln(x) + 0.8802$ and $R^2 = 0.9613$.

Discussion

In this experiment, we confirmed that grazing by *Heterocapsa rotundata* in cultures indigenous from Chesapeake Bay is inducible at low light levels. This experiment provides a necessary foundational basis for further developing an efficient and cost-effective procedure that will allow for the quantification of mixotrophy in marine ecosystems.

We observed a significant negative relationship between bead grazing and irradiance in a culture of *Heterocapsa rotundata*. Previously, bead ingestion rates increased with lower light levels (Fig. 3). In a prior bead grazing experiment conducted with *Heterocapsa rotundata,* the species was of Scandinavian origin (Millette et al. 2017). Here, we used an isolate from Chesapeake Bay. Cultures subjected to the 4-mesh treatment had bead ingestion rates of approximately 0.6 beads/hour, while the cultures that had no mesh had bead ingestion rates of a little less than .2 beads/hour. Although the data did show the anticipated trend, when compared to a similar figure depicting bead grazing rates, our grazing rates were significantly lower than those observed previously (Millette et al. 2017). The prior experiment reported grazing rates as high as 15 beads/hour and as low as 3 beads/hour. Our observed rates could be lower than previous reported rates because the *Heterocapsa rotundata* used in this study were cultures for an extensive time versus samples isolated directly from the environment. The cultures were not axenic and did have naturally occurring populations of bacteria. The dinoflagellates could potentially have been discriminating between the fluorescent beads and bacteria.

The lowest light treatments (2 mesh and 4 mesh) exhibited a decline in algal density likely due to the degree of low light conditions. Despite the less robust growth rates exhibited with decreased irradiance, the data shown from the absorbance spectra measurements indicates a strong relationship between exposure to light and chlorophyll concentrations (Fig.2). It was anticipated that when introduced to low light conditions, *Heterocapsa rotundata* would increase its chlorophyll concentration. But, further, we hypothesized it would gain a greater proportion of its energy from grazing. The cultures that were exposed to the lowest levels of light revealed an increase chlorophyll a concentration. This shows that *Heterocapsa rotundata* increases its chlorophyll concentration when introduced to low light conditions in the effort to maximize

photosynthetic efficiency. Given that these cells also increase their bacterial grazing, this may indicate that the heterotrophic energy acquisition is used to support greater photosynthetic efficiency.

Future research could explore the natural abundances of stable isotopes in *Heterocapsa rotundata* under different trophic modes. It has been demonstrated that $\Delta^{15}N$ ratios increase at higher trophic levels (Cabana and Rasmussen 1996), while predominately photosynthetic organisms have lower a $\Delta^{15}N$ ratios. Such a method could potentially eliminate the need for bead grazing (with its associated limitations) and provide a better assessment of the carbon that flows through mixotrophic pathways in aquatic food webs.

Conclusion

This study concludes that feeding can successfully be induced in *Heterocapsa rotundata* endemic to Chesapeake Bay and that grazing is higher at decreasing light levels. Successful feeding with local *Heterocapsa rotundata* sets the groundwork for further experimentation. Being able to quantify mixotrophy in *Heterocapsa rotundata*, a prominent dinoflagellate in the Chesapeake Bay, will have significant implications in the study of aquatic protists' metabolic processes. This is important in the case of protists species responsible for Harmful Algal Blooms (HABs). HABs occur when phytoplankton undergo massive population growth that has adverse effects on plants, animals, and humans. Some algae produce toxins that can kill large populations of fish and shellfish, as well as indirectly cause illness in humans (US Department of Commerce). However, not all HABs involve toxic algal species. When non-toxic algae bloom and die, the decaying process can cause aquatic hypoxia which leads to fish kills and dead zones (US Department of Commerce). HABs are becoming more frequent and many HAB species exhibit mixotrophic behavior, which in turn allows these algae to thrive compared to other species in the phytoplankton community (Caron 2016).

Acknowledgments

I would like to thank Maryland Sea Grant for allowing me to partake in research with the University of Maryland Center for Environmental Science at Horn Point Laboratory. Many thanks to Dr. Emily Brownlee and Dr. Sairah Malkin for mentorship, assistance, and guidance. Also, I would like to thank Dr. Mike Allen for organizing this summer program. This study was supported by the Maryland Sea Grant REU program and NSF grant OCE-1756244.

References

Caron, D. A. 2016. Mixotrophy stirs up our understanding of marine food webs. Proc. Natl. Acad. Sci. U. S. A. 113: 2806–8. doi:10.1073/pnas.1600718113

Flynn, K. J., D. K. Stoecker, A. Mitra, J. A. Raven, P. M. Glibert, P. J. Hansen, E. Granéli, and J. M. Burkholder. 2013. Misuse of the phytoplankton–zooplankton dichotomy: the need to assign organisms as mixotrophs within plankton functional types. J. Plankton Res. 35: 3–11. doi:10.1093/plankt/fbs062

Hartmann, M., C. Grob, G. A. Tarran, A. P. Martin, P. H. Burkill, D. J. Scanlan, and M. V. Zubkov. 2012. Mixotrophic basis of Atlantic oligotrophic ecosystems. Proc. Natl. Acad. Sci. 109: 5756–5760. doi:10.1073/pnas.1118179109

Johnson, M. D. 2015. Inducible Mixotrophy in the Dinoflagellate *Prorocentrum minimum*. J. Eukaryot. Microbiol. 62: 431–443. doi:10.1111/jeu.12198

Millette, N. C., J. J. Pierson, A. Aceves, and D. K. Stoecker. 2017. Mixotrophy in *Heterocapsa rotundata* : A mechanism for dominating the winter phytoplankton. Limnol. Oceanogr. 62: 836–845. doi:10.1002/lno.10470

Neufeld, J. D., J. Vohra, M. G. Dumont, T. Lueders, M. Manefield, M. W. Friedrich, and J. C. Murrell. 2007. DNA stable-isotope probing. Nat. Protoc. 2: 860–866. doi:10.1038/nprot.2007.109

Santoferrara, L. F., S. Guida, H. Zhang, and G. B. McManus. 2014. De Novo Transcriptomes of a Mixotrophic and a Heterotrophic Ciliate from Marine Plankton R.F. Waller [ed.]. PLoS One 9: e101418. doi:10.1371/journal.pone.0101418

Stoecker, D. K., P. J. Hansen, D. A. Caron, and A. Mitra. 2017. Mixotrophy in the Marine Plankton. Ann. Rev. Mar. Sci. 9: 311–335. doi:10.1146/annurev-marine-010816-060617

Terrado, R., A. L. Pasulka, A. A.-Y. Lie, V. J. Orphan, K. B. Heidelberg, and D. A. Caron. 2017. Autotrophic and heterotrophic acquisition of carbon and nitrogen by a mixotrophic chrysophyte established through stable isotope analysis. ISME J. 11: 2022–2034. doi:10.1038/ismej.2017.68

US Department of Commerce, N. O. and A. A. What is a red tide?

Worden, A. Z., M. J. Follows, S. J. Giovannoni, S. Wilken, A. E. Zimmerman, and P. J. Keeling. 2015. Rethinking the marine carbon cycle: Factoring in the multifarious lifestyles of microbes. Science (80-.). 347: 1257594–1257594. doi:10.1126/science.1257594

Figures and Tables

Table 1. Irradiance measurements of each mesh treatment.

Layers of Mesh	Irradiance (μE m^{-2} s^{-1})
0	37.0
1	20.5
2	13.5
4	4.5

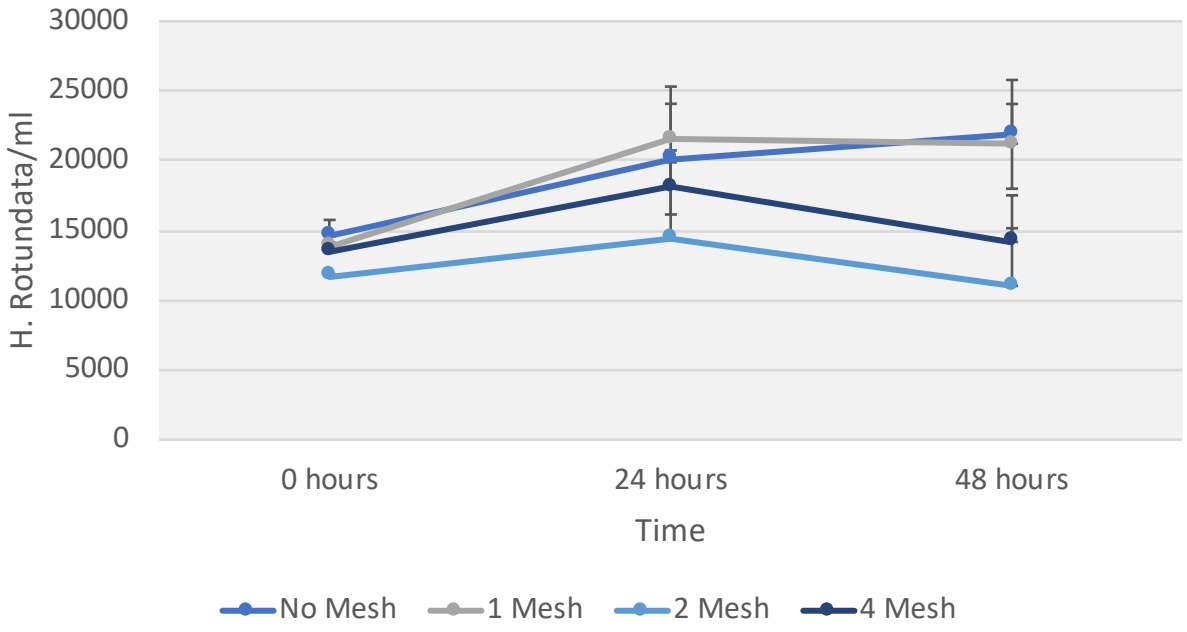

Figure 1. *Heterocapsa rotundata* growth rates over 48-hour period.

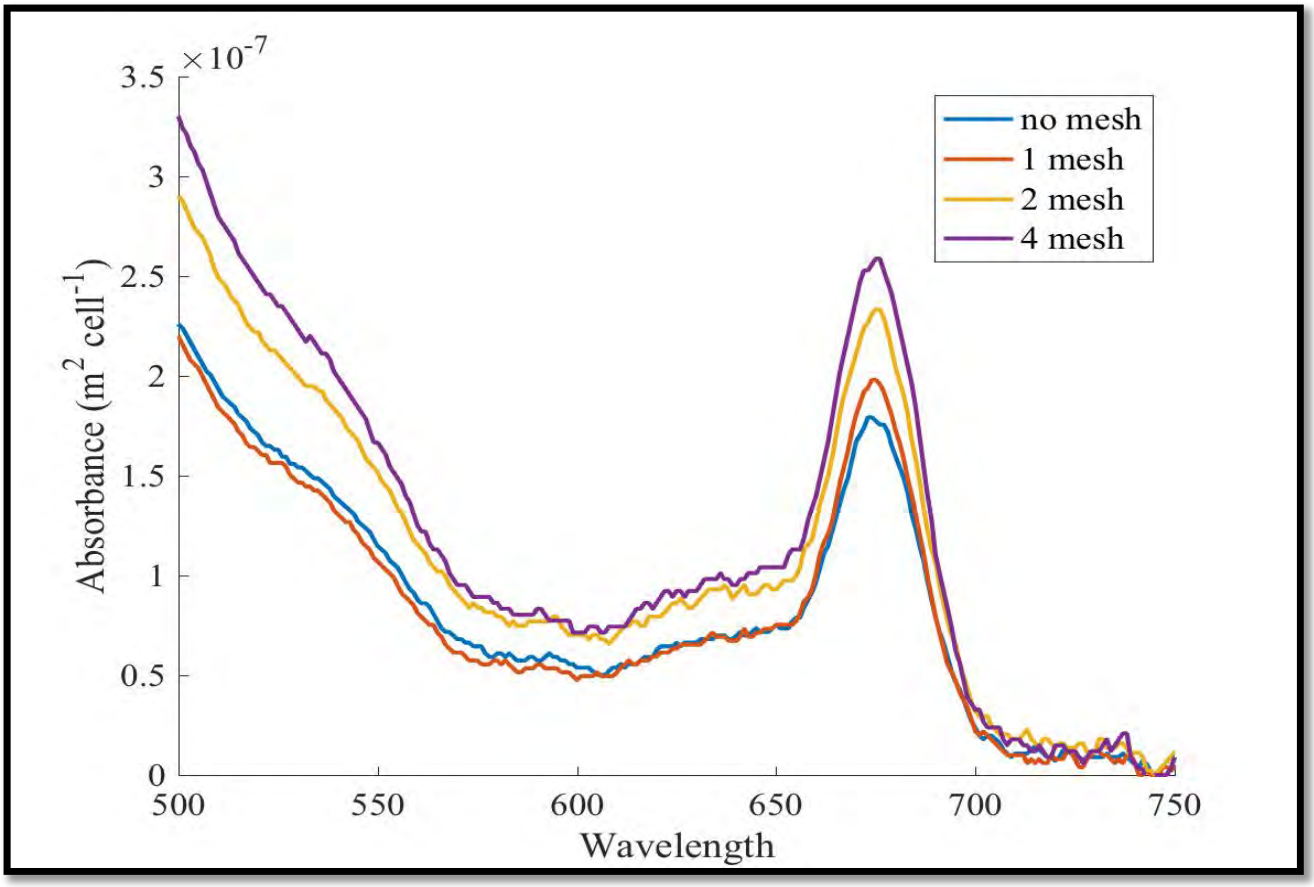

Figure 2. Absorbance spectrum of *Heterocapsa rotundata* under different light levels

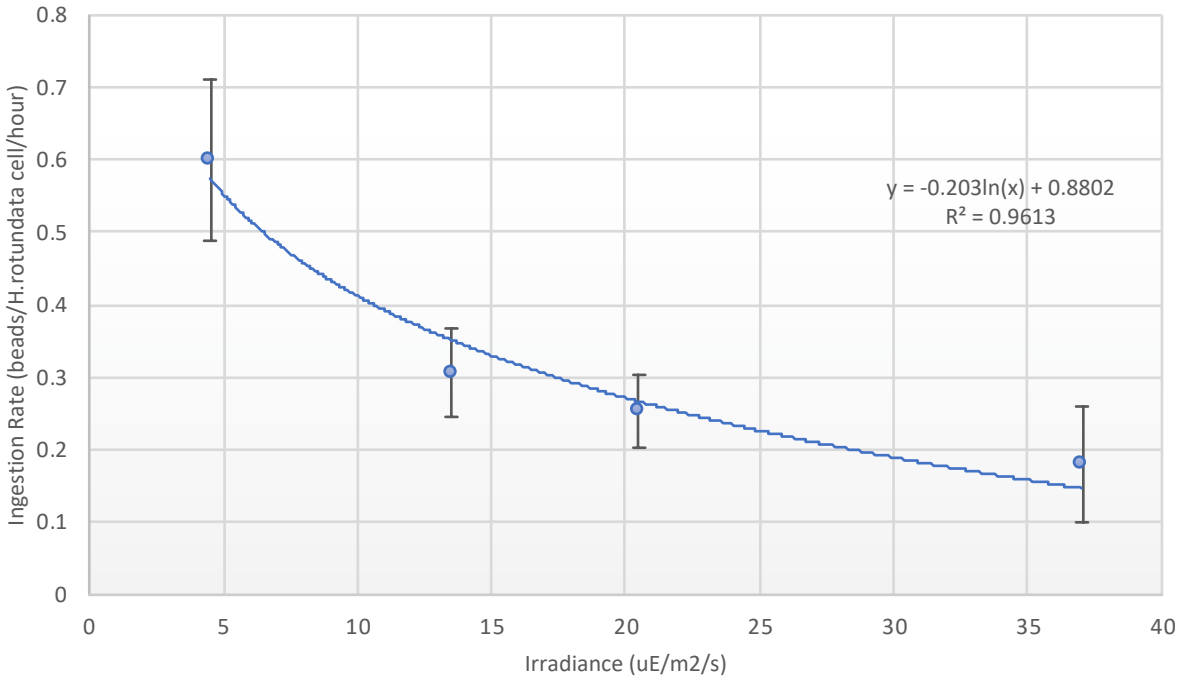

Figure 3. Bead ingestion rates of *Heterocapsa rotundata* at different light levels.

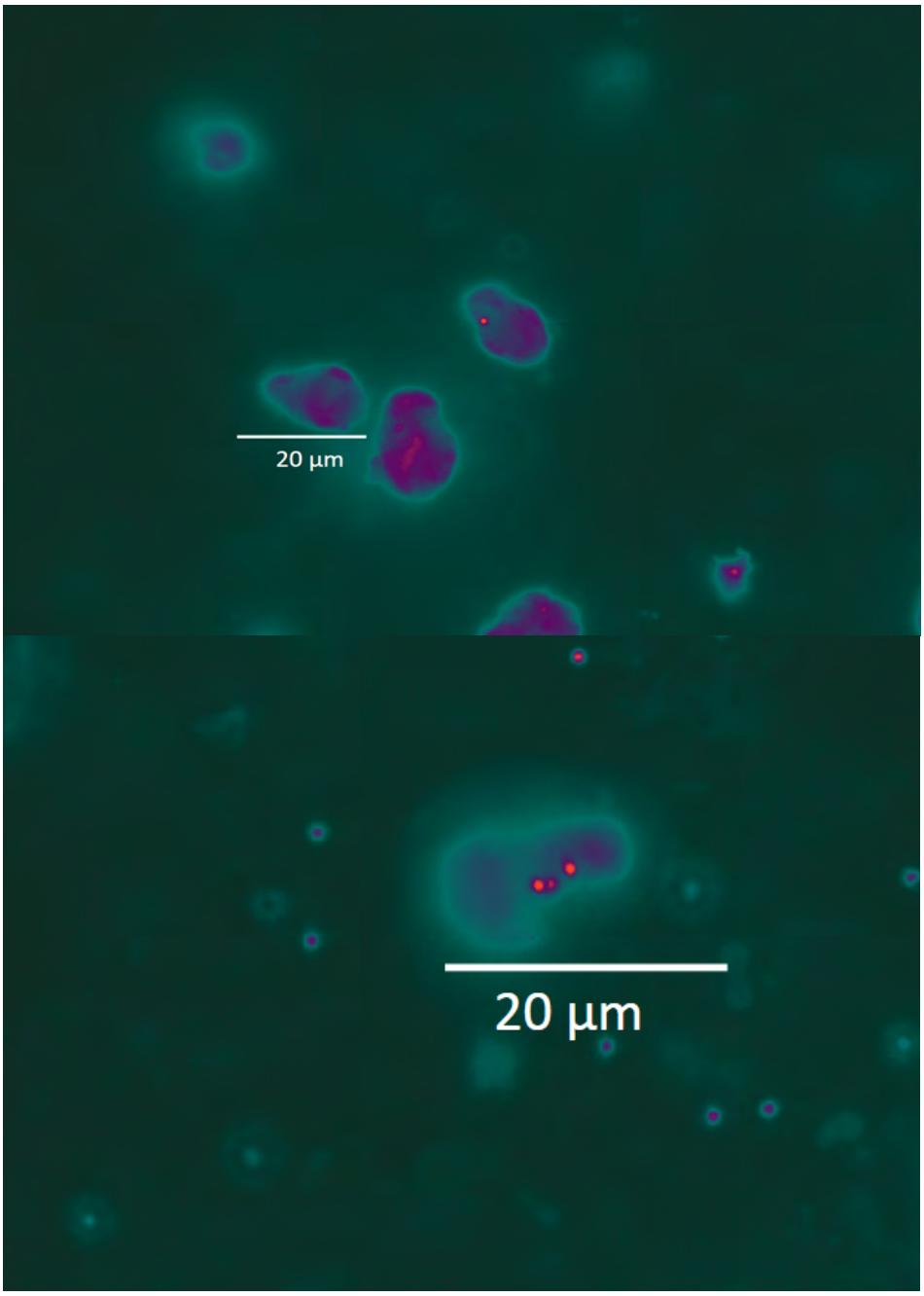

Figure 4. Pictures of ingested beads within *Heterocapsa rotundata* at 100x magnification with immersion oil. Pictures were taken using DAPI fluorescent filter.

Examining the Effects of 3-D Reef Structures on the Mixing and Reaeration of Hypoxic Waters

Ella A. Kaplan, REU Fellow
Maryland Sea Grant

Larry Sanford, Professor
Horn Point Laboratory, University of Maryland Center for Environmental Science

Abstract

The Chesapeake Bay and its tidal tributaries experience significant bottom water hypoxia during the summer months. This study investigates the effects of a field of concrete reef balls in the Severn river, a tidal tributary of the Chesapeake Bay, on the overlying water column, and whether these effects have any significant impact on disruption of the summer pycnocline and reaeration of hypoxic bottom waters. Current velocities, turbulence, and several indicators of water quality were measured at the study site using an Acoustic Doppler Current Profiler and a Yellow Springs Instrument (YSI) Exo1 probe. These instruments were deployed for a 16-day period before reef balls were placed at the site. Following placement of the reef balls the instruments were deployed at the site for another 16 days. Comparison of these two data sets revealed a 5.62% decrease in time averaged velocity and a 28.26% increase in turbulence intensity following the placement of the reef balls. However, wind influence was detected to a depth of six meters. Considering only the portion of the water column not influenced by wind, there was a 7.49% decrease in time averaged velocity and 2.63% increase in turbulence intensity. Although, the increase in turbulence intensity in the lower water column was minimal, and dissolved oxygen concentrations at depth were not improved, the results have enough significance to conclude that further investigation is warranted.

Introduction

Hypoxic waters are areas where dissolved oxygen concentrations are below those required by most aquatic organisms. If this hypoxia persists, organisms must either leave or suffocate; these areas become dead zones (NCCOS). Dead zones are formed by a combination of physical factors such as stratification, wind, temperature, and biological factors such as excess nutrients (Murphy et al. 2011). While dead zones may occur naturally, they may also be created or exacerbated by anthropogenic contributions. The main anthropogenic cause of dead zones is nutrient pollution, often from agricultural fertilizers containing nitrate and phosphate. This nutrient surplus results in eutrophication. During this process phytoplankton growth is stimulated

by the excess nutrients causing algal blooms. These large phytoplankton populations eventually die and are decomposed via aerobic processes, causing substantial depletion of dissolved oxygen. Eutrophication has become a major issue in the world's waterways, leading to widespread dead zones where hypoxia and anoxia leave many areas unable to sustain endemic populations (USGS 2016).

Estuaries and coastal areas are highly influenced by their contributing watershed, leaving them particularly susceptible to excessive runoff and nutrient pollution (Breitburg et al. 2018). The Chesapeake Bay and its tributaries experience significant hypoxia, due to agricultural and industrial development along its shores. These hypoxic areas are observed almost exclusively below the pycnocline (Cerco and Cole 1993). Sub pycnocline hypoxia, or bottom water hypoxia, is typically the worst in the summer due to decreased mixing and decreased aeration associated with the increased stratification of the water column, both of which are important processes for the diffusion of oxygen. Additionally, dissolved oxygen is less soluble in warmer water, further exacerbating hypoxic episodes (Sanford et al. 1990). In addition to nutrient pollution, climate change is predicted to further contribute to formation of dead zones as sea level rise can lead to increased stratification, increased water temperatures, and decreased oxygen solubility (Irby et. al 2018).

Hypoxia has many adverse effects on estuarine ecosystems including loss of benthic habitat, disruption of food webs, and species loss (Muller et. al 2016). Areas that were previously thermal refugees for fish during the summer are now barren during the summer due to seasonal hypoxia. The coupling of high surface temperatures and hypoxic bottom waters, known as a habitat squeeze, can reduce growth, fecundity, and survival for aquatic organisms (Costantini et. al 2008).

Oyster reefs were historically a major feature of the Chesapeake Bay, but years of over harvesting, pollution and habitat loss have led to a severe decline in oyster population. It is estimated that current oyster populations are less than 1% of what they once were (NOAA). Oysters have been recognized for both their economic and ecologic value, as they support a multimillion dollar fishing industry and efficiently filter large volumes of water (Lenihan 1999). This has made them a target species for restoration. Many restoration projects have already been completed using artificial reef structures to replace habitat that had been destroyed through dredging and other anthropogenic practices. However, restoration has not yet been attempted as a means to remediate other aspects of impaired waters, such as hypoxia.

The goal of this study was to determine the effect that a field of reef balls had on mixing in the overlying water column and to establish whether this effect was sufficient to improve dissolved oxygen concentrations at depth. It was hypothesized that the bottom roughness created by the three-dimensional reef modules would decrease current velocity immediately over the reef and increase turbulence. Additionally, it was hypothesized that the increase in turbulent mixing would be sufficient to disrupt the summer pycnocline by increasing vertical mixing, thus improving dissolved oxygen concentrations at depth.

Materials and Methods

Site Description

The study site is an area known as the Winchester Lump located in the Severn river, a tidal tributary of Chesapeake Bay (Figure 1). The Severn river is in the central portion of Anne Arundel County and has a watershed drainage area of approximately 179 km^2 (Anne Arundel County Department of Public Works). The site contains 240 reef balls set with oyster spat placed by the Chesapeake Bay Foundation (CBF) on 4/25/18. The field has an area of approximately 2090 m^2 and is centered at (39°0.809 N,-76°30.864 W). This site is known to become hypoxic during the summer months.

Acoustic Doppler Current Profiler

An Acoustic Doppler Current Profiler (ADCP) was deployed at the study site from 4/9/18 to 4/25/18, covering a full spring-neap tidal cycle. Data from this deployment were analyzed to determine current velocity and turbulence to establish a baseline prior to the placement of the reef balls. Reef balls were placed at the site on 4/25/18 as shown in Figure 2. The ADCP was redeployed at the site from 6/27/18 to 7/12/18. The data from the second deployment were analyzed to determine current velocity and turbulence following the deployment of the reef balls. These two data sets were compared to determine whether the reef balls had a significant impact on turbulence and current velocity at the site.

Velocity Analyses

The ADCP measured velocities along each of the four beams at two seconds intervals. Using the transformation outlined in Gilcoto et al. 2008, beam velocities were translated into East, North and Up (ENU) velocities. From these velocities the angle and velocities along the major and minor axis of flow were calculated. Additionally, corrections for pitch and roll were performed following Woodgate and Holroyd 2011.

Turbulence Analyses

A Reynolds Decomposition was used to calculate the velocity fluctuations, $u'(t)$, i.e the difference between the velocity as a function of time, $u(t)$ and the time averaged velocity, $\overline{U}$.

$$u'(t) = u(t) - \overline{U} \tag{1}$$

$$\overline{U} = \sqrt{\overline{U_u}^2 + \overline{U_v}^2 + \overline{U_w}^2} \tag{2}$$

The time averaged velocity was defined as the 15-minute average velocity and the instantaneous velocity was defined as the 2 second velocity.
Next the root mean squared of the velocity fluctuations,u_{RMS}, was calculated.

$$u_{RMS} = \sqrt{\frac{\overline{u_{u'(t)^2}} + \overline{u_{v'(t)^2}} + \overline{u_{w'(t)^2}}}{3}} \tag{3}$$

The turbulence intensity was then calculated as the quotient of the root mean squared and the time averaged velocity.

$$Turbulence\ Intensity = \frac{u_{RMS}}{\overline{U}} \quad (4)$$

Tidal Cycle

In addition to analysis of velocity and turbulence data over the whole of each deployment, data were also sectioned into individual tidal cycles. Each tidal cycle was assumed to correspond to the 12.41-hour semidiurnal tide, with each cycle beginning at high tide and continuing to the next high tide. This allowed for comparison of velocity and turbulence parameters averaged over all tidal cycles that occurred during the deployment. Additionally, this allowed for tides with heavy wind or precipitation influence, such as flood events, to be filtered out. Finally, the influences of wind and wind-waves were quite apparent during much of the record. A reasonable estimate of the maximum depth of wave influence was calculated as 6 m, and only depths greater than this were also compared as consistently under the influence of bottom processes.

YSI and Water Quality

A Yellow Springs Instrument (YSI) EXO1 probe was deployed in tandem with the ADCP to measure dissolved oxygen concentrations at the site prior to the installation of the reef balls. It was redeployed with the ADCP to obtain a second set of measurements. These two data sets were compared to determine whether there was an increase in dissolved oxygen relative to the surrounding waters.

Additionally, water quality data collected by J.P Williams, and archived by CBF allowed for investigations of changing water quality depth profiles over the site. The data were collected using a YSI probe measuring temperature, salinity, dissolved oxygen concentration, and dissolved oxygen saturation. Using this data, a robust sequence of profiles of the water column from March to early August was constructed through interpolation.

Data Analysis

Data analysis was completed using MATLAB. Data from the ADCP was imported using MATLAB scripts created by Dr. Rich Pawlowicz of the Ocean Dynamics Laboratory at the University of British Columbia.

Results

Tidal Heights

The average tidal heights occurring over a tidal cycle for each deployment are depicted in Figure 3. Rain and wind were prominent over both deployments, so tidal averages were recalculated excluding tidal cycles with unusually large standard deviations. The average tidal

heights occurring over a tidal cycle for each deployment, excluding extreme events, are depicted in Figure 4. Even with the extremes removed, the average tidal height was greater during the first deployment. This is likely due to a slight difference in the deployment locations and water depths.

Velocity

The ENU velocities for both deployments are shown in Figures 5 through 7. Although there are clear differences between the east and north velocities between the two deployments, the difference is more meaningful when the east and north velocities are shifted to the major and minor axis of flow. Derivation of the major axis of flow is shown in Figure 8. The angles of the major axis of flow were 334.6° and 331.8° for the first and second deployments respectively. Figures 9 and 10 show the relationship between flood and ebb tide and depth averaged current velocity along the major and minor axis, though upon visual inspection there is no consistent difference between the first and second deployment.

The time average velocity averaged over the water column and deployment period was 0.0908 m/s for the first deployment and 0.0857 m/s for the second deployment (Figure 11), corresponding to a 5.62% decrease in velocity following the placement of the reef balls. For near-bottom depths at which wind and wave influence is essentially zero, the time averaged velocity was 0.0921 m/s and 0.0852 m/s for the first and second deployments respectively (Figure 12). This corresponds to a 7.49% decrease in time averaged velocity following the placement of the reef balls. When considering averages over the tidal cycle excluding extremes (Figure 13), the time average velocity averaged over the entire water column was 0.0880 m/s for the first deployment and 0.0832 m/s for the second deployment, corresponding to a 5.45% decrease in velocity following the placement of the reef balls. Using this same method of excluding tidal extremes for the lower water column (Figure 14), the time average velocity averaged over the whole water column was 0.0926 m/s for the first deployment and 0.0846 m/s for the second deployment, corresponding to an 8.46% decrease in velocity following the placement of the reef balls.

Turbulence

The turbulence intensity over the whole of each deployment is shown in Figure 15. The average turbulence intensity over the entire water column and time period was 26.75% and 34.31% for the first and second deployments respectively. This corresponds to a 28.26% increase in turbulence intensity over the whole water column following the placement of the reef balls. However, for depths for which wind and wave influence is essentially zero (Figure 16), the turbulence intensity was 24.35% and 24.99% for the first and second deployments respectively. This corresponds to an increase in turbulence intensity of only 2.63%. When considering averages over the tidal cycle excluding extremes (Figure 17), the turbulence intensity was 27.50% and 34.81% for the first and second deployments respectively. This corresponds to a 28.58% increase in turbulence intensity over the whole water column following the placement of the reef balls. At depths for which wind and wave influence is essentially zero (Figure 18), the

turbulence intensity was 24.79% and 25.76% for the first and second deployments respectively. This corresponds to an increase in turbulence intensity of 3.91%.

Water Quality

Interpolated water quality data for the whole water column is shown in Figure 19. Data from the YSI deployed in tandem with the ADCP is shown in Figure 20. Dissolved oxygen concentrations at the site were high for the duration of the first deployment, remaining at or above saturation throughout the water column for nearly the entire 16-day deployment period (Figure 19 and 20). Dissolved oxygen concentrations at the site were extremely poor during much of the second deployment, with the bottom water remaining anoxic for approximately 44% of the 16-day deployment period (Figure 19 and 20).

Discussion

Influence of Physical Processes

The turbulence intensity values observed in the top portion of the water column are unreasonable for a natural environment. Based on the observed wind speeds at the site during both deployments (Figure 21 and 22) it is reasonable to conclude that these values were inflated by surface wind waves. This is the justification for conducting further analysis focusing on the lowest depths. Additionally, in an attempt to reduce the influence of precipitation and wind velocity on turbulence calculations, tidal average calculations were performed once for all data and a second time, excluding tidal extremes, i.e. tidal cycles for which the standard deviation of water levels over the 12.41-hour cycle was high.

Focus on Lower Water Column

Though there is value in examining velocity and turbulence throughout the whole water column, despite possible wind wave influence, for the purpose of this particular study it is more pertinent to focus on the near bottom results as this is where the change was expected to occur. Additionally, calculations of velocities and therefore turbulence, using data from the ADCP, are based on the assumption that all four beams are measuring the same water mass. As the distance up the water column increases, and the distance between the beams increases, this assumption may break down, especially in physically dynamic environments such as a tidal tributary. This is further justification for focusing on the lower portion of the water column.

Changes in Turbulence Intensity and Time Averaged Velocity

There was a measured increase in turbulence intensity and decrease in time averaged velocity at the site which supports the first hypothesis. However, considering only the bottom portion of the water column, where wind wave influence is not inflating values, this increase is small at only 2.6% over all tides or 3.91% excluding tidal extremes. This small but consistent increase in turbulence intensity is likely due to the influence of the reef balls. The decrease in time

averaged velocity is more significant with a decrease of 7.49% over all tides and 8.64% excluding tidal extremes.

Conclusions

This study aimed to investigate the effects of a field of concrete reef balls in the Severn river, a tidal tributary of the Chesapeake Bay, on the overlying water column, and whether these effects have any significant impact on disruption of the summer pycnocline and reaeration of hypoxic bottom waters. Physical processes dominated the site conditions in the upper portion of the water column and analysis of the data even before the placement of the reef balls revealed that the Winchester lump was a much more dynamic environment than originally anticipated.

Considering only the portion of the water column not influenced by wind, over all tidal cycles, there was a 7.49% decrease in time averaged velocity and 2.63% increase in turbulence intensity. Again, considering the same portion of the water column but excluding tidal extremes, there was an 8.64% decrease in time averaged velocity, and a 3.91% increase in turbulence intensity. These results support the primary hypothesis that the reef balls would increase turbulence and decrease current velocity. However, large variability in water quality due to other, non-local factors dominated water quality at this site. The secondary hypothesis that the increase in turbulence intensity would improve dissolved oxygen concentrations at depth was rejected in favor of the null hypothesis as the site was anoxic for approximately 44% of the second deployment. Although, the increase in turbulence intensity in the lower water column was minimal, and dissolved oxygen concentrations at depth were not improved, the results have enough significance to conclude that further investigation is warranted.

Acknowledgements

I would like to thank the Maryland Sea Grant and the University of Maryland Center for Environmental Science Horn Point Laboratory for the opportunity to conduct this research. Additionally, I would like to thank Dr. Sanford for his ongoing guidance and mentorship. This research was funded by NSF grant OCE-1756244. All reef balls at the site were funded through the Chesapeake Bay Foundation(CBF). Additional thanks are due to Dr. Allison Colden and her colleagues at CBF for inviting us to be part of their study and for allowing us to use their research vessel to deploy probes at the site.

References

Anne Arundel County Department of Public Works. Severn River Watershed. *In* Watershed Protection and Restoration Program [ed.].

Breitburg, D. and others 2018. Declining oxygen in the global ocean and coastal waters. Science 359: 46-+.

Cerco, C. F., and T. Cole. 1993. 3-DIMENSIONAL EUTROPHICATION MODEL OF CHESAPEAKE BAY. Journal of Environmental Engineering-Asce 119: 1006-1025.

Chesapeake Bay Office,Oyster Reefs. *In* National Oceanic and Atmospheric Administration [ed.].

Costantini, M., S. A. Ludsin, D. M. Mason, X. S. Zhang, W. C. Boicourt, and S. B. Brandt. 2008. Effect of hypoxia on habitat quality of striped bass (Morone saxatilis) in Chesapeake Bay. Canadian Journal of Fisheries and Aquatic Sciences 65: 989-1002.

Gilcoto, M., E. Jones, and L. Farina-Busto. 2009. Robust Estimations of Current Velocities with Four-Beam Broadband ADCPs. Journal of Atmospheric and Oceanic Technology 26: 2642-2654.

Irby, I. D., M. A. M. Friedrichs, F. Da, and K. E. Hinson. 2018. The competing impacts of climate change and nutrient reductions on dissolved oxygen in Chesapeake Bay. Biogeosciences 15: 2649-2668.

Lenihan, H. S. 1999. Physical-biological coupling on oyster reefs: how habitat form influences function. Ecological Monographs 69: 251-275.

Muller, A. C., D. L. Muller, and A. Muller. 2016. Resolving spatiotemporal characteristics of the seasonal hypoxia cycle in shallow estuarine environments of the Severn River and South River, MD, Chesapeake Bay, USA. Heliyon 2: 26.

Murphy, R. R., W. M. Kemp, and W. P. Ball. 2011. Long-Term Trends in Chesapeake Bay Seasonal Hypoxia, Stratification, and Nutrient Loading. Estuaries and Coasts 34: 1293-1309.

National Centers for Coastal Ocean Science 2017. Hypoxia Research Program. National Oceanic and Atmospheric Administration.

Sanford, L. P., K. G. Sellner, and D. L. Breitburg. 1990. Covariability of Dissolved Oxygen with Physical Processes in the Summertime Chesapeake Bay. Journal of Marine Research 48: 567-590.

Woods Hole Coastal and Marine Science Center. 2016. Eutrophication. Estuarine Processes, Hazards, and Ecosystems. U.S Geological Survey.

Woodgate, R. A., and A. E. Holroyd. 2011. Correction of Teledyne Acoustic Doppler Current Profiler(ADCP) Bottom-Track Range Measurements for Instrument Pitch and Roll.

Figures

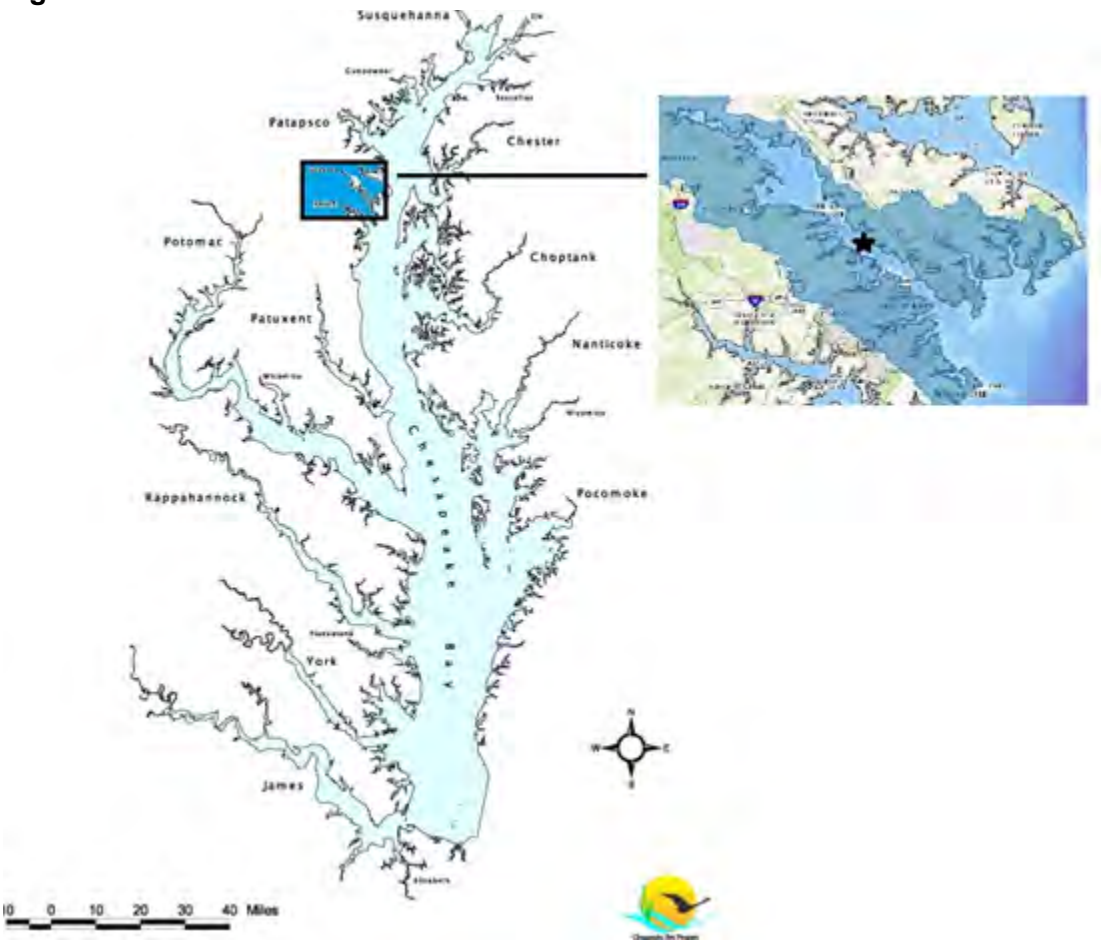

Figure 1. Map showing location Severn river within the Chesapeake Bay and of the study site within the Severn (marked with a black star). Image Credit (Chesapeake Bay Map): Chesapeake Bay Program. Image Credit (Severn River Watershed): Anne Arundel County Department of Public Works.

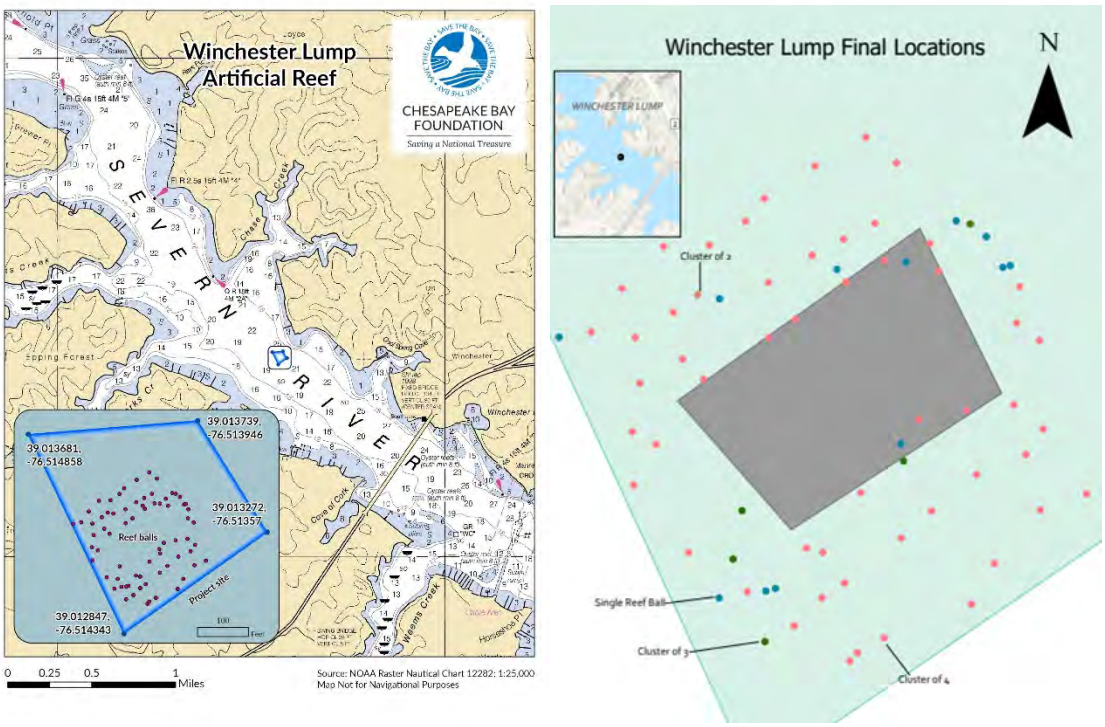

Figure 2. The image on the left shows the field within the Severn River (outlined with a blue rectangle). The image on the right shows the specific deployment locations of the reef balls. Different colors represent different cluster sizes. Image Credit: Chesapeake Bay Foundation

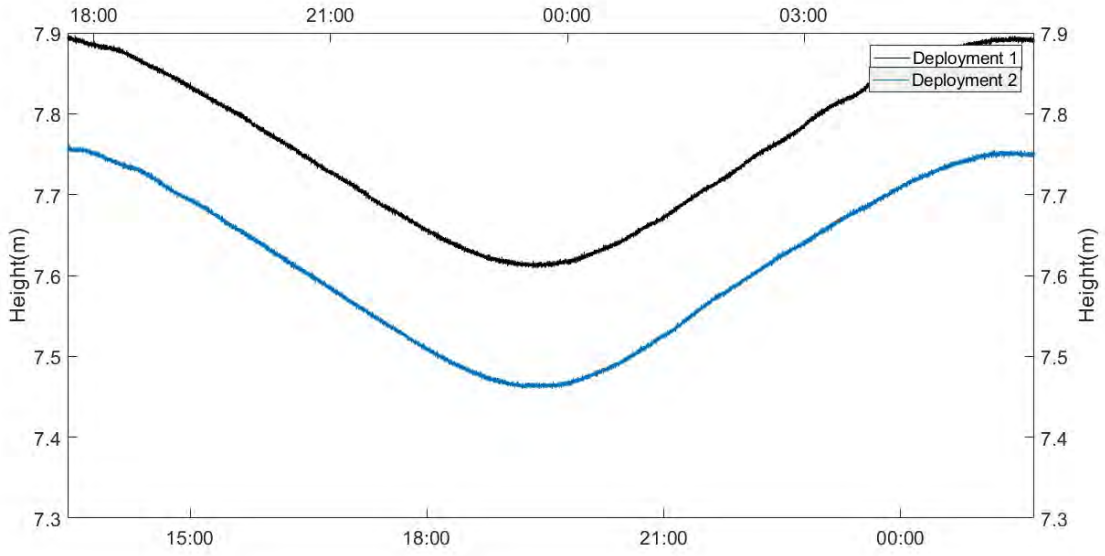

Figure 3. Tidal heights representing the average tidal heights over the entire deployment period for both deployments.

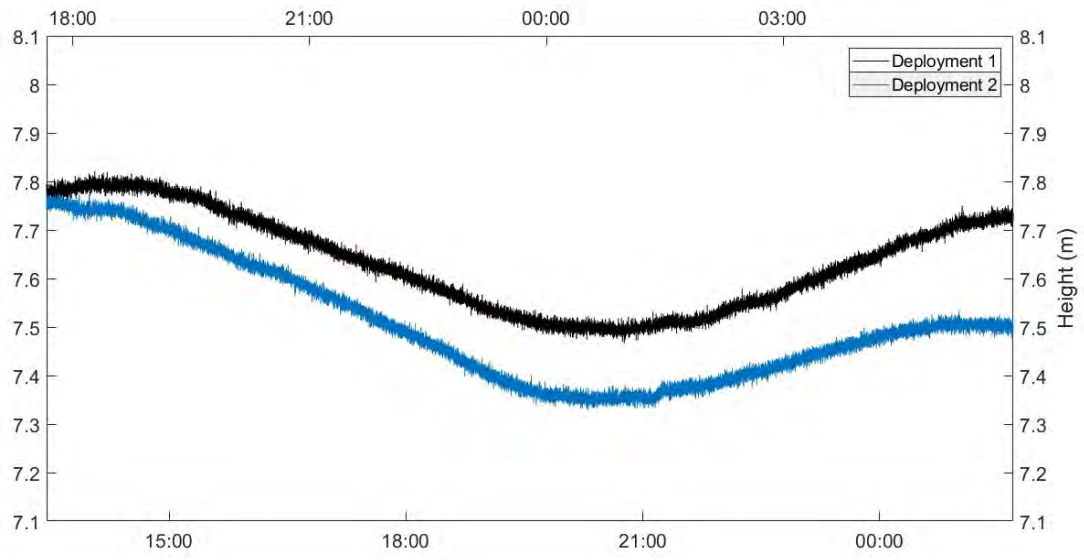

Figure 4. Tidal heights representing the average tidal heights over the entire deployment period excluding extreme tides, for both deployments.

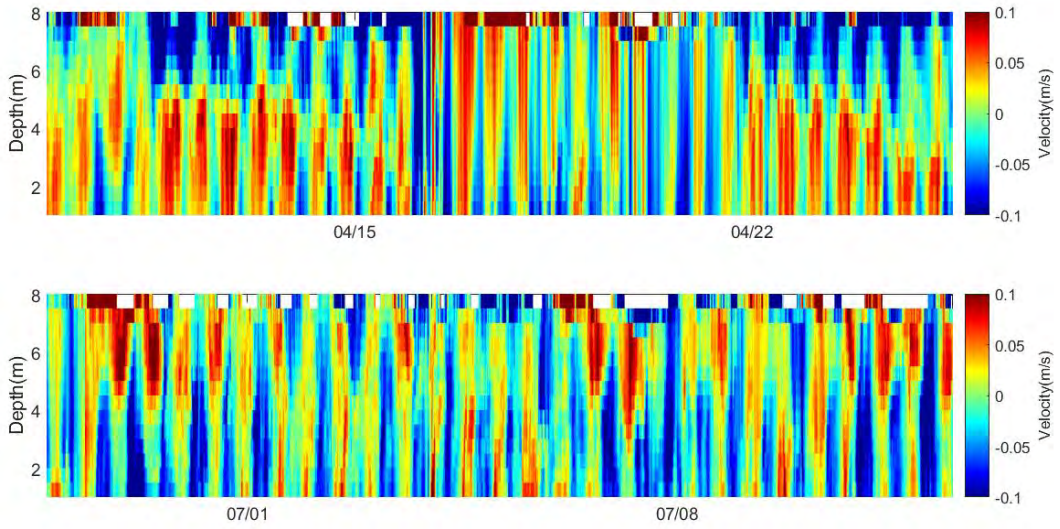

Figure 5. East velocities over entire deployment period for first (top) and second (bottom) deployments.

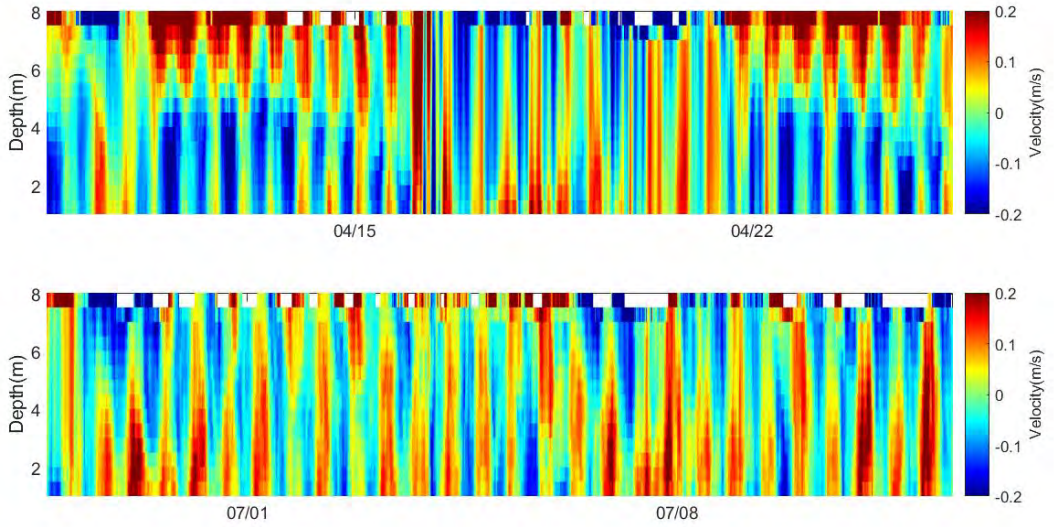

Figure 6. North velocities over entire deployment period for first (top) and second (bottom) deployments.

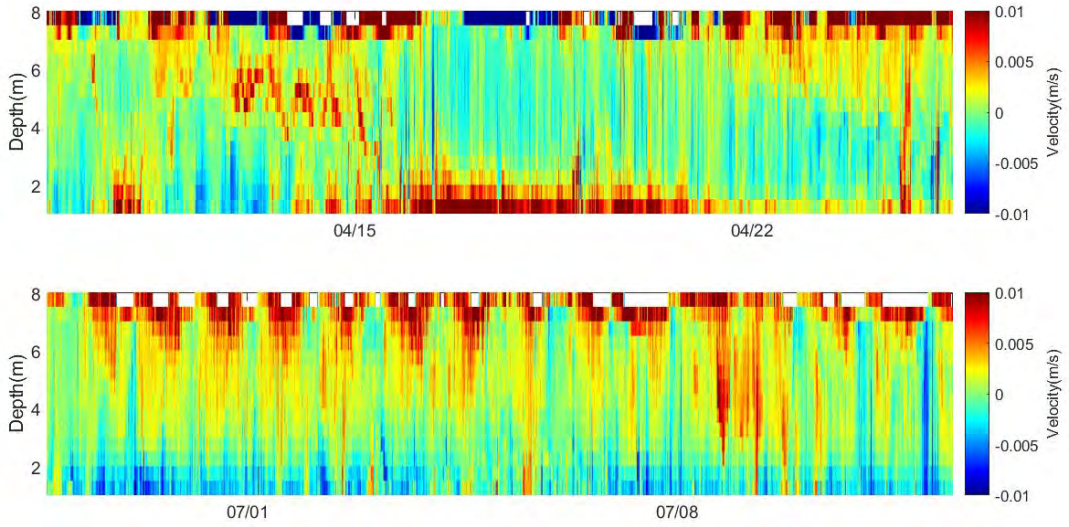

Figure 7. Vertical velocities over entire deployment period for first (top) and second (bottom) deployments.

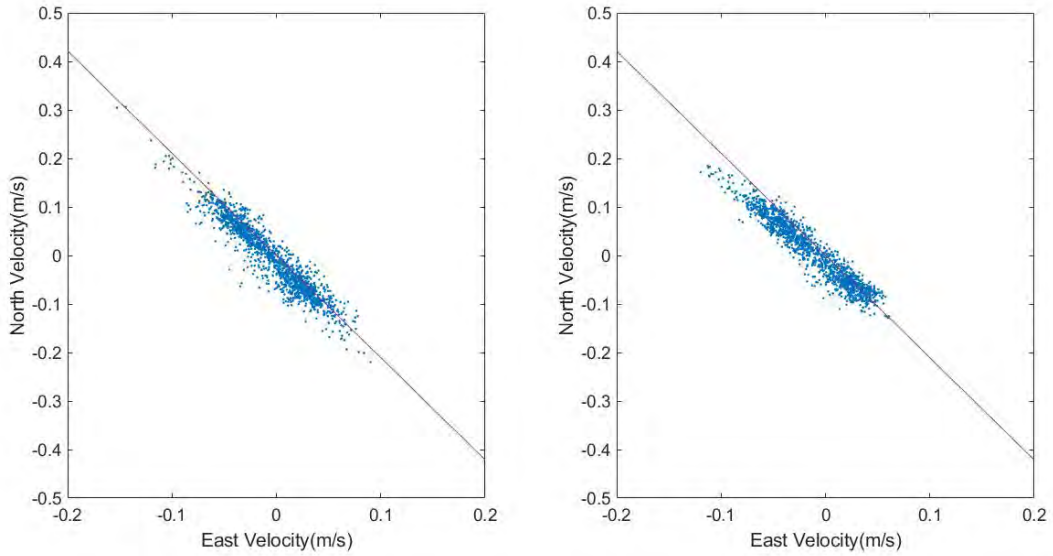

Figure 8. Angle of major axis of flow represented by solid line. First deployment shown on right and second deployment shown on left.

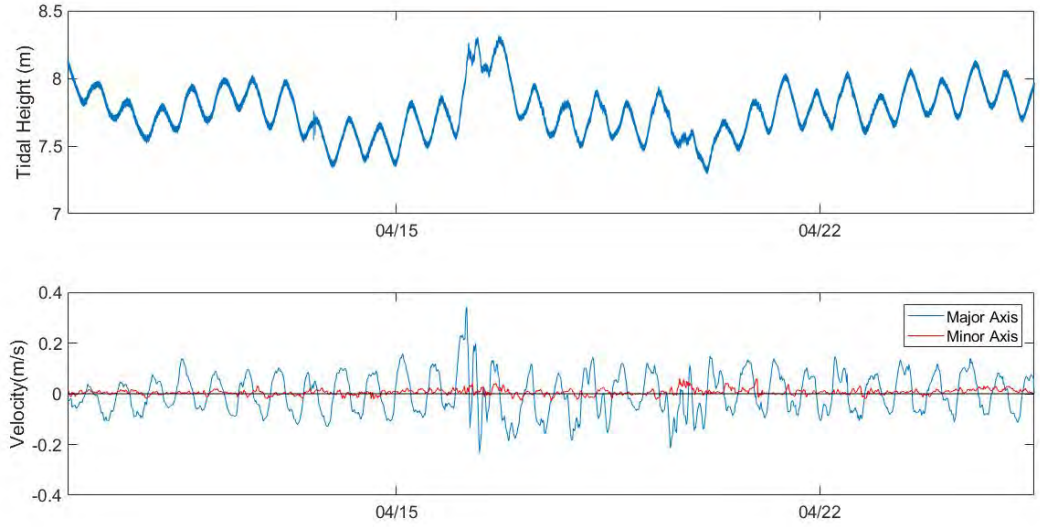

Figure 9. Relationship between tidal height and velocities along axis of flow for first deployment.

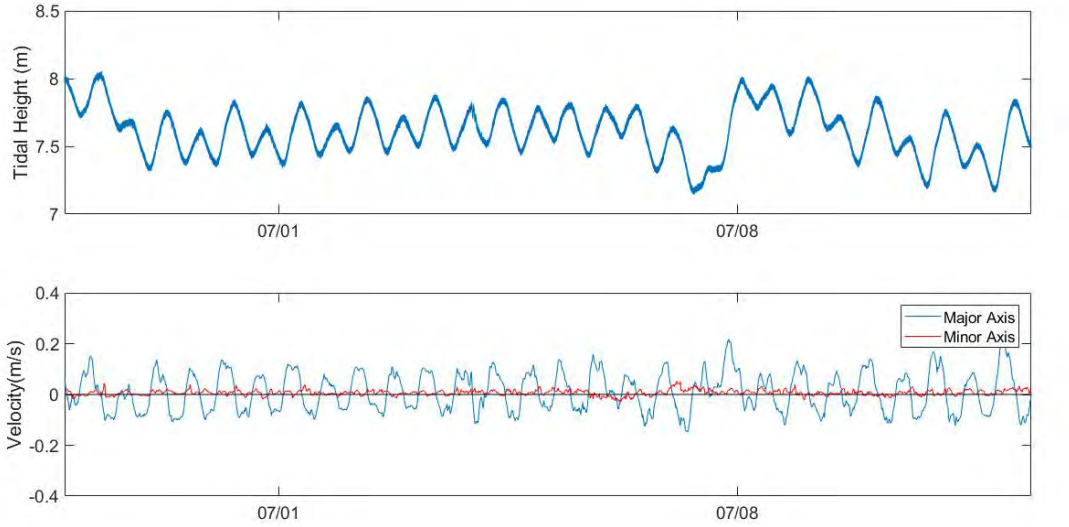

Figure 10. Relationship between tidal height and velocities along axis of flow for first deployment.

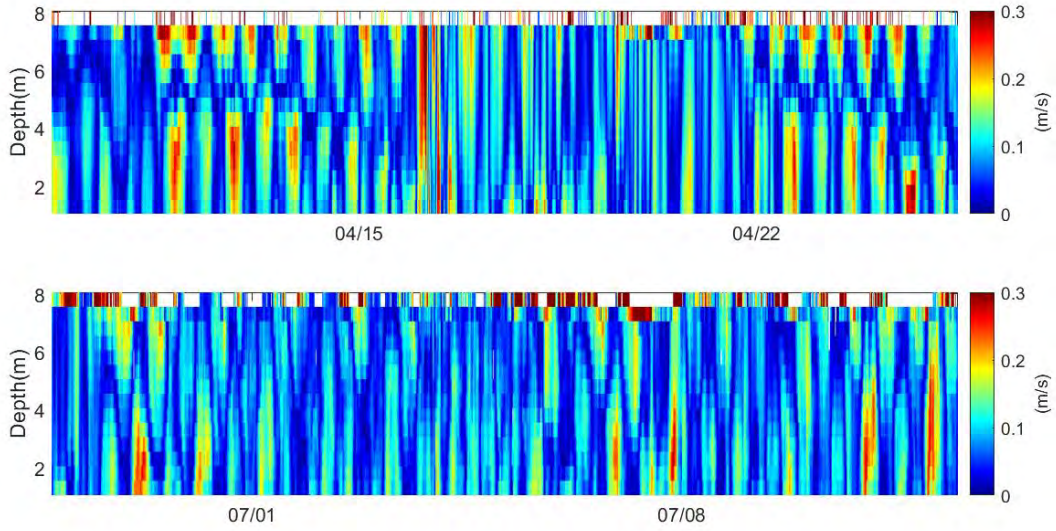

Figure 11. Continuous record of time averaged velocities over the entire water column for first (top) and second (bottom) deployments.

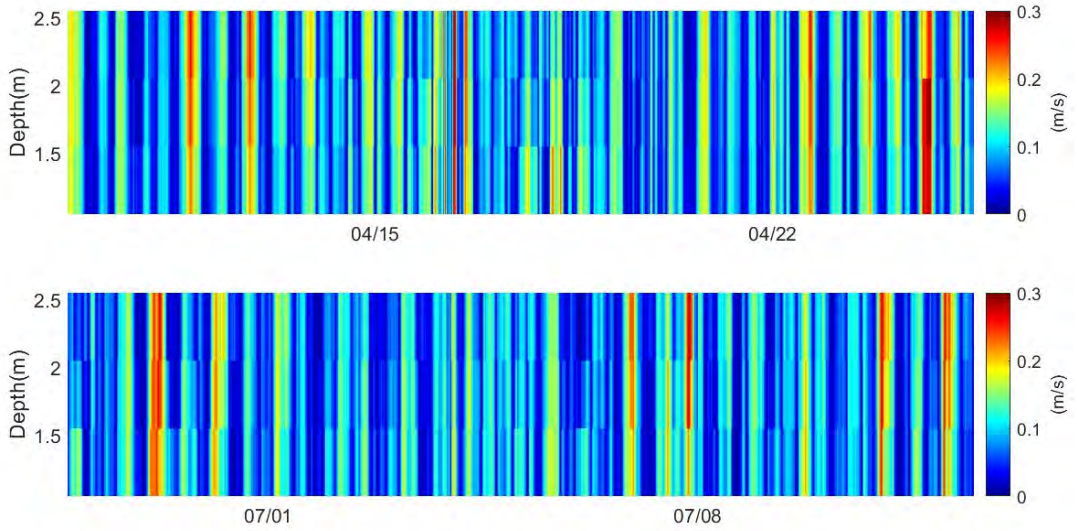

Figure 12. Continuous record of time averaged velocities over the lower water column for first (top) and second (bottom) deployments.

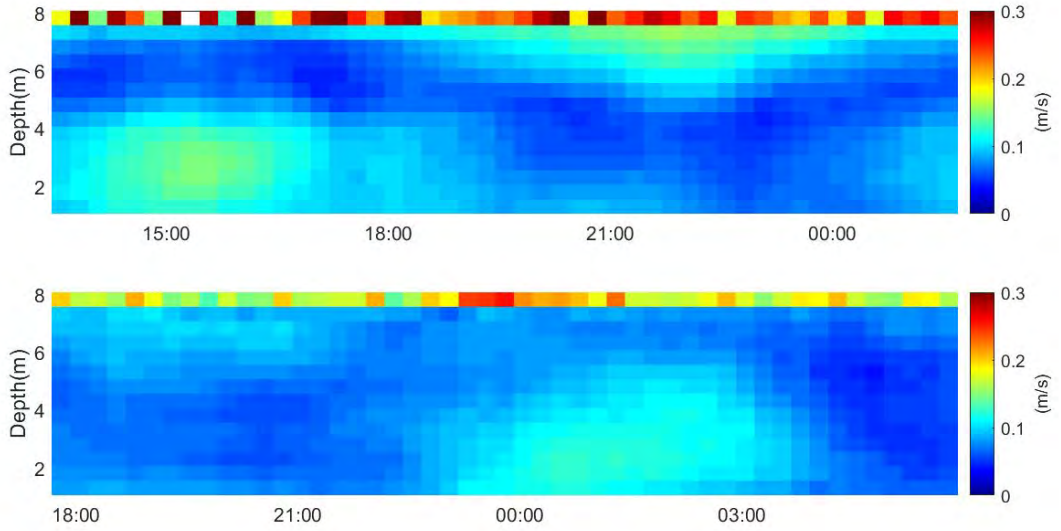

Figure 13. Time averaged velocities for entire water column over tidal cycle excluding tidal extremes for first (top) and second (bottom) deployments.

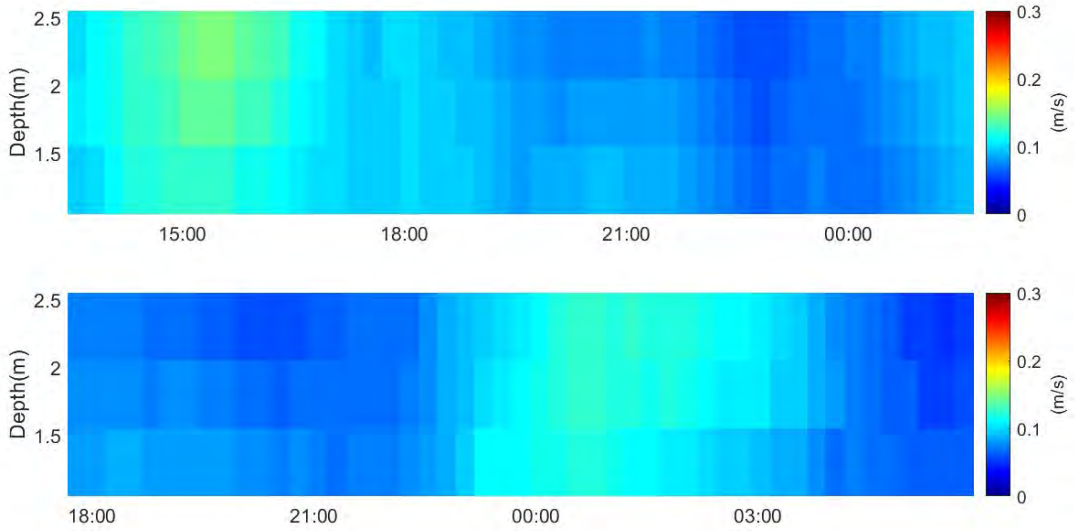

Figure 14. Time averaged velocities for lower water column over tidal cycle excluding tidal extremes for first (top) and second (bottom) deployments.

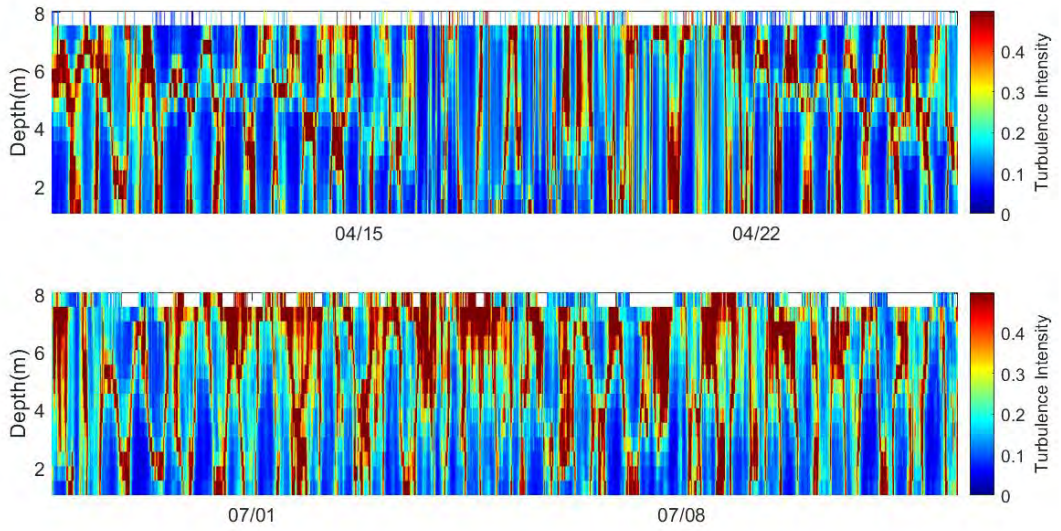

Figure 15. Continuous record of turbulence intensity over entire water column for first (top) and second (bottom) deployments.

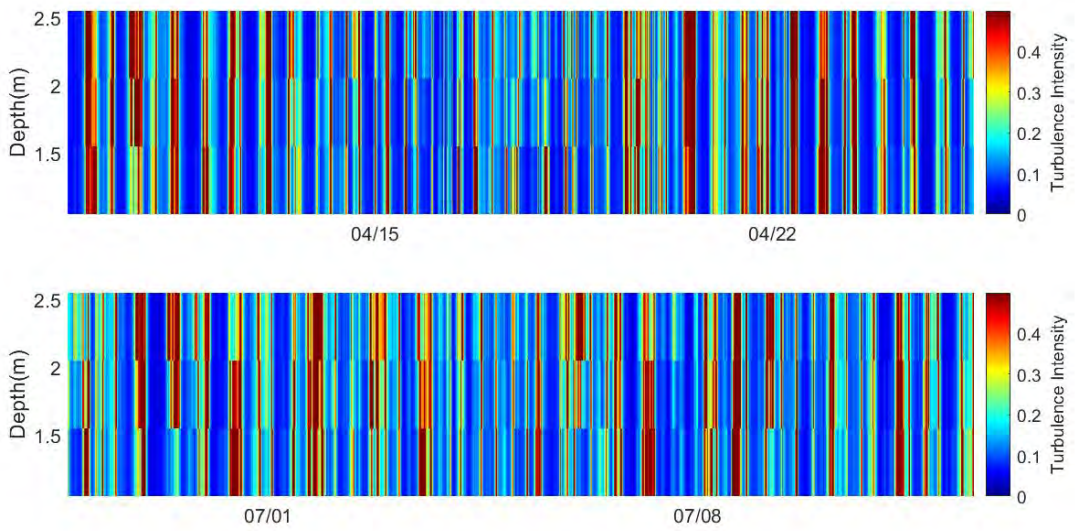

Figure 16. Continuous record of turbulence intensity over lower water column for first (top) and second (bottom) deployments.

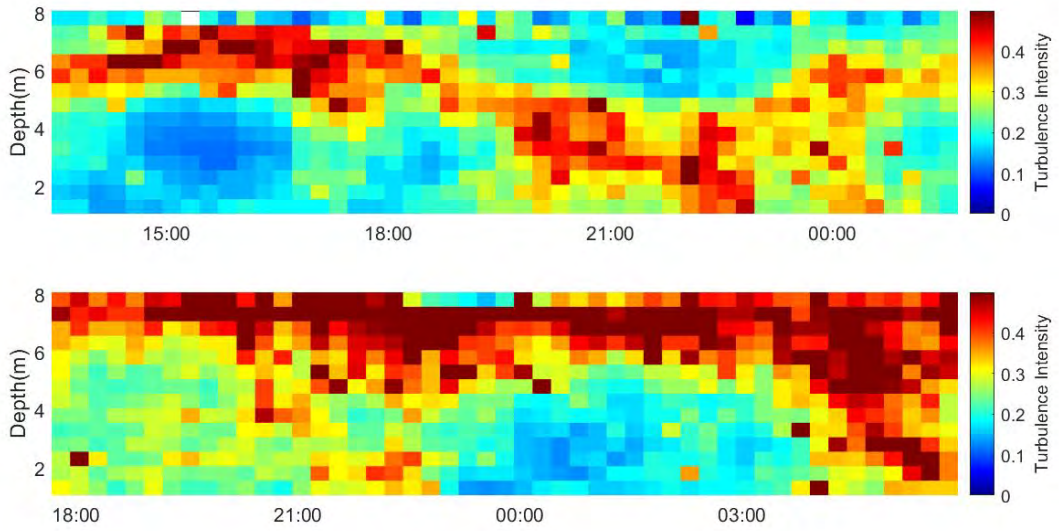

Figure 17. Turbulence Intensity over tidal cycles, excluding extreme tides over entire water column for first (top) and second (bottom) deployments.

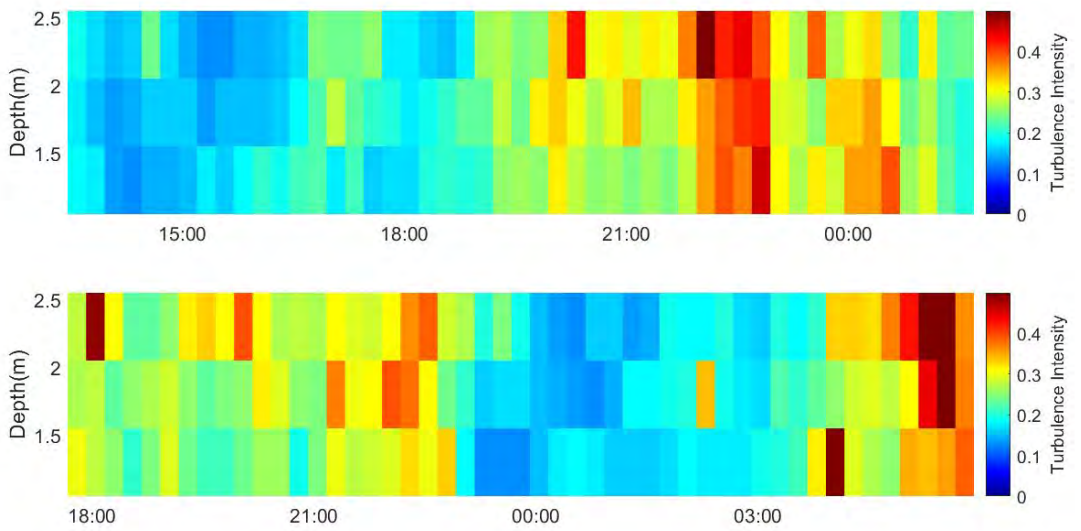

Figure 18. Turbulence Intensity over tidal cycles, excluding extreme tides over lower water column for first (top) and second (bottom) deployments.

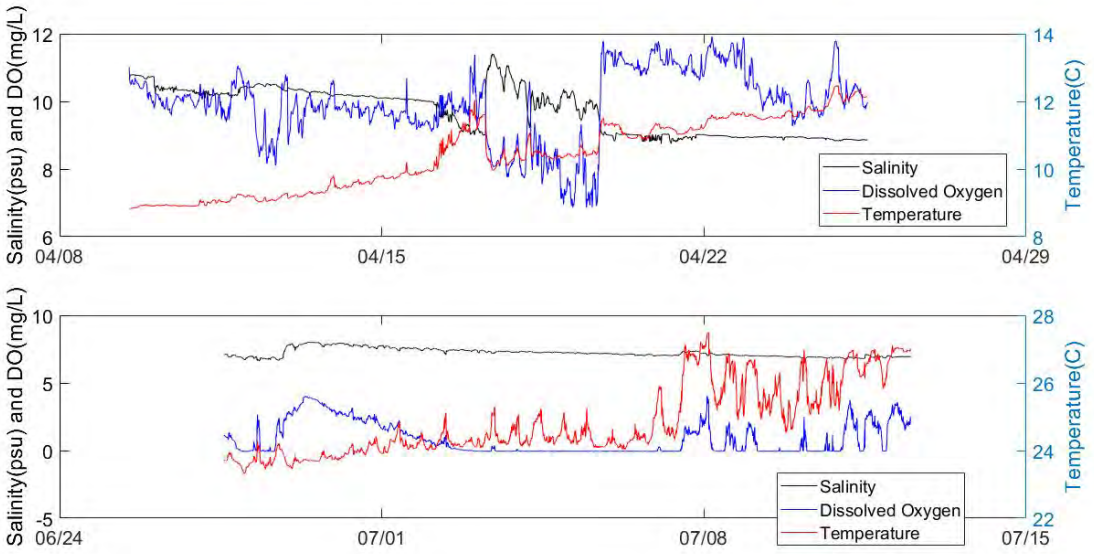

Figure 19. Data from YSI EXO1 probe deployed at study site in tandem with ADCP for first (top) and second deployment (bottom).

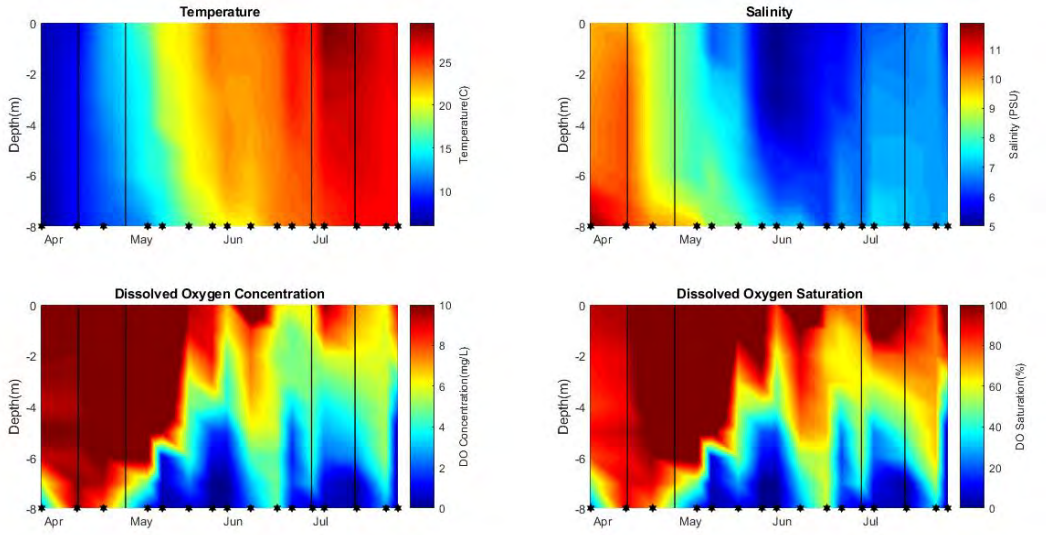

Figure 20. Interpolated water quality parameters. Black dots along x axis indicate dates data was collected. Areas between first and second vertical black lines indicate time during which ADCP was at site for first deployment. Areas between third and fourth vertical black lines indicate time during which ADCP was at site for second deployment.

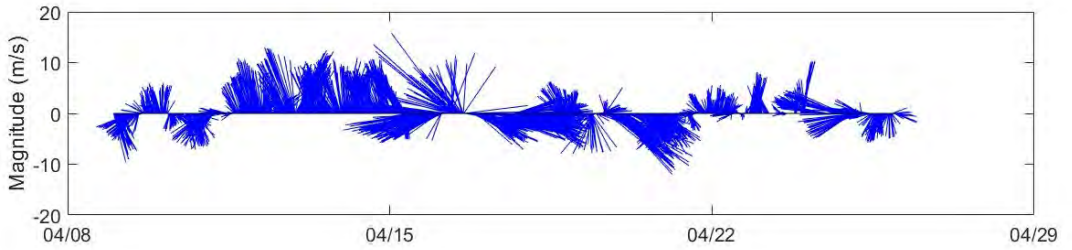

Figure 21. Wind Speeds at Thomas Point Lighthouse during first deployment. Data is from station TPLM2 of NOAA's National Buoy Data Center. This is the location closest to the study site for which wind data is readily available.

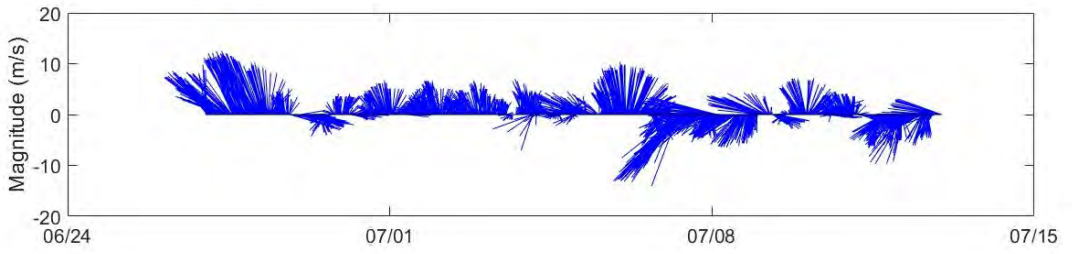

Figure 22. Wind Speeds at Thomas Point Lighthouse during second deployment. Data is from station TPLM2 of NOAA's National Buoy Data Center. This is the location closest to the study site for which wind data is readily available.

Coupling Plastic Degradation with Coastal Processes

Benjamin William Stalheim Lane, REU Fellow
Maryland Sea Grant

William Nardin, Assistant Professor
Horn Point Laboratory, University of Maryland Center for Environmental Science

Corinne Corbau, Visiting Scholar
Università degli Studi di Ferrara, Dipartimento di Scienze della Terra

Abstract

Plastic degrades overtime into smaller particles of plastic known as microplastics through a process of fragmentation. The development of microplastics has been studied in a variety of contexts, such as salt marshes and the open ocean. However, little is known about the factors that influence plastic degradation and microplastic production in coastal environments, even though the majority of the plastic that ends up in the ocean must pass through coastal environments on its way from land to ocean. To understand this process, this experiment takes the experimental design from Weinstein et al. (2016) and adapts it to coastal processes such as tides, erosion and deposition, wave action, biomass development, and other coastal factors. As a result, strips of high-density polyethylene plastic and polystyrene plastic were field deployed in a variety of locations corresponding to critical variables such as erosion, deposition, and subtidal and intertidal influences. These strips were collected at four weeks, eight weeks, sixteen weeks, and thirty-two weeks from the start of the experiment and were analyzed for mass loss, biomass development, microplastic production, and fragmentation. The experiment remains in progress, but the four-week results show the development of biofilm and no significant plastic strip mass loss, as expected. The results also show large scale macroplastic fragmentation occurring in the subtidal polystyrene strips in the erosion zone.

Introduction

The global demand for plastics is staggering. The global production of plastic has grown consistently since the middle of the 20th century, and millions of tons of plastics have been produced in total (Barnes et al. 2009; Andrady 2011; Ivar do Sul and Costa 2014). However, much of the plastic produced eventually ends up in the world's oceans as plastic debris (Barnes et al. 2009; Andrady 2011). Furthermore, as suggested by Barns et al., the impact of plastic on marine and estuarine environment is persistent (2009). There is no easy way to eliminate the current plastic accumulation in the oceans, and even if the production of plastic was stopped immediately, the plastics would persist in marine environments for hundreds of years into the future (Barns et al. 2009). As a result, the presence of plastic litter and debris in the world's oceans and estuaries has become a widely recognized anthropogenic threat (Barnes et al. 2009; Andrady 2011; Cole et al. 2011; Ivar do Sul and Costa 2014; Barboza and Gimenez 2015; Weinstein et al. 2016; Cannas 2017).

The development of microplastics in marine environments has been identified as a particularly pressing concern (Barnes et al. 2009; Andrady, 2011; Ivar do Sul and Costa 2014). Recent estimates conclude that around 4.85 trillion microplastic particles smaller than 5 mm are present in the world's oceans (Hurley et al., 2018). The term "microplastics" is still being debated and defined, but a recent NOAA workshop on the issue has started to identify some consensus on the term within the field. Following recent studies, microplastics will be defined here as plastic particles smaller than 5 mm (Arthur et al. 2008; Andrady, 2011; Barboza and Gimenez 2015).

Two general types of microplastics have been identified: primary and secondary. Plastics that are created to be a specific microscopic size are defined as primary microplastics (Andrady 2011; Cole et al. 2011). Primary microplastics include plastics found in facial cleansers and sand-blasting materials. Primary microplastics typically enter the oceans as runoff from wastewater (Andrady 2011; Cole et al. 2011). Secondary microplastics are small plastic fragments that occur due to the breakdown of larger plastic debris (Cole et al. 2011). Secondary microplastics offer a serious threat to the environment because unlike primary microplastics, secondary microplastics cannot be eliminated at their source. Without removing the extensive amount of plastic already present the ocean, secondary microplastic production cannot be stopped. Secondary microplastic production is the focus of this study.

There are five generally recognized ways in which plastic degrades into microplastic fragments (Andrady 2011).

- Biodegradation: action of living organisms usually microbes
- Photo-degradation: action of light (usually sunlight in outdoor exposure)
- Thermo-oxidative degradation: slow oxidative breakdown at moderate temperatures
- Thermal degradation: action of high temperatures
- Hydrolysis: reaction with water

With the plastic polymers high-density polyethylene (HDPE) and polystyrene (PS) located in the marine environment, it is primarily UV-B radiation from sunlight that starts the photo-oxidative degradation (Andrady 2011; Cole et al. 2011; Weinstein 2016). Once initiated, further degradation can proceed thermo-oxidatively without constant exposure to UV radiation so long as oxygen is present (Andrady 2011; Weinstein 2016). The other degradation processes identified by Andrady are orders of magnitude slower than the light-induced degradation process (2011). However, once plastic has been embrittled due to photo-oxidation, mechanical processes such as abrasion, wave action and turbulence can increase fragmentation and microplastic production (Barnes et al. 2009; Cole et al. 2011). As a result, location is critical to the production of microplastics because local environmental conditions such as sunlight, temperature, and oxygen play a critical role in determining the rate of the degradation of plastic (Weinstein et al. 016). Local factors such as wave action, turbulence, local bacteria and organisms, and sediment type also are influential (Andrady 2011; Weinstein 2016).

Microplastics are of particular concern because they can be ingested by organisms, block digestive systems, cause internal abrasions, transfer harmful chemicals into living organisms, have the potential to bioaccumulate in marine populations, and more generally threaten ecosystem health. (Barnes et al. 2009; Ivar do Sul and Costa 2014; Hurley et al. 2018). In addition, microplastics once created and dispersed in the world's oceans are hard if not impossible to remove or collect (Barnes et al. 2009). Microplastics can also act as pollutant vectors due to toxic chemicals added to the plastics and as reservoirs of toxic chemicals in the

environment (Andrady 2011, Ivar do Sul and Costa 2014). Due to the pervasive and persistent nature of plastic and the existence of large amounts of plastic currently in the world's oceans, microplastics have become a global environmental concern and a potential hazard to human populations (Barnes et al. 2009; Andrady 2011; Ivar do Sul and Costa 2014).

Further analysis is needed to understand the interactions between local environmental conditions and the development of microplastics. As Weinstein notes, although there is a growing body of literature available on the abundance of microplastics in estuarine environments, there is little information concerning the rate of plastic degradation and the process by which microplastic particles are produced (2016). As a result, this study expands upon Weinstein et al.'s methodology to understand the effects of coastal processes and erosion and deposition on microplastic production.

We expect that:

- The presence of erosion will contribute to enhanced microplastic fragmentation, while plastic located in deposition areas will have normal or lower levels of microplastic production.
- Plastic located in intertidal locations will have higher fragmentation rates than plastic located in subtidal locations.
- Microplastic concentration in the sediment will be higher in the deposition location than the erosion locations.
- Sandy sediment will contribute to microplastic production more than muddy sediment.
- Coastal influences will cause microplastic fragmentation to occur faster than recorded in coastal marshes by Weinstein et al. (2016).
- More biomass will develop in subtidal than intertidal location and more biomass will develop in the deposition location than the erosion location.

The purpose of this study is to better understand the process of degradation and the production of microplastics in coastal regions. Specifically, this study seeks to compare the role of tides on microplastic production and plastic degradation. This study also examines the importance of coastal processes such as erosion and deposition with regard to microplastics. Potential differences due to sediment composition will also be addressed by the conclusion of this research. Finally, this study examines the effects of coastal processes on the degradation of two plastic polymers, high-density polyethylene and polystyrene, into microplastic fragments. Our work attempts to understand the timeline of microplastic production beginning with pre-introduction and extending to thirty-two weeks in the water.

Materials and Methods

Experimental Design

Adapting the experimental design of Weinstein et al. (2016), this project seeks to understand how coastal processes influence and impact degradation of marine plastic litter. Two different types of plastic are compared, high-density polyethylene (HDPE) and polystyrene (PS). These two plastics were chosen due to the large quantities of each that are believed to be present in marine environments and to follow the work of Weinstein et al. (Andrady 2011; Weinstein 2016). Following Weinstein et al., both of the plastics are cut into strips (15.24 cm x 2.54 cm). 110 HDPE and 110 PS strips are made. Ten strips of each plastic type will be left unattached and serve as control strips.

Next, ten sample apparatuses are created using a board (82 cm x 14.5 x 2 cm) and attaching wooden dowels (1.2 cm diameter, 10 cm height) to the board in two corresponding rows of twenty (Figure 1). The two rows of dowels are 2.54 cm from the lengthwise edges of the board and 3 cm apart from each other. A plastic strip is then attached to each end of a wooden dowel with a nail so that the strip stands the width of the board between the two rows of dowels. Twenty identical plastic strips are attached to each board. The result is five sample apparatuses for each type of plastic, for a total of ten sample apparatuses (Figure 1).

Two sample boards (one of each plastic type) are field deployed in each zone of interest (Figure 2). For convenience, the two sample boards that are deployed next to each other are called a sample set. One sample set is placed in a tidal erosion zone. In this location, erosion due to coastal processes is present and the boards are placed so that the tide covers the sample set about half the time. The second sample set is placed in the same erosion zone, but in a location where the boards will always be covered by the tide.

The third sample set is placed in a tidal deposition zone. In this zone, deposition due to coastal processes is present and the board is placed so that the tide covers the two sample boards about half the time. The fourth sample set is placed in the same deposition zone, but in a location where the boards will always be covered by the tide. Finally, the fifth sample set is deployed on the beach of the deposition zone and this sample set serves as the control boards. Due to extenuating circumstances the control boards are deployed exactly two weeks after the other boards.

Five plastic strips from each of the ten sample boards will be randomly removed from the apparatuses at four-week, eight-week, sixteen-week, and thirty-two-week intervals. The zero-week control strips will not be field-deployed.

After being removed from the field, the strips will be analyzed for changes in weight and biomass development. Sediment sample will also be taken to find the microplastic composition of the nearby sediment. Parameters such as wind, tide, temperature, light intensity, and sediment composition are also recorded using a HOBO sensor and data from NOAA.

Sample Site

The sample sites were chosen due to the presence of erosion in one spot and corresponding deposition at the other (Figure 3). The erosion site is a mix of mud and sand and is located on the edge of a salt marsh. The deposition side is primarily sand and is located along a sandy beach. In both locations, shade is negligible (Figure 4).

The intertidal sample sets were field deployed so that on average, the tide would cover the plastic strips about half the time. The sub-tidal sample sets were deployed at low tide so that approximately 33 cm of water was located above the strips. However, local tides are irregular and dependent on local weather conditions. The control sample set was deployed on the beach so that the boards would be not be covered by tides or waves.

Analysis of Microplastics Cove Experiment

Corresponding to the four-, eight-, sixteen-, and thirty-two week removal dates, five plastic strips are removed from each of the field-deployed boards. Samples are collected and brought to the

lab where each strip is identified by a number written on it and all of the samples are weighed after drying at room temperature in the dark. The strips are placed in the freezer and not exposed to natural light when not being worked on to preserve chlorophyll A concentrations on the strips. Next the five samples from each are separated into a group of three samples that will be analyzed for mass and a group of two strips that will be analyzed for chlorophyll A.

The three samples being analyzed for mass loss are then cleaned and processed. Each of the strips is gently washed with water to remove dirt and sand attached to the strips. Next, each of the three strips is placed in hydrogen peroxide (30% in water) to remove the attached biomass. The three strips are left in the hydrogen peroxide for approximately two hours and then gently washed with water to remove more biomass. This process is repeated until the biomass has been removed. The three strips are then dried in an oven at 50 degrees Celsius for five hours to remove any trapped water vapor. Finally, the strips are analyzed using a Mettler AT261 DeltaRange electronic balance and the new mass is recorded.

The two samples being analyzed for chlorophyll concentration per unit surface area are kept in the dark for the entirety of the analysis process to ensure chlorophyll concentrations are not affected by sunlight. The two strips are divided into two pieces so that an average tested area of plastic is half of the total average surface area. Because the strips are all cut identically the average is about 19.5 cm^2. One piece of the divided strip is saved and stored while the other half of the strip is cut into small pieces and placed in a 5 ml vial. 3 ml of 90% acetone is added to each of the vials and the vials are placed in the freezer for twenty-four hours. After twenty-four hours the samples are analyzed using a Thermo Scientific Evolution 60s UV-Visible Spectrophotometer. The spectrophotometer analyzes the samples at 665.0 nm and at 750.0 nm. Using the methodology from Lorenzen, this data is translated into the concentration of chlorophyll A with units of (ug/cm^2) (Lorenzen 1967).

Data on windspeed and direction will be obtained from *WindFinder.com GmbH & Co. KG* (https://www.windfinder.com/#13/38.5739/-76.0772). Tide data will also be obtained from NOAA (https://tidesandcurrents.noaa.gov/map/index.shtml?region=Maryland). Temperature and light information will be recorded using a HOBO UA-002-08 sensor. This information is analyzed to find the average conditions of the cove during the experiment.

Plastic fragmentation will be analyzed in the future with the *DeFishGear protocols for sea surface and beach sediment sampling and sample analysis* methodology (Palatinus 2015). Sediment composition will also be analyzed by taking sediment samples and using the *DeFishGear protocols for sea surface and beach sediment sampling and sample analysis* methodology (Palatinus 2015). The deployment sites will also be analyzed for sediment grain size, water content, organic matter content, and microplastic composition.

Results

The Impact of Erosion vs. Deposition

The mass of the plastic strip increased significantly due to the development of a biofilm on the surface of the plastic strip. However, there is no significant change in the mass of the plastic itself after four weeks. Results that will illuminate the impact of erosion and deposition on microplastic production and plastic degradation will need to wait until more samples have been collected during the remainder of this experiment. See Table 1.

The Impact of Subtidal vs. Intertidal

There is no significant change in the mass of the plastic after four weeks. See Table 1.

Macroplastic Fragmentation

Plastic fragmentation occurred on the macro scale for polystyrene at the erosion subtidal location (Figure 5). Approximately 24% of the polystyrene was lost from almost all of the plastic strips and only six of twenty remained whole at the four-and-a-half-week removal. For the other polystyrene boards, while some macroplastic fragmentation occurred, it occurred on a small scale with less than 5% of the total mass lost. Macro level plastic fragmentation was not observed with any HDPE strips.

Biomass Development

Using an ANOVA test, tidal location and hydrodynamic characteristic were identified as significant determinants of biomass development as proxied by chlorophyll A concentrations (Figure 6). Tidal location (subtidal vs. intertidal) was highly significant and had a F statistic of 104.188 with 1,8 degrees of freedom. Hydrodynamic characteristic (erosion vs deposition) was significant with a F statistic of 13.850 and 1,8 degrees of freedom.

Water levels, Light Intensity, and Temperature

Data on light intensity and temperature was successfully collected from the HOBO sensor. The intertidal sensor shows a great amount of variability in both temperature and light likely due to tidal influences (Figure 7). The subtidal sensor has little variation in comparison, probably because the water above the sensor acts as a buffer (Figure 8). Water levels in the region are highly dependent on meteorological influences but otherwise the data is consistent with general tidal effects (Figure 9).

Discussion

The Impact of Erosion vs. Deposition

There is no significant change in the mass of the plastic after four weeks. This result was expected and follows the findings of Weinstein et al. (2016). Plastic generally takes a longer period for microplastic particles to begin to form, as noted by Weinstein et al. (2016). Further analysis will need to wait for the conclusion of the experiment.

The Impact of Subtidal vs. Intertidal

There is no significant change in the mass of the plastic after four weeks. This again is expected and the reasoning is the same as above.

Macroplastic Fragmentation

Drastic macroplastic fragmentation was observed in the subtidal erosion polystyrene and the entire board lost 24% of its total mass within only four-and-a-half weeks. In addition, while none of the other boards lost as much mass, the polystyrene deployed elsewhere did show the presence of a small amount of macroplastic loss far under an estimated 5% of total mass loss.

However, there are no visual signs of plastic fragmentation on any of the high-density polyethylene strips. This is in direct contrast to the observations found in Weinstein et al. (2016). In a salt marsh, Weinstein et al. found that a visual inspection of the plastic strips revealed no evidence of fragmentation of any of the collected strips. Furthermore, repeated measures ANOVA comparing surface area over time did not produce significant models for either high-density polyethylene or polystyrene.

The loss of the subtidal plastic but not the intertidal plastic was surprising because we had proposed that coastal effects such as waves, tides, and the constant expanding and contracting of the plastic particles associated with continuous drying and submersion would cause more fragmentation to develop on the subtidal plastic. However, while correct about erosion being an indicator or cause of the plastic being fragmented, the subtidal plastic fragmented first. We believe that one potential cause of this result may be the effect of an undertow produced by the waves hitting the nearby shore. As a result, the subtidal polystyrene would be exposed to continuous wave energy, unlike the intertidal plastic. For brittle or soft plastics such as polystyrene, being located in a subtidal region with erosion due to high wave energy may result in macro fragmentation increasing the surface area of the plastic and producing rough edges that may result in higher microplastic production. We originally expected the process of degradation to proceed from macro to micro directly, but the results from the subtidal erosion polystyrene suggest that for some plastics a middle stage in intermediate plastic size may exist and may play a critical role in coastal microplastic production. This possible middle stage may connect the large macroplastic degradation to microplastic production. However, until the completion of this research project, caution is needed before any strong claims are made about the cause of the macroplastic fragmentation.

Biomass Development

The development of biomass on the plastic strips was expected. Weinstein et al. (2016). reported the development of a similar biomass. However, unlike Weinstein et al., there are more significant differences between the different sample strips analyzed in this study than just plastic type. We expected that plastic strips located in a deposition zone would develop biomass in a different way than the biomass develops in the erosion zone. This conclusion is validated with the results of the four-week samples. There was a significant difference between erosion and deposition plastic strip biofilm with a reported p value of 0.00586.

We also proposed that the tidal zone location associated with the plastic sample would be a significant factor in biomass development. After four weeks the ANOVA test suggests that tidal location may be the most important factor analyzed with regards to biomass development, with a reported p value of 7.28e-06 (see results section for F statistic and degrees of freedom for both factors).

Biomass development is important to analyze because UV radiation, which traditionally plays a major role in plastic degradation, likely plays a more limited role in coastal plastic degradation after four weeks as a result of the development of a biofilm layer. This layer should reduce UV transmittance to the plastic. This means that plastic degradation and microplastic production are likely the result of a more complex set of factors than plastic found elsewhere.

The importance of biomass in plastic degradation and microplastic production is acknowledged, but also poorly understood. Specifically, there is currently some confusion about if biomass contributes to microplastic growth or inhibits it (Weinstein et al. 2016). Because of the quantity

of biomass attached to the plastic in the subtidal and depositional coastal regions, the development of the biofilm has the potential to either inhibit or enhance fragmentation of the plastic and the production of microplastic. Further study is needed to understand the potentially immense impact of biofilm development on plastic degradation and to characterize this impact as either enhancing or inhibiting.

Light Intensity, Temperature, and Water Levels

The data collected on light intensity and temperature at the subtidal and intertidal levels matches expectations. The subtidal data was less variable likely as a result of near continuous submergence. The water would act as a buffer preventing dramatic changes in temperature or light intensity found at the intertidal level. Water level also matched expectations but was somewhat variable due to meteorological influences.

Methodology

The sampling apparatus described by Weinstein et al. was an effective way of studying microplastic production and plastic degradation due to coastal processes (Weinstein et al. 2016). However, the sampling apparatus constructed could be enhanced. The use of some form of clip such as a paperclip to hold the plastic strips in place would eliminate the need to make a hole in the plastic and make removal of the strips faster and easier. In addition, because coastal regions have far more energy in them than marsh systems, leaving extra room on either end of the plastic strip board for the addition of weights would help avoid the accidental loss of the sampling apparatus. Finally, while the loss of plastic is the focus of the project, a future design of the sampling apparatus that prevented the loss of plastic to the environment would be preferable.

Conclusion

The accumulation of plastic fragments is dangerous to marine and estuary environments because they are difficult to remove and because they have the potential to be ingested and so damage the entire food chain. As a result, understanding the mechanisms that affect microplastic fragmentation and production is critical. Because many of the conditions that affect plastic degradation and microplastic production are location-dependent, such as radiation intensity and abrasive wave action, studying the influence of coastal processes is critical. In particular, tidal and erosion/deposition processes and sediment characteristics (sand vs. mud), which are studied and compared in this study. While it is too soon to make any general predictions based on only the four-week data collected, there are some conclusions that can be made concerning macroplastic loss and biofilm development. In particular, we propose that in coastal environments, the effects of wave action, tidal effects, and biofilm development on microplastic production may play a larger role than first imagined, and that these effects are evident at four weeks.

Microplastic development and plastic degradation needs to be studied in more detail and more attention needs to be payed to location-dependent factors. The process of plastic degradation that occurs on the ocean floor is likely very different from the process that occurs in a salt marsh or in a coastal system. This study has validated the use of the sampling apparatus proposed by Weinstein et al. (2016) and has suggested some improvements for the adoption of this sampling mechanism to coastal systems and obtained some of the first results about the effects of coastal processes on microplastic production and plastic degradation. The quick destruction of the

polystyrene plastic strips is one example of how coastal processes may be accelerating the rate of plastic degradation in coastal regions all around the world, resulting in a potential increase of microplastic production. Microplastics are a significant health threat to ecosystems around the world and the threat produced will only grow as more and more plastic is washed off of land and enters the world's oceans and passes through coastal regions where microplastic production rates may be higher than expected.

Acknowledgments

I would like to thank Maryland Sea Grant for the opportunity to participate in research with the University of Maryland Center for Environmental Science at Horn Point Laboratory. I would like to recognize the mentorship and support of Dr. William Nardin and Dr. Corinne Corbau. I would also like to thank Dr. Sairah Malkin, Carol Kim and Dr. Mike Allen for their assistance and support with the project. This study was supported by NSF grant OCE-1756244.

References

Andrady, A. L. 2011. Microplastics in the marine environment. Marine Pollution Bulletin. 62: 1596–1605. doi:10.1016/j.marpolbul.2011.05.030

Barboza, L. G. A., and B. C. G. Gimenez. 2015. Microplastics in the marine environment: Current trends and future perspectives. Marine Pollution Bulletin. 97: 5–12. doi:10.1016/j.marpolbul.2015.06.008

Barnes, D. K. A., F. Galgani, R. C. Thompson, and M. Barlaz. 2009. Accumulation and fragmentation of plastic debris in global environments. Philosophical Transactions of the Royal Society B: Biological Sciences. 364: 1985–1998. doi:10.1098/rstb.2008.0205

Cannas, S., P. Fastelli, C. Guerranti, and M. Renzi. 2017. Plastic litter in sediments from the coasts of south Tuscany (Tyrrhenian Sea). Marine Pollution Bulletin. 119: 372–375. doi:10.1016/j.marpolbul.2017.04.008

Cole, M., P. Lindeque, C. Halsband, and T. S. Galloway. 2011. Microplastics as contaminants in the marine environment: A review. Marine Pollution Bulletin. 62: 2588–2597. doi:10.1016/j.marpolbul.2011.09.025

Hurley, R., J. Woodward, and J. J. Rothwell. 2018. Microplastic contamination of river beds significantly reduced by catchment-wide flooding. Nature Geoscience. 11: 251–257. doi:10.1038/s41561-018-0080-1

Ivar do Sul, J. A., and M. F. Costa. 2014. The present and future of microplastic pollution in the marine environment. Environmental Pollution. 185: 352–364. doi:10.1016/j.envpol.2013.10.036

Lorenzen, C. J. 1967. Determination of Chlorophyll and Phep-pigments: Spectrophotometric Equations. Limnology and Oceanography. 12: 343–346. doi:10.4319/lo.1967.12.2.0343

Palatinus, Andreja, Manca Kovač Viršek, and Eleni Kaberi. 2015. “DeFishGear Protocols for Sea Surface and Beach Sediment Sampling and Sample Analysis.” DeFishGear funded by Adriatic IPA program. 27pp.

Weinstein, J. E., B. K. Crocker, and A. D. Gray. 2016. From macroplastic to microplastic: Degradation of high-density polyethylene, polypropylene, and polystyrene in a salt marsh habitat: Degradation of plastic in a salt marsh habitat. Environmental Toxicology and Chemistry. 35: 1632–1640. doi:10.1002/etc.3432

Figures and Tables

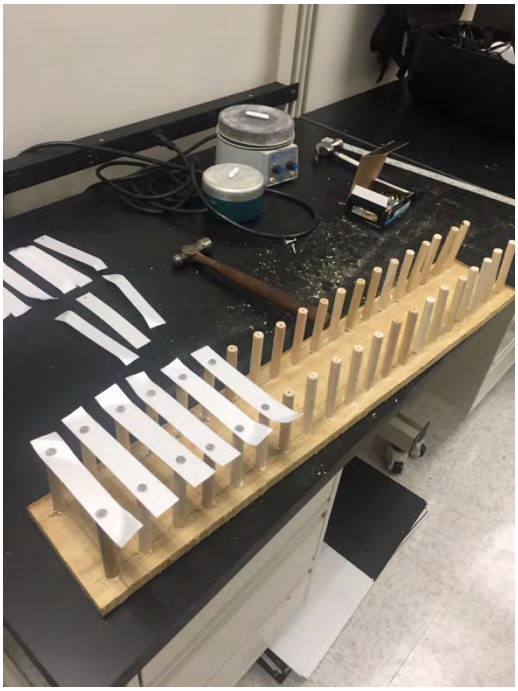

Figure 1. Half built sample board. This picture clearly shows the orientation of the plastic strips and the arrangement of the dowels.

Figure 2. The Intertidal sampling apparatus deployed in the deposition zone.

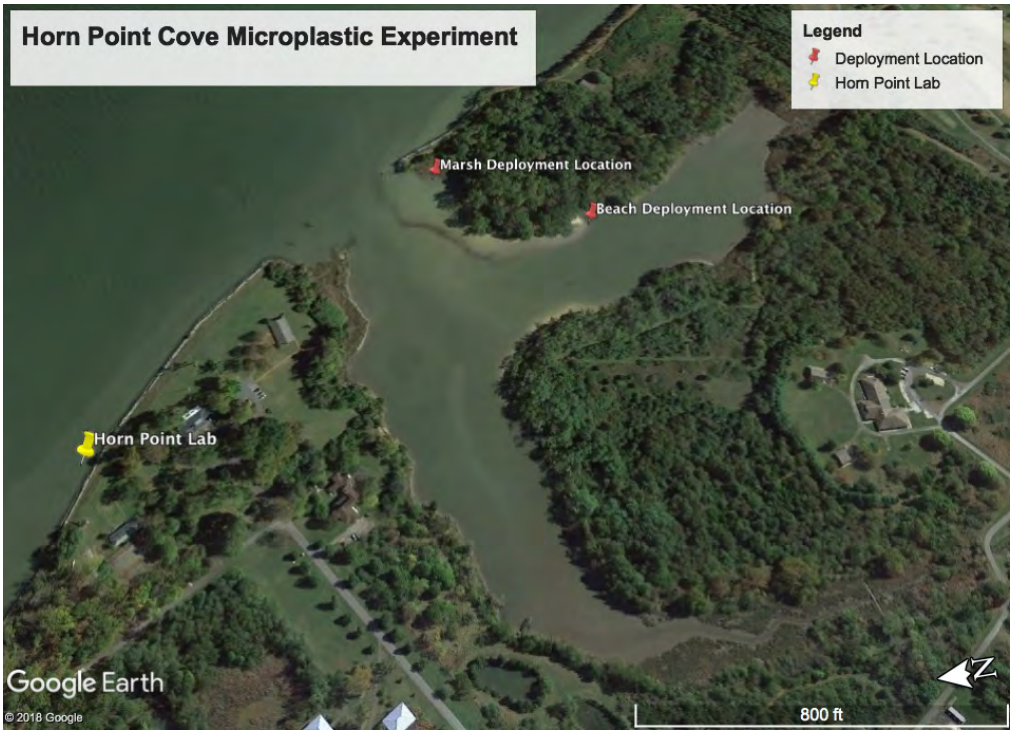

Figure 3. The locations of the boards in the Horn Point cove.

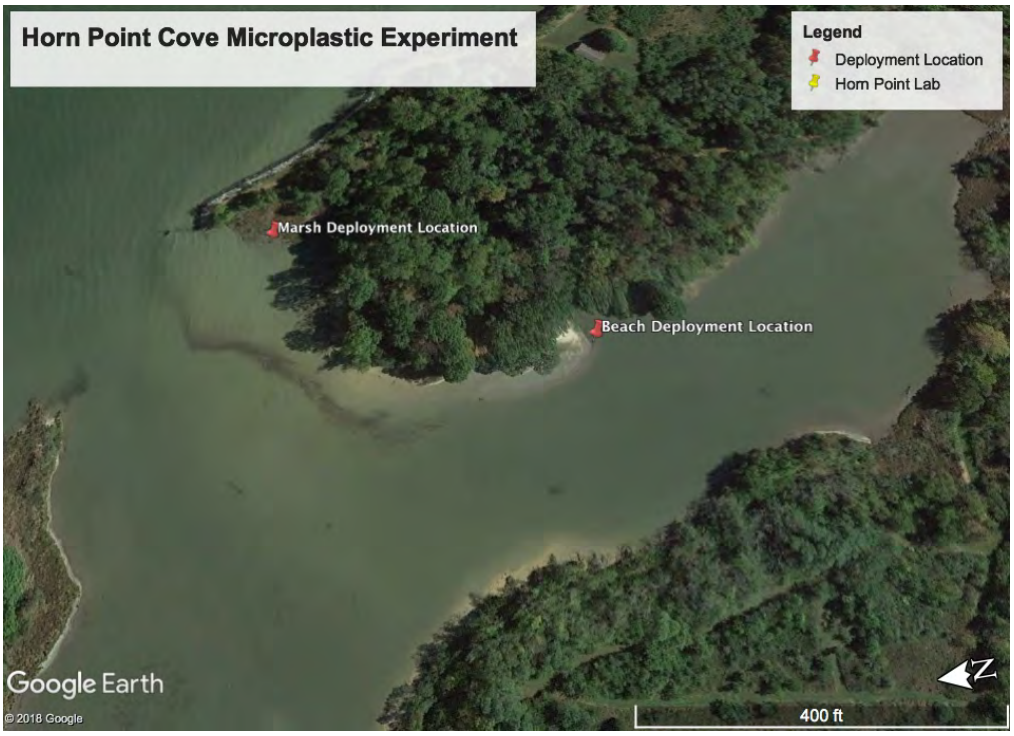

Figure 4. A closer picture of the board deployment locations.

Figure 5. A visual of the four-week difference in large scale mass loss in subtidal polystyrene between erosion location (top) and deposition location (bottom).

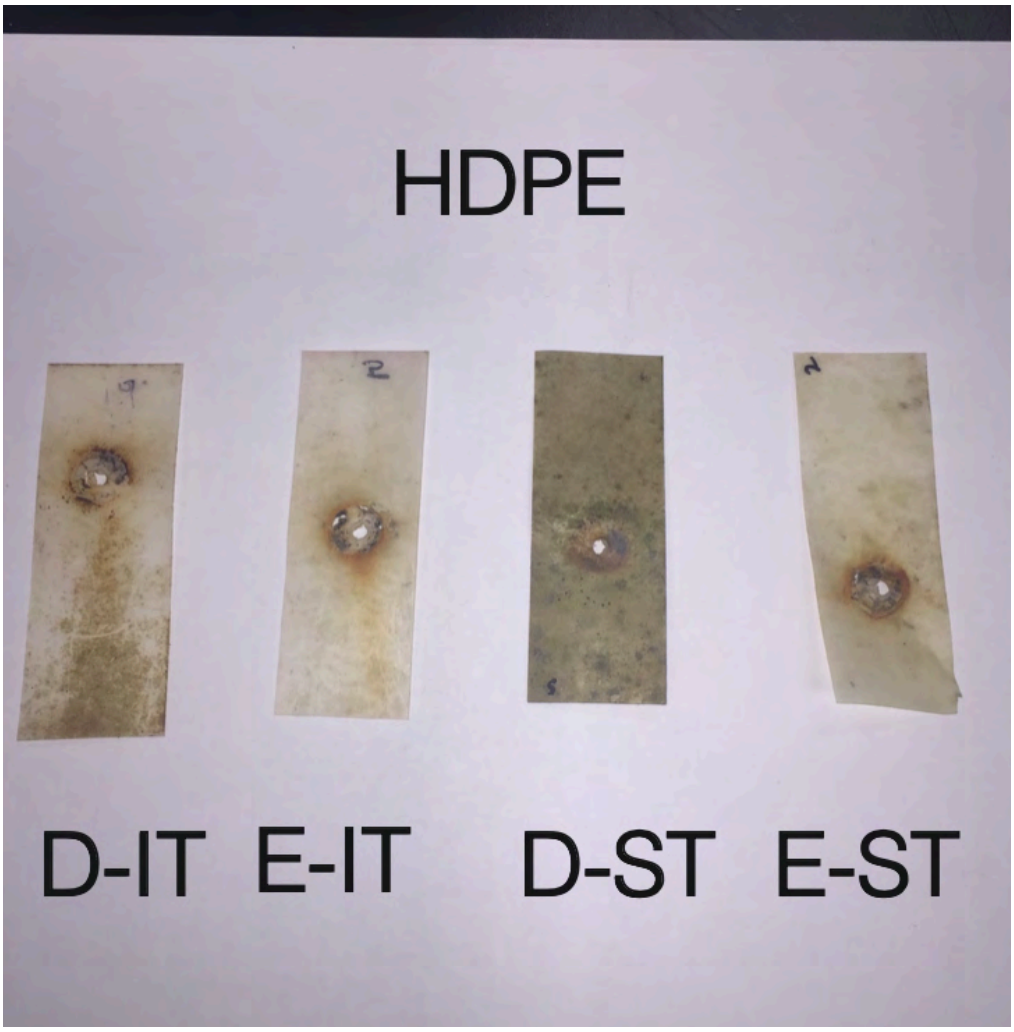

Figure 6. Visual of differences in biomass development at week 4 for HDPE plastic.

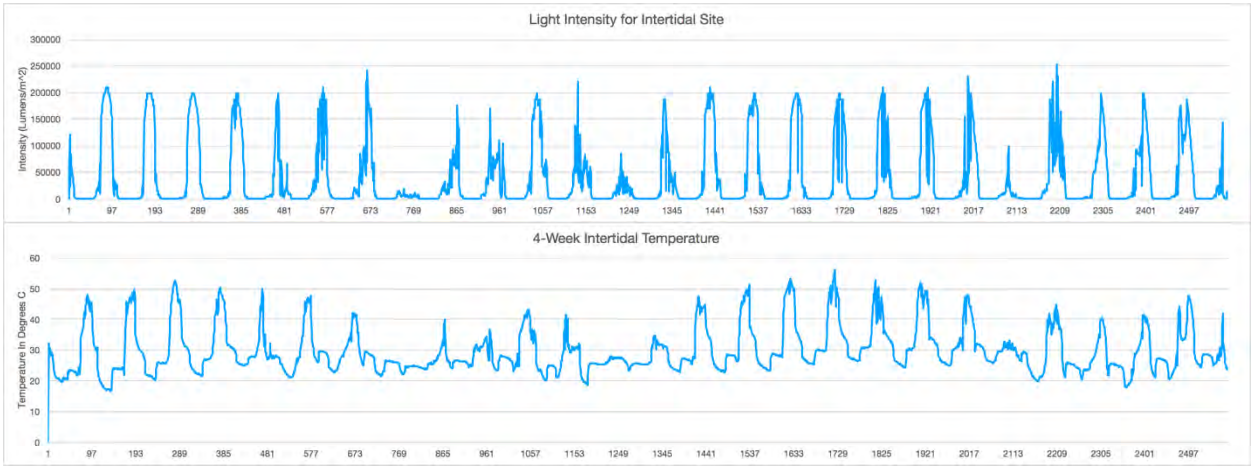

Figure 7. Intertidal light intensity and temperature during the four-week interval.

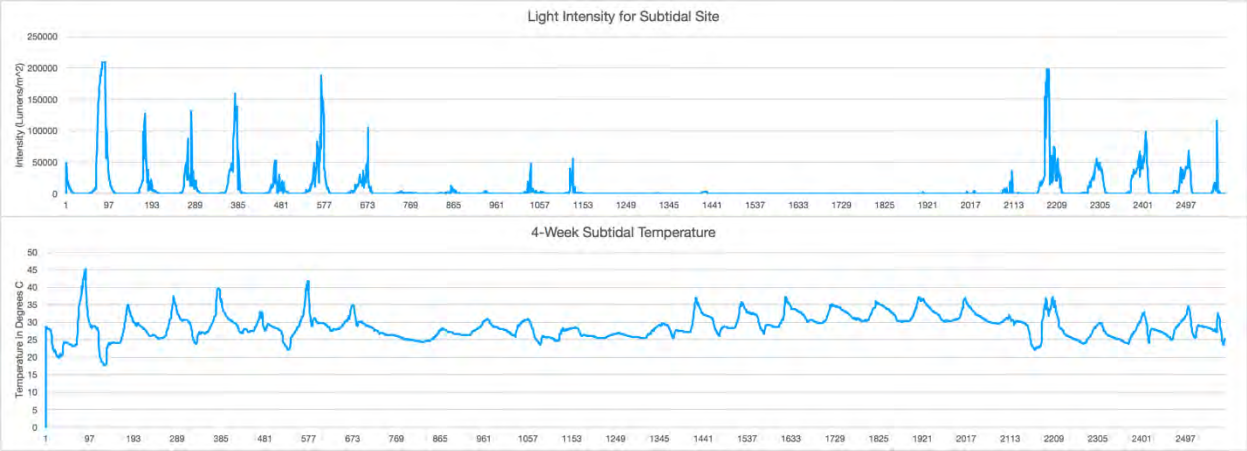

Figure 8. Subtidal light intensity and temperature during the four-week interval.

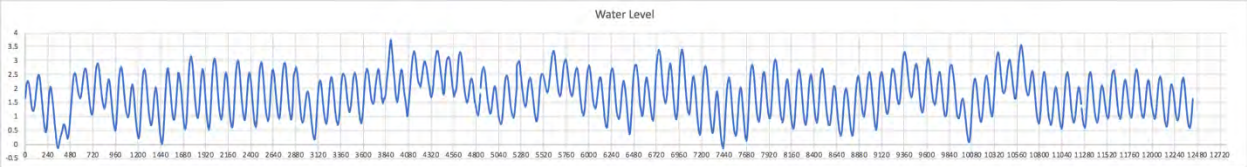

Figure 9. Water levels during the four-week interval.

Table 1. Showing the average percent change in mass after four weeks.

	Intertidal Average Percent Change (g)	Subtidal Average Percent Change (g)
Erosion HDPE	0.000589855	0.000623045
Erosion PS	-0.004620732	0.001208927
Deposition HDPE	-0.00013396	0.0000856339
Deposition PS	0.009054637	0.006225329

Tracking microbial contaminants in Baltimore Harbor: Are current techniques sufficient for assessing human risk?

Norberto Latorre Arzola, REU Fellow
Maryland Sea Grant

Judith O'Neil, Associate Research Professor
Horn Point Laboratory, University of Maryland Center for Environmental Science

Abstract

Coastal waterways receive fecal pollution from many sources each year in varying proportions around the world. Waters that have been polluted with storm water and urban runoff, sewage treatment plants, combined sewage overflows and sanitary sewer overflows can contain human pathogens. Methods that use fecal indicator bacteria (FIB), including *E. coli* and *Enterococci*, have traditionally been used to assess the human pathogen risk in waterways. However, these culture methods can be unreliable for several reasons: (1) FIB presence does not necessarily indicate pathogen presence, (2) they can appear from sources other than humans, and (3) sediments help FIB to persist and survive over the long term. Molecular methods are being developed that are more reliable in pointing to sources and pathogen presence. The World Harbour Project compares these two methods in twelve harbor systems around the world. Baltimore Harbor is one of the sites. We measured FIB and water quality parameters in eight sites that reflect more to less impacted in June and July and correlated them. Significantly higher FIB was present in a wet period sampling compared to a dry and there was also a gradient of FIB numbers from more to less impacted sites. This was also reflected in the relationship with salinity, with higher numbers of FIB in lower salinity (i.e. indicative of higher rainfall and also more impacted inner harbor sites). Additionally, a positive correlation of FIB numbers with total nitrogen was determined, but generally inverse correlations with all other water quality parameters. A longer time scale of sampling will be necessary to make more quantitative assessments. Samples are also being analyzed using next generation Illumina sequencing, and these molecular results will be analyzed across the World Harbour Project cities to help determine whether molecular techniques are more informative in predicting actual human pathogens rather than traditional FIB culturing methods and whether new methods could be implemented on a broader global scale to improve human health impacts associated with the fecal pollution problem worldwide.

Introduction

Estuaries around the world, including the Chesapeake Bay, receive fecal pollution from many sources. Some of these sources are septic systems; storm water and urban runoff; sewage treatment plants; combined sewage overflows (CSOs); sanitary sewer overflows (SSOs); and waterfowl, wildlife, domestic, and pet feces (EPA 2006; Newton et al. 2011). According to Newton et al (2011), CSOs and SSOs introduce close to 4 trillion liters of untreated sewage

each year in national waterways of the United States (US). Water that has fecal pollution can contain diverse pathogens (Richkus et al. 2016), making urban and recreational waters unsafe for use. That is why organizations and agencies like the US Environmental Protection Agency (EPA) set guidelines for recreational use of water-ways and perform tests of waterways using traditional culture methods. During these tests, water is filtered and indicator bacteria is grown on different agar to assess the human pathogen risk in them (EPA 2006). There are four main indicators used: Total Coliform, Fecal Coliform, *E. coli*, and *Enterococcus* (EPA 2006). These fecal indicator bacteria (FIB) are found in the intestines and feces of warm-blooded animals, which makes them useful (Boehm and Sassoubre 2014; EPA 2006; Mote et al 2012).

According to Boehm and Sassoubre (2014), *Enterococcus* has been strongly correlated with the number of swimmers becoming sick with gastrointestinal illness in marine waters polluted by wastewater. Additionally, according to Richkus et al. (2016) FIB have been consistently linked to increase risk of gastroenteritis. Therefore, when monitoring groups culture FIB, and the results exceed prescribed numbers, that is taken as sufficient justification for closing the water bodies because of their potential risk to human health. Those prescribed numbers are the EPA primary contact standard that are defined as 126 colony forming units (CFU) per 100 ml for *E. coli* and 35 CFU per 100 ml for *Enterococcus* (EPA 2015). According to McLellan and Eren (2014), more than 44% of the rivers and 30% of the bays and estuaries in the US are deemed impaired, with pathogens usually being cited as the number one cause of these impairments. This represents a public health, economic, and industry problem. It is also a concern for the 42% of the US residents who swim in lakes, ponds, oceans, or rivers in a given year (Richkus 2016) and more specifically in the Chesapeake Bay, the 18.1 million people who live close to the bay (Chesapeake Bay Program 2018). It is estimated that there are approximately 800,000 cases of enterococcal infection in the US each year, which adds $500 million to annual healthcare costs (Boehm and Sassoubre 2014). For the shellfish industry in Maryland and Virginia, approximately 8% of the bivalve beds were estimated to have been closed due to potential for pathogen-related illness, and it had a cumulative economic impact valued at approximately $13 million for both states in 2008 (Richkus 2016). As recently as the 13th of July of 2018, some communities in Washington D.C. could not drink from their tap water at their residences unless it was boiled, due to a warning by the authorities when the city's water supply was potentially contaminated with bacteria or other pollutants (Jamison et al 2018).

Although FIB are currently used to assess the human pathogen risk in waterways, they can be unreliable. FIB generally exist in the intestinal tract of mammals and birds (Boehm and Sassoubre 2014; Chariton et al. unpub; EPA 2006; Feng et al. 2018; McLellan and Eren 2014; Mote et al 2012), so their presence doesn't necessarily indicate that fecal pollution comes from a human source. As stated by Newton et al (2013): "In ecosystems containing numerous modes of fecal contamination, these culture-based methods cannot discriminate among sources." Sometimes even the distribution of FIB cannot help to detect sources, thus Ferguson et al (2005) stated: "The *Enterococci* species distribution found in sediments and water were similar to that of humans, animals and birds. Thus, species distribution was not useful in pinpointing major source(s) of beach contamination in this study". The persistence and survival of FIB in extra enteric environments casts some doubt on the reliability of the traditional methods. This is in part due to the fact that sediments can also act as reservoirs for FIB, allowing them to persist and survive for greater lengths of time (Pachepsky and Shelton 2011). According to Ferguson et al (2005), laboratory studies indicate that FIB survive longer in water with sediments. This could be because sediments can protect FIB from predators and UV inactivation, and can even enhance the availability of nutrients originating from algae, plankton, and debris (Ferguson et al. 2005). *Enterococci* have been shown to replicate on beach sands and in water containing kelp and plankton (Boehm and Sassoubre 2014). Therefore, Ferguson et al (2005) stated: "The long-

term persistence/regrowth of indicators in sediments, particularly *Enterococci*, calls into question the reliability of this indicator for determining recent faecal contamination of water."

Additionally, FIB have not always been found to always correlate with the presence of human pathogens (Feng et al. 2018; Ferguson et al. 1996; Leight et al. 2018). Some studies have failed to establish a positive correlation between FIB levels and pathogens (Feng et al 2018; Leight 2018; Newton et al 2011). This could be because according to Chariton et al. (unpub), FIB levels do not necessarily indicate a risk to human health. For example, higher levels of FIB can be due to a higher number of aquatic birds and therefore pose minor risk to humans given the small concentration of human pathogens; conversely, there could be lower levels of FIB but higher concentrations of pathogens in a low concentration of untreated sewage. Using single indicators to detect a wide range of human pathogens may not be feasible (Leight 2018). There are even human pathogens that are not of fecal origin (e.g. *Vibrio vulnificus*), which FIB cannot point to their presence (Leight 2018). The culture media could even be a factor in making a false positive or negative when assessing human pathogen risk. For example, one of the traditional culture media used for *Enterococci* is mEI agar, in which the presence of an *Enterococcus* colony will be determined by a blue halo. In a study by Ferguson et al (2005) they used mEI agar and after sub-culturing the colonies to speciate them, they found that 17.1% of the species in that media with a blue halo were not *Enterococcus*. This has implications for the reliability of the traditional methods.

Given these reasons that cast doubt on the traditional methods, scientists have been developing molecular methods that can more reliably assess the human pathogen risk and determine the sources of fecal pollution in waterways to better manage and mitigate them. These methods use next-generation sequencing techniques to identify alternative indicators using the 16S rRNA gene. These alternative indicators have been fecal anaerobes, which may be more indicative of human pathogens given that they will very unlikely grow outside the host once out in the environment (McLellan and Eren 2014). One of the advantages of these molecular methods is that they use more than one indicator to determine the source of fecal pollution. This is because it is very probable that there is not a single indicator which is 100% specific to a host, making the use of a combination of indicators a necessity (McLlellan and Eren 2014). There are two bacterial families which are potentially useful alternate indicators, called *Bacteroidales* and *Lachnospiraceae* (McLellan and Eren 2014). In a recent study *Lachnospiraceae* genetic markers were shown to improve the detection of fecal pollution sources in urban waters (Feng et al 2018).

The World Harbour Project (WHP), which is based out of the Sydney Institute of Marine Science in Australia, has designed a microbial investigation by a group of scientists to assess and monitor sewage-derived inputs in twelve harbor systems around the world (Fig. 1) using molecular and traditional methods (www.worldharbourproject.org 6/15/18). The overarching project aims to evaluate, on a global scale, if the traditional approaches used to assess the risks associated with human pathogens are suitable for determining pathogen risk, in comparison to molecular approaches. This is based on the conviction that molecular approaches can give more detailed information than traditional approaches and hence assess precisely the risks associated with human pathogens. The current project worked in collaboration with the UMCES WHP in Baltimore, MD.

Baltimore is a very urbanized area in Maryland, US. Its population is approximately 621,445 with a density of 7,677/m^2 (Statistical Atlas 2015a). Compared to the population of Cambridge, MD that is 12,465 and its population density is 1,182/m^2 (Statistical Atlas 2015b), Given the population size, Baltimore Harbor is therefore subjected to high inputs of fecal pollution. The

water circulation of the harbor is a three-layered circulation which flows more rapidly in high discharge periods (wet periods) mostly because it receives a lot of input from the Susquehanna river, and run-off during rain events due to more paved surfaces. However, in dry periods Baltimore Harbor receives input from the south part of the Chesapeake Bay (Hong et al 2011). Baltimore Harbor is a tourist center with a lot of recreational activities undertaken on the water of the harbor. But given that it is a very urbanized area, it can receive a lot of fecal pollution input from CSOs, SSOs, and urban water runoff.

Some variables have been found to correlate with FIB. Periods of frequent rainfall cause increased concentrations of FIB in both the water column and the sediments (Boehm and Sassoubre 2014; Leight et al. 2018; Pachepsky and Shelton 2011). Rain can cause urban runoff, CSOs, and high-discharge from the tributaries of the Chesapeake Bay, carrying FIB and potential pathogens into waterbodies. Boehm and Sassoubre (2014) mentioned that in Doheny Beach, CA, because of urban runoff there was a correlation between *Enterococci* and swimmer illness, in contrast with other sites where urban runoff didn't occur. Runoff can cause resuspension of sediments which increases the concentration of FIB, given that they can persist and survive for greater lengths of time in sediments than in the water column (Pachepsky and Shelton 2011). The variable turbidity may be correlated with FIB, given that FIB can attach to suspended particles (Pachepsky and Shelton 2011; Mote et al. 2012). Additionally, high concentrations of organic matter can promote the survival of FIB (Mote et al. 2012). Therefore, our research questions for this study were: (1) What are the correlations between water quality parameters, nutrients, total suspended solids (TSS) and volatile suspended solids (VSS, a measure of organic content) with FIB in the Baltimore Harbor, and (2) are molecular methods more informative than traditional ones?

The objectives of this study were: (1) to use traditional methods to culture *E. coli* and *Enterococci* in sites from the Baltimore Harbor which reflect a gradient from more to less impacted; (2) asses water quality parameters in the sites; and (3) correlate the water quality parameters with the cultures of *E. coli* and *Enterococci* from each site, and (4) ultimately compare to molecular methods. Our hypotheses were: (1) There are higher concentrations of FIB in wet periods compared to dry periods, (2) There are higher concentrations of FIB in the sites in Baltimore Harbor that are more impacted compared to the ones that are less, (3) There are higher concentrations of FIB in sites with higher turbidity, higher nutrients, organic matter, and TSS compared to sites with lower values (e.g. correlated with water quality), and (4) molecular methods will be more informative in the detection of fecal pollution sources than traditional ones.

Materials and Methods

Sites

Eight sites where chosen for this study; six of these sites were within Baltimore Harbor and the other two were in Stoney Creek and Sandy Point Beach. Of the six sites in Baltimore Harbor, three represented very impacted and the other three represented less impacted areas. The other two sites were chosen because of their recreational uses: Stoney Creek is used for boating and kayaking, and Sandy Point Beach for swimming. They were used as reference points to the other six (Figs. 2A and 2B).

Field methods

Samples for all parameters were taken a month apart in June and July. Water samples were taken either by boat in association with Blue Water Baltimore (www.bluewaterbaltimore.org 6/15/18) or by land. Polycarbonate sampling bottles were used (1 or 2 L). Water quality parameters were measured *in situ* for temperature, dissolved oxygen (DO), and salinity with a YSI meter, and pH was measured with a hand-held pH meter. Transparency was measured using a Secchi disk. At each site, sampling bottles were rinsed with the water from the site three times. Nitrile gloves were used to submerge the water bottles under the surface for taking the samples. After taking the three water samples, they were immediately put in a cooler and taken immediately to the Institute of Marine and Environmental Technology (IMET) in Baltimore, MD, for processing.

Laboratory methods

At IMET the water samples were filtered for DNA analysis, plating *E. coli* and *Enterococci*, chlorophyll *a*, Total Nitrogen (TN), and Total Phosphorus (TP). The membrane filters used had pore-sizes of 0.22 µm and 0.45 µm for the DNA analysis and for the FIB, respectively. The agar used for *Enterococci* and *E. coli* was mEI and mTEC - respectively. The microbial plates were taken to Horn Point Laboratory (HPL) in the University of Maryland Center for Environmental Science (UMCES), Cambridge, and placed in temperature-controlled incubators at 41 ± 0.5℃ and 44.5 ± 0.2℃, respectively for *Enterococci* and *E. coli* for 24 hours. Resulting colonies were enumerated using a Nikon SMZ800 light dissecting microscope. Chlorophyll *a* was analyzed fluorometrically on 50 ml samples that had been filtered through a 25mm GF/F and extracted in 90% acetone overnight and read at 685 nm. Phaeophytin was measured after addition of 10% HCl and the sample re-read fluorometrically (Arar and Collins 1997). TN and TP were analyzed by Analytical Services at UMCES HPL according to standard protocols (Valderrama 1981). Samples were analyzed for TSS and VSS by filtering 50 ml of samples through a pre-weighed 47mm GF/F filter which was subsequently dried and re-weighed to determine TSS. The filter was then combusted for 4 hours at 450 ℃ in a muffle-oven to drive off the organic matter. The percent organic matter was then determined for each site. Precipitation information was taken from the National Oceanic Atmospheric Association (NOAA).

Results

Fecal Indicator Bacteria abundance

E. coli had the highest numbers of CFU in all sites compared to *Enterococci* for the two months sampled (Table 1). *E. coli* had a maximum mean of 180.28 CFU in June and a minimum of 1.15 CFU, both in June and July. *Enterococci* had a maximum mean of 63.07 CFU in June and a minimum of 0 CFU, both in June and July (Table 1). The site Main A had the highest numbers for *E. coli* (Fig. 3A) and *Enterococci* (Fig. 3B) in June. In both months, they exceeded the EPA primary contact standard (Figs. 3A and B). Three sites for *E. coli* had significant differences ($p \leq 0.05$) between June and July, and for *Enterococci* was four sites (Fig. 3).

Correlation with rainfall and water quality parameters

As for precipitation, in June before the sampling period the rain was reported at Baltimore–Washington Airport (BWI) as 11.15 cm and 0.076 cm in July. On the other hand, TSS showed a general gradual increase from Jones Fall to Sandy Point Beach in both months (Fig. 4). The highest TSS mean value was 9.02 in July, with the lowest being 2.07 in June (Table 3). There

was an inverse relationship between FIB and TSS, *E. coli* in both months (Figs. 15A), whereas *Enterococci* had an inverse correlation in July, but a positive relationship in June (Figs. 15B). The correlation was higher in July for both FIB compared to June. There was not an obvious trend for either VSS or expressed in percent organic matter (Figs. 5 and 6). FIB had an inverse correlation in June but a positive one in July with VSS (Fig. 16). The correlations were higher in July for both FIB compared to June. *E. coli* and *Enterococci* had a positive correlation with each other, in June and July, although the correlation was higher in July than in June (Fig. 17).

Correlation with physical parameters

E. coli and *Enterococci* had a positive correlation with temperature which was higher in July than June (Fig. 7). There was an inverse correlation in both months for salinity with FIB, but the correlation was higher in July for both FIB (Fig. 8). Additionally, salinity was higher at the time of sampling in July compared to June. There was an inverse correlation between DO and FIB, were the highest correlation was in July (Fig. 9). DO was higher in July for all sites compared to June (Table 2). There was an inverse correlation for both FIB with pH (Fig. 10). *E. coli* had a higher correlation in July while *Enterococci* had a higher correlation in June. The pH was higher for all sites in June compared to July (Table 2). There was an inverse correlation in June for both FIB with water transparency, but a positive correlation for both in July (Fig. 11). July had the highest correlation for both FIB. Water transparency, as determined by secchi-depth, was higher for all sites in July compared to June, except for Stoney Creek where it was the same in both months (Table 2). Chlorophyll *a* was only measured in July, the samples from June were not measured because Blue Water Baltimore did not include that month in their summer period (MTAC 2011). However, chlorophyll *a* had an inverse correlation with both FIB (Fig. 12). In terms of nutrients, TN had a positive correlation with FIB, with a higher correlation in June for both FIB than in July (Fig. 13). TP had an inverse correlation in June for both FIB but a positive one in July for both FIB (Fig. 14). Although the correlation was much higher in June than in July for *E. coli*. TN and TP were higher for all the sites of July compared to June (Table 2).

Discussion

E. coli and Enterococci abundance

Our results indicate that in June there was a higher concentration of *E. coli* and *Enterococci* compared to July and that the June sample had a significantly higher amount of rainfall than July. The July sample was taken before the heavy rain later in the month. This fits well with previous observations in the literature and our hypothesis, which predicted higher numbers in wet periods than in dry periods. Five and six sites for *E. coli* and *Enterococci*, respectively, exceeded the EPA primary contact standard in June, which shows the contamination of fecal pollution due possibly to urban runoff, CSOs, etc. Additionally, there was a general gradient of abundances from the most impacted sites to the reference sites (least impacted). Our hypothesis that the concentrations would be higher in the Baltimore Harbor sites than in the reference sites found support with the results. It makes sense to see more FIB in the more urbanized areas than in the less urbanized ones as stated by Newton et al (2013). Although it is interesting that we found a slightly higher number of FIB in Sandy Point Beach in July than June, which may have been due to windy conditions and resuspension of sediments (Table 1). There was a significant difference for both FIB in the study sites Canton and Main A, the latter usually had higher numbers even though it was a less impacted site. These high numbers could be because Main A is found in the intersection of two waterways that are urbanized and therefore, receives more fecal pollution than the rest of the outer harbor sites (Fig. 2A). The

correlations between *E. coli* and *Enterococci* indicate that they co-occurred, which suggest fecal pollution.

TSS, VSS, and percent organic matter

Total suspended solids (TSS) had a gradual increase from more to less impacted sites in both months. The site Sandy Point Beach had the highest TSS in July. This could be because in the day of sampling it was windy, which can resuspend sediments. Additionally, this is the only site where we took samples from the shore by land, in which suspended particles are higher (i.e. that is the reason of why there is no secchi-depth data for this site). In correlating the FIB data with TSS, in general there is an inverse correlation, except for *Enterococci* in June. That was unexpected given that literature suggests that FIB attaches to suspended particles, which is even a means of how they get to sediments. Volatile suspended solids (VSS) nor percent organic matter, showed an obvious trend. But the site at Stoney Creek had the highest value for the month of July. This value could be explained given the quantity of chlorophyll *a* available in July compared to June (Table 2B). On the other hand, North West A had the highest value for June. Although we do not have the chlorophyll *a* data for June, it may have been high given the possibility of nutrients coming from urban runoff. The correlation between FIB and VSS showed a strong inverse correlation ($r^2 = 0.91$) for *E. coli* in July. July, in general, had the most organic material compared to June. This was unexpected given that literature indicates that they persist longer in sediments because there is organic matter. It could be that much of that organic matter was detritus from runoff.

Correlations with water quality parameters

Temperature was much higher for all sites in June compared to July. It was much warmer and dryer given precipitation data. We found an inverse correlation in both months. We found less numbers of CFU for both FIB in July than in June, this could be because high temperatures in waterways reduce the survival time of FIB (Mote et al 2012). Salinity reflected the rainfall in June. There was lower salinity in June compared to July. There was a higher number of FIB when there was less salinity. DO correlations showed a high inverse correlation in July, though we are not sure why. The pH correlations suggest that FIB may be sensitive to higher pH. Transparency correlations in July are unexpected, given that more transparency mean less suspended particles. Which like TSS, is unexpected given previous literature results. For chlorophyll *a* there was an inverse correlation for both FIB. More could be said if we had the data from June to compare and even if the correlations were much higher. In the case of nutrients, TN showed a positive correlation for both FIB in June and July. This was expected given that literature says that nutrients enhance FIB survival and persistence. But we found quite the opposite for TP. There was an inverse correlation for June, suggesting high CFU numbers with even zero TP values. In July we saw the opposite, positive correlation suggesting higher CFU numbers with higher TP. This could indicate that FIB use more nitrogen for their nutrition than phosphorus.

Molecular methods

The DNA analysis samples have been sent to the University of Wisconsin–Milwaukee for processing by Dr. Sandra McLellan. There will be several more data time points collected in August and September. Therefore, we do not have the data currently. We will, however, get the full results in a few months and be able to make comparisons between the other time points in Baltimore Harbor, as well as comparisons to the 11 other World Harbour Project cities participating in this global study.

Conclusions

The first two hypotheses of this study, that there would be more fecal pollution in urban areas and wet periods compared to less urban areas and dry periods, were supported in the months sampled. Many sites were also above the EPA primary contact standards which highlights the importance of developing more informative methods for mitigating these fecal sources for a safer aquatic environment which benefits the public health. There was also higher FIB with lower salinity, consistent with higher rainfall as well as total nitrogen values (TN). However, a longer timescale of samples is needed for a better analysis of these hypotheses, as well as the comparison to other cities, which will be possible in the coming months.

Acknowledgment

I want to first thank my mentor, Dr. Judy O'Neil, for helping and guiding me in this summer marine science journey. I learned much and had an incredible experience, I could not have had a better mentor for this summer. Dr. Eric Schott for helping us in this research at IMET. Dr. Rosemary Jagus for letting us use their lab facilities and equipment. Blue Water Baltimore for taking the time to take some additional samples and even changing their sampling days for us, we could not be more thankful. Dr. Jamie Pierson for guidance and comments for the presentations. Thanks to Dr. Michael Allen and Dr. Fredrika Moser for giving me the privilege of participating in this summer internship and letting me gather research, academic, cultural, and personal experience through it. I could not be more grateful with them for this opportunity. Last but not least, the National Science Foundation (NSF) for supporting this study with the NSF grant OCE-1756244.

References

Arar, E. J., and Collins, G. B. 1997. EPA method 445.0 – In vitro determination of chlorophyll a and pheophytin a in marine and freshwater algae by fluorescence. USEPA. Washington DC.

Boehm, A.B., and Sassoubre, L.M. 2014. Enterococci as indicators of environmental fecal contamination. From url: https://www.ncbi.nlm.nih.gov/books/NBK190421/, accessed 6/4/2018.

Chariton, A., McLellan, S., and Steinberg, P. n.d. World harbours project: Indicators of sewage inputs. Unpublished. Chesapeake Bay Program. 2018. Population growth. From url: https://www.chesapeakebay.net/issues/population_growth, accessed 6/15/2018.

EPA. 2006. Bacteria Indicators of Potential Pathogens, p. 17–1 and 17–20. In Voluntary Estuary Monitoring Manual: A Methods Manual.

EPA. 2015. Recreational water quality criteria. From url: https://www.epa.gov/sites/production/files/2015-10/documents/rwqc2012.pdf, accessed 08/10/2018.

Feng, S., Bootsma, M., and McLellan, S.L. 2018. Novel human-associated *Lachnospiraceae* genetic markers improve detection of fecal pollution sources in urban waters. Appl. Environ. Microbiol. doi: 10.1128/AEM.00309-18

Ferguson, C. M., Coote, B. G., Ashbolt, N. J., and Stevenson, I. M. 1996. Relationships between indicators, pathogens and water quality in an estuarine system. Wat. Res. 30: 2045-2054.

Ferguson, D. M., Moore, D. F., Getrich, M. A., and Zhowandai, M. H. 2005. Enumeration and speciation of enterococci found in marine and intertidal sediments and coastal water in southern California. Journal of Applied Microbiology, doi: 10.1111/j.1365-2872.2005.02660.x

Hong, B., Panday, N., Shen, J., Wang, H.V., Gong, W., and Soehl, A. 2011. Modeling water exchange between Baltimore Harbor and Chesapeake Bay using artificial tracers: seasonal variations. Marine Environmental Research, 70:1, doi: 10.1016/j.marenvres.2010.03.010

Jamison, P., Hedgpeth, D., and Thebault, R. 2018. Notice of boil-water order came too late, many D.C. residents say. The Washington Post. From url: https://www.washingtonpost.com/local/dont-drink-the-water-if-you-live-in-parts-of-northeast-and-northwest-washington/2018/07/13/4a316812-8680-11e8-9e80-403a221946a7_story.html?utm_term=.d4104750d2b3&wpisrc=nl_buzz&wpmm=1, accessed 08/10/2018.

Leight, A.K., Crump, B.C., and Hood, R.R. 2018. Assesment of fecal indicator bacteria and potential pathogen co-occurrence at a shellfish growing area. Front. Microbiol., 9:384, doi: 10.3389/fmicb.2018.00384

Newton, R. J., Bootsma, M. J., Morrison, H. G., Sogin, M. L., and McLellan, S. L. 2013. A microbial signature approach to identify fecal pollution in the waters off an urbanized coast of lake Michigan. Microbiol. Environ., doi: 10.1007/s00248-013-0200-9

Newton, R. J., VandeWalle, J. L., Borchardt, M. A., Gorelick, M. H., and McLellan, S. L. 2011. *Lachnospiraceae* and *Bacteroidales* alternative fecal indicators reveal chronic human sewage contamination in an urban harbor. Appl. Environ. Microbiol., doi: 10.1128/AEM.05480-11

McLellan, S. and Eren, A.M. 2014. Discovering new indicators of fecal pollution. Trends in Microbiology. doi: 10.1016/j.tim.2014.08.002

MTAC. 2011. Sampling and data analysis protocols for Mid-Atlantic tidal tributary indicators. IAN Press.

Mote, B.L., Turner, J.W., and Lipp, E.K. 2012. Persistence and growth of the fecal indicator bacteria Enterococci in detritus and natural estuarine plankton communities. Appl. Environ. Microbiol. 78:8, 2569-2577, Doi: 10.1128/AEM.06901-11

Pachepsky, Y.A. and Shelton, D.R. 2011. Escherichia coli and fecal coliforms in freshwater and estuarine sediments. Critical Reviews in Environmental Science and Technology, 41:12, 1067-1110, doi: 10.1080/10643380903392718

Richkus, J., Wainger, L. A., and Barber, M. C. 2016. Pathogen reduction co-benefits of nutrient best management practices. Pub. Med.

Statistical analysis. 2015a. Population of Baltimore, Maryland. From url: https://statisticalatlas.com/place/Maryland/Baltimore/Population, accessed 08/10/2018.

Statistical analysis. 2015b. Population of Cambridge, Maryland. From url: https://statisticalatlas.com/place/Maryland/Cambridge/Population, accessed 08/10/2018.

Valderrama, J. 1981. The simultaneous analysis of total nitrogen and total phosphorus in natural waters. Marine Chemistry, 10, 109-122

Tables and Figures

Table 1. Colony forming units per 100 ml of *E. coli* and *Enterococcus* in June and July.

SE – Standard error

	E. coli						*Enterococcus*					
	June			July			June			July		
Sites	cfu 100 ml^{-1}	cfu 100 ml^{-1} mean	SE (±)	cfu 100 ml^{-1}	cfu 100 ml^{-1} mean	SE (±)	cfu 100 ml^{-1}	cfu 100 ml^{-1} mean	SE (±)	cfu 100 ml^{-1}	cfu 100 ml^{-1} mean	SE (±)
Jones Fall	316	142.97	82.55	256	28.94	16.71	114	63.07	36.41	66	16.37	9.45
	498			208			156			76		
	216			260			238			98		
NWA	162	180.28	104.08	276	71.45	41.25	54	11.55	6.67	52	28.31	16.34
	412			170			54			2		
	512			140			34			4		
Canton	274	97.04	56.03	10	1.15	0.67	64	21.20	12.24	0	1.15	0.67
	366			8			80			2		
	172			8			38			0		
Ft. McHenry	10	153.44	88.59	38	6.11	3.53	146	26.46	15.28	0	1.15	0.67
	216			26			156			2		
	310			34			106			0		
Main A	256	127.01	73.33	40	5.29	3.06	460	63.00	36.37	0	0.00	0.00
	342			32			396			0		
	506			30			522			0		
Main B	2	39.26	22.67	NA	NA	NA	42	20.03	11.57	NA	NA	NA
	70			NA			72			NA		
	2			NA			34			NA		
Stoney Creek	16	10.58	6.11	2	6.00	3.46	6	1.15	0.67	0	1.15	0.67
	0			8			4			0		
	20			14			4			2		
Sandy Point Beach	2	1.15	0.67	8	2.00	1.15	2	0.00	0.00	4	2.00	1.15
	0			6			2			2		
	2			4			2			6		

Table 2A. Water quality parameters in June.

Sites	Water quality parameters							
	Temperature (C)	Salinity	DO (mg/L)	pH	Transparency (m)	Chlorophyll a (µg/L)	Total Nitrogen (µM)	Total Phosphorus (µM)
Jones Fall	19.77	0.91	8.91	7.93	1.10	NA	21000.00	0.00
North West A	22.48	2.64	9.77	8.32	0.60	NA	16100.00	0.00
Canton	22.54	2.65	9.53	8.38	0.50	NA	19320.00	0.00
Ft. McHenry	22.35	2.61	9.41	8.34	0.50	NA	18480.00	0.00
Main A	21.79	1.59	8.70	7.90	0.40	NA	24220.00	0.00
Main B	22.39	3.05	9.77	8.40	0.50	NA	18480.00	0.00
Stoney Creek	24.00	3.20	10.68	8.60	0.98	22.96	49.80	2.10
Sandy Point Beach	22.70	5.80	6.83	8.20	NA	8.24	44.30	1.26

Table 2B. Water quality parameters in July.

Sites	Water quality parameters							
	Temperature (C)	Salinity	DO (mg/L)	pH	Transparency (m)	Chlorophyll a (µg/L)	Total Nitrogen (µM)	Total Phosphorus (µM)
Jones Fall	25.50	3.43	3.80	7.24	17.00	2.30	18480.00	1145.89
North West A	26.71	5.15	4.72	7.16	11.00	2.30	11676.00	1269.77
Canton	27.41	5.94	7.28	7.69	9.00	2.30	10178.00	1022.01
Ft. McHenry	27.44	5.65	6.42	7.34	9.00	2.20	11788.00	1455.59
Main A	27.32	5.75	6.89	7.56	7.00	2.10	12152.00	1300.74
Main B	NA	NA	NA	NA	NA	NA	NA	NA
Stoney Creek	28.50	5.10	8.80	8.34*	0.98	33.88	71.20	3.38
Sandy Point Beach	27.10	6.40	5.30	8.04*	NA	10.43	47.60	1.94

* - Measured in laboratory, not *in situ*.

Table 3. Total suspended solids in June and July.

	Total Suspended Solids					
	June			July		
Sites	TSS (mg)	mean	SE (±)	TSS (mg)	mean	SE (±)
Jones Fall	2.68	2.07	0.54	2.34	2.48	0.07
	2.54			2.55		
	1.00			2.55		
North West A	3.86	3.83	0.06	3.84	3.89	0.15
	3.71			3.98		
	3.91			3.86		
Canton	4.30	4.20	0.10	4.69	4.68	0.01
	4.00			4.66		
	4.31			4.69		
Ft. McHenry	4.49	4.64	0.10	4.60	4.59	0.13
	4.59			4.81		
	4.84			4.35		
Main A	5.61	5.83	0.19	4.85	4.90	0.08
	6.20			5.06		
	5.68			4.80		
Main B	4.57	4.67	0.07	NA	NA	NA
	4.63			NA		
	4.81			NA		
Stoney Creek	3.30	3.37	0.12	5.28	5.32	0.08
	3.61			5.21		
	3.21			5.48		
Sandy Point Beach	6.23	6.40	0.11	9.02	9.02	0.04
	6.61			8.95		
	6.36			9.09		

Table 4. Volatile suspended solids in June and July.

	Volatile Suspended Solids					
	June			July		
Sites	VSS (mg)	mean	SE (±)	VSS (mg)	mean	SE (±)
Jones Fall	2.69	2.61	0.22	2.55	2.53	0.01
	3.00			2.53		
	2.14			2.51		
North West A	3.51	3.74	0.11	2.71	2.76	0.02
	3.73			2.79		
	3.98			2.77		
Canton	3.33	3.28	0.16	3.48	3.54	0.03
	2.95			3.54		
	3.56			3.59		
Ft. McHenry	3.34	3.14	0.17	3.40	3.43	0.07
	2.78			3.57		
	3.29			3.33		
Main A	3.41	3.48	0.04	3.49	3.52	0.04
	3.58			3.46		
	3.45			3.60		
Main B	3.51	3.23	0.17	NA	NA	NA
	3.00			NA		
	3.19			NA		
Stoney Creek	3.22	3.13	0.06	4.00	4.00	0.02
	2.98			4.03		
	3.18			3.96		
Sandy Point Beach	3.28	3.27	0.04	3.72	3.76	0.03
	3.34			3.82		
	3.19			3.73		

Table 5. Percent organic matter in June and July.

	Percent organic matter					
	June			July		
Sites	VSS%	mean	SE (±)	VSS%	mean	SE (±)
Jones Fall	2.40	2.38	0.22	2.34	2.33	0.03
	2.74			2.37		
	1.98			2.27		
North West A	3.14	3.16	0.11	2.48	2.49	0.01
	3.35			2.49		
	2.99			2.50		
Canton	2.99	2.92	0.16	3.19	3.27	0.04
	2.62			3.31		
	3.14			3.30		
Ft. McHenry	2.99	2.80	0.17	3.02	3.14	0.09
	2.46			3.32		
	2.94			3.06		
Main A	3.03	3.06	0.04	3.10	3.13	0.03
	3.14			3.10		
	3.02			3.19		
Main B	3.22	2.90	0.17	NA	NA	NA
	2.63			NA		
	2.85			NA		
Stoney Creek	2.92	2.83	0.06	3.67	3.64	0.03
	2.72			3.69		
	2.86			3.57		
Sandy Point Beach	2.87	2.86	0.04	3.19	3.24	0.06
	2.92			3.36		
	2.77			3.17		

Figure 1. From left to right: Los Angeles, CA; Milwaukee, WI; Baltimore, MD; Boston, MA; Vigo, Spain; Plymouth, UK; Ravenna, Italy; Hong Kong, China; Xiamen, China; Darwin, Australia; Hobart, Australia; Sydney, Australia.

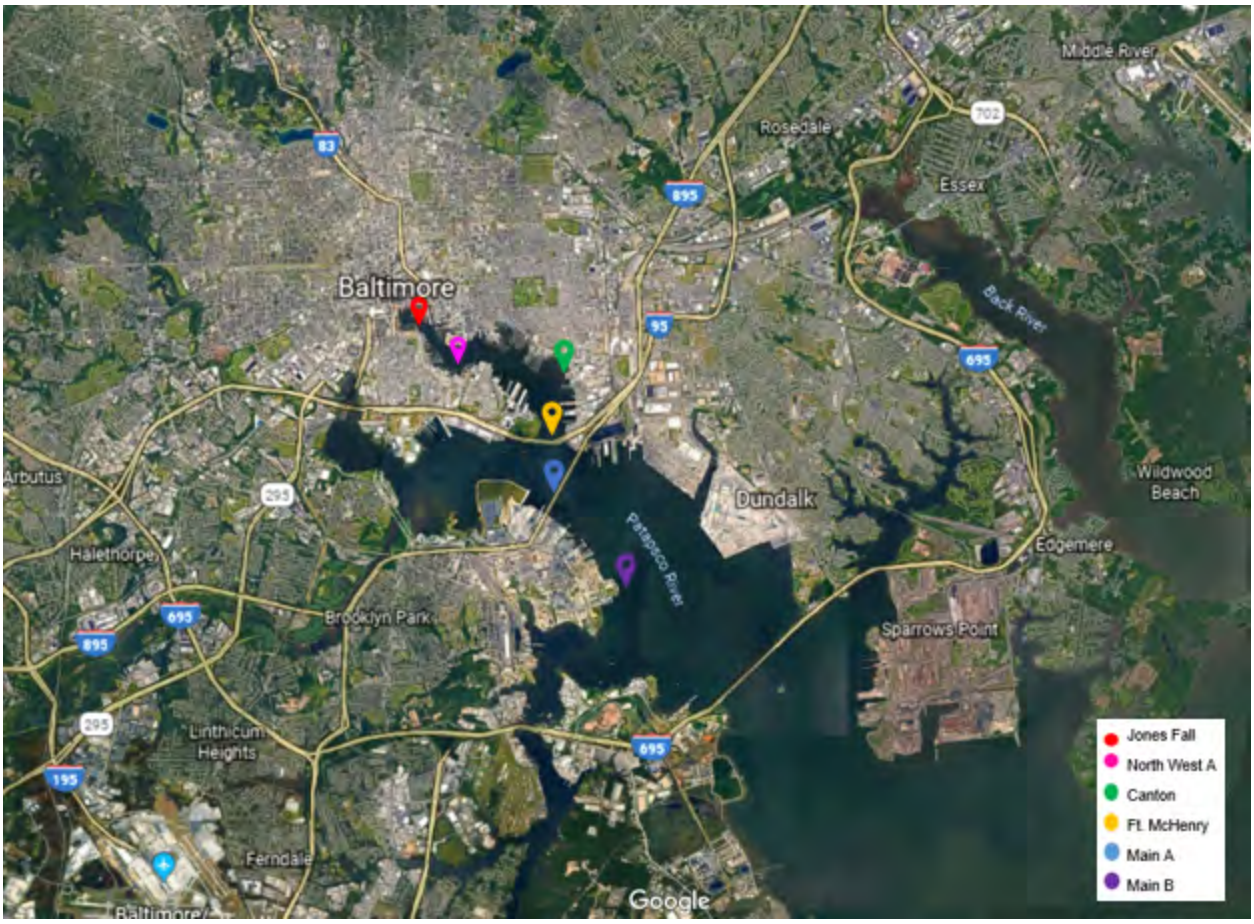

Figure 2A. Baltimore Harbor sites locations.

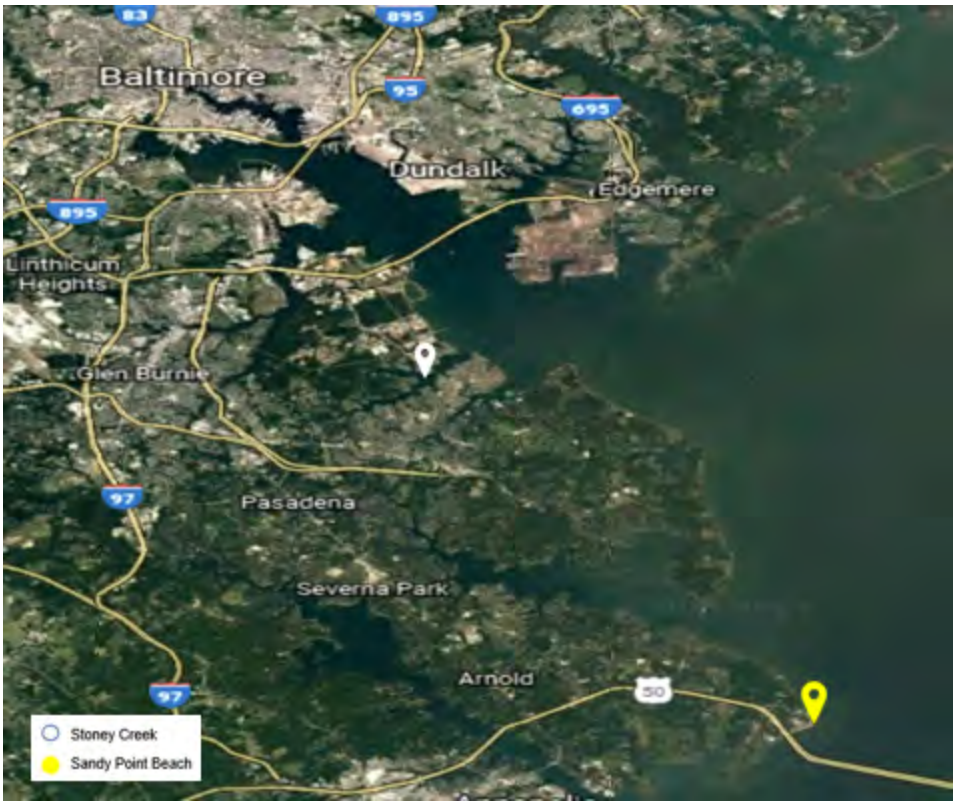

Figure 2B. Stoney Creek and Sandy Point Beach locations.

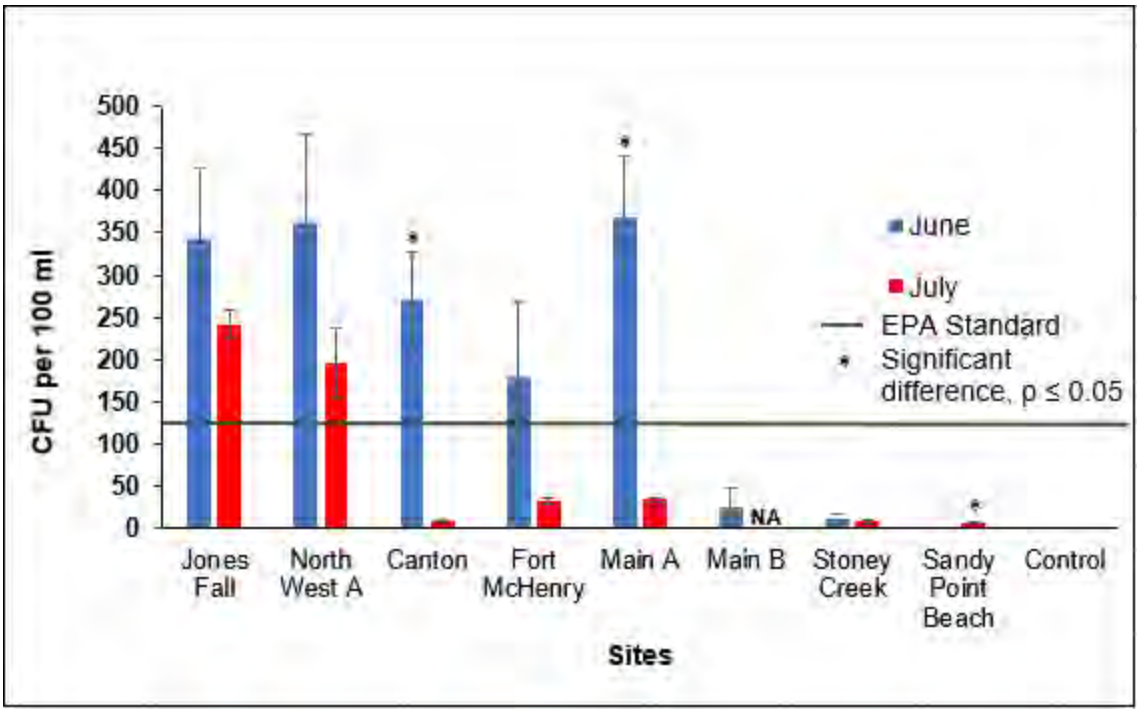

Figure 3A. *E. coli* abundance in June and July.

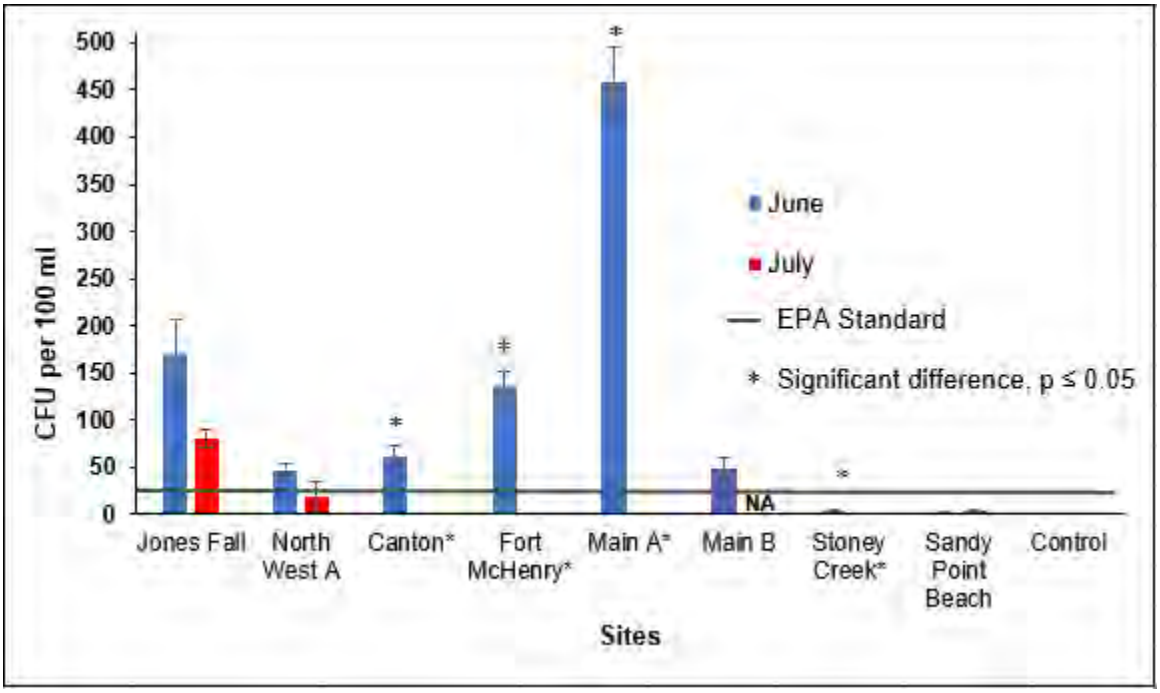

Figure 3B. *Enterococcus* abundance in June and July.

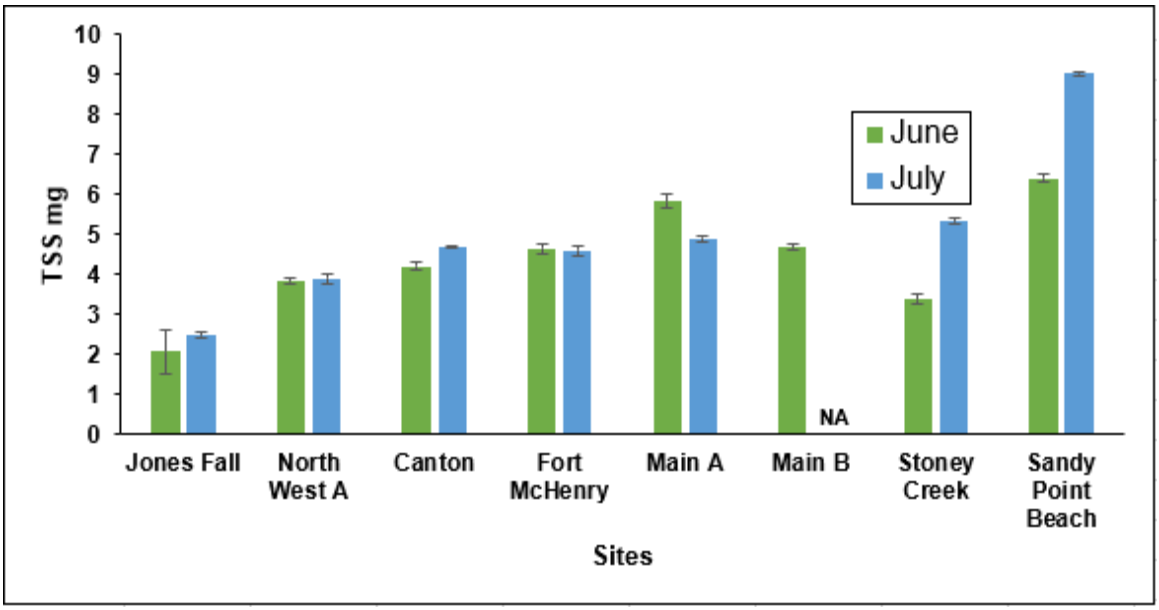

Figure 4. Total suspended solids in June and July.

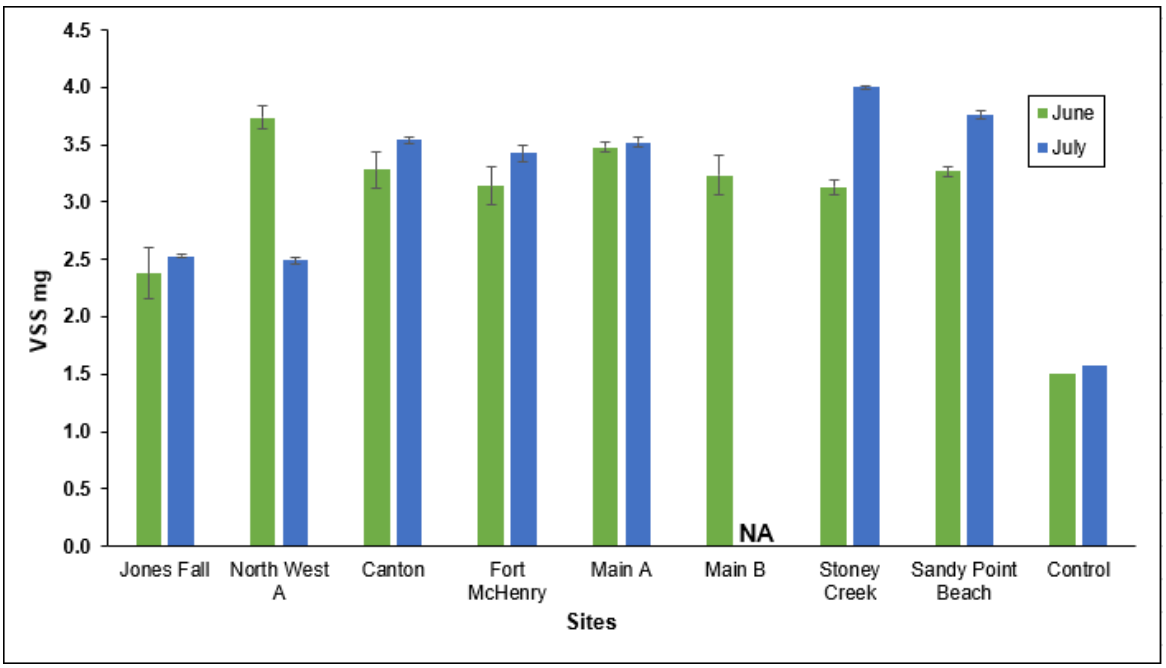

Figure 5. Volatile suspended solids in June and July.

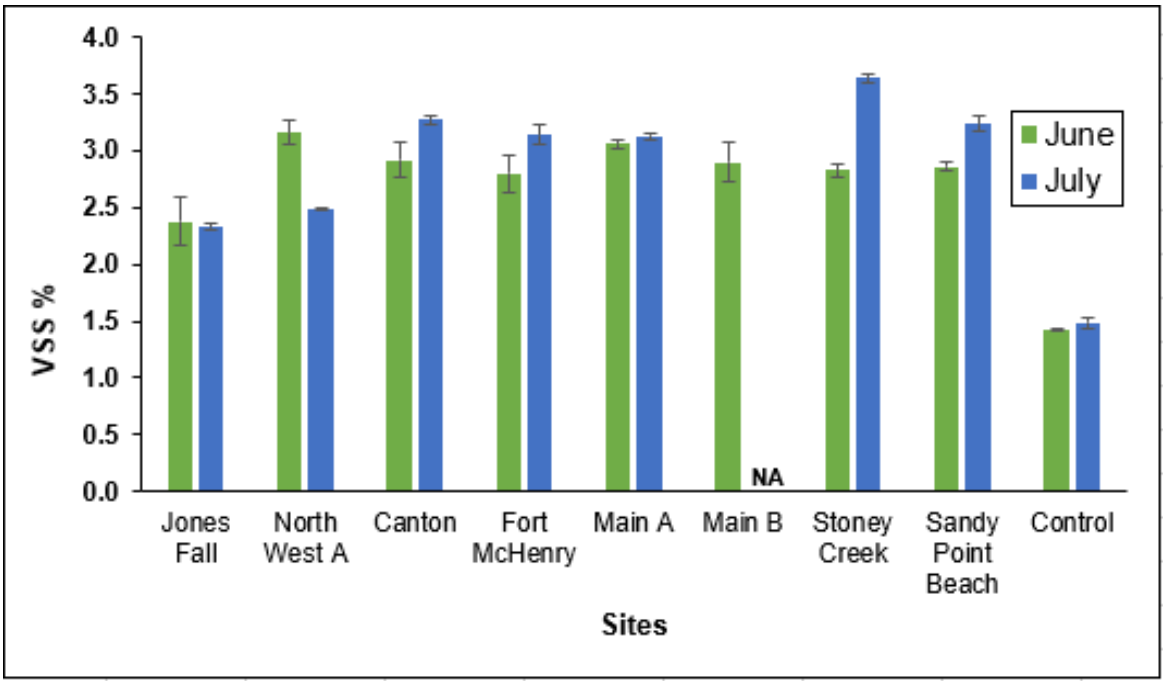

Figure 6. Percent organic matter in June and July.

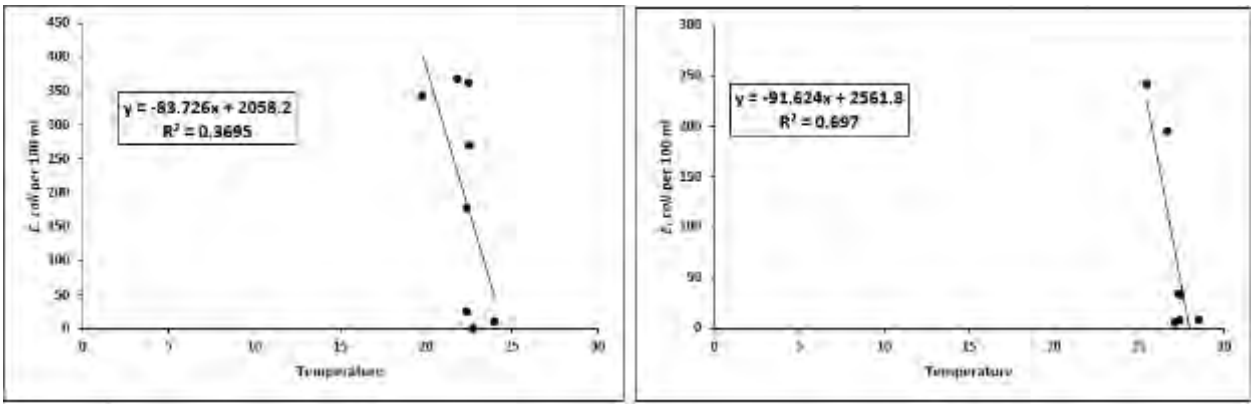

Figure 7A. Temperature with *E. coli* in June (left) and July (right).

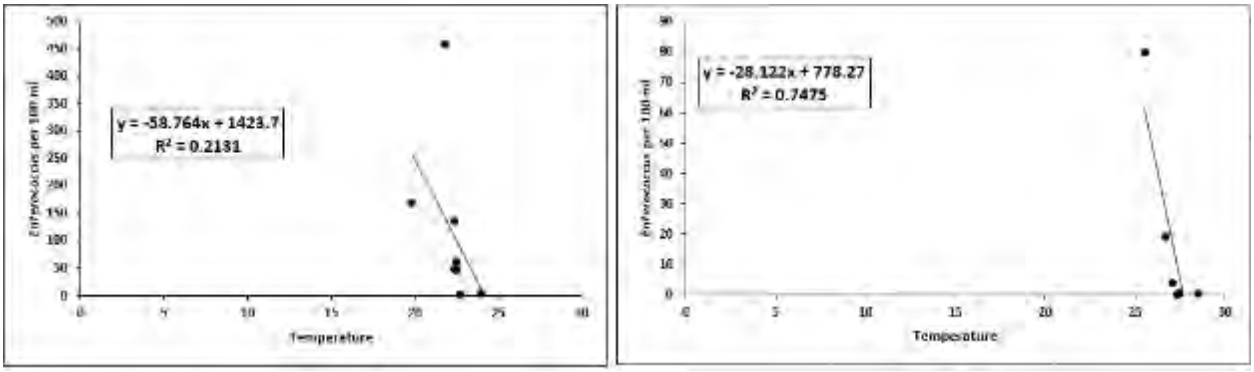

Figure 7B. Temperature with *Enterococcus* in June (left) and July (right).

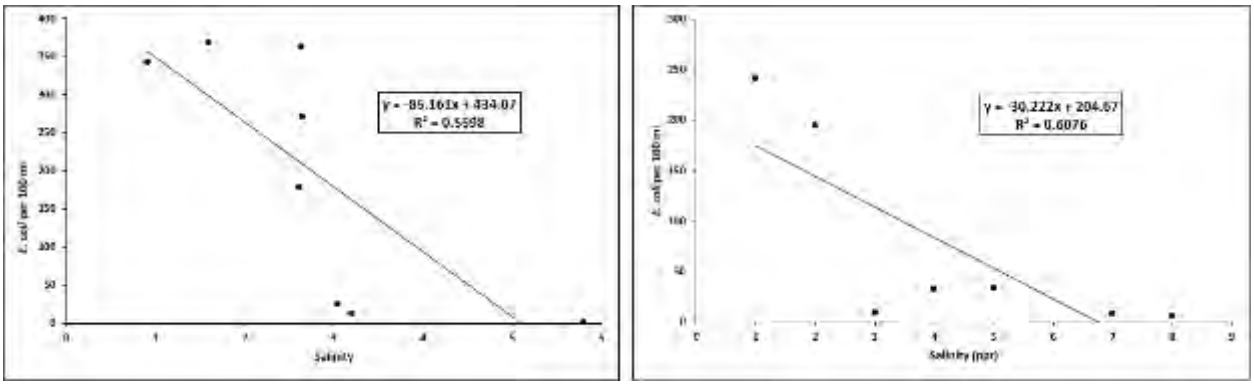

Figure 8A. Salinity with *E. coli* in June (left) and July (right).

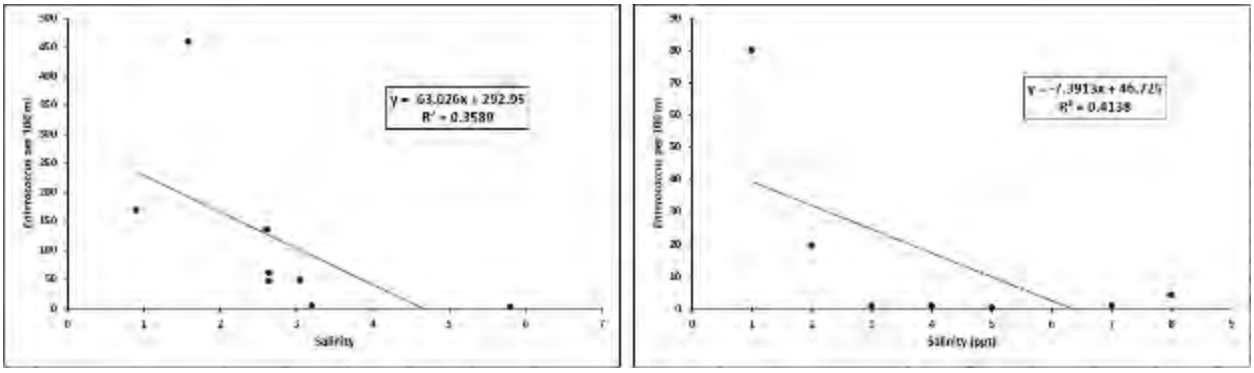

Figure 8B. Salinity with *Enterococcus* in June (left) and July (right).

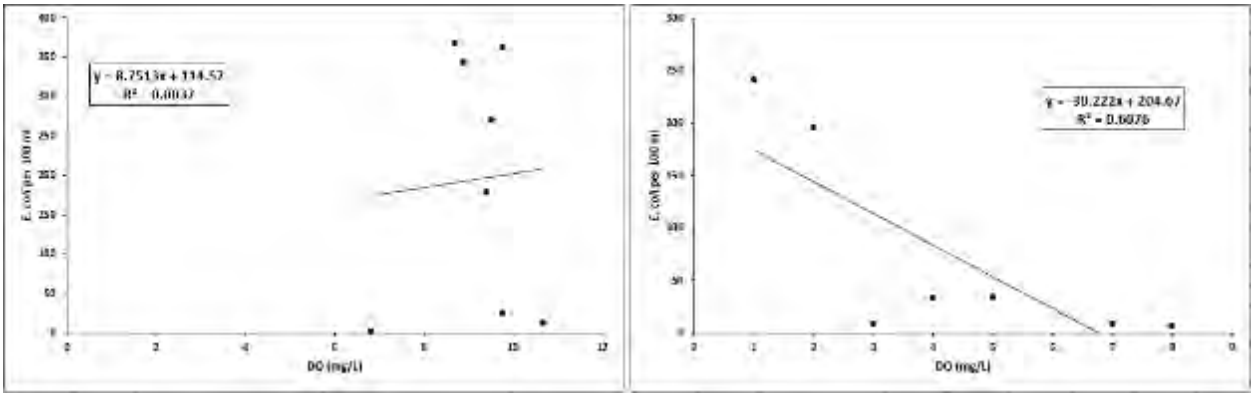

Figure 9A. Dissolved oxygen with *E. coli* in June (left) and July (right).

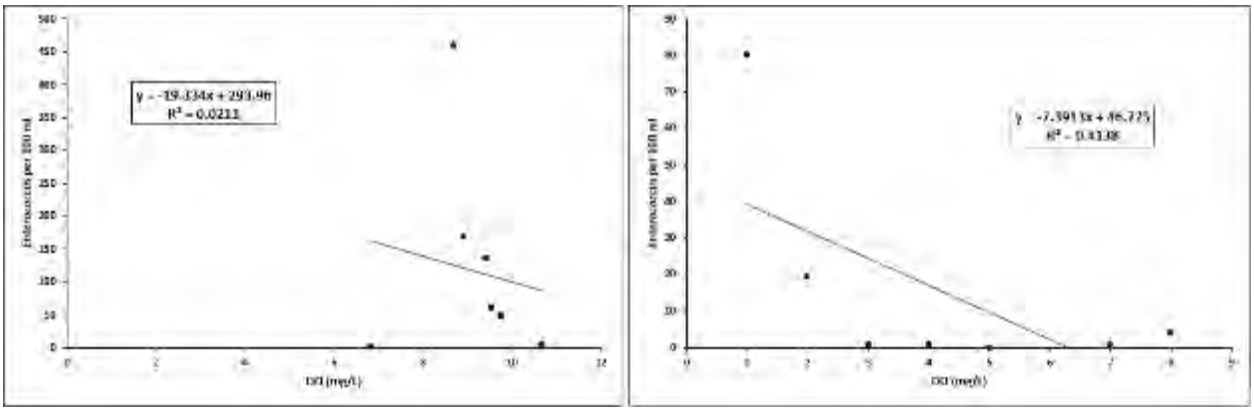

Figure 9B. Dissolved oxygen with *Enterococcus* in June (left) and July (right).

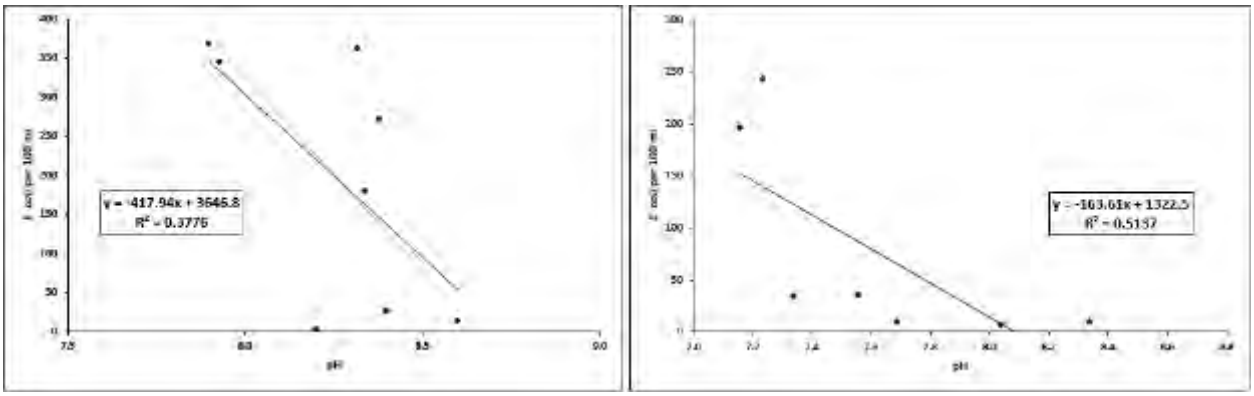

Figure 10A. pH with *E. coli* in June (left) and July (right).

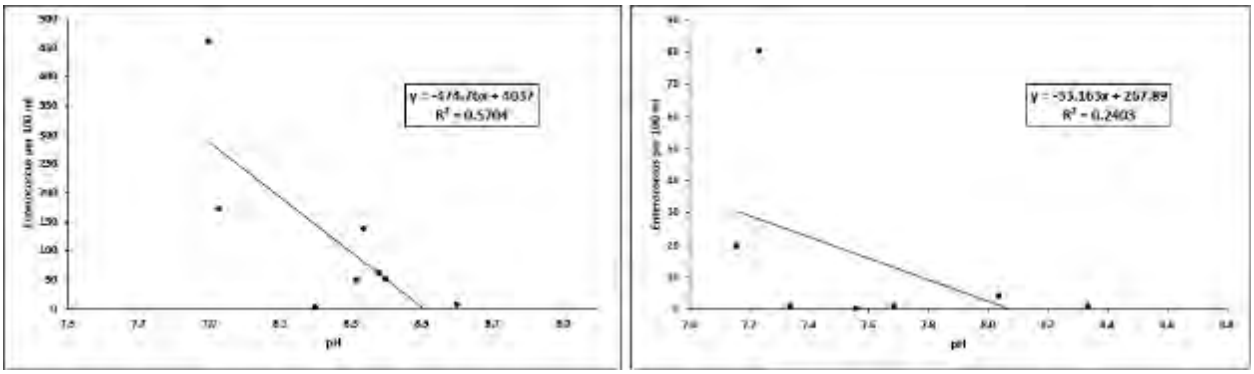

Figure 10B. pH with *Enterococcus* in June (left) and July (right).

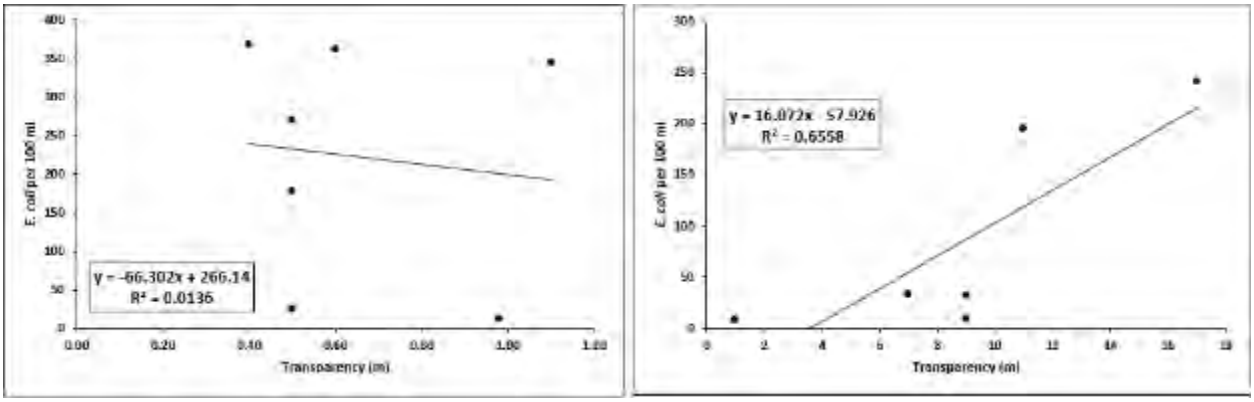

Figure 11A. Transparency with *E. coli* in June (left) and July (right).

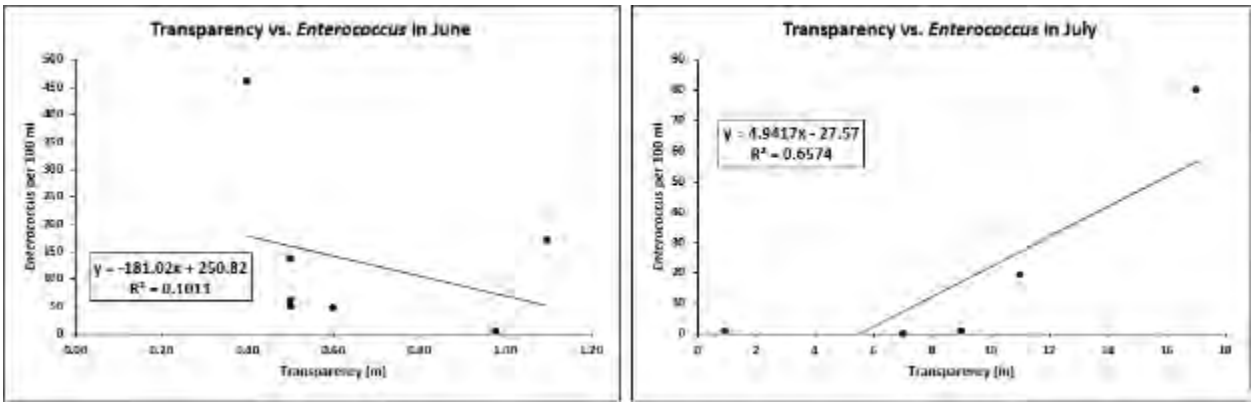

Figure 11B. Transparency with *Enterococcus* in June (left) and July (right).

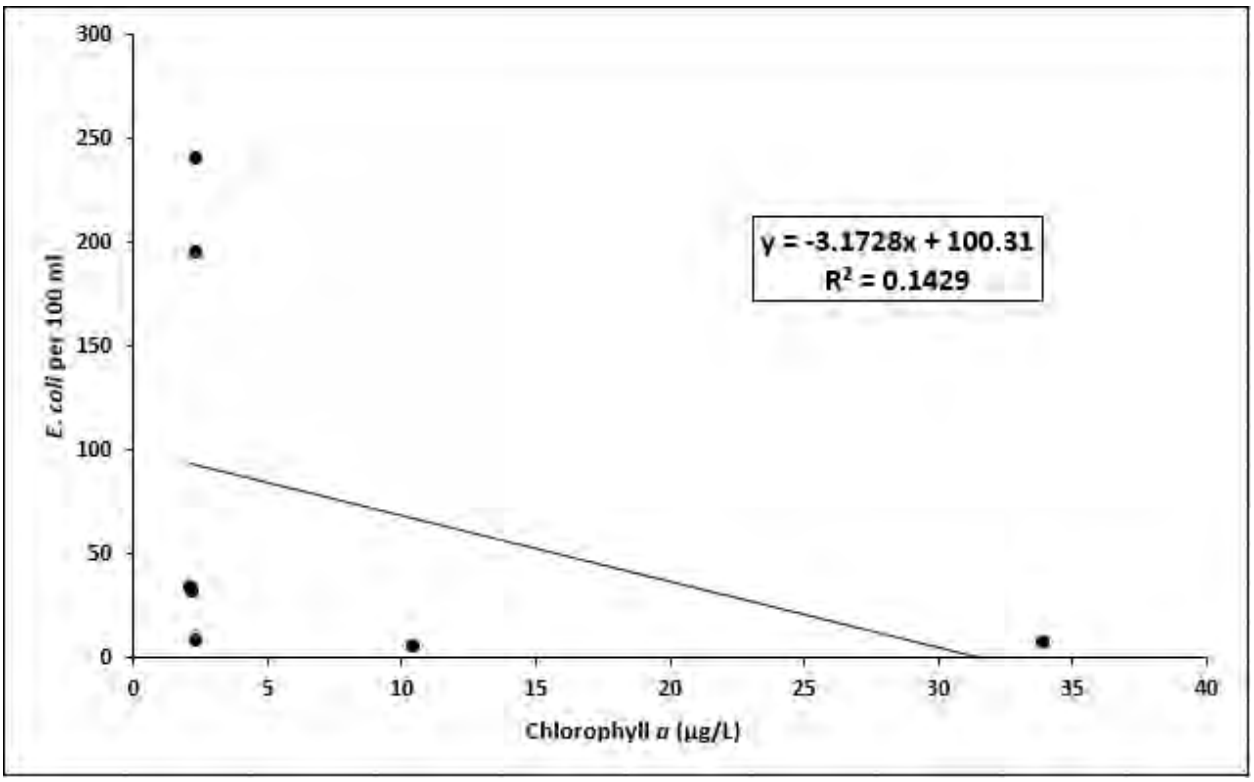

Figure 12A. Chlorophyll *a* with *E. coli* in July.

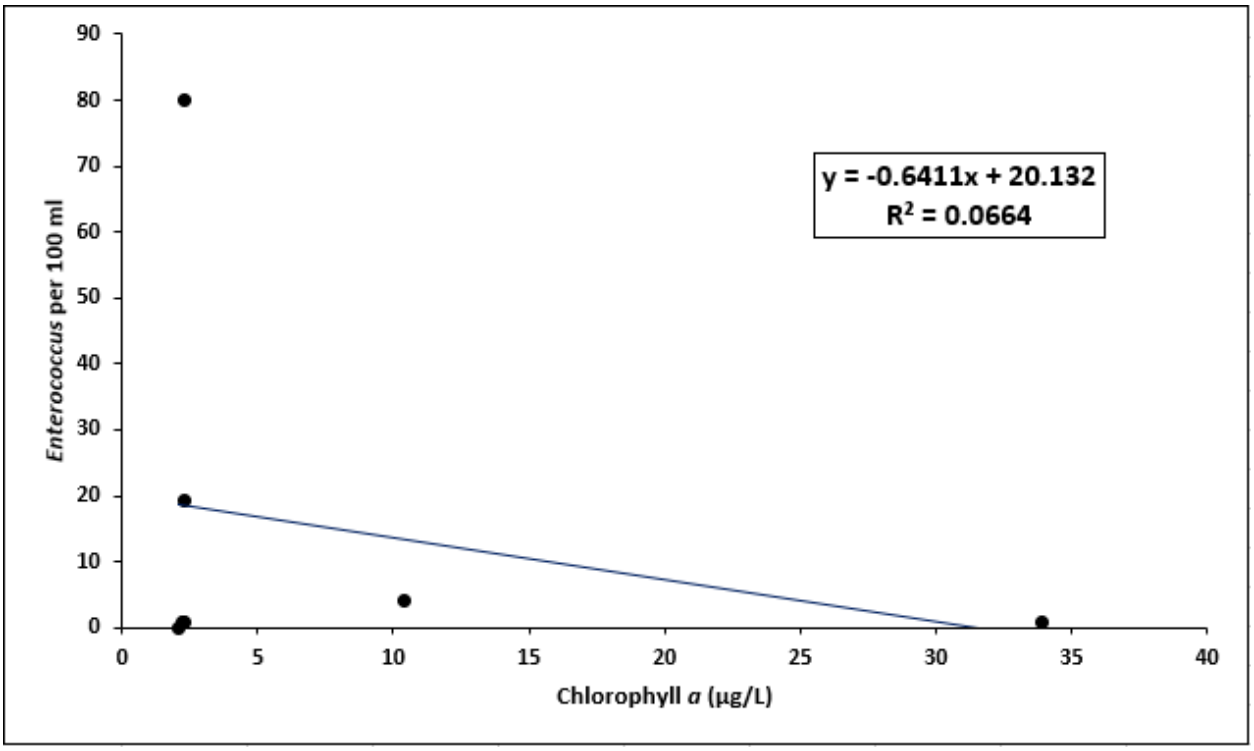

Figure 12B. Chlorophyll *a* with *Enterococcus* in July.

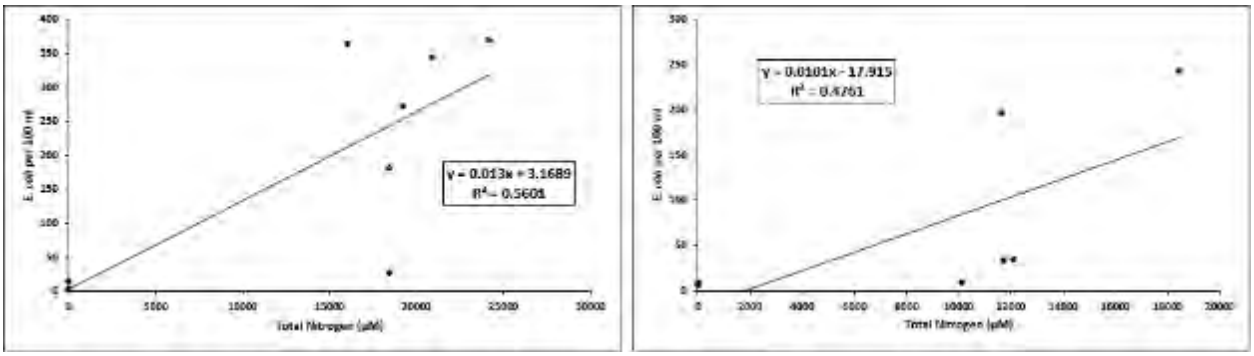

Figure 13A. Total Nitrogen with *E. coli* in June (left) and July (right).

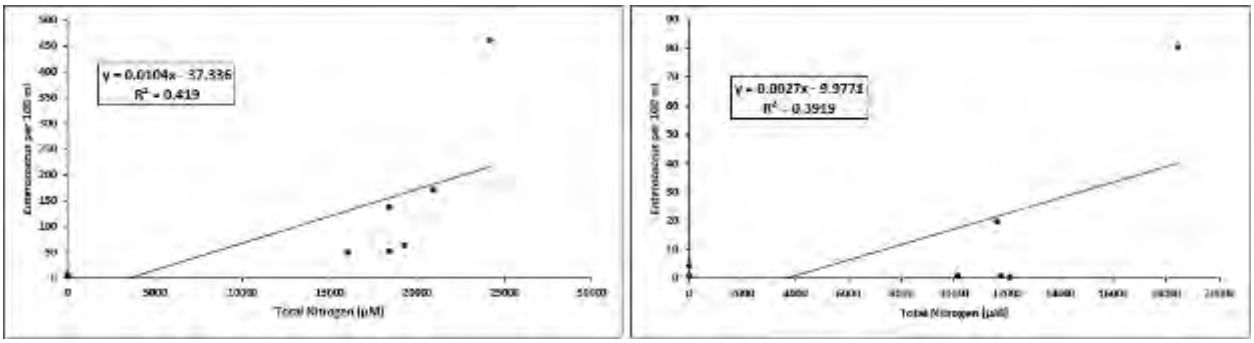

Figure 13B. Total Nitrogen with *Enterococcus* in June (left) and July (right).

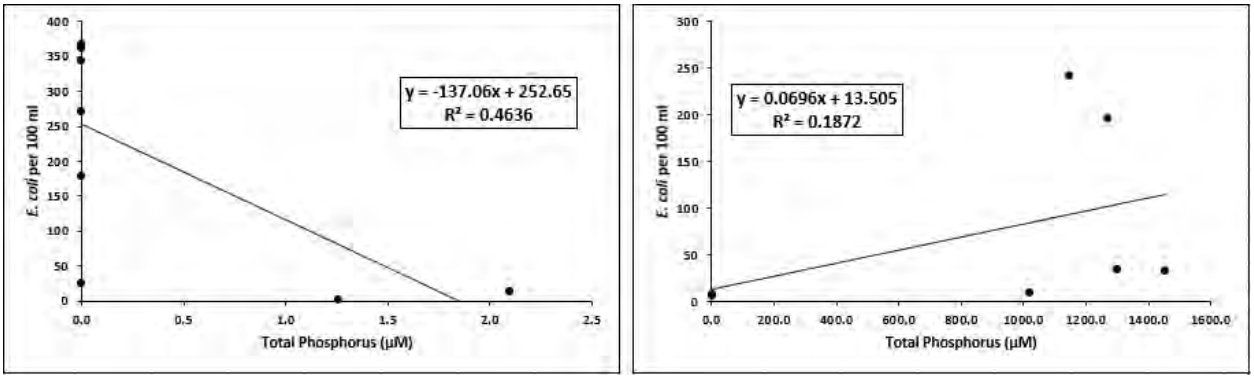

Figure 14A. Total Phosphorus with *E. coli* in June (left) and July (right).

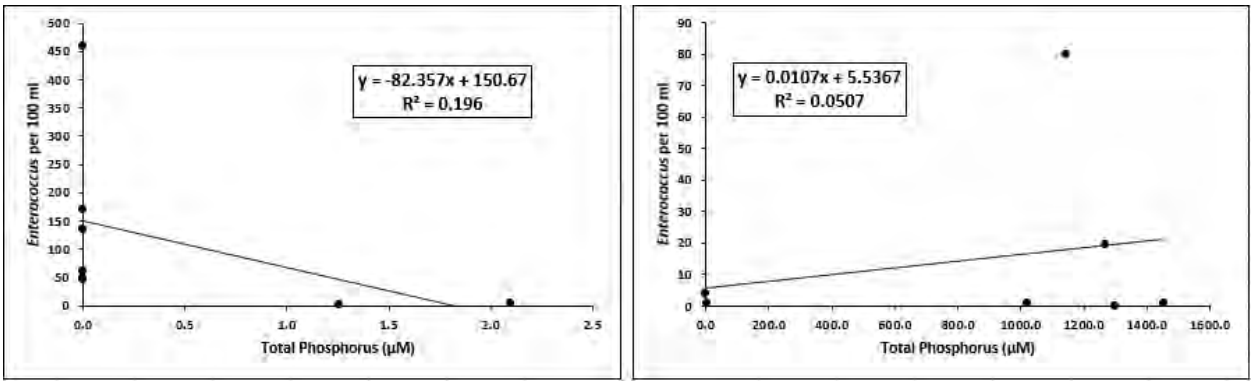

Figure 14B. Total Phosphorus with *Enterococcus* in June (left) and July (right).

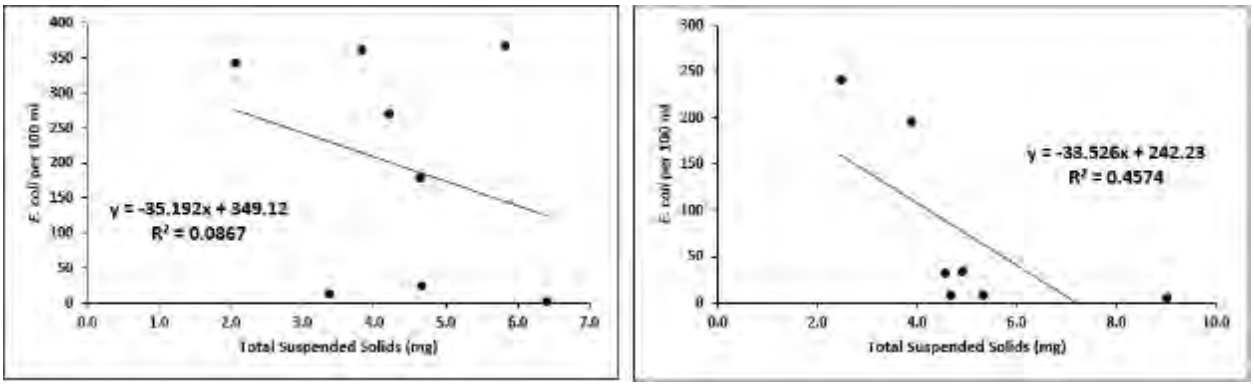

Figure 15A. Total suspended solids with *E. coli* in June (left) and July (right).

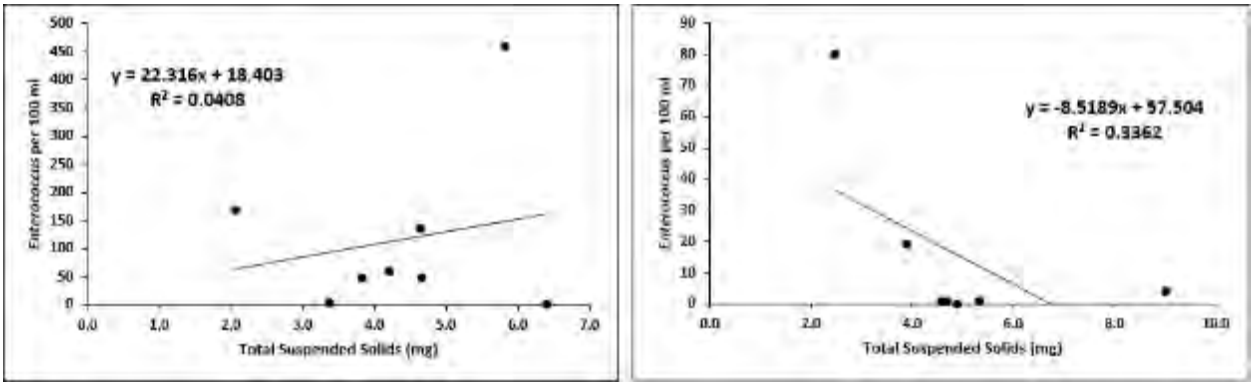

Figure 15B. Total suspended solids with *Enterococcus* in June (left) and July (right).

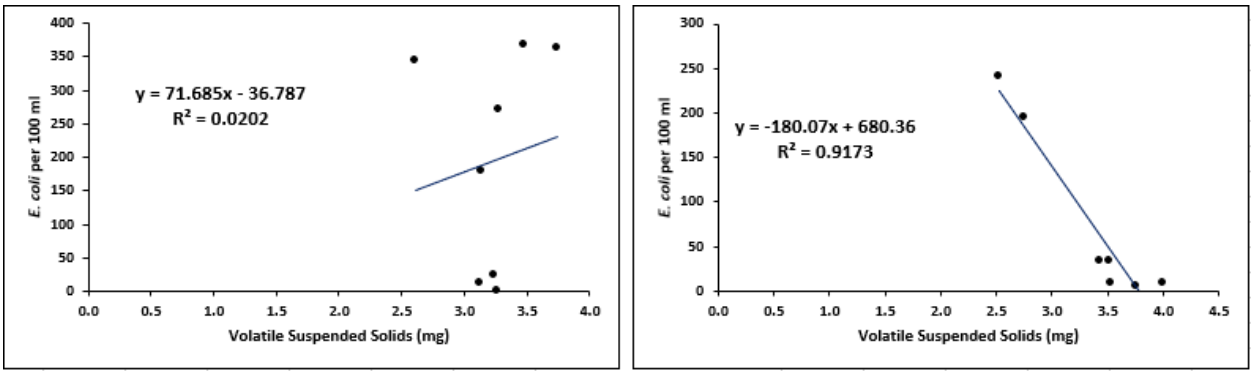

Figure 16A. Volatile suspended solids with *E. coli* in June (left) and July (right).

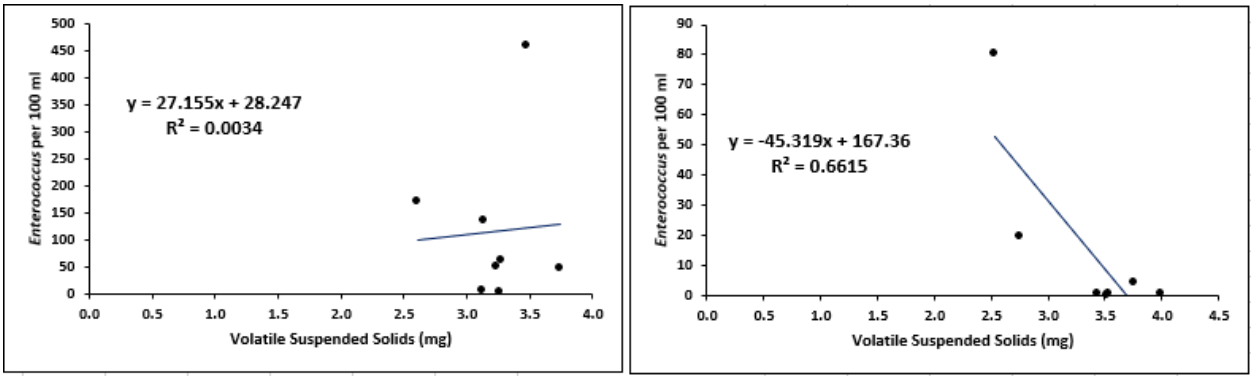

Figure 16B. Volatile suspended solids with *Enterococcus* in June (left) and July (right).

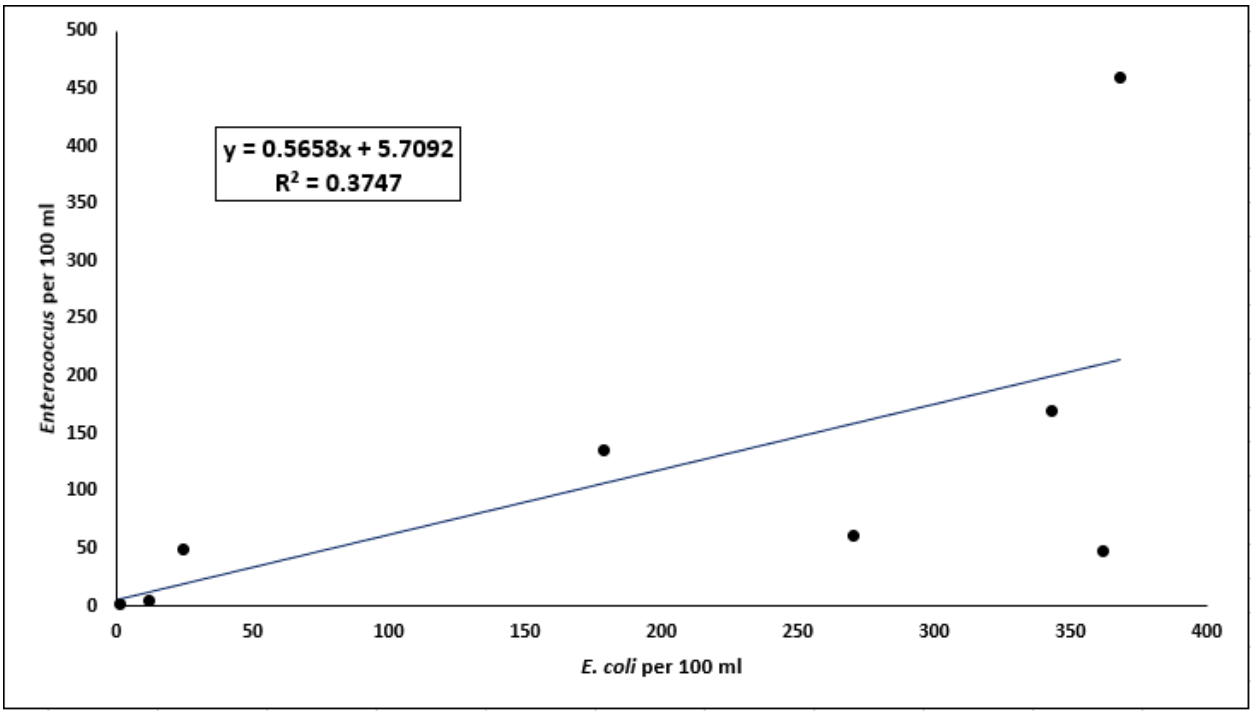

Figure 17A. *E. coli* with *Enterococcus* in June.

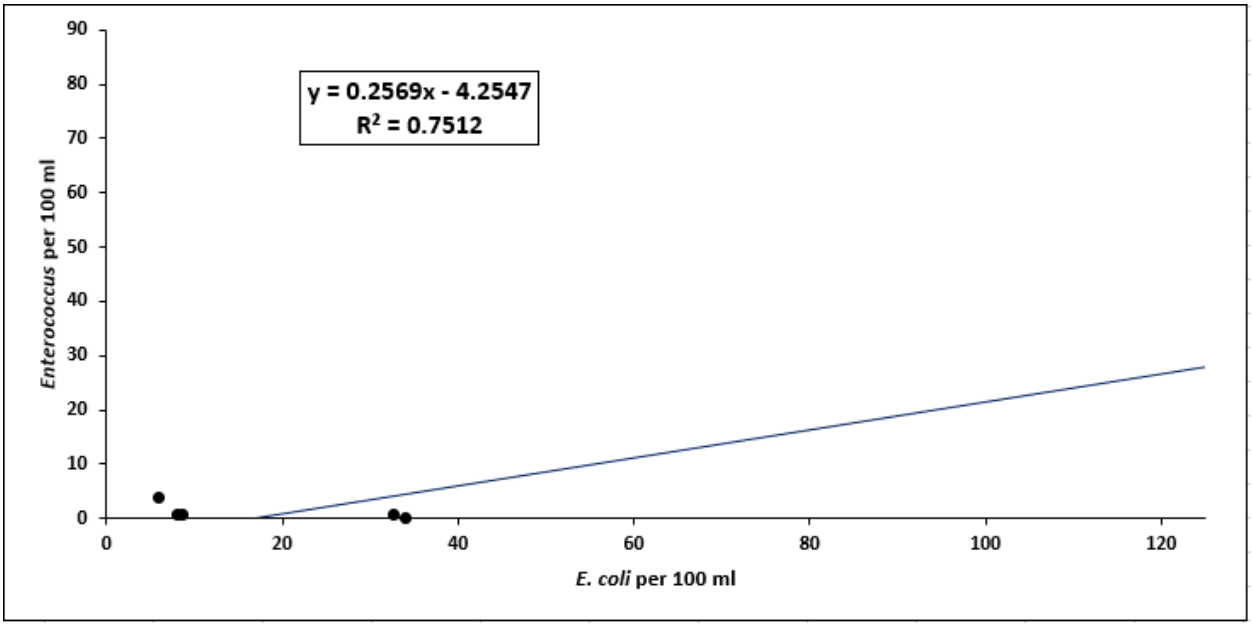

Figure 17B. *E. coli* with *Enterococcus* in July.

Relationships among sediments, nutrients, and submersed aquatic vegetation in upper Chesapeake Bay

Margaret Martinez, REU Fellow
Maryland Sea Grant

Cindy Palinkas, Associate Professor
Horn Point Laboratory, University Maryland Center for Environmental Science

Abstract

The Susquehanna River is the Chesapeake Bay's largest tributary, providing half of the bay's freshwater and 2 x 10^6 tons of sediment on average annually. This discharge passes over the Susquehanna Flats at the mouth of the river, the most upstream part of the bay. Submersed Aquatic Vegetation (SAV) presence here was found to have an important influence on water quality as it initiates a feedback loop that decreases turbidity and eutrophication, improving the health of ecosystems in the area. Additionally, this feedback loop adds to the strength and resilience of the beds during flood events. Previous research was conducted on the larger, more permanent beds in the center of the flats; we identified smaller, periphery beds for this study. We gathered push-core samples inside and outside of the perimeters of 15 beds before the peak of SAV growing season to study sedimentation patterns and composition. We used Beryllium-7 activity, grain size, and nutrient composition to infer sedimentation patterns of the ephemeral beds in the Flats. We found that there is preferential sedimentation to the southeast of the Flats, and that the geomorphology of the beds plays an important role in deposition patterns when SAV is not present.

Introduction

Sediment deposition, abundance of submersed aquatic vegetation (SAV), and water quality are all closely related and interdependent. For example, once an SAV bed is established, it perpetuates a feedback loop that contributes to its survival by attenuating wave energy and allowing for more organic, nutrient-rich sediment particles to settle out of the water column. This decreases the turbidity of the water column, allowing light to penetrate deeper into the water (Moore 2004). When an SAV bed is thriving, it can even allow clear water to extend beyond its perimeter, allowing the bed to expand its area (Gurbisz 2016). A reduction in suspended organic sediments also decreases the nutrients available to phytoplankton and epiphytic organisms, further improving water quality for SAV growth and decreasing the ecological dangers of eutrophication (Gruber and Kemp 2010). In turn, sediment composition and deposition rate affect the health and viability of an SAV bed. SAV prefer sandy sediments with relatively low organic content, and deposition rates must be high enough to bury seeds for germination (Katwijk et al 2010, Palinkas and Koch 2012). The geomorphology of SAV beds can also influence

sedimentation, with deeper channels having more sediment than shallow areas (Russ and Palinkas 2018).

An excellent example of this feedback loop is the reestablishment of the SAV beds in the Susquehanna Flats after their decimation following record flood events from hurricane Agnes in 1972 (Langland 2015, Gurbisz and Kemp 2014). The beds reappeared in 2001, becoming more abundant and resilient through the years, so that they were able to withstand the effects of two major storms (Hurricane Irene and Tropical Storm Lee) in 2011 and show signs of expansion as soon as the following year (Gurbisz and Kemp 2014).

Large SAV beds act as a sieve, filtering fluvial sediment, trapping the nutrients adhered to the particles (Gacia and Duarte 2001). Without these properties, the sediment would be released into the bay, contributing to eutrophication, a decrease in water quality, and depletion of SAV (Ward et al 1984, Cerco and Moore 2001). Previous research has shown that the large SAV beds of the Susquehanna Flats trap sediment efficiently, but less is known about the smaller beds on the periphery of the flats (Palinkas and Koch 2012). These beds are ephemeral and more susceptible to environmental changes than the larger, more stable beds. In the wake of the 2011 flood events, the beds did lose some area around the periphery, but maintained 80–100% coverage in the center, large bed of the Flats (Gurbisz et al 2016). This implies the greater resilience of the larger bed, and the susceptibility of smaller SAV beds. In order to further understand the extent of this susceptibility and the influence of small beds, more information needs to be gathered. In the past, the smaller beds showed little sedimentation, and had a lesser effect than the larger beds.

The goal of this study is to quantify sediment and nutrient burial rates in SAV patches around the Susquehanna Flats in the absence of plants. These data will be compared with previous observations to assess the role of river discharge variability and placed within the context of bed size. Past research focused on the effect of larger beds in the Flats; we will be paying close attention to the smaller, more ephemeral beds of the area.

Little deposition was noted in 2015 at small SAV beds in the Flats (Russ and Palinkas 2018). However, with the increased amount of precipitation in 2018 and a greater river discharge, we expect to see higher deposition rates. The peak river discharge of 2017 was 178,000 m^3s^{-1}, whereas the peak in 2018 before sampling was 201,000 m^3s^{-1} (USGS National Water Information System http://www.water.usgs.gov; station 01578310). Sedimentation rates observed in our samples should not surpass the summer deposition values of 2015, however, as sampling occurred during the peak of SAV growth, which allows for more sediment deposition.

Deposition rates are higher in larger SAV beds, because of their larger surface area. More plants present creates a stronger feedback loop, straining more sediment from the water column. Our samples taken at smaller beds should be less than the large beds.

Methods and Materials

Physical Setting

The Susquehanna River is the largest tributary to the Chesapeake Bay. It provides 50% of the bay's fresh water and has a significant influence on most other tributaries to the

bay (Schubel and Pritchard 1986). The Susquehanna River delivers an average annual freshwater discharge of 1100 m^3s^{-1} and 2 x 10^6 t of sediment (Schubel and Pritchard 1986, Langland 2015).

Beryllium-7 is a naturally occurring radioactive isotope that forms in the atmosphere. Of the beryllium-7 on earth's surface, 94% has landed via precipitation, where the isotopes are then adsorbed by sediment particles (Broderick 2015). Beryllium-7 has a half-life of 53.24 days and is commonly used to date recent sediment deposition. Beryllium-7 is only derived from the atmosphere; its presence in aquatic sediments is evidence of recent migration delivery from land. In times of increased precipitation—spring and early summer months—the amount of beryllium-7 is higher in coastal and estuarine waters than in dry seasons (Olsen 1986). Additionally, after just one day, 70% of beryllium-7 introduced to an estuarine system will be removed from the water column and adhere to sediment particles (Fitzgerald et al. 2001). This suggests the high efficiency and strong signal of this isotope in studying recent sedimentations. Beryllium-7 is commonly used to track spatial and temporal sedimentation patterns, especially in the Chesapeake Bay (Dibb and Rice 1989, Dibb 1989). We used beryllium-7 activity to track how smaller SAV beds affect sedimentation patterns.

Sediment Sampling and Analysis

Push-core samples will be taken at sites in Figure 1 and immediately transported to the lab for analysis. Cores will not be frozen to conserve the natural grain size. These cores will be sectioned at 1-cm intervals and analyzed for grain size through wet and dry sieving. A 64-um sieve will be used to separate the sand and mud particles after being dispersed with sodium metaphosphate and placed in an ultrasonic bath (Palinkas and Koch 2012). The sand fraction will be dried in a 60°F oven, and then dry sieved from 64–500 microns using a standard set of 13 sieves. Mud and sand data will be used in combination to determine the median diameter. If the mud fraction is >20%, it will be analyzed with a Sedigraph 5120. Gamma spectroscopy of the 477.7 keV photopeak will be used to measure beryllium-7 activities (Palinkas et al. 2005), calibrated following the procedures of Larsen and Cutshall (1981). Analysis began with the 0–1 cm interval of each core and proceeded downward in the core until beryllium-7 is no longer detected.

Results/Discussion

Statistical tests were run on the raw data collected using three groupings for each data parameter (grain size, beryllium-7 activity, and nutrient composition): inside and outside beds, northern beds to southern beds, and western to eastern beds. These comparisons were done to investigate spatial patterns of sediment deposition in the Flats.

After a paired t-test on the outside and inside bed data, a p-value greater than 0.1 was calculated, suggesting that there was no significant statistical difference between sediment size, beryllium-7 activity, or nutrient concentration between the samples collected inside and outside the selected SAV beds. These samples were taken in mid-June, well before the peak of SAV growth. Without a great amount of SAV present, there is no expected difference between outside and inside the bed. With little SAV present, there is little influence made on sedimentation encouraged inside the bed. Therefore, we see no significant difference in deposition composition or rate because there were not enough plants present to influence a change.

When comparing the data from the northern and southern beds, no statistically significant difference was found in nutrient composition or beryllium-7 activity; p-values were greater than 0.1 (Figure 2). However, there was a difference seen in sediment size, with finer sediments favoring the southern beds. This pattern was noted through a t-test with a p value of 0.06. This is logical as the southern beds were farther from the mouth of the Susquehanna River, indicating it took more time for the sediments to deposit in the southern beds, allowing for finer sediments to deposit. SAV interaction the sediments encountered between the river mouth and the southern beds may also have encouraged the finer sediments to settle out of the water column.

Comparisons between the western and eastern beds resulted in statistically significant patterns in beryllium-7 activity, grain size, and nutrient composition. Beryllium-7, carbon percentage, and nitrogen percentage were all higher in eastern beds than western beds (p values 0.02, 0.03, and 0.02 respectively). A higher beryllium-7 activity is indicative of a higher deposition rate, which would logically explain an increased nutrient percentage as more sedimentation would bring more nutrients. This pattern is shown in Figures 3, 4, and 5. Average sediment size was higher in the western beds, which could be explained partly by similar reasons to why southern beds had finer sediments. Eastern beds are closer to the center of the river mouth and downstream from more SAV beds. This means the sediments that settle in eastern beds may have a greater SAV interaction and more time to fall through the water column, as they are also farther in distance from the mouth of the river. However, there may be a geomorphic influence as well. There is a channel dividing the eastern beds and western beds that is too deep for SAV to grow; visualized as white space between sampled beds seen in figures 7 and 8. The greater water velocities through this channel could prevent as much fine sediment from settling, whereas the eastern beds are under the protection of the adjacent large SAV bed and its established, resilient feedback loop.

Conclusion

SAV presence is an important factor in estuarine water quality, as well as the base of many ecosystems. The health of SAV beds play an integral role in improving water quality. This research will add to our knowledge of SAV function and how to further aid restoration of the Chesapeake Bay and other estuarine systems. Through improved knowledge of their role in sediment and nutrient trapping, we can gain insight on the relationship between SAV beds and sedimentation in different climate influences. This study is in the unique position to study these relationships in a year with relatively high spring river discharge and when plants are absent in the spring season. The next step in this study is to sample the same sites in late summer to observe the influence of SAV growth.

After our sampling period, there was a record amount of summer rain in the Susquehanna watershed and the Chesapeake Bay region. The peak 2018 river discharge to date is 365,000 m^3s^{-1}, suggesting abnormally high deposition rates. The data gathered during this project could serve as valuable before data for sampling in the late summer.

The Susquehanna Flats are in a vital upstream location. Any ecological activity has the potential to influence the entire Chesapeake Bay. Further understanding of the interdisciplinary, ecological relationships that influence the flats could lend knowledge to the further protection and restoration of the Chesapeake Bay. This information is

especially important in predicting the impact of unique natural conditions, such as the increased sedimentation, nutrient loading, and SAV survival after flood events.

Acknowledgements

Special thanks to Dr. Cindy Palinkas and Emily Russ for their time, guidance, and encouragement through this project. Additional thanks to Maryland Sea Grant, the University of Maryland Center for Environmental Science, and Horn Point Laboratory for the opportunity to conduct this research, lending their facilities, and having such a welcoming community. This project was graciously funded by NSF grant OCE-1756244.

References

Broderick, C. A. 2015. Tracing Sediment in the Subsurface Using Beryllium-7: Green River Basin, KY. Master's Thesis. Louisiana State University.

Cerco, C. F., and K. Moore. 2001. System-wide submerged aquatic vegetation model for Chesapeake Bay. Estuaries. 24: 522–534. doi:10.2307/1353254

Dibb, J. E. 1989. Atmospheric deposition of beryllium 7 in the Chesapeake Bay region. Journal of Geophysical Research. 94: 2261–2265. doi:10.1029/JD094iD02p02261

Dibb, J. E., and D. L. Rice. 1989. Temporal and Spatial Distribution of Beryllium-7 in the Sediments of the Chesapeake Bay. Estuarine, Coastal and Shelf Science. 28: 395–406. doi:doi.org/10.1016/0272-7714(89)90087-5

Fitzgerald, S. A., J. V. Klump, P. W. Swarzenski, R. A. Mackenzie, and K. D. Richards. 2001. Beryllium-7 as a Tracer of Short-Term Sediment Deposition and Resuspension in the Fox River, Wisconsin. Environmental Science & Technology. 35: 300–305. doi:10.1021/es000951c

Gacia, E., and C. M. Duarte. 2001. Sediment Retention by a Mediterranean *Posidonia oceanica* Meadow: The Balance between Deposition and Resuspension. Estuarine, Coastal and Shelf Science. 52: 505–514. doi:10.1006/ecss.2000.0753

Gurbisz, C., W. M. Kemp, L. P. Sanford, and R. J. Orth. 2016. Mechanisms of Storm-Related Loss and Resilience in a Large Submersed Plant Bed. Estuaries and Coasts. 39: 951–966. doi:10.1007/s12237-016-0074-4

Gruber, R. K., and W. M. Kemp. 2010. Feedback effects in a coastal canopy-forming submersed plant bed. Limnology and Oceanography. 55: 2285–2298. doi:10.4319/lo.2010.55.6.2285

Katwijk, M. M. van, A. R. Bos, D. C. Hermus, and W. Suykerbuyk. 2010. Sediment modification by seagrass beds: Muddification and sandification induced by plant cover and environmental conditions. Estuarine, Coastal and Shelf Science. 89: 175–181. doi:10.1016/j.ecss.2010.06.008

Langland, M. J. 2015. Open-File Report. Open-File Report 2014–1235. 2014–1235 US Department of the Interior, US Geological Survey.

Larsen, I. L., and N. H. Cutshall. 1981. Direct determination of 7Be in sediments. Earth and Planetary Science Letters. 54: 379–384. doi:10.1016/0012-821X(81)90053-4

Moore, K. A. 2004. Influence of Seagrasses on Water Quality in Shallow Regions of the Lower Chesapeake Bay. Journal of Coastal Research 162–178. doi:10.2112/SI45-162.1

Olsen, C. R. 1986. Geochemistry and Deposition of 7Be in River-Estuarine and Coastal Waters. Journal of Geophysical Research. 91: 896–908.

Palinkas, C. M., C. A. Nittrouer, R. A. Wheatcroft, and L. Langone. 2005. The use of 7Be to identify event and seasonal sedimentation near the Po River delta, Adriatic Sea. Marine Geology. 222–223: 95–112. doi:10.1016/j.margeo.2005.06.011

Russ, E. R., and C. M. Palinkas. 2018. Seasonal-Scale and Decadal-Scale Sediment-Vegetation Interactions on the Subaqueous Susquehanna River Delta, Upper Chesapeake Bay. Estuaries and Coasts. doi:10.1007/s12237-018-0413-8

Schubel, J. R., and D. W. Pritchard. 1986. Responses of Upper Chesapeake Bay to Variations in Discharge of the Susquehanna River. Estuaries. 9: 236–249. doi:10.2307/1352096

Ward, L. G., W. Michael Kemp, and W. R. Boynton. 1984. The influence of waves and seagrass communities on suspended particulates in an estuarine embayment. Marine Geology. 59: 85–103. doi:10.1016/0025-3227(84)90089-6

Figures

Figure 1. Marked above are the locations of the SAV beds to be sampled. The outside and inside of each bed will be sampled in triplicate. This pattern was chosen in order to compare sedimentation within and along the exterior of SAV beds.

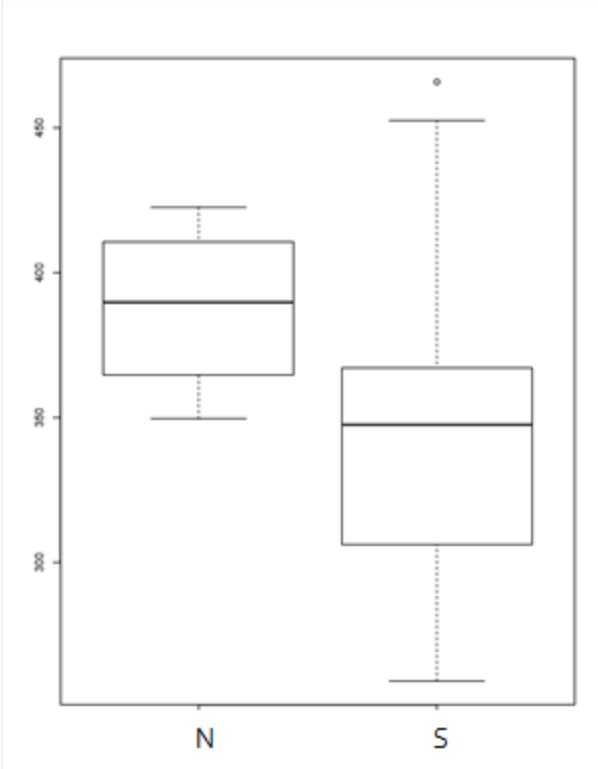

Figure 2. Average sediment sizes in northern and southern beds of top 1 cm layer of cores taken in micrometers. Sizes are statistically different with a p value of 0.06. Southern beds have significantly smaller sediments.

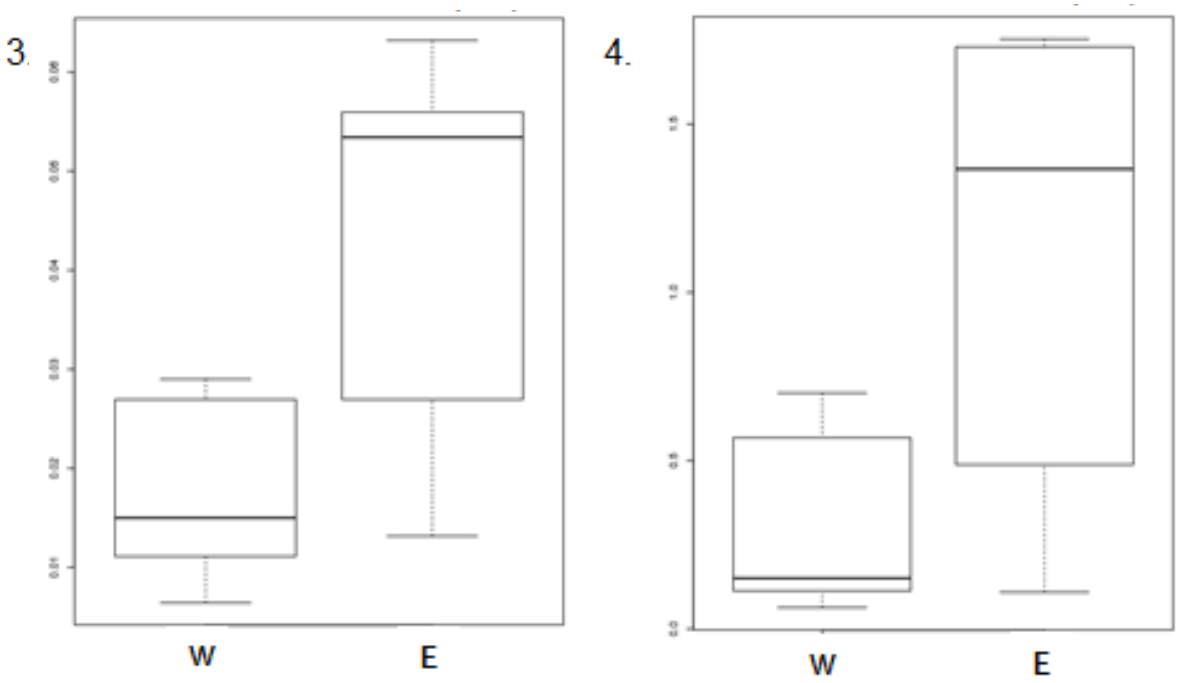

Figures 3. and 4. Percent of nutrient composition. Comparing western and eastern beds, eastern beds have significantly higher carbon and nitrogen compositions, supported by a t test resulting in a p-values of 0.02 and 0.03, respectively.

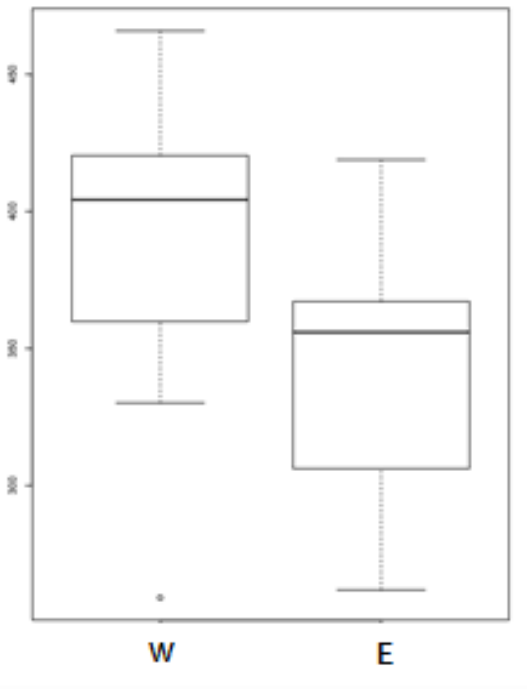

Figure 5. Comparison of average sediment size in western and eastern beds. Western beds have a significantly larger grain size than eastern beds supported by a p-value of 0.04.

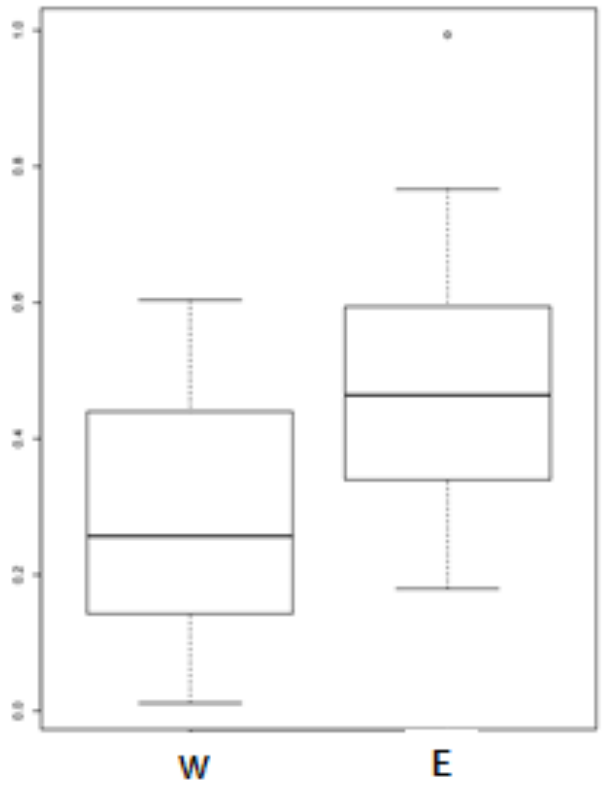

Figure 6. Average Beryllium-7 activity. Western beds compared to eastern beds. Eastern beds show significantly higher activity than western beds, supported by p-value of 0.02.

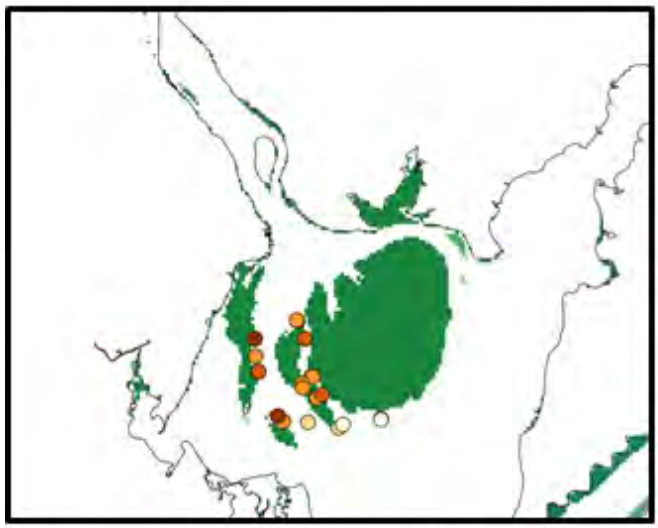

Figure 7. Each dot is the location of a sampled SAV bed. Darker dots signify larger sediment grain size, lighter is smaller grain size.

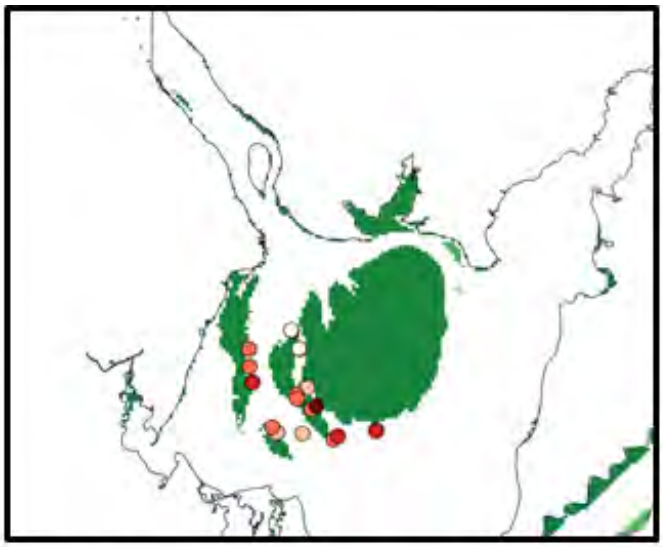

Figure 8. Each dot is the location of a sampled SAV bed. Darker red indicates higher 7Be activity, lighter is lower 7Be activity. In beds where there were multiple samples analyzed, an average was taken.

Evaluating the effect of nutrient enrichment on phytoplankton growth rate in the Chesapeake Bay

Kristin Ratliff, REU Fellow
Maryland Sea Grant

Greg Silsbe, Assistant Research Professor
Horn Point Laboratory, University of Maryland Center for Environmental Science

Abstract

Phytoplankton are important photosynthetic microorganisms that support aquatic food webs and influence the physical and biogeochemical properties of aquatic ecosystems. This project examined how nitrogen, phosphorus, and light regulated phytoplankton growth rates during summer months in the Chesapeake Bay. Water samples from a mesohaline monitoring station and the Choptank River were collected monthly, incubated, and analyzed to assess how phytoplankton respond to experimental enrichment of nitrogen and phosphorus by using both flow cytometry and chlorophyll concentrations. Growth rates between 0 and 1.0 day^{-1} in the Bay and 0.5 and 2.0 day^{-1} in the Choptank River were observed. Comparing growth between treatments showed no statistically significant differences, suggesting light limitation. However, large within treatment variations revealed a need for more rigorous methodology moving forward. As growth rates are measured into the future, Chesapeake Bay models can be evaluated for accuracy, thus improving predictions of nutrient management plans seeking to improve water quality and ecosystem services.

Introduction

Phytoplankton are microscopic photosynthetic organisms that live in the surface layers of aquatic environments. Included in this group are diatoms, dinoflagellates, and cyanobacteria, among others. At a healthy level of abundance, they are important to ecosystem quality. They produce over half of global oxygen (Field et al. 1998) and form the base of aquatic food webs that support commercially and ecologically important fisheries such as fish, blue crabs, and oysters in the Chesapeake Bay. At greater population densities, phytoplankton have negative impacts on ecosystem health. Their biomass decreases water clarity and blocks sunlight from penetrating the water column, prohibiting the growth of submersed aquatic vegetation that other organisms rely on for food and habitat. In addition, decomposition of phytoplankton biomass is a contributor to bottom water anoxia, or lack of oxygen, that makes the water uninhabitable (Kemp et al. 2005).

Phytoplankton need resources for growth and reproduction including sunlight, carbon dioxide, and nutrients such as nitrogen and phosphorus (Behrenfeld et al. 2008). Excessive enrichment of the water with nutrients is called eutrophication and it stimulates phytoplankton growth. Since European settlement of the watershed, the Chesapeake Bay has experienced a six to eight-fold increase in nitrogen inputs and a 13- to 24-fold increase in phosphorus inputs (Boynton et al.

1995). Evidence from sediment cores analyzed for phytoplankton sedimentation rates, the abundance of sulfur, and other chemical indicators of low dissolved oxygen concentration also reveal that eutrophication and hypoxia have increased since European settlement (Cooper and Brush 1991). The nutrients come from a variety of sources including agricultural runoff, atmospheric deposition, and point and nonpoint source pollution, in addition to those recycled and stored in sediments. Temporal variability in nutrient inputs creates a cycle of variable phytoplankton biomass throughout year (Kemp et al. 2005).

In the spring, the Chesapeake Bay watershed receives a high volume of precipitation, which generates large volumes of runoff that carry a heavy load of nitrogen and silica into the Chesapeake. It feeds a large bloom of phytoplankton, particularly silicate-rich diatoms (Conley and Malone 1992; Harding et al. 2015), called the biomass maximum (Malone et al. 1996). The Bay's nutrient budget shows a net flow of nitrogen from freshwater to the ocean (Boynton et al. 1995) as evidence of the excess loading. The abundance of nitrogen and silica makes phosphorus the nutrient limiting to phytoplankton growth, with most phosphorus inputs going to the lower segment of the Bay near the Atlantic Ocean where there is flux of phosphate from the sediment into the water (Boynton et al. 1995). However, phytoplankton require less phosphorus relative to nitrogen in a ratio of 16:1 (Goldman et al. 1979), so excessive growth occurs even in waters with little phosphorus enrichment. This is called an algal bloom, and the decomposition of biomass by aerobic bacteria in late spring depletes dissolved oxygen.

Nitrogen is not depleted relative to phosphorus until the end of spring when the volume of freshwater input decreases. The main nitrogenous source in the summer is mediated by the decomposition and remineralization of spring blooms (Boynton and Kemp 1985). Its available supply is dependent upon upwelling and the strength of stratification of the water column that suppresses vertical transportation (Behrenfeld et al. 2008). Depleted silica resources also induce a shift from diatoms to dinoflagellates and cyanobacteria (Harding et al. 2015). Into the summer, more active zooplankton grazers control biomass (Malone et al. 1996), and depleted nutrients are thought to regulate phytoplankton growth. Oceanic waters intrude further into the Bay, carrying a greater ratio of phosphorus relative to nitrogen. Multiple experiments have recorded nitrogen limitation during the summer in the Chesapeake Bay, supported by environmental nutrient concentrations, enzyme activity, nutrient turnover rates, and responses of phytoplankton to nutrient inputs by increased growth rates (Fisher et al. 1992, Fisher et al. 1999).

Spring is a crucial time for nutrient reduction because decomposition of the large spring biomass is what contributes bottom-water anoxia. Scientists and managers use the Chesapeake Bay Environmental Model Package to predict how phytoplankton in the Bay will respond under different nutrient scenarios by projecting the magnitude, time, and location of blooms (https://www.chesapeakebay.net/what/programs/modeling, 15 June 2018) with the Corps of Engineers Integrated Compartment Water Quality Model (CE-QUAL-ICM) of eutrophication. The eutrophication model simulates nutrient cycles and phytoplankton growth. It is paired with the Computational Hydrodynamics in Three-Dimensions (CH3D) hydrodynamic model that simulates how nutrients will be transported throughout the water, and a sediment diagenesis model that simulates how nutrients are remineralized back into the water column. Nutrient input information is provided by the Watershed Model for solid and nutrient loads, and the Community Multiscale Air Quality Model for atmospheric deposition of nitrogen and phosphorus. The eutrophication model has been shown to provide robust predictions that match observed physical conditions and nutrient concentrations in the Bay from 1984 to 1986 (Cerco and Cole 1993), and on a larger time scale from 1985 to 2005 (Cerco and Noel 2013). This model allows for continuous projection of conditions in the Chesapeake Bay so that events in

one season are evaluated for future impacts. Nutrient reduction goals to improve dissolved oxygen, water clarity, and chlorophyll concentration can then be accurately assessed (Cerco and Cole 1993; Cerco and Noel 2013).

It is important that Chesapeake Bay eutrophication model predictions are accurate because watershed nutrient management practices are informed by this model. In order to detect patterns of phytoplankton growth and make an assessment of model performance sufficient temporal resolution is necessary. Critically, data on phytoplankton growth rates and their response to artificial nutrient amendment within Chesapeake Bay have not been collected in almost two decades (Fisher et al. 1992, Fisher et al. 1999). To verify the accuracy of model predictions of phytoplankton growth rates, comparison to actual rates under different nutrient conditions is paramount. Therefore, this study aims to update the research record by collecting new information on phytoplankton growth and to allow comparison between growth rates and model predictions after the collection of additional growth rate data into the future. Another way that management action success will be assessed is by determining phytoplankton growth limitation. If nutrients are sufficiently reduced by current actions, then they will be limiting.

Materials and methods

Study location

Surface water samples were collected from two locations within the Chesapeake Bay watershed, shown in Figure 1. The first is the Chesapeake Bay Program's long-term monitoring station CB4.3C. It is in the mesohaline segment of the main channel of the Bay, approximately 100 kilometers south of the mouth of the Susquehanna River. The second location is the Horn Point Laboratory pier, approximately 20 kilometers upriver from the mouth of the Choptank River, an eastern shore tributary to the Bay.

Sample collection

We completed two research cruises during the study period on June 7 and July 10 to the Chesapeake Bay site to collect environmental field data and water samples. A CTD instrument (SeaBird, Bellevue WA) measured water conductivity, temperature, and depth to determine the location of the surface mixing layer. A vertical light profile was obtained using a hyperspectral irradiance sensor (TRIOS, Rastede Germany) that assessed light attenuation, and water transparency was measured with a Secchi disk. A 2 m water sample was collected during each research cruise with a Niskin bottle for lab analysis and experiments. Two experiments were also performed in the Choptank River off the Horn Point Lab pier on June 25 and July 24. During each event, a water sample was collected at subsurface and light attenuation in the water column was measured using the TRIOS sensor.

Environmental conditions

Temperature and conductivity measurements from the CTD were used to determine the location of the surface mixing layer. The surface mixing layer is found above the pycnocline, where salinity and temperature change drastically, and is where phytoplankton live in the water column. The average light level across the surface mixing layer was used during experimental nutrient amendment incubations. Ambient nutrient concentrations of nitrate and nitrite, ammonium, total dissolved nitrogen, phosphate, total dissolved phosphorus, silicate, and chlorophyll were also measured. As of August 9, data on ambient concentrations were still pending analysis through Horn Point Lab's analytical services.

Experimental design

Water samples collected from the two field sites were used in nutrient amendment experiments. They were filtered, amended, then incubated, following the methodology of Fisher et al. (1992), and phytoplankton populations were measured.

Some whole water was set aside for nutrient analysis, then the remaining water samples were passed through a 200 µm screen to remove larger microorganisms such as zooplankton that feed on phytoplankton. The filtered and unfiltered water was used to make a 5% solution of the field sample. It has been shown that dilution reduces grazing in a 1:1 relationship, as small dilution factors were observed to have the same effect on net growth rate as low levels of grazing across multiple species of phytoplankton (Landry et al. 1995). Dilution brought observed growth rates closer to actual growth rates by separating predators from prey, thus decreasing phytoplankton mortality due to grazing (Worden and Binder 2003). Grazing rates were derived through a complementary Maryland Sea Grant funded study.

The water was divided into three replicates of four nutrient treatments. They included addition of no nutrients as a control to assess potential light limitation, or addition of nitrogen, phosphorus, or nitrogen and phosphorus together. Samples were prepared for nutrient amendment in 500 mL media bottles filled to capacity. Nutrients were added by 1 mL of either 30 mM ferric ammonium citrate solution or 2 mM potassium phosphate solution. Amended bottles were incubated for 24 hours on a rotating plankton wheel in an environmental chamber set to mimic natural conditions. *In situ* water temperature was maintained in the environmental chamber and the average natural light level was used between sunrise and sunset.

Measures of phytoplankton population

Two indicators of growth were measured before and after incubation. Cell concentrations, as well as the size and chlorophyll-a fluorescence of each cell counted, in the initial diluted water and each treated sample were measured using a BD Accuri C6 flow cytometer.

Bulk chlorophyll-a concentrations were also measured. Each treated sample and 300 to 400 mL of the diluted water were filtered on 4.25 cm, 0.7 µm pore size Whatman GF/F glass microfiber filters. The filters were placed in 20 mL of 90% acetone solution and put in a fridge to extract. After 24 hours, the fluorescence of each acetone solution was measured with a Turner fluorometer before and after acidification with 0.1 mL of 0.5 N HCl (Holm-Hansen et al. 1965; Welschmeyer 1994). Chlorophyll-a fluorescence measurements were compared to a calibration curve to determine chlorophyll-a concentration.

Data analysis and calculations

From the final and initial chlorophyll and flow cytometry determined concentrations, phytoplankton growth rates, μ, were calculated following Equation (1), where T was time in days, P_T was phytoplankton biomass at time T, and P_0 was initial phytoplankton biomass (Landry et al. 1995).

$$\mu = \frac{1}{T} * \ln \frac{P_T}{P_0} \quad (1)$$

To determine growth limitation, responses of the nutrient treatments were compared to the control treatment using final chlorophyll and flow cytometry concentrations.

Results

The chlorophyll concentration data in Table 1 and cell concentration data in Table 2 were used to calculate growth rates of the different treatments and determine limitation.

Observed growth rates from the Chesapeake Bay samples are displayed in Figure 2. In June, the average growth rate of the control treatment was 0.36 cell divisions per day according to changes in chlorophyll concentration and 0.15 according to cell concentration. Average chlorophyll growth rates increased with nutrient amendment, up to 0.72 with the addition of both nitrogen and phosphorus. The same pattern was not observed in cell concentration growth rates. There was a slight decrease in the average phosphorus treatment growth rate, to 0.06. In July, the average growth rate of the control treatment was -0.18 according to chlorophyll concentration and 0.23 according to cell concentration. Neither method showed a great change in growth rate in response to nutrient additions, except for a decrease in the phosphorus treatment's average growth rate to 0.06 by cell concentrations. In July, Chesapeake Bay samples had a visible copepod population that was not present in the other samples. This may have resulted in increased grazing mortality and decreased apparent growth. No consistent patterns were observed. Chlorophyll growth rates were greater than flow cytometry growth rates in June, but less in July. Also, growth rates calculated by the two methods did not agree.

Figure 3 shows observed growth rates from the Choptank River samples. In June, the average growth rate of the control treatment was 0.90 according to chlorophyll concentration and 1.12 according to cell concentration. Average chlorophyll growth rates exhibited very little change with nutrient addition. However, there was an increase in the average nitrogen treatment growth rate to 1.50 by cell concentrations. In July, the average growth rate of the control treatment was 0.43 according to chlorophyll concentration and 0.55 according to cell concentration, with the two methods producing similar growth rates. There were slight increases in average growth rates of the nitrogen and nitrogen plus phosphorus treatments. Chlorophyll growth rates were slightly less than flow cytometry growth rates for most treatments.

Growth responses of the nutrient treatments determined by final chlorophyll and cell concentrations were compared to the control response and characterized as either light, co-nutrient, or primary nutrient limited as exemplified in Figure 4.

Growth responses of nutrient treatments relative to the control from the Chesapeake Bay samples are visualized in Figure 5. All nutrient treatment responses were statistically indistinguishable from the control in June and July, suggesting light limitation in the Bay. However, all average treatment responses calculated by chlorophyll data in June show a greater growth response than the control, from 103% to 104%.

Figure 6 displays the growth of nutrient treatments relative to the control from the Choptank River samples. Again, all nutrient treatment responses were statistically indistinguishable from the control in both June and July, with the exception of the nitrogen treatment response determined by cell concentration in June. It was 145% of the control response. However, a similar response was not observed when both nutrients were added, as only an average 112% of the control response was attained. In addition, the average response of the nitrogen plus phosphorus treatment in July was greater than the control at 138%.

Discussion

Growth rates in the Chesapeake Bay were less than those observed in the Choptank River. This is to be expected because the Choptank sampling site was closer to land and sources of nutrient runoff, fueling phytoplankton growth. Comparison of treatment-relative responses at both sites indicated light limitation in the mesohaline segment of the Chesapeake Bay and a major eastern shore tributary during June and July of 2018, suggesting that nutrients remain at a great enough concentration to be non-prohibitive to phytoplankton growth. In contrast, Fisher et al. identified nitrogen as the primarily limiting factor on phytoplankton growth in the Chesapeake Bay near the CB4.3C station during the summer between 1982 and 1988 by environmental nutrient concentrations and nutrient bioassay results (1992). Similar results were seen in bioassay results from 1989 to 1994, with nitrogen limitation becoming more common than light limitation, indicating improved nutrient conditions in the Bay (Fisher et al. 1999). It is possible that nutrient inputs to the Bay have increased since that time. However, nutrient assessment by the University of Maryland Center for Environmental Science has revealed improvement in both nitrogen and phosphorus conditions in the Bay since 1986 at the beginning of monitoring (https://ecoreportcard.org/report-cards/chesapeake-bay/health/, 09 August 2018).

An alternative explanation for light limitation is that spring 2018's higher than average rainfall increased erosion of sediments and turbidity, blocking light penetration more than usual. Additionally, more rigorous methodology may be needed to decrease variability in the data, revealing patterns that are not currently apparent. This need was illustrated by statistically insignificant but average increases in some nutrient treatment responses and the significant increase in nitrogen treatment response in the Choptank River in June.

This experiment compared two methodologies, flow cytometry and measuring chlorophyll concentration, for calculating growth. They returned growth rates that differed by up to 227%. The relationships between chlorophyll and cell concentration calculated growth rates across both sites and all dates were weak, shown in Figure 4, and quantified by small correlation coefficients around 0.5. This exemplifies why refinement of methodology is necessary.

Flow cytometry is an emerging tool for phytoplankton analysis. It has been used to collect information about cell fluorescence, cell size, and growth rates by DNA staining. Cell counts have proven more difficult to accurately collect because flow cytometers were designed for qualitative, not quantitative, measurements. Flow speed is a large factor in count accuracy, with decreases at high speeds and a maximum recommended speed of 1000 events per second (Veldhuis and Kraay 2000). Samples in this experiment were run at a maximum of 144 events per second for the initial, control, and phosphorus treatments, and 1292 events per second for the nitrogen and nitrogen plus phosphorus treatments. Instrument output was gated to exclude particles smaller than 1 μm with a low chlorophyll concentration such as bacterial cells, detritus, and sediment from consideration. Without gating, these would have artificially decreased differences between treatments. In an effort to improve gating in the future, the signals of specific phytoplankton species found in the Chesapeake Bay were mapped and are displayed in Figure 8.

Welschmeyer concluded that chlorophyll-a fluorescence measurements obtained by the same protocol employed in this experiment yielded chlorophyll concentrations with only 10% deviation from known concentrations (1994). However, this set of data reveals wide variation in chlorophyll-a fluorescence measurements, with large standard deviations shown in Table 1. It is known that chlorophyll-a fluorescence measurements are susceptible to interference by other pigments in the sample. Holm-Hansen et al. cited reabsorption of fluoresced radiation by other pigments and fluorescence of red light by pigments other than chlorophyll-a as sources of error (1965). In these samples, interference with chlorophyll-a extraction by sediments and dissolved

organic matter could also play a role in the variable measurements. By using more rigorous methods to extract chlorophyll-a from the phytoplankton cells, variation in the concentration data could be reduced. A combination of freeze drying the samples and extracting in methanol, acetone, dimethylformamide, and water proved effective for extracting pigments from a mixed sample of cyanobacteria, green algae, and diatoms (Hagerthey et al. 2006). Worden and Binder have also noted that changes in phytoplankton physiology induced by incubation conditions could artificially alter growth rates (2003). Average natural light levels were measured in the field and used for incubation in an effort to prevent this, but parallel monitoring of phytoplankton physiology could be employed in the future to ensure that observed changes in chlorophyll-a concentration are due to population growth instead of increased pigmentation per cell.

The data from this project have demonstrated a need for more rigorous methodology throughout the remainder of the two-year study and will contribute to year-round efforts to collect information on phytoplankton growth in the Chesapeake Bay. By producing data with less variation and calculating more accurate growth rates in the future, comparisons can be made to eutrophication model predictions of growth rate to verify the accuracy of model performance. This may lead to improvements in model predictions of the outcomes of nutrient management actions meant to prevent algal blooms and improve water quality, having a positive environmental and economic impact on the Chesapeake Bay.

Conclusions

Using flow cytometry and chlorophyll fluorescence, phytoplankton growth rates and the resources limiting them were determined at two locations in the Chesapeake Bay and Choptank River. Results of this study were not indicative of the success of nutrient management actions taken in the Chesapeake Bay watershed thus far because there was no strong indication of nutrient limitation. However, variation in the results also indicated the need for refinement of methodology. Improved methodology in the future will produce more accurate data for comparison against and verification of eutrophication models.

Acknowledgments

The Maryland Sea Grant Research Experiences for Undergraduates (REU) program was funded by the National Science Foundation Division of Ocean Science grant OCE-1756244. Additional funding for this research project was provided by Maryland Sea Grant grant SA07528187-G. Thank you to Maryland Sea Grant and Dr. Mike Allen for administering and coordinating the REU program and providing me with the opportunity to conduct summer research at the University of Maryland Center for Environmental Science Horn Point Laboratory. Thank you to my mentor at Horn Point Laboratory, Dr. Greg Silsbe, for allowing me to work in his lab and for providing an educational experience of the research process. Also, thank you to Dr. Emily Brownlee for providing technical instruction. I would like to acknowledge Andy McCarthy for his assistance in sample collection.

References

Behrenfeld, M., K. Halsey, and A. Milligan. 2008. Evolved physiological responses of phytoplankton to their integrated growth environment. Phil. Trans. R. Soc. B. 363: 2687–2703, doi:10.1098/rstb.2008.0019

Boynton, W., and W. Kemp. 1985. Nutrient regeneration and oxygen consumption by sediments along an estuarine salinity gradient. Mar. Ecol.: Prog. Ser. 23: 45–55.

Boynton, W., J. Garber, R. Summers, and W. Kemp. 1995. Inputs, transformations, and transport of nitrogen and phosphorus in Chesapeake Bay and selected tributaries. Estuaries. 18: 285–314.

Cerco, C.F. and T. Cole. 1993. Three-dimensional eutrophication model of Chesapeake Bay. Journal of Environmental Engineering. 119: 1006–1025.

Cerco, C.F. and M.R. Noel. 2013. Twenty-one year simulation of Chesapeake Bay water quality using the CE-QUAL-ICM eutrophication model. JAWRA. 49: 1119–1133.

Conley, D. and T. Malone. 1992. Annual cycle of dissolved silicate in Chesapeake Bay: Implications for the production and fate of phytoplankton biomass. Mar. Ecol.: Prog. Ser. 81: 121–128.

Cooper, S. and G. Brush. 1991. Long-term history of Chesapeake Bay anoxia. Science. 254: 992–996.

Field, C.B., M.J. Behrenfeld, J.T. Randerson, and P. Falkowski. 1998. Primary production of the biosphere: Integrating terrestrial and oceanic components. Science. 281: 237–240

Fisher, T., E. Peele, J. Ammerman, and L. Harding Jr. 1992. Nutrient limitation of phytoplankton in Chesapeake Bay. Mar. Ecol.: Prog. Ser. 82: 51–63.

Fisher, T. and others. 1999. Spatial and temporal variation of resource limitation in Chesapeake Bay. Marine Biology. 133: 763–778.

Goldman, J.C., J.J. McCarthy, and D.G. Peavey. 1979. Growth rate influence on the chemical composition of phytoplankton in oceanic waters. Nature. 279: 210–215.

Hagerthey, S.E., J.W. Louda, and P. Mongkronsri. 2006. Evaluation of pigment extraction methods and a recommended protocol for periphyton chlorophyll a determination and chemotaxonomic assessment. J. Phycol. 42: 1125–1136, doi: 10.1111/j.1529-8817.2006.00257.x

Harding, L. and others. 2015. Climate effects on phytoplankton floral composition in Chesapeake Bay. Estuarine, Coastal Shelf Sci. 162: 53–68, doi: 10.1016/j.ecss.2014.12.030

Holm-Hansen, O., C.J. Lorenzen, R.W. Holmes, and J.D.H. Strickland. 1965. Fluorometric determination of chlorophyll. ICES J. Mar. Sci. 30: 3–15.

Kemp, W. and others. 2005. Eutrophication of Chesapeake Bay: Historical trends and ecological interactions. Mar. Ecol.: Prog. Ser. 303: 1–29.

Landry, M., J. Kirshtein, and J. Constantinou. 1995. A refined dilution technique for measuring the community grazing impact of microzooplankton with experimental tests in the central equatorial Pacific. Mar. Ecol.: Prog. Ser. 120: 53–63.

Malone, T., D. Conley, T. Fisher, P. Glibert, and L. Harding. 1996. Scales of nutrient-limited phytoplankton productivity in Chesapeake Bay. Estuaries. 19: 371–385.

Veldhuis, M. and G. Kraay. 2000. Application of flow cytometry in marine phytoplankton research: Current application and future perspectives. Sci. Mar. 64: 121–134.

Welschmeyer, N. 1994. Fluorometric analysis of chlorophyll *a* in the presence of chlorophyll *b* and pheopigments. Limnol. Oceanogr. 39: 1985–1992.

Worden, A. and B. Binder. 2003. Application of dilution experiments for measuring growth and mortality rates among *Prochlorococcus* and *Synechococcus* populations in oligotrophic environments. Microb. Ecol. 30: 159–174.

Figures and Tables

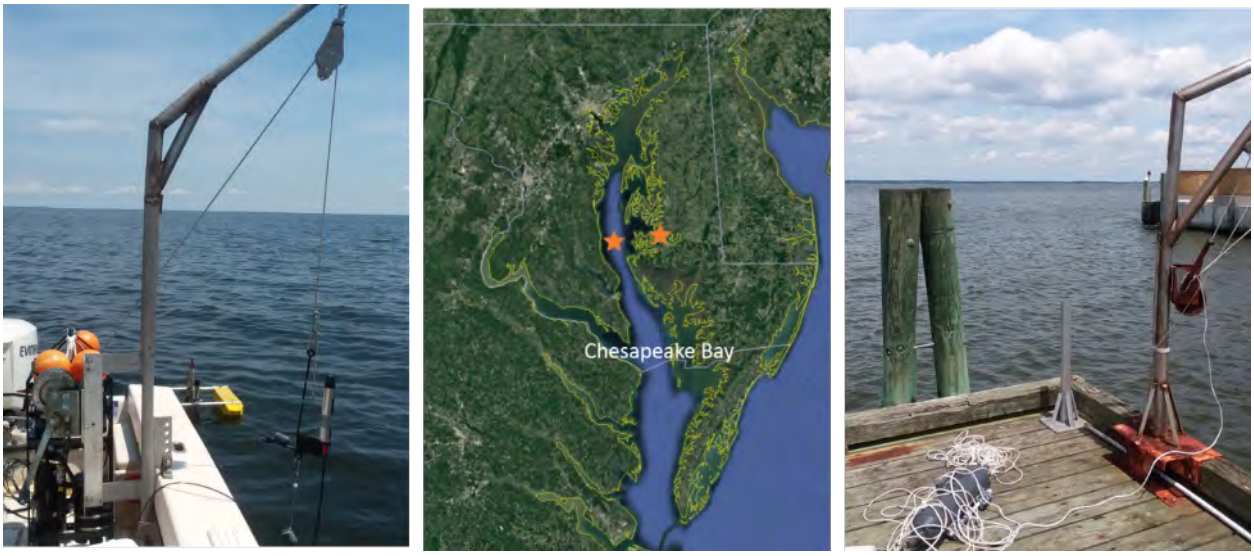

Figure 1. Sample locations in the Chesapeake Bay (left) and on the Choptank River (right), represented by stars on the map (Google Earth Pro).

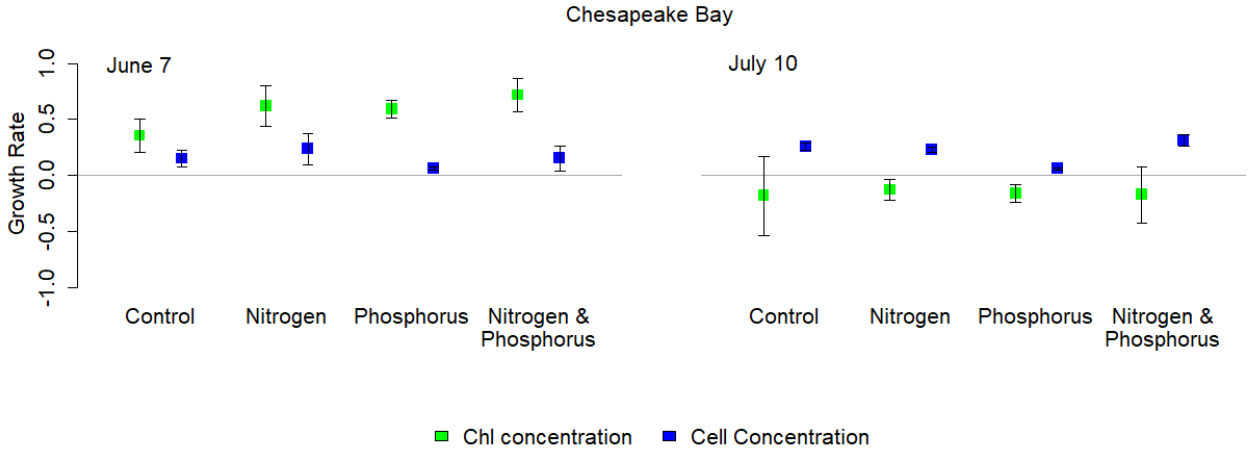

Figure 2. Growth rates of each treatment at the Chesapeake Bay site in cell divisions per day in June and July.

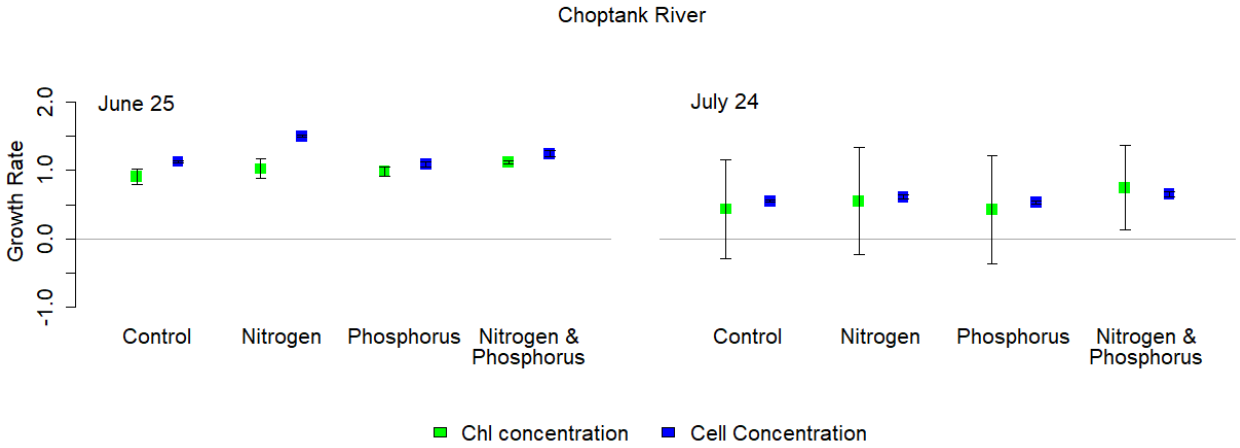

Figure 3. Growth rates of each treatment at the Choptank River site in cell divisions per day in June and July.

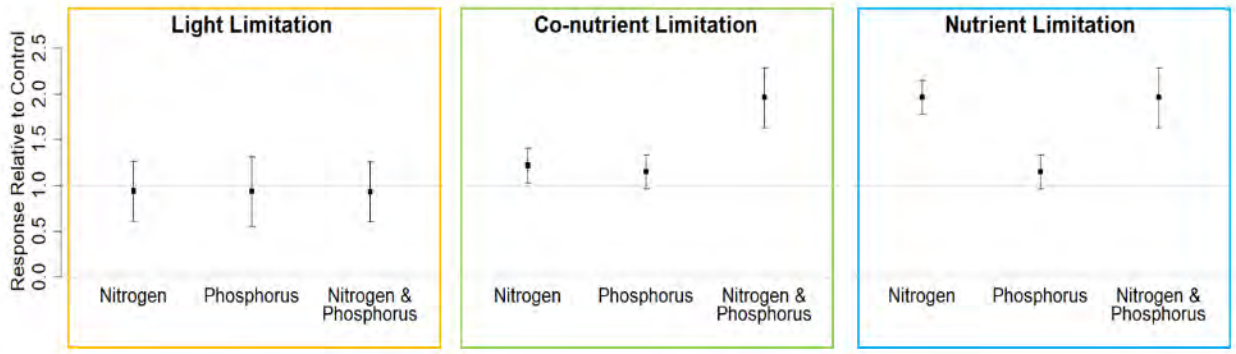

Figure 4. Categorization of relative responses: light limitation, co-nutrient limitation, or primary nutrient limitation. Growth responses of the nutrient treatments are compared to the control on the vertical axis with the nutrient treatments across the horizontal axis. The dashed line at 1 indicates a treatment with growth equal to the control. Under light limitation, all nutrient treatments have growth equal to the control. Adding both nutrients produces the most growth if both are limiting. Under primary nutrient limitation, adding one nutrient induces growth equal to adding both.

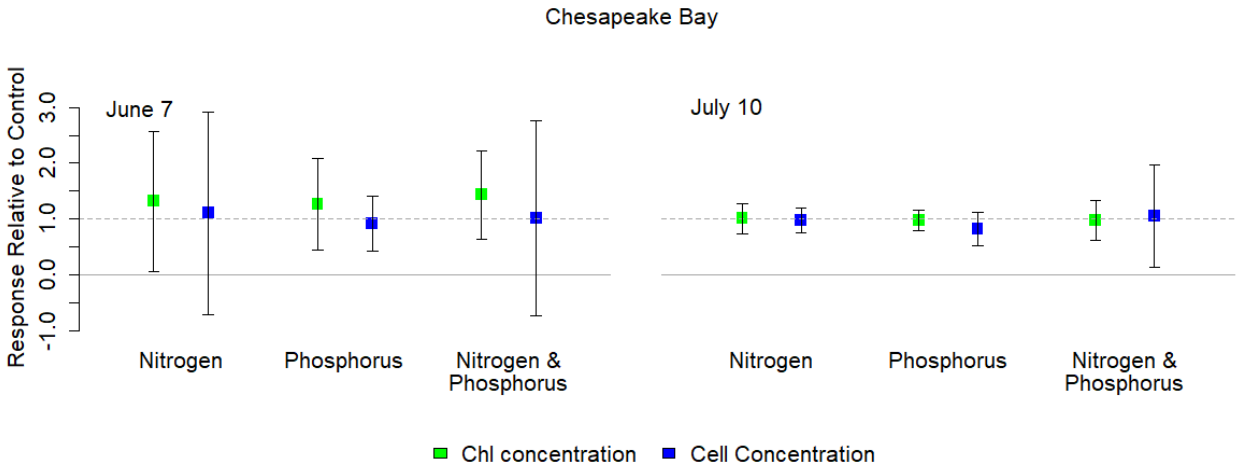

Figure 5. Relative response of each nutrient treatment as a proportion of the control response at the Chesapeake Bay site in June and July.

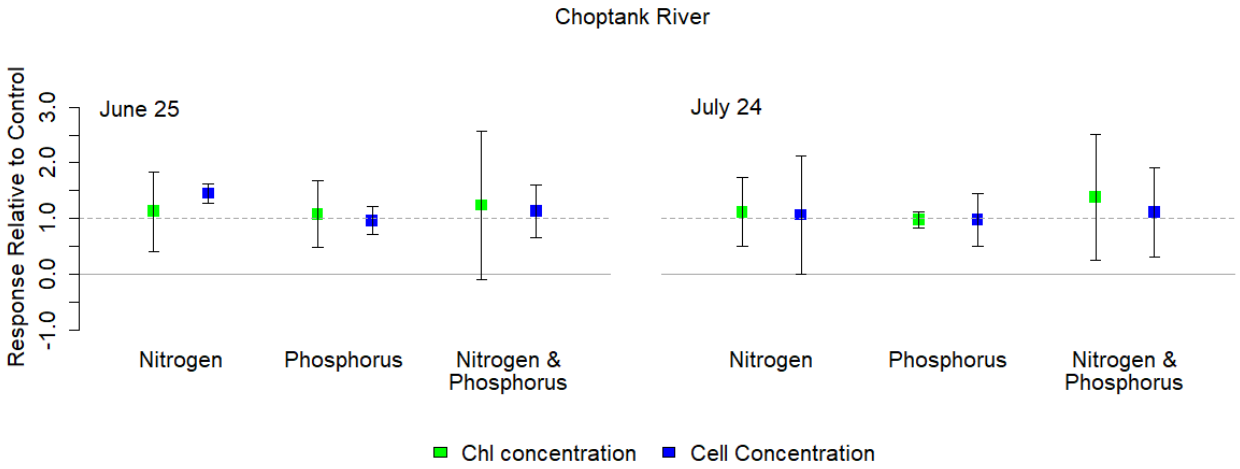

Figure 6. Relative response of each nutrient treatment as a proportion of the control response at the Choptank River site in June and July.

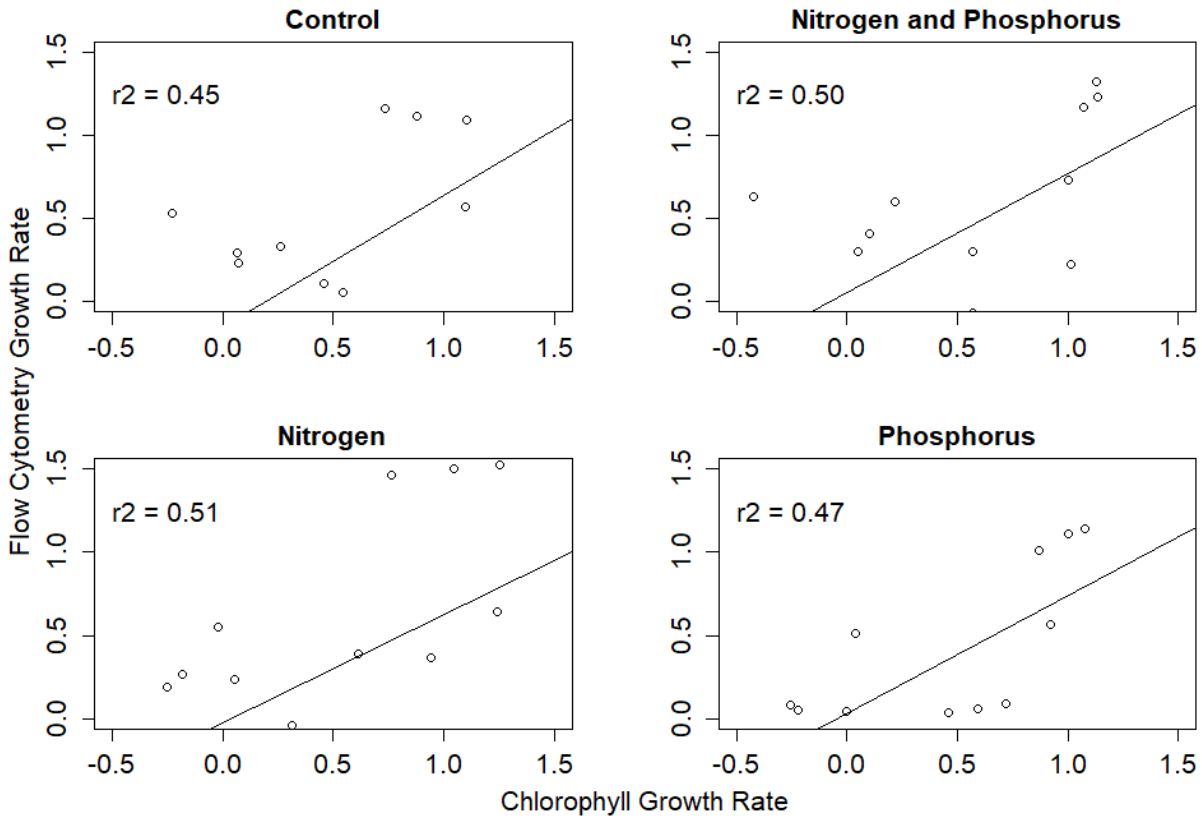

Figure 7. Scatterplots showing the relationship between chlorophyll growth rates on the x-axis and flow cytometry growth rates on the y-axis of each treatment. All sites and dates are plotted, with each point corresponding to a single replicate.

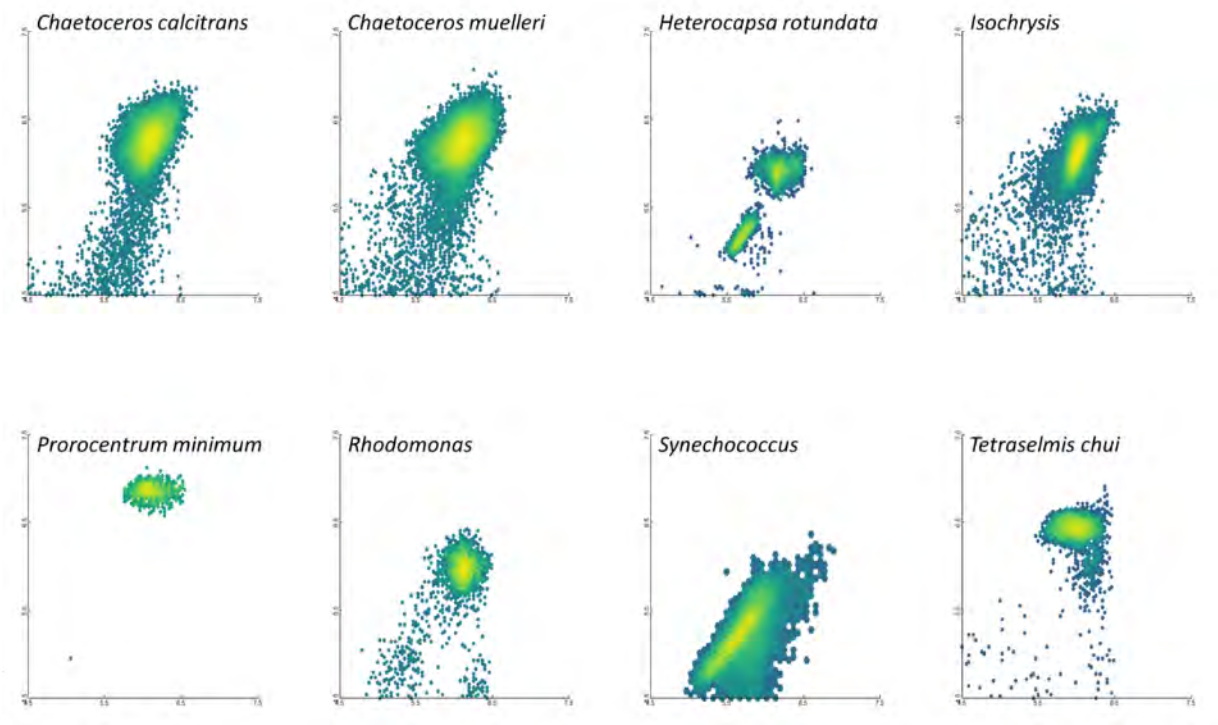

Figure 8. The flow cytometry signals of eight different phytoplankton species, with SSC (side scatter) on a log scale across the x-axis and FL3 (fluorescence at 670 nm) on a log scale along the y-axis, gated from (4.5, 8).

Table 1. Average chlorophyll-a concentration and standard deviation in micrograms of chlorophyll-a per liter for the initial diluted solution and each treatment after 24 hours, calculated by chlorophyll-a fluorescence measurements.

	Initial	SD	Control	SD	+ N	SD	+ P	SD	+ N & P	SD
June 7 CB4.3C	1.51	0.23	2.15	0.30	2.84	0.65	2.73	0.43	3.08	0.41
June 25 HPL	0.70	0.13	1.71	0.13	1.92	0.16	1.84	0.13	2.11	0.30
July 10 CB4.3C	0.43	0.09	0.38	0.14	0.38	0.07	0.37	0.05	0.37	0.08
July 24 HPL	1.53	1.93	1.33	0.28	1.49	0.30	1.31	0.07	1.84	0.54

Table 2. Average cell concentration and standard deviation in cells per milliliter for the initial diluted solution and each treatment after 24 hours, measured by flow cytometry.

	Initial	SD	Control	SD	+ N	SD	+ P	SD	+ N & P	SD
June 7 CB4.3C	2402	121	2795	210	3093	660	2564	180	2851	634
June 25 HPL	1652	62	5090	363	7387	108	4885	157	5718	297
July 10 CB4.3C	1507	48	1951	108	1901	41	1599	55	2069	171
July 24 HPL	2775	110	4812	103	5110	188	4705	85	5339	144

Statistically Downscaling the Community Climate Systems 4 Global Climate Model to Project Hypoxia in the Chesapeake Bay

Samantha Roth, REU Fellow
Maryland Sea Grant

Ming Li, Professor
Horn Point Laboratory, University of Maryland Center for Environmental Science

Wenfei Ni, Graduate Assistant
Horn Point Laboratory, University of Maryland Center for Environmental Science

Andrew C. Ross, Postdoctoral Research Associate
Princeton University/NOAA Geophysical Fluid Dynamics Laboratory

Abstract

The goal of this research was to statistically downscale and bias-correct several climate variables from the most recent Community Climate Systems Model (CCSM) to the American Mid-Atlantic and Northeastern region, encapsulating the Chesapeake Bay watershed. The downscaling and bias-correction of a global climate model (GCM) increases the spatial resolution and reduces some of its biases, making the model more useful at the regional scale. The Coupled Model Intercomparison Project (CMIP) 5 CCSM4 Representative Concentration Pathway (RCP) 8.5 GCM was downscaled and bias-corrected with the intention of enabling the projection of hypoxia in the Chesapeake Bay from 2081 to 2100. Although the main cause of hypoxia is nutrient loading (Li et. al. 2016), climate change is also a factor that influences the timing and extent of hypoxic zones in the Chesapeake Bay. Specifically, air temperature has been shown to be the most influential climate variable in its effect on hypoxia (Altieri & Gedan 2015). The results project an increase in mean temperature, air pressure, and downward longwave radiation flux (DLWRF) and a decrease in relative humidity between the historical period (1986-2005) and the future period (2081-2100). These climate variables, including their seasonal and geographical focuses, can have varying impacts on the timing and extent of hypoxia, thus deserving further study.

Introduction

In this experiment, climate variables from the CCSM4 GCM were statistically downscaled and bias-corrected to enable the projection of hypoxia in the Chesapeake Bay into the late 21st century. A hypoxic zone, or dead zone, is a mass of water with less than 2 mg/L of oxygen that becomes dearth of marine life by killing the organisms or forcing them out because there is too little oxygen to support them (https://oceanservice.noaa.gov/facts/deadzone.html). Some commonly known causes of dead zones are nutrient-rich runoff from farmland, suburban, and urban areas; treated water from wastewater treatment plants; and air pollution from fossil fuel-

powered cars, factories, and other machinery (http://www.cbf.org/issues/dead-zones/). In addition to nutrient loading, many sources posit that climate change significantly contributes to the world-wide increase of hypoxic zones (Hansen & Bendsten 2009, Altieri & Gedan 2015, Irby et. al 2018). Although nutrient loading has been observed to have a stronger impact on hypoxia than climate change (Rabotyagov et. al. 2014, Li et. al. 2016), the exacerbation of hypoxia could be climate change's greatest blow to estuarine marine life (Hansen & Bendsten 2009). In this experiment, we used equidistant cumulative distributive function (CDF) matching and equiratio CDF matching to statistically downscale and bias-correct the CMIP5 CCSM4 RCP 8.5 GCM (the highest emissions scenario) to the Mid-Atlantic and Northeastern United States to enable the projection of hypoxia in the Chesapeake Bay for the years 2081 to 2100. We used CMIP5 CCSM4 historical climate simulations and NARR data for the years 1986 to 2005 to obtain the bias-correction functions.

Numerous aspects of climate change such as changes in temperature, precipitation, sea-level rise, ocean acidification, storm patterns, and wind impact hypoxia in varying manners and to varying degrees (Altieri & Gedan 2015). Some changes in these variables have been shown to contribute a net positive effect on hypoxia, and others a net negative, but overall climate change has been shown to negatively impact hypoxic zones (Irby et. al 2018, Altieri & Gedan 2015). Although some studies have come to the conclusion that temperature and climate change as a whole could have mediating effect on hypoxia, these studies have taken the approach of selecting a subset of variables to focus on, such as hydrography or nutrient dynamics (Altieri & Gedan 2015).

Warming has been cited as the most influential factor of climate change in its impact on dead zones (Altieri & Gedan 2015) and has been shown to exert a negative impact (Irby et. al 2018, Wang et. al 2017, Scully 2013). Increased temperatures worsen hypoxia mainly by reducing the oxygen solubility of the water, meaning that warmer water can hold less dissolved oxygen than colder water (Irby et. al 2018, Scully 2013). In estuaries like the Chesapeake Bay, temperature is an especially critical factor in projecting hypoxia, as estuaries respond relatively quickly to changes in air temperature due to limited interaction with the open ocean (Altieri & Gedan 2015, Scully 2013). Data from buoys in the Chesapeake Bay show a strong correlation between air temperature and surface water temperature (Muhling et. al. 2017). Accordingly, statistically downscaled models estimate that the surface water here could see an increase in temperature ranging from 2 to 5.5ºC by 2100 (Muhling et. al. 2017). The seasonal focus of warming can also impact the timing and extent of hypoxia (Testa et. al. 2018) through its impact on oxygen solubility of the water (Scully 2013) and through its impact on water stratification, or when masses of water with different densities form layers (Wang 2017). For example, the maximum amount of dissolved oxygen in the water was found in February, whereas the lowest amount was found in August, when the water was much warmer due to prolonged exposure to high air temperatures (Scully 2013). Warming also has been shown to increase water stratification, which can prolong hypoxic conditions by inhibiting mixing between layers (Wang, 2017). In addition to its direct effects on hypoxia, temperature also influences many other climate variables that also affect hypoxia, such as precipitation, cloud cover, storms, and sea level rise.

Another critical variable in determining hypoxic volume is wind, with the direction, frequency, and speed of the wind determining if hypoxia will be exacerbated or mediated and to what degree (Scully 2013). In the Chesapeake Bay, wind impacts hypoxia by transporting organic matter (Lee et. al. 2013) or oxygenating the bottom waters (Scully 2010). Specifically, southerly winds have been shown to provide more oxygen to hypoxic zones, and westerly winds were shown to provide less oxygen (Scully 2010). Higher frequencies of northeasterly winds were observed to transport more organic matter, exacerbating hypoxia, while higher frequencies of

southwesterly winds transported less organic matter and were associated with less hypoxia (Lee et. al. 2013). The timing and frequency of storms, such as hurricanes that hit the Chesapeake Bay, impact dead zones through changes in nutrient input, stratification, and suspension of sediment particles (Rabalais et. al. 2009). Cloud cover also impacts hypoxia by affecting the phytoplankton populations that mainly depend upon sunlight (Winder & Sommer 2012). However, the responses of wind, storms, and cloud cover are less predictable than other variables (Justic et. al. 2005, IPCC 2013). Many researches anticipate that sea level rise will mediate hypoxia and has been posited to have varying intensities of impact (Irby et. al. 2018, Wang et. al 2017). The mechanism by which sea level rise impacts hypoxia is by increasing estuarine circulation, in turn lowering the amount of time water spends at the bottom of the bay. This leads to a projected increase in the amount of dissolved oxygen (DO) in bottom waters and a projected decrease in DO at mid-depths (3<DO<5mg/L), overall alleviating hypoxia (Irby et. al. 2018). However, other sources believe that sea level rise could worsen hypoxia by increasing stratification, in addition to adding more hypoxia-susceptible coastal water (Van Der Zwaan & Jorissen 1991, Davies & Xing 2007). It could also spill over into wetlands and compromise their nutrient filtration services, leading to more nutrient run-off (Kemp et. al. 2005).

Ocean acidification works synergistically with hypoxia to amplify its impact on marine life by impeding survival rates, feeding patterns, reproduction, and development of larva, partially because increasing acidity decreases hemoglobin's oxygen-binding affinity (Doney 2012, Portner 2010). It can also make species more vulnerable to diseases by compromising their immune systems (Boyd & Burnett 1999) and to predators by altering their behavior (Rosa & Seibel 2008). Lastly, ocean acidification could decimate populations of bivalves that act to control the algal blooms that precede hypoxia (Kroeker et. al. 2010).

Concerning precipitation, Irby et. al. predict that climate change will adversely affect hypoxia via higher precipitation in winter and spring months that increase fresh water flow from the Susquehanna river (the main tributary of the Chesapeake Bay) and other tributaries, thereby delivering more freshwater and a greater nutrient load to the bay (2018). However, some warmer climate models project less freshwater flow to the bay due to higher rates of evapotranspiration, which would lead to a smaller nutrient load (Muhling et. al. 2017). Larger nutrient loads are well-established to be the most significant factor in exacerbating hypoxia (Li et. al. 2016). In the Chesapeake Bay, researchers even find that climate change will not do much to increase hypoxia in comparison to the expected reduction in hypoxia due to nutrient input regulations (Li et. al 2016, Irby et. al 2018). However, some studies assert that in many estuaries, climate change alone plays a large enough role in hypoxia to expand hypoxic volume in spite of nutrient reduction measures being taken (Cartensen et. al. 2014, Villate et. al. 2013, Meier et. al. 2011).

The future of hypoxia and how it will be impacted by climate has been projected by many researchers, but many of these were only looking at a subset set of variables. Although many scientists agree that climate change as a whole will negatively impact hypoxia, there is still a bit of disagreement in the scientific community about the effects of individual climate variables. Hypoxia is a world-wide problem, and other states and countries with similar problems could use modeling of hypoxia in the Chesapeake Bay for comparison. Furthermore, adding to the body of research projecting how climate change will affect hypoxia is more than worthwhile. The quantile method is an established method of bias-correction to downscale global climate models that is cost-effective and time-efficient, and equidistant CDF matching and equiratio CDF matching have the same time and cost benefits, but are considered superior to this method in some aspects of performance (Wang & Chen 2013). Based upon the research summarized above, I expect climate change to negatively impact hypoxia in the Chesapeake Bay. The goal

of this research was to statistically downscale and bias-correct the following climate variables from CMIP5 CCSM4: near-surface air temperature, wind speed and direction, surface downwelling longwave radiation, surface upwelling shortwave radiation, and surface downwelling shortwave radiation, and near-surface relative humidity, with the intention of using these bias-corrected variables to project hypoxia in the Chesapeake Bay into the late 21st century.

Materials and Methods

GCMs are useful for projecting climate change on a global scale based on different emissions scenarios but have biases and do not have a high enough spatial resolution to be useful at the regional scale. Downscaling and bias-correcting GCMs can help to make them more accurate and useful for smaller regions by reducing their biases and increasing their spatial resolution. In this experiment, we ran a Python code that statistically downscaled variables from a GCM and then bias-corrected them using equidistant cumulative distribution function (CDF) matching and equiratio CDF matching. This code was derived from GFDL's FUDGE software (https://github.com/NOAA-GFDL/FUDGE) and used the analytical package R. There are two forms of downscaling: dynamical and statistical. Statistical downscaling is a fast, low-cost (Muhling et. al. 2017) method that determines the statistical relationship between large-scale and regional climate variables to predict future values of the regional climate variables using projections of the large-scale climate variables (Tang et. al. 2016). However, differences in up-estuary and down-estuary conditions make the area more dynamically complex and compromise the reliability of statistical downscaling (Muhling et. al. 2017). Dynamical downscaling derives surface and lateral boundary conditions for an area that encapsulate critical summary and intermediate atmospheric circulation features that dictate that area's climate using a global climate model (http://regclim.coas.oregonstate.edu/dynamical-downscaling/background/index.html).

The basis of the two bias-correction methods used in this experiment is CDF matching, a method similar to quantile mapping (Li et. al. 2010). First, quantile mapping will be explained, and then the two methods used. To start with quantile mapping, each climate variable of interest was modeled for a predetermined length of time in the recent past using a GCM. In this experiment, the GCM modeled historical data for every three hours from 1986 to 2005. For each time and day in the designated time frame, the modeled values of each climate variable generate the modeled CDF, denoted by $F_{h,v,m}$, where h represents historical, v represents the climate variable and m represents the model. The observed values of each climate variable generate the observed CDF, denoted by $F_{h,v,o}$, where o represents observed. The inverse CDF or quantile function of the observed values for a given variable is represented by $F^{-1}_{h,v,o}$. For a given climate variable, each modeled value for a specific day and time is assigned a quantile on its corresponding modeled CDF. Then the observed value with the same cumulative probability for that time and day in the observed CDF is used as the corrected value for the GCM historical model (Teutschbein & Seibert 2012). This process is mathematically described below, where * signifies corrected value, and t is a time and day between the years 2086 and 2005:

$$x^{*}_{h,v,m}(t) = F^{-1}_{h,v,o}\left(F_{h,v,m}\left(x_{h,v,m}(t)\right)\right) \quad (1)$$

This same correction function is then used to correct the bias of future projections of that variable, where p signifies projection t will be an hour and day between the years 2081 and 2100. (Boé et. al. 2007).

$$x^*_{p,v,m}(t) = F^{-1}_{h,v,o}(F_{h,v,m}(x_{p,v,m}(t))) \quad (2)$$

However, the CDFs for both the observed and modeled data are estimated empirically, meaning that any projections for the years 2081 to 2100 that lie outside the range of the modeled historical data would have to be mapped using a form of extrapolation. Common forms of extrapolation are parametric distribution usage and the constant correction approach (Cannon et. al. 2015). A general illustration of quantile mapping can be found at the end of the paper (Figure 23).

Quantile mapping is an established bias correction method that outperforms methods that only relate to mean and/or variance (Wang & Chen 2013, Passow & Donner 2017) and is efficient in fixing historical biases in global climate models. A method that only relates to the mean is linear scaling, and a method that only relates to the variance is variance scaling (Teutschbein & Seibert 2012). In linear scaling, the mean is calculated for each time frame of interest, perhaps each month, for the observed data and for the simulated recent data. Then, a correction factor is either multiplied by or added to each simulated monthly mean value so that it matches the long-run observed monthly mean value. For precipitation, a factor is multiplied, and for temperature, the correction factor is added to the simulated monthly mean. Example equations for linear scaling of precipitation and temperature are shown below, where m stands for monthly, d stands for day, P stands for precipitation, T stands for temperature, obs stands for observed, contr stands for past RCM simulated, scen stands for future RCM simulated, and * signifies the final bias-corrected form.

$$P^*_{contr}(d) = P_{contr}(d) \cdot \left[\frac{\mu_m(P_{obs}(d))}{\mu_m(P_{contr}(d))}\right]$$

$$P^*_{scen}(d) = P_{scen}(d) \cdot \left[\frac{\mu_m(P_{obs}(d))}{\mu_m(P_{contr}(d))}\right]$$

$$T^*_{contr}(d) = T_{contr}(d) + \mu_m(T_{obs}(d)) - \mu_m(T_{contr}(d))$$

$$T^*_{scen}(d) = T_{scen}(d) + \mu_m(T_{obs}(d)) - \mu_m(T_{contr}(d))$$ (Teutschbein & Seibert 2012)

The delta method of bias correction is unique in that it does not simulate the historical data, it only uses observed data and the RCM change signals to predict future values of climate variables. By definition, its historical values match the observed values exactly (Teutschbein & Seibert 2012).

In an experiment comparing different bias correction models' abilities to correct regional climate model (RCM) simulations, distribution mapping outperformed numerous other methods of bias correction for temperature and precipitation, resulting in the least variability and the closest fit to the observed means (Teutschbein & Seibert 2012). Still, all the bias-corrected RCM models were found to improve upon the uncorrected RCM model (Teutschbein & Seibert 2012). Even though the delta method was hailed as the most stable and robust as its corrected values always match the observed values perfectly, it would not be as reliable in reflecting future changes in the climate, and so the quantile mapping method was concluded to be superior (Teutschbein & Seibert 2012).

None the less, quantile mapping has its downsides in future projections (Cannon et. al., 2015). Some drawbacks are that the variables are bias-corrected independently of each other, although the variables may not be independent (Boé et. al. 2007). Also, this method assumes,

like other bias correction methods, that the relationship between the local climate and larger-scale climate will not change, so the same algorithm used to correct current/past data will work for correcting future data (Teutschbein & Seibert 2012, Muhling et. al. 2017). Lastly, it assumes that the distribution of the variable of interest will stay similar in the future (Wang & Chen 2013). One possible fix for this would be a bias-correction that changes based on the emissions scenario, but this method needs further studying and additional assumptions (Buser, et. al. 2009). The two methods that we used are equidistant CDF matching and equiratio CDF matching, which are considered to outperform quantile mapping (Wang & Chen 2013).

The code in this experiment first spatially interpolated the simulation data to match the spatial resolution and grid locations of the observed data, then made use of two forms of bias-correction. The specific bias-correction methods used were equidistant CDF matching and equiratio CDF matching. In equidistant CDF matching, simulated data was corrected by adding the difference between the observed and simulated values at each simulated data quantile (Wang & Chen 2014). This method improves upon the traditional quantile method in that it considers possible changes in the distribution of the model data (Li et. al. 2010). It has been shown to be especially advantageous for bias-correction for more extreme values, which is important for changing climates (Li et. al. 2010). However, it assumes that the difference between modeled and observed values in the historical period will not change for the projection period. Equidistant CDF matching works quite well for variables like temperature that can take on positive or negative values (Wang & Chen 2014), but can be problematic in modeling non-negative climate variables, such as precipitation. This is expressed mathematically below, where $F_{p,v,m}$ is the CDF function of the projected values and $F^{-1}_{h,v,m}$ is the quantile function of the projected values.

$$x^*_{p,v,m}(t) = x_{p,v,m}(t) + F^{-1}_{h,v,o}(F_{p,v,m}\left(x_{p,v,m}(t)\right)) - F^{-1}_{h,v,m}(F_{p,v,m}\left(x_{p,v,m}(t)\right)) \quad (3)$$

For a future projection $x_{p,v,m}(t)$ and its percentile $F_{p,v,m}\left(x_{p,v,m}(t)\right)$, the numerical value of the bias between the modeled and observed values at this percentile in the historical period is the difference between the historically modeled observation at that percentile and the observed observation at that quantile:

$$F^{-1}_{h,v,m}\left(F_{p,v,m}\left(x_{p,v,m}(t)\right)\right) - F^{-1}_{h,v,o}\left(F_{p,v,m}\left(x_{p,v,m}(t)\right)\right) \quad (4)$$

This quantity is subtracted from the projected value $x_{p,v,m}(t)$ to get the bias-corrected value, $x^*_{p,v,m}(t)$. Equiratio CDF matching is similar to equidistant CDF matching, but it multiplies the correction by simulated data rather than adding to it (Wang & Chen 2014).

$$x^*_{p,v,m}(t) = x_{p,v,m}(t) * \frac{F^{-1}_{h,v,o}(F_{p,v,m}\left(x_{p,v,m}(t)\right))}{F^{-1}_{h,v,m}(F_{p,v,m}\left(x_{p,v,m}(t)\right))} \quad (5)$$

This method is more fitting for variables with a lower bound at zero. Its primary assumption is that at each quantile, the ratio of the observed value to the modeled value in the historical period will be the same for the projection period. Accordingly, for a projection $x_{p,v,m}(t)$ and its corresponding percentile $F_{p,v,m}\left(x_{p,v,m}(t)\right)$ in the projection period, the bias between the modeled and observed values in the historical period can be expressed numerically as $\frac{F^{-1}_{h,v,m}\,(F_{p,v,m}\left(x_{p,v,m}(t)\right))}{F^{-1}_{h,v,o}\,(F_{p,v,m}\left(x_{p,v,m}(t)\right))}$ (Wang & Chen 2014). By multiplying the projection $x_{p,v,m}(t)$ by the reciprocal of the bias $\frac{F^{-1}_{h,v,o}(F_{p,v,m}\left(x_{p,v,m}(t)\right))}{F^{-1}_{h,v,m}(F_{p,v,m}\left(x_{p,v,m}(t)\right))}$, we obtain the bias-corrected projection $x^*_{p,v,m}(t)$.

Equidistant CDF matching was used for surface air temperature. The delta method was intended to be employed for eastward wind speed and northward wind speed, because there is not enough data for those variables to enable reliable CDF matching. Equiratio CDF matching was be used for the variables that cannot be negative: precipitation, surface upwelling shortwave radiation, surface downwelling shortwave radiation, surface longwave downwelling radiation, near-surface relative humidity, and near-surface air pressure.

Results

***The distributions referred to are the distributions of the regional daily averages, unless otherwise specified.

Historical Models: Reductions in Bias of GCM: Temperature

The mean (a measure of center) for the raw model (Figure 2) was 13.4766ºC and the standard deviation (std., a measure of spread defined as the average distance from the mean) was 8.8927ºC. The mean for the observational data (Figure 1) was 11.7546ºC and the std. was 8.56102ºC. For the BC model (Figure 3), the mean and std. were, respectively,11.7354ºC and 8.4431ºC. The difference between the means and standard deviations of the raw model and the observations were, respectively, 1.722ºC and .3317ºC, whereas these differences between the BC model and the observation were, respectively, -0.0192ºC and -0.1179ºC. In addition, the skewness (a measure of asymmetry with a negative or positive direction) is -0.2168 for the observed histogram, -0.5225 for the raw model, and -0.2675 for the BC model. The difference between the raw model and the BC model can also be visualized by the line plot (Figure 5) of the daily regional average temperature for each calendar day of the year from day 1 to 365, excluding 2/29 on leap years.

Historical Models: Reductions in Bias of GCM: Downward Longwave Radiation Flux

The mean of the distribution for the DLWRF observed data (Figure 6) was 321.4455 W/m^2, the std. was 47.4246 W/m^2, and the skewness was -0.0799. For the raw model (Figure 7), the mean of this distribution was 321.5875 W/m^2, the std. was 51.4211 W/m^2, and the skewness was -0.2285. For the BC model (Figure 8), these same measures were 321.3716 W/m^2, 49.8028 W/m^2, -0.1985, respectively. The differences between the raw model and observational mean, std., and skewness were 0.142 W/m^2, 32.9965 W/m^2, and -0.1486. The differences between the BC model and observational mean, std., and skewness were -0.0739 W/m^2, 2.3782 W/m^2, and -0.1186.

Historical Models: Reductions in Bias of GCM: Air Pressure

The mean, std., and skewness for the observational data (Figure 10) were 99181.4214 Pa, 588.7515 Pa, and -0.0991, respectively. For the raw model (Figure 11), the mean, std., and skewness were 99463.4664 Pa, 653.4179 Pa, and 0.1420, while for the BC model (Figure 12) they were 99184.5172 Pa, 597.0914 Pa, and -0.0951 respectively. The difference between the raw model's and the observation data's measures of center, spread, and skew were 282.045 Pa, 64.7204 Pa, and 0.2411. The difference between the BC model's and the observation data's measures of center, spread, and skew were 3.0958 Pa, 8.3399 Pa, and 0.004.

Historical Models: Reductions in Bias of GCM: Relative Humidity

For the observational data (Figure 14), the mean, std., and skewness were 78.2411%, 6.7121%, and -0.3014, in that order. For the raw model (Figure 15), these measures were 74.7880%, 9.0503%, and -0.4085, and for the BC model (Figure 16) they were 74.9820%, 6.7996%, and 0.2400. The difference between these values for the raw model and observational data were -3.4531%, 2.3382%, and -1.071, and these differences between the BC model and observation data were -3.2591%, 0.0875%, and 0.5414.

Bias-Corrected Projections of GCM: Temperature

The distribution of the future model (Figure 4) has mean 16.0591ºC, std. 8.5531ºC, and skewness -0.1590. This represents an increase in mean by 4.3237ºC, in std. by .11ºC, and a skewness closer to 0 by .1085. The regional daily average temperature for each day of the year is projected to increase by 4.3237ºC on average. This projected change in temperature is illustrated in Figure 8. The change in seasonal temperature is shown across the region in Figures 9, 10, 11 and 12. Figure 9 shows the average change in winter temperature between the historical period and the future period. The greatest winter temperature increases can be expected in the Northwestern corner of the grid, with temperature increases around 5ºC throughout much of New York and upwards of 5.5ºC along the Canadian border of New York, Pennsylvania, and Ohio. In the more southern states we can expect winter temperature increases of around 4ºC, with the lowest temperature increases over land occurring along the coast, illustrating the mitigating effect of the ocean. The average winter temperature increase across the region is 4.0927ºC. In the spring the highest temperature increases a bit less extreme, maxing out around 4.8ºC. In the US, the highest temperature increases are expected in the more Southern states, ranging from around 4.5 to 4.8ºC with none of the states seeing much less than a 4ºC spring temperature increase. The average spring temperature increase across the region 3.9096 ºC. In the summer, most of the states can expect temperature increases between 5 and 5.5ºC, with the lowest temperature increases over land at around 4.5ºC near the coast line. The Great Lakes also have a mitigating effect in summer temperature increases. The average summer temperature increase over the whole region is 4.3980ºC. In the fall, temperature increases tend to get higher moving west, moving from around 4ºC at the coast line to around 5.5ºC in Ohio. The average change in fall temperature over the whole region is 4.1799ºC.

Bias-Corrected Projections of GCM: Air Pressure

The mean of the distribution of air pressure from the BC future model (Figure 13) is 99198.5866 Pa, with a std. of 572.5136 and a skewness of -0.2262. The differences between the future BC model mean, std., and skewness are 14.0694, -24.5778, and -0.1311.

Bias-Corrected Projections of GCM: Downward Longwave Radiation Flux

For the BC future model DLWRF distribution (Figure 9), the mean was 349.0011 W/m^2, the std. was 52.2221 W/m^2, and the skewness was -0.1790. The differences between the future and historical model mean, std. and skewness are 27.5556 W/m^2, .8010 W/m^2, and -0.0991.

Bias-Corrected Projections of GCM: Relative Humidity

The mean of the BC future model distribution (Figure 17) was 73.1714%, the std. was 7.7107%, and the skewness was 0.3292. The differences between the future and historical model mean, std., and skewness are -1.8106%, 0.9111%, and 0.0892.

Discussion

Considering surface air temperature, the distribution of the raw model (Figure 2) did not look very similar to that of the observed data (Figure 1). The mean, std., and skewness for the BC model (Figure 3) were both closer to those observed than they were for the raw model, as quantified by the differences between them. Reducing the difference between the model and the observational data's measures of center, spread, and shape signifies that the bias-correction improved the model's distribution for the given region. In addition, Figure 5 visualizes the improvement between the average temperature for each day of the year over the region, as the average distance between the line for the BC model and the observations is much smaller than that for the raw model and the observations. This indicates that the future BC model for air temperature should not be too far off from what we can expect if we continue on the track of this greenhouse gas emissions scenario. As increases in temperature have been associated with worsening hypoxia, we would expect that the increase in temperature would likely exacerbate the issue. The seasonal focus of temperature increases also affects hypoxia. For example, in this region, summer temperatures are projected to experience a greater average increase than in any other season, which would likely make summer hypoxic zones larger and last longer due to decreased oxygen solubility and increased water stratification (Wang 2017). However, more research is needed to confirm this, in addition to how warming in other seasons in this region will influence hypoxia.

For DLWRF, the mean, std., and skewness of the BC model distribution were all closer to the values of the observational distribution than the values from the raw model distribution were, representing an improvement in the accuracy of the model for the given region. Despite the improvement in the model's accuracy, the BC historical projection still had a bit more of a left skew, meaning that it had higher frequencies of observations that were greater than the mean than the observed data did. Intuitively, the BC future projection may evince the same tendency. In the BC future model, the mean would increase by around 28 W/m^2, the std. would increase by around .8 W/m^2, and the distribution would see higher frequencies of observations above the mean. The increase in the mean of DLWRF was expected, as radiation and temperature are related.

Looking at air pressure, the values of the mean, std., and skewness of the BC model distribution were much closer to the values of the observed data than the values of the raw model distribution were. The distributions of the BC model and the observed data were very similar, which would likely make the BC future model much more feasible if we continue on track for the given greenhouse gas scenario. Under this BC future model, we would see an increase in the mean of the distribution of around 14 Pa, a decrease in the std. of around 25 Pa, and a decrease in the skewness of the distribution of .1311, meaning that there would be higher frequencies above the mean air pressure than there are as of current. Higher air pressure is usually associated with clear skies, but the average across the whole region for a twenty-year period does not account for changes within the region and interannually. Further research on air pressure changes should include more detail on high- and low-pressure points across the region and over time, as storms, typically associated with low-pressure areas, influence hypoxia.

Unfortunately, for relative humidity, the downscaling and bias-correction did not improve as much upon the raw model as it had for other variables. Although the BC model mean is slightly closer to the observational mean than the raw model mean and the std. is more similar, the skewness of the histogram switched from negative to positive, meaning that the value with the highest frequency went from being greater than the mean to less than the mean, changing the shape of the distribution. I cannot say for certain why this happened, but because the raw model's histogram had a more negative skewness than the observations' histogram, it would appear that the bias-correction method overcorrected the skewness. Because the distribution of the future BC model looks similar to that of the BC historical model, and the BC historical model underestimates the mean and overestimates the skew in the positive direction, I would recommend trying a different bias-correction method on this variable to hopefully obtain a more realistic BC historical model, and in turn a more realistic BC future model. However, the decrease in mean relative humidity over the region would make sense, because if the average amount of water vapor in the air does not increase as much as temperature does, then the mean relative humidity would decrease. Still, there were missing time points in both the bias-corrected historical and future models, 72 in the current model, and 4,264 time points missing in the future model. The reason for the missing data is currently unknown, and the data and code will need to be explored further to find the source of the problem.

As a side note, as the regional daily averages of these variables are taken over the entire region, which includes area over the ocean, some of the distributions will be slightly different than if they were only taken over land. Originally, we were also going to downscale and bias-correct the variables downward shortwave radiation flux, upward shortwave radiation flux, and eastward and westward wind. Unfortunately, for the two radiation variables, there were "bad" or missing data values that we did not have time to correct within the ten-week research period. In addition, the CCSM4 model of CMIP5 only provides wind projections with a monthly frequency. Because we did not have enough data points to use CDF matching we started to alter the code to enable correction using the delta method but ran out of time. Future work will include downscaling and bias-correcting the remaining variables to enable the hypoxia projection. Other directions that this work could be taken in include modeling how these variables and other aspects of climate change impact the timing, growth, and yield of agriculture, as agriculture in the Chesapeake Bay watershed largely influences hypoxia.

Conclusion

Based on the statistically downscaled and bias-corrected data currently available, I would conclude that the increase in temperature and its impact on the solubility of dissolved oxygen will likely have a negative impact on hypoxia on the Chesapeake Bay. However, I cannot confidently say if hypoxia will be worsened or improved overall after taking the changes in all variables into consideration, because I am still in the process of downscaling and bias-correcting four of the eight variables needed to run the Regional Oceanic Modeling System (ROMS) coupled with the biogeochemical model, Row-Column Aesop (RCA), and project hypoxia in the Chesapeake Bay. Work on downscaling and bias-correcting the remaining variables will continue into the fall to obtain more definitive results.

Acknowledgments

I would like to thank Dr. Ming Li for his mentorship, Wenfei Ni for her guidance, and Dr. Andrew C. Ross for his code and Python help. I would also like to thank Dr. Mike Allen and Maryland

Sea Grant for the opportunity to conduct this research. This study was supported by NSF grant OCE-1756244.

References

Altieri, A.H., K.B. Gedan. 2015. Climate Change and Dead Zones. Global Change Biology. 21: 1395-1406. doi: 10.1111/gcb.12754

Boé, J., L. Terray, F. Habets, E. Martin. 2007. Statistical and dynamical downscaling of the Seine basin climate for hydro-meteorological studies. International Journal of Climatology. 27: 1643–1655. doi: 10.1002/joc.1602

Boyd, J.N., L.E. Burnett. 1999. Reactive oxygen intermediate production by oyster hemocytes exposed to hypoxia. Journal of Experimental Biology, 202, 3135–3143. Rpt. In: A.H. Altieri, K.B. Gedan. 2015. Climate Change and Dead Zones. Global Change Biology. 21: 1395-1406. doi: 10.1111/gcb.12754

Buser, C.M., H.R. Künsch, D. Lüthi, M. Wild, C. Schär. 2009. Bayesian multi-model projection of climate: bias assumptions and interannual variability. Climate Dynamics. 33. 6: 849–868. doi: 10.1007/s00382-009-0588-6

Cannon, A.J., S.R. Sobie, T.Q. Murdock. 2015. Bias Correction of GCM Precipitation by Quantile Mapping: How Well Do Methods Preserve Changes in Quantiles and Extremes?. Journal of Climate. 28: 6938-6959. doi: 10.1175/JCLI-D-14-00754.1

Carstensen, J., J.H. Andersen,B.G. Gustafsson, D.J. Conley. 2014. Deoxygenation of the Baltic Sea during the last century. Proceedings of the National Academy of Sciences of the United States of America. 111: 5628–5633. doi: 10.1073/pnas.1323156111 Rpt. In A.H. Altieri, K.B. Gedan. 2015. Climate Change and Dead Zones. Global Change Biology. 21: 1395-1406. doi: 10.1111/gcb.12754

Chapin, III., F.S., E.S. Zavaleta, V.T. Eviner, R.L. Naylor, P.M. Vitousek, H.L. Reynolds, et al. 2000. Consequences of changing biodiversity. Nature. 405: 234–242. doi: 10.1038/35012241 Rpt. In: S.S. Hale, G. Cicchetti, C.F. Deacutis. 2016. Eutrophication and Hypoxia Diminish Ecosystem Functions of Benthic Communities in a New England Estuary. Frontiers in Marine Science. 3: 249. doi: 10.3389/fmars.2016.00249

Covitch, A.P.,M.C. Austen, F. Bärlocher, E. Chauvet, B.J. Cardinale, C.L. Biles, et al. (2004). The role of biodiversity in the functioning of freshwater and marine benthic ecosystems. BioScience. 54: 767–775. doi: 10.1641/0006-3568(2004)054[0767:TROBIT]2.0.CO;2 Rpt. In: S.S. Hale, G. Cicchetti, C.F. Deacutis. 2016. Eutrophication and Hypoxia Diminish Ecosystem Functions of Benthic Communities in a New England Estuary. Frontiers in Marine Science. 3: 249. doi: 10.3389/fmars.2016.00249

Davies, A.M., J.X. Xing. 2007. On the influence of stratification and tidal forcing upon mixing in sill regions. Ocean Dynamics. 57: 431–451. Rpt. In: A.H. Altieri, K.B. Gedan. 2015. Climate Change and Dead Zones. Global Change Biology. 21: 1395-1406. doi: 10.1111/gcb.12754

Doney, S.C., M. Ruckelshaus, J.E. Duffy et al. 2012. Climate change impacts on marine ecosystems. Annual Review of Marine Science. 4: 11–37. Rpt. In: A.H. Altieri, K.B. Gedan. 2015. Climate Change and Dead Zones. Global Change Biology. 21: 1395-1406. doi: 10.1111/gcb.12754

Goulletquer, P., P. Gros, G. Boeuf, J. Weber. 2014. Biodiversity in the Marine Environment. Springer: Cham. Rpt. In: S.S. Hale, G. Cicchetti, C.F. Deacutis. 2016. Eutrophication and Hypoxia Diminish Ecosystem Functions of Benthic Communities in a New England Estuary. Frontiers in Marine Science. 3: 249. doi: 10.3389/fmars.2016.00249

Hale, S.S., G. Cicchetti, C.F. Deacutis. 2016. Eutrophication and Hypoxia Diminish Ecosystem Functions of Benthic Communities in a New England Estuary. Frontiers in Marine Science. 3: 249. doi: 10.3389/fmars.2016.00249

Hansen, J.L.S., J. Bendtsen. 2009. Effects of climate change on hypoxia in the North Sea – Baltic Sea transition zone. IOP Conference Series: Earth and Environmental Science. 6. doi:10.1088/1755-1307/6/0/302016.

IPCC (2013) Working Group I Contribution to the Fifth Assessment Report of the Intergovernmental Panel on Climate Change 2013: The Physical Science Basis Summary for Policymakers. Stockholm, Sweden. Rpt. In: A.H. Altieri, K.B. Gedan. 2015. Climate Change and Dead Zones. Global Change Biology. 21: 1395-1406. doi: 10.1111/gcb.12754

Irby, I.D., M.A.M. Friedrichs, F. Da, K.E. Hinson. 2018. The competing impacts of climate change and nutrient reductions on dissolved oxygen in Chesapeake Bay. Biogeosciences. 9: 2649-2668. https://doi.org/10.5194/bg-15-2649-2018.

Justic, D., N.N. Rabalais, R.E. Turner. 2005. Coupling between climate variability and coastal eutrophication: evidence and outlook for the northern Gulf of Mexico. Journal of Sea Research. 54: 25–35. Rpt. In: A.H. Altieri, K.B. Gedan. 2015. Climate Change and Dead Zones. Global Change Biology. 21: 1395-1406. doi: 10.1111/gcb.12754

Kemp, W.M., W.R. Boynton, J.E. Adolf et al. (2005) Eutrophication of Chesapeake Bay: Historical trends and ecological interactions. Marine Ecology-Progress Series, 303: 1–29. Rpt. In: A.H. Altieri, K.B. Gedan. 2015. Climate Change and Dead Zones. Global Change Biology. 21: 1395-1406. doi: 10.1111/gcb.12754

Kroeker, K.J., R.L. Kordas, R.N. Crim, G.G. Singh. 2010. Meta-analysis reveals negative yet variable effects of ocean acidification on marine organisms. Ecology Letters. 13: 1419–1434. Rpt. In: A.H. Altieri, K.B. Gedan. 2015. Climate Change and Dead Zones. Global Change Biology. 21: 1395–1406. doi: 10.1111/gcb.12754

Lee, Y.J., W.R. Boynton, M. Li, Y. Li. 2013. Role of Late Winter–Spring Wind Influencing Summer Hypoxia in Chesapeake Bay. Estuaries and Coasts. 36: 683-696. https://doi.org/10.1007/s12237-013-9592-5

Li, H., J. Sheffield, E.F. Wood. 2010. Bias correction of monthly precipitation and temperature fields from Intergovernmental Panel on Climate Change AR4 models using equidistant quantile matching. Journal of Geophysical Research. 115: D10101. doi: 10.1029/2009JD012882

Li, M., Y.J. Lee, J.M. Testa, Y. Li, W. Ni, W.M. Kemp, D.M. De Toro. 2016. What drives interannual variability of hypoxia in Chesapeake Bay: Climate forcing versus nutrient loading?. Geophysical Research Letters. 43: 2127–2134. doi: 10.1002/2015GL067334

Meier, H.E.M., H.C. Andersson, K. Eilola et al. 2011. Hypoxia in future climates: a model ensemble study for the Baltic Sea. Geophysical Research Letters. 38: L24608. Rpt. In: A.H. Altieri, K.B. Gedan. 2015. Climate Change and Dead Zones. Global Change Biology. 21: 1395-1406. doi: 10.1111/gcb.12754

Muhling, B.A., C.F. Gaitán, C.A. Stock, V.S. Saba, D. Tommasi, K.W. Dixon. 2017. Potential Salinity and Temperature Futures for the Chesapeake Bay Using a Statistical Downscaling Spatial Disaggregation Framework. Estuaries and Coasts. doi: 10.1007/s12237-017-0280-8

Passow, C., R. Donner. 2017. Linear Regression Quantile Mapping (RQM) - A new approach to bias correction with consistent quantile trends. Geophysical Research Abstracts. 19: 12203.

Portner, H.O., HO. 2010. Oxygen- and capacity-limitation of thermal tolerance: a matrix for integrating climate-related stressor effects in marine ecosystems. Journal of Experimental Biology. 213: 881–893. Rpt. In: A.H. Altieri, K.B. Gedan. 2015. Climate Change and Dead Zones. Global Change Biology. 21: 1395–1406. doi: 10.1111/gcb.12754

Rabalais, N.N., R.E. Turner, R.J. Diaz, D. Justic. 2009. Global change and eutrophication of coastal waters. Ices Journal of Marine Science, 66, 1528–1537. Rpt. In: A.H. Altieri, K.B. Gedan. 2015. Climate Change and Dead Zones. Global Change Biology. 21: 1395–1406. doi: 10.1111/gcb.12754

Rabotyagov, S.S., C.L. Klingy, P.W. Gassman, N. N. Rabalais, R.E. Turner. 2014. The Economics of Dead Zones: Causes, Impacts, Policy Challenges, and a Model of the Gulf of Mexico Hypoxic Zone. Review of Environmental Economics and Policy. 8. 1: 58–79. doi: 10.1093/reep/ret024

Rosa, R., B.A. Seibel. 2008. Synergistic effects of climate-related variables suggest future physiological impairment in a top oceanic predator. Proceedings of the National Academy of Sciences of the United States of America. 105: 20776–20780. Rpt. In: A.H. Altieri, K.B. Gedan. 2015. Climate Change and Dead Zones. Global Change Biology. 21: 1395–1406. doi: 10.1111/gcb.12754

Scully. M.E., 2010. Wind Modulation of Dissolved Oxygen in Chesapeake Bay. Estuaries and Coasts 33. 5: 1164–1175. doi: 10.1007/s12237-010-9319-9

Scully. M.E., 2013. Physical controls on hypoxia in Chesapeake Bay: a numerical study. Journal of Geophysical Research: Oceans. 118: 1239-1256. doi:10.1002/jgrc.20138, 2013

Snelgrove, P.V.R., 1998. The biodiversity of macrofaunal organisms in marine sediments. *Biodivers. Conserv.* 7, 1123–1132. doi: 10.1023/A:1008867313340. Rpt. In: S.S. Hale, G. Cicchetti, C.F. Deacutis. 2016. Eutrophication and Hypoxia Diminish Ecosystem Functions of Benthic Communities in a New England Estuary. Frontiers in Marine Science. 3: 249. doi: 10.3389/fmars.2016.00249

Tang, J., X. Niu, S. Wang, H. Gao, X. Wang, J. Wu. 2016. Statistical downscaling and dynamical downscaling of regional climate in China: Present climate evaluations and future climate projections. Journal of Geophysical Research. 121. 5: 2110-2129. doi: 10.1002/2015JD023977

Testa, J.M., R.R. Murphy, D.C. Brady, W.M. Kemp. 2018. Nutrient- and Climate-Induced Shifts in the Phenology of Linked Biogeochemical Cycles in a Temperate Estuary. Frontiers in Marine Science. 5. doi: 10.3389/fmars.2018.00114

Teutschbein, C., J. Seibert. 2012. Bias correction of regional climate model simulations for hydrological climate-change impact studies: Review and evaluation of different methods. Journal of Hydrology: 456–457: 12–29. doi: 10.1016/j.jhydrol.2012.05.052

Van Der Zwaan, G.J., F.J. Jorissen. 1991 Biofacial patterns in river-induced shelf anoxia. In: Modern and Ancient Continental Shelf Anoxia (ed. Pearson RVTaTH), pp. 65–82. The Geological Society, London. Rpt. In: A.H. Altieri, K.B. Gedan. 2015. Climate Change and Dead Zones. Global Change Biology. 21: 1395-1406. doi: 10.1111/gcb.12754

Villate, F., A. Iriarte, I. Uriarte, L. Intxausti, A. De La Sota. 2013. Dissolved oxygen in the rehabilitation phase of an estuary: influence of sewage pollution abatement and hydro-climatic factors. Marine Pollution Bulletin. 70: 234–246. Rpt. In: A.H. Altieri, K.B. Gedan. 2015. Climate Change and Dead Zones. Global Change Biology. 21: 1395–1406. doi: 10.1111/gcb.12754

Wang, L., W. Chen. 2014. Equiratio cumulative distribution function matching as an improvement to the equidistant approach in bias correction of precipitation. Atmospheric Science Letters. 15: 1–6. doi: 10.1002/asl2.454

Wang, P., L. Linker, H. Wang, G. Batt, G. Yactayo, K. Hinson, R. Tian. 2017. Assessing water quality of the Chesapeake Bay by the impact of sea level rise and warming. IOP Conference Series: Earth and Environmental Science. 82: 012001. doi: 10.1088/1755-1315/82/1/012001

Winder, M., U. Sommer. 2012. Phytoplankton response to a changing climate. Hydrobiologia. 698, 5–16. Rpt. In: A.H. Altieri, K.B. Gedan. 2015. Climate Change and Dead Zones. Global Change Biology. 21: 1395–1406. doi: 10.1111/gcb.12754

Worm, B., E.B. Barbier, N. Beaumont, J.E. Duffy, C. Folke, B.S. Halpern, et al. 2006. Impacts of biodiversity loss on ocean ecosystem services. Science. 314: 787–790. doi: 10.1126/science.1132294 Rpt. In: S.S. Hale, G. Cicchetti, C.F. Deacutis. 2016. Eutrophication and Hypoxia Diminish Ecosystem Functions of Benthic Communities in a New England Estuary. Frontiers in Marine Science. 3: 249. doi: 10.3389/fmars.2016.00249

Figures

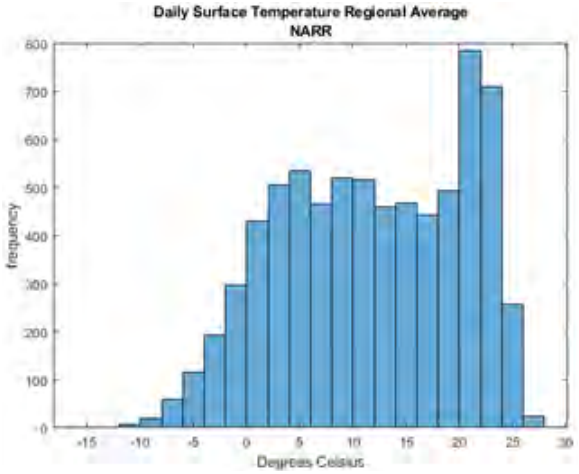

Figure 1

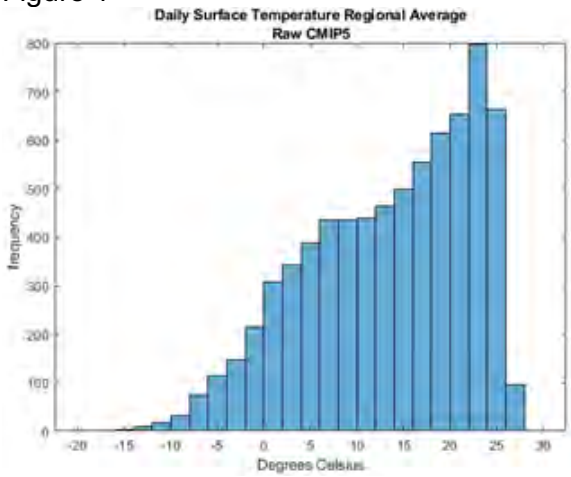

Figure 2

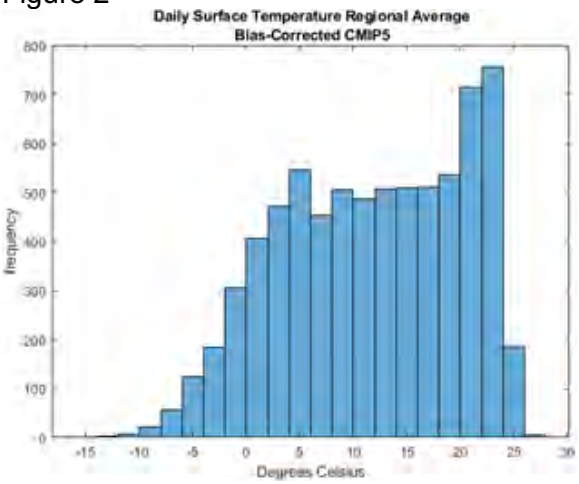

Figure 3

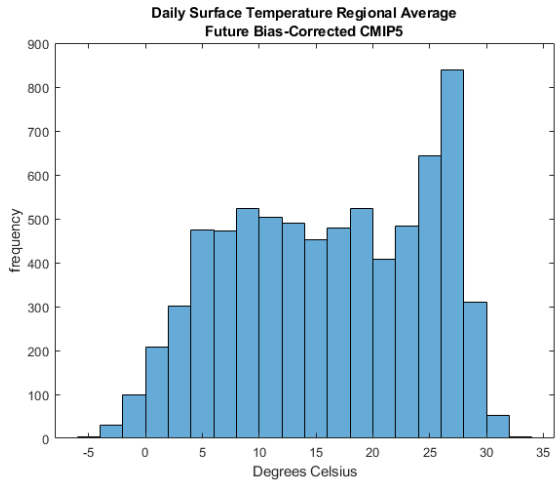

Figure 4

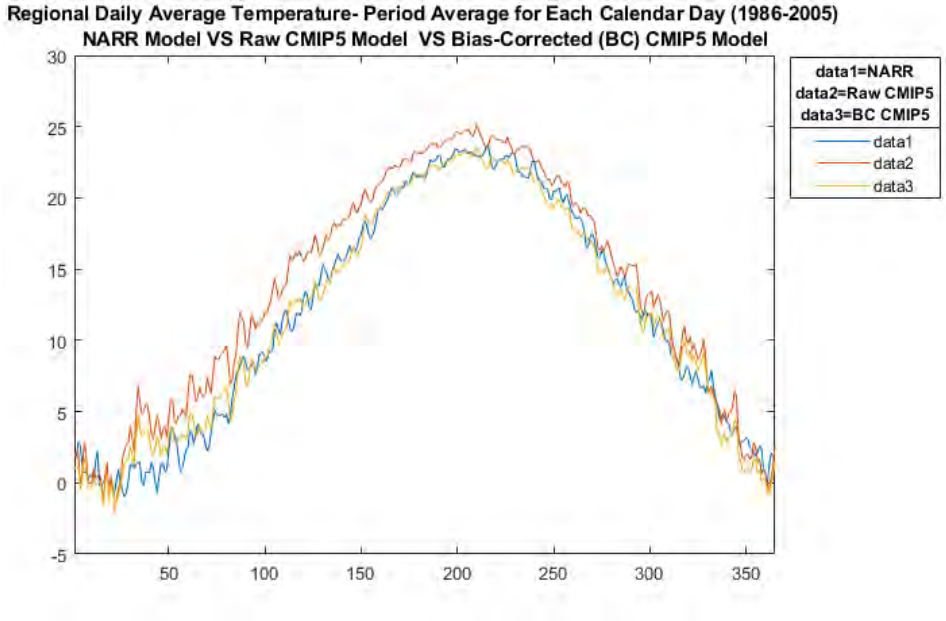

Figure 5

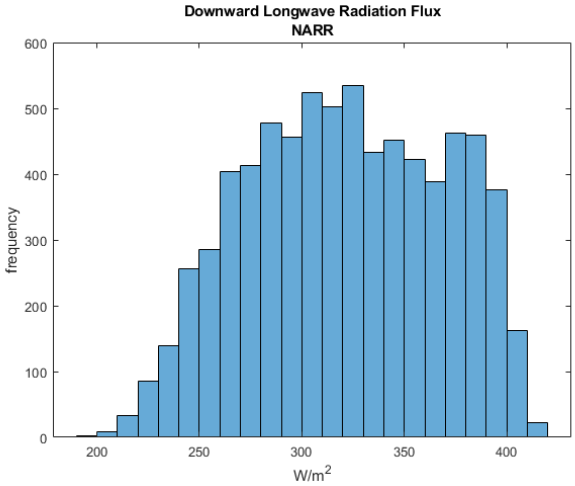

Figure 6

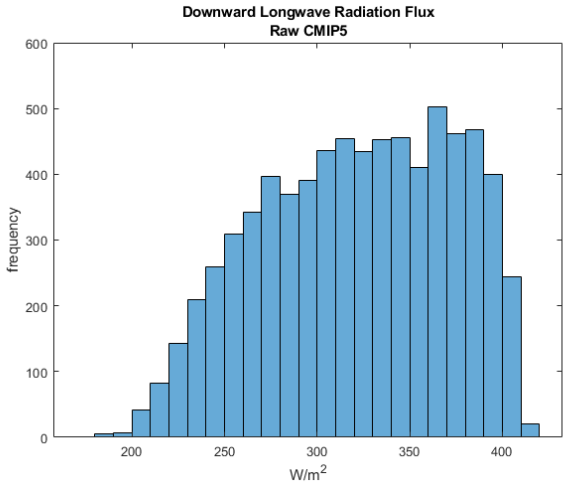

Figure 7

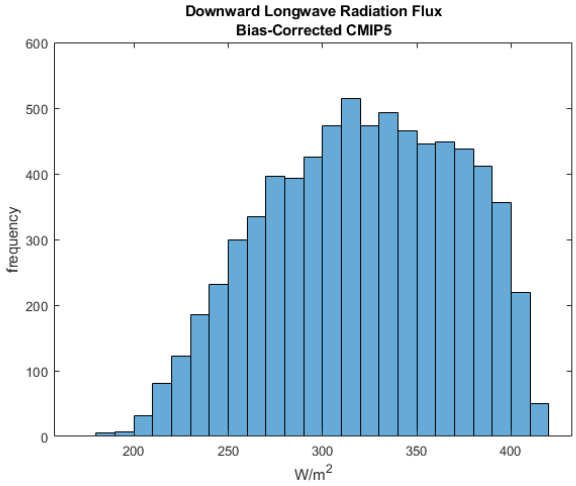

Figure 8

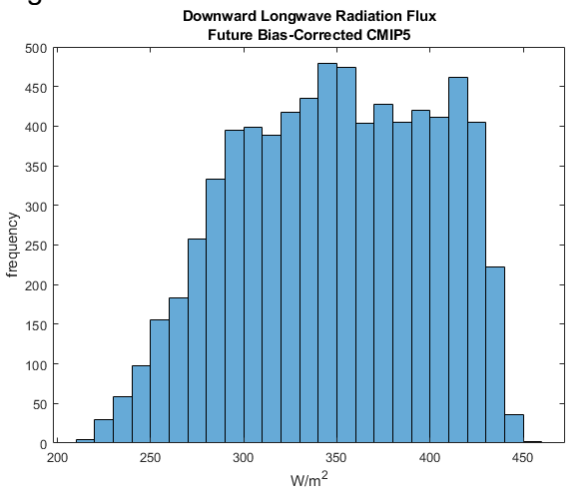

Figure 9

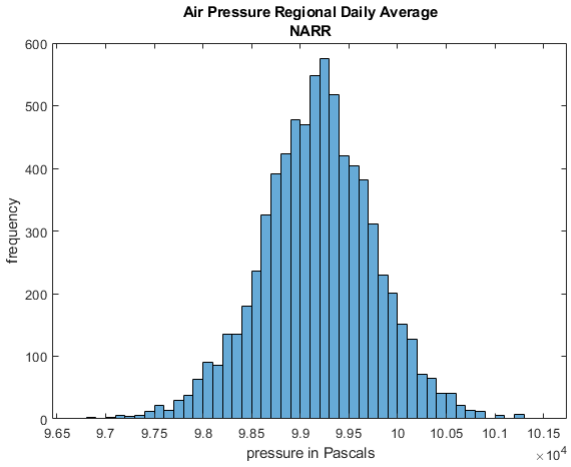

Figure 10

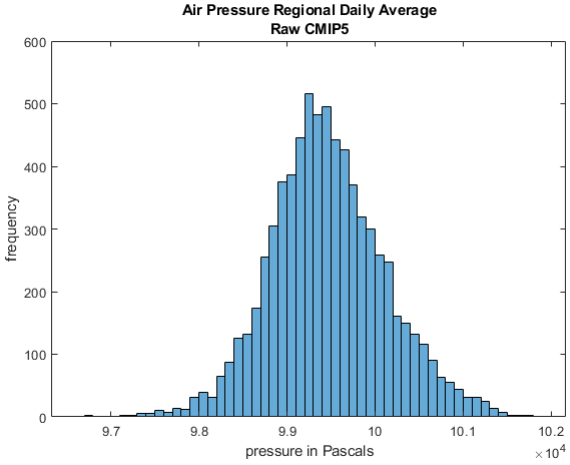

Figure 11

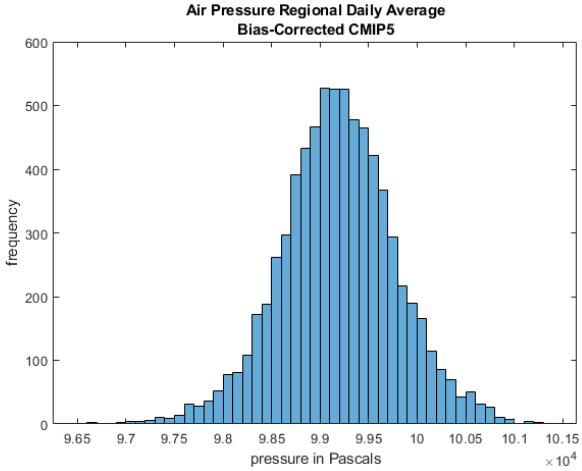

Figure 12

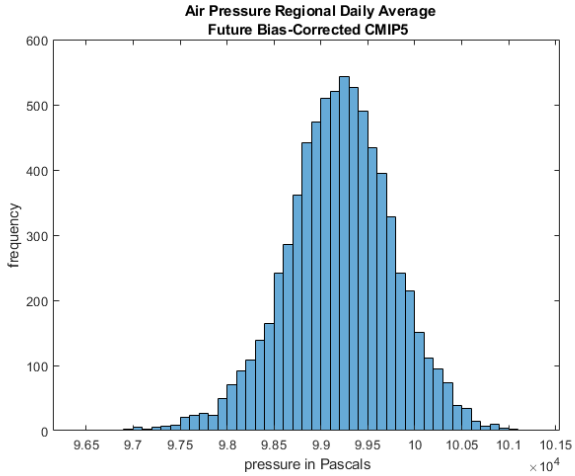

Figure 13

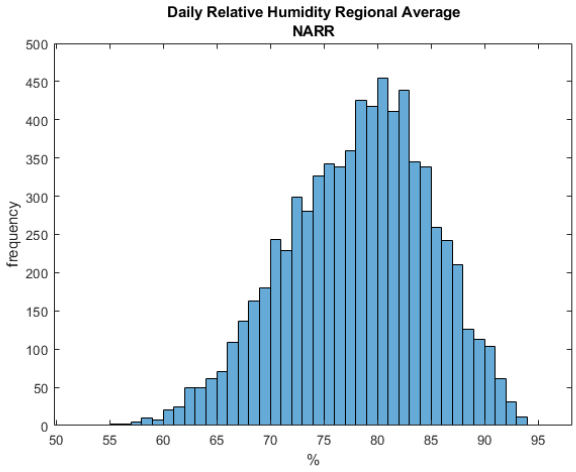

Figure 14

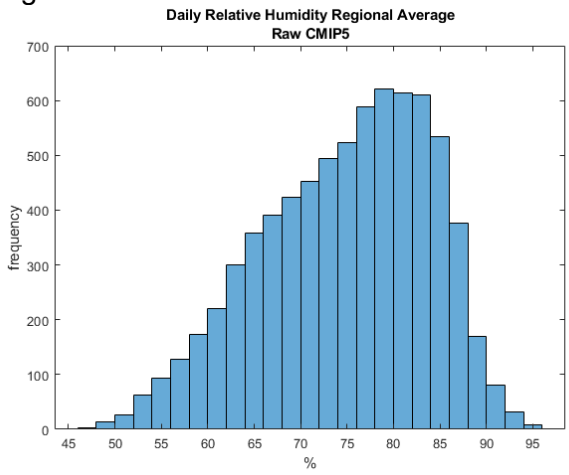

Figure 15

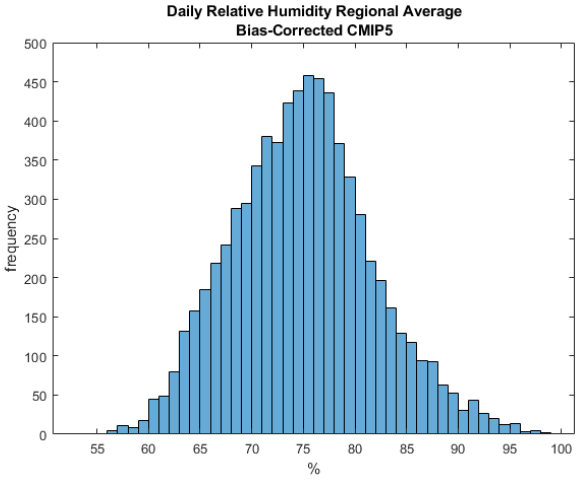

Figure 16

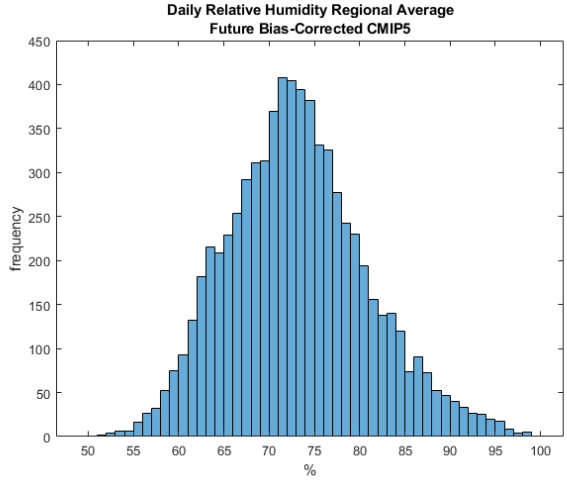

Figure 17

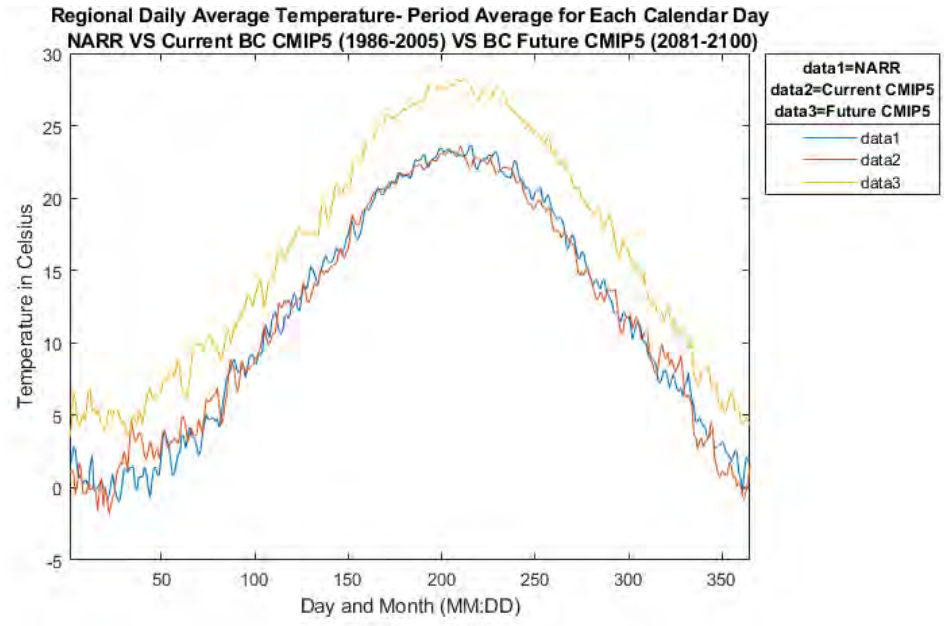

Figure 18

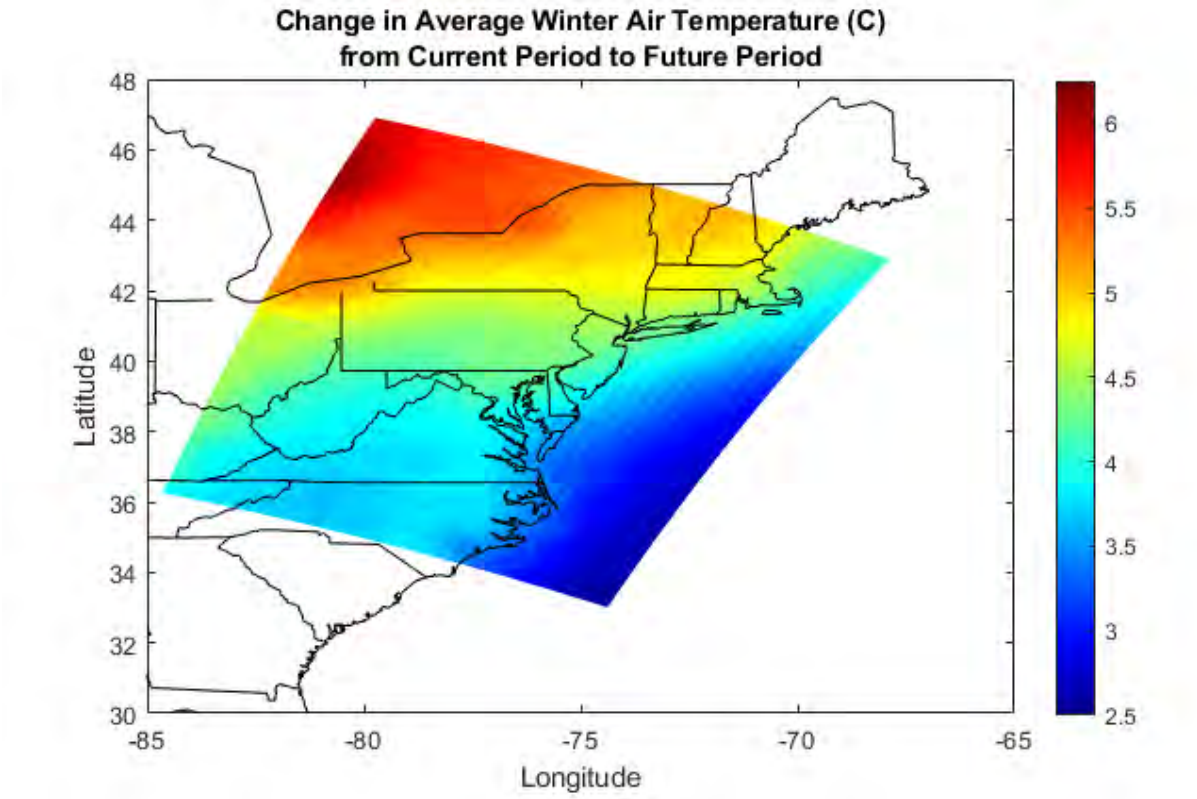

Figure 19

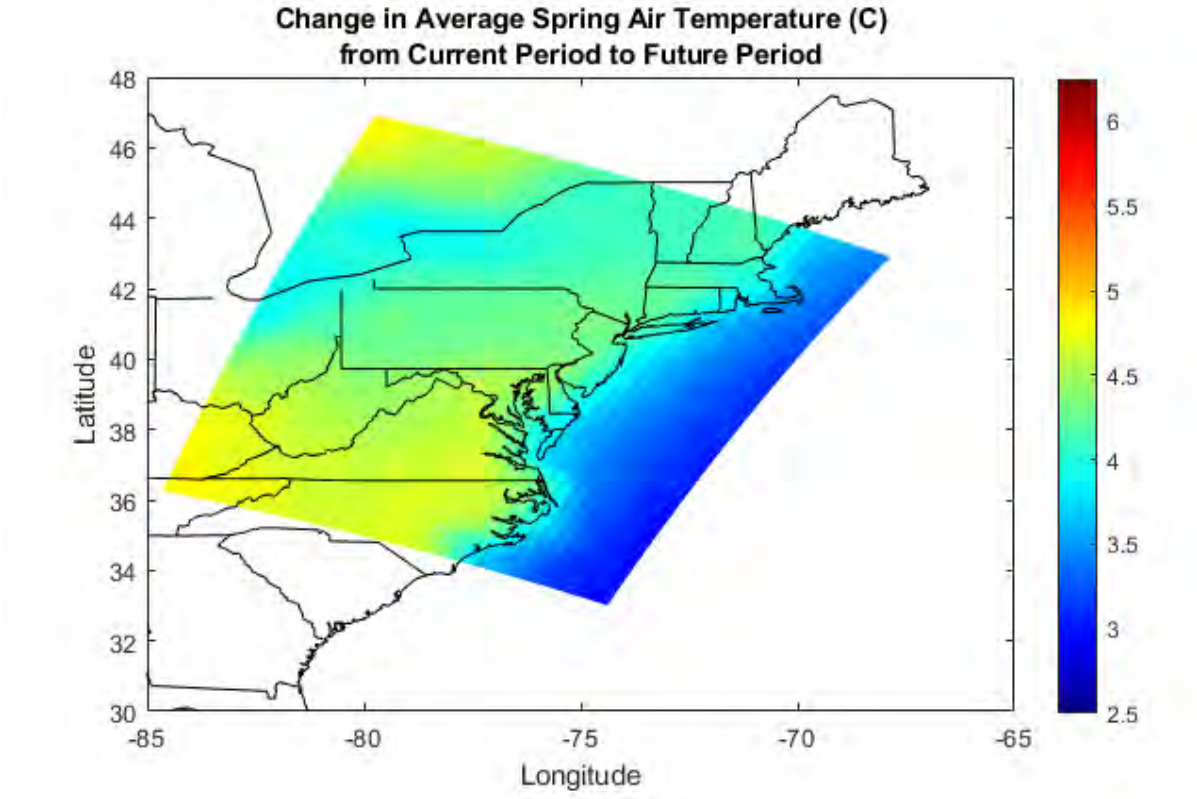

Figure 20

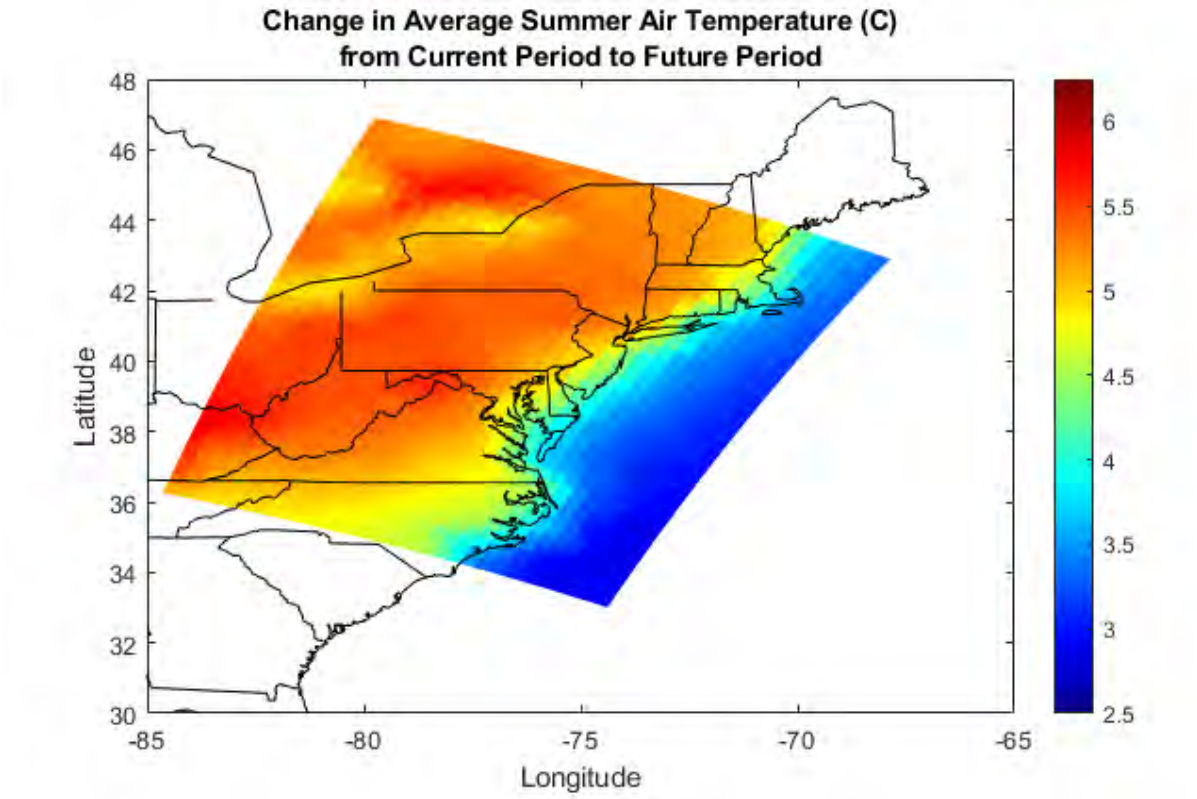

Figure 21

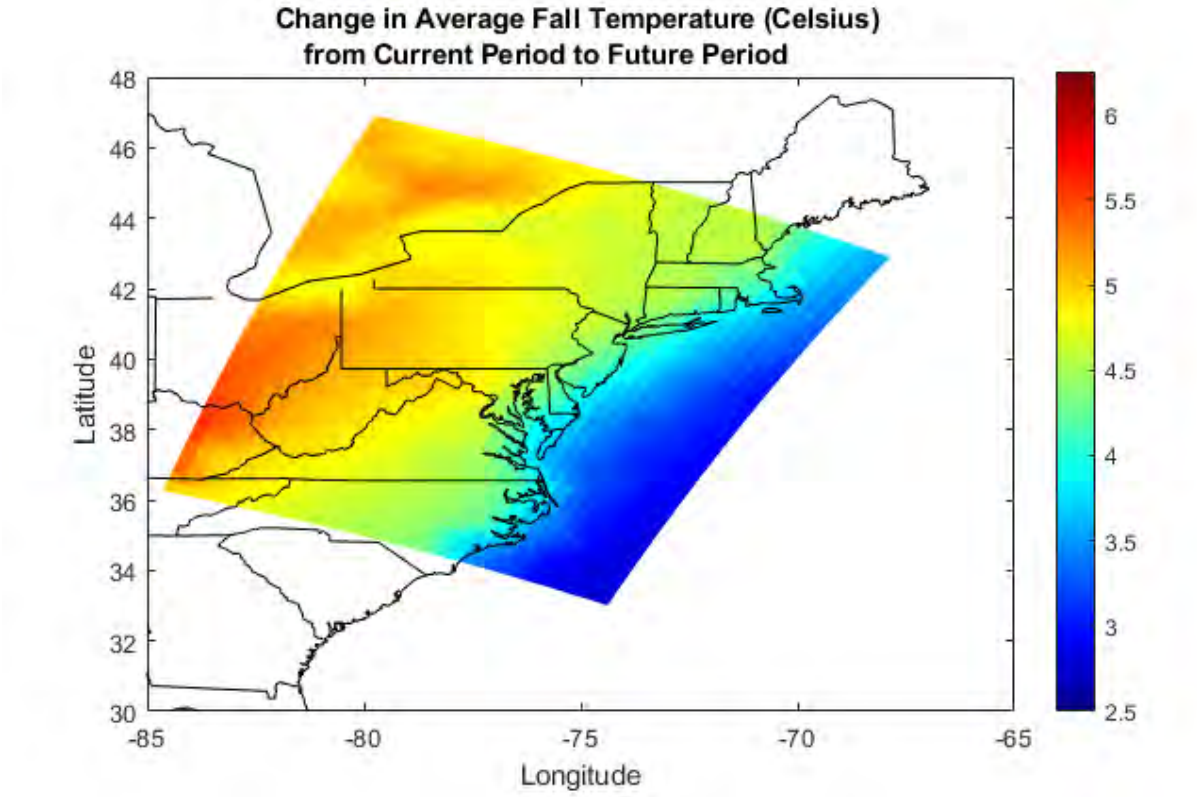

Figure 22

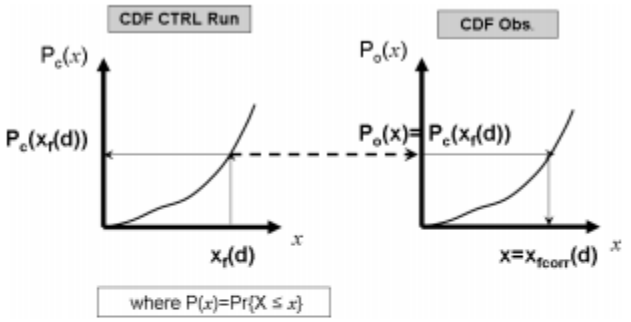

Figure 2. Principle scheme of bias correction using quantile–quantile mapping technique. cdf is empirical Cumulative Distribution Function. The subscript f, c, o stand for the climate scenario, the control simulation and the observations respectively. For the value xf(d) of the variable x for the day d in the climate scenario, the corresponding seasonal cumulative frequency Pc(xf(d)) where $P(x) = Pr\{X \le x\}$ is searched on the empirical cdf of the present climate control simulation. Then, the value of x such as $Po(x) = Pc(xf(d))$ is searched on the cdf of the observations. This value, named *xfcorr(d)*, is finally used as the corrected value of xf(d) in the climate scenario.

Figure 23 (Boé, et. al 2007)

.

A deployable autonomous CO_2 sensor (DACS): Improving pCO_2 spatial resolution in Chesapeake Bay, Maryland

Victoria Williams, REU Fellow
Maryland Sea Grant

Matthew Gray, Associate Professor
Horn Point Laboratory, University of Maryland Center for Environmental Science

Abstract

Ocean acidification disrupts the carbonate chemistry of marine ecosystems and threatens calcifying organisms, which then harms coastal communities that depend on them. There is a lack of understanding of the effects of ocean acidification in estuaries due to their complexity and the minimal spatial and temporal monitoring being conducted. Because high-quality commercial CO_2 sensors are very expensive, monitoring at greater frequencies is a costly and difficult task that is never accomplished. Acknowledging the need to understand the carbonate chemistry, the objective of this project was to design and build a deployable autonomous CO_2 sensor (DACS) at a price of under a thousand dollars. The study consisted of the construction of a DACS followed by verification of the product through field testing and laboratory analysis. The laboratory analysis consisted of a collection of water samples and measurement of total alkalinity and dissolved oxygen to calculate pCO_2. The construction of the DACS was a success after several design iterations. The DACS CO_2 measurements were verified with the laboratory results. While the DACS and laboratory monitoring of Horn Point Laboratory (HLP) hatchery water data exhibited similar trends, results somewhat diverged indicating the need for further development of the DACS to improve accuracy. Despite inaccuracy, optimizing and verifying the DACS performance will continue, as development of an inexpensive and reliable CO_2 sensor is imperative for future ocean acidification research.

Introduction

Anthropogenic factors have increased global atmospheric CO_2, subsequently causing climate change and ocean acidification. Ocean acidification describes the increased CO_2 absorption by global oceans, resulting in a decline in pH. The decline in oceanic pH results from the absorption of CO_2 that reacts with seawater to form carbonic acid (H_2CO_3). H_2CO_3 dissociates into a bicarbonate ion (HCO_3^-) and a hydrogen ion (H^+), resulting in an increased ocean acidity or [H^+] (Figure 1). The alterations in the seawaters' carbonate chemistry threaten to disrupt global ecological and socioeconomic processes, such as tourism efforts and the success of fisheries and hatcheries (Ekstrom et al. 2015). A decline in global pH can affect marine food chains, organismal metabolic rates and development, and other processes. In addition, a net decrease in carbonate ions (CO_3) makes it challenging for calcifying marine organisms, such as shellfish, to build their shells, which leaves these organisms in a vulnerable position against dissolving in corrosive water (Orr et al. 2005). In the year 2015, the United States collected

approximately 48.7 million pounds of shellfish, equating to about 306 million dollars in profit (National Marine Fisheries Service 2017). However, in the recent decades, shellfish populations have decreased because of overfishing and disease, which has adversely influenced socioeconomic processes in coastal communities (National Marine Fisheries Service 2017). Ocean acidification adds an additional threat to these valuable marine resources and subsequent stress to industries. Industries and communities that are dependent on the cultivation of shellfish as a major resource are experiencing threats of ocean acidification alongside the coastal habitats that shellfish reside in (Scavia et al. 2002).

In addition to ocean acidification, many coastal habitats are exposed to another anthropogenic source of acidification known as coastal acidification. Coastal acidification has similar consequences to ocean acidification, but the source is different. Coastal and estuarine habitats that receive large amounts of nutrient runoff may experience eutrophication. Eutrophication causes coastal waters to become hypoxic and hypercapnic, which challenges the survival of organisms dependent on oxygen. Therefore, coastal acidification has negative ecological and communal implications because acidification hampers the ability of coastal ecosystems to remain highly productive for dependent communities. As one of the largest estuaries in North America, the Chesapeake Bay is home to over 250 species and brings over 22 billion in revenue to numerous communities through tourism, recreation, and industrial fisheries (Task Force to Study the Impact of Ocean Acidification on State Waters 2015). However, the Chesapeake Bay is a primary example of an estuary that is vulnerable to further ecological effects from coastal acidification, as its fisheries have seen a decline in their populations of fish and shellfish in recent years. This has subsequently hurt the labor market and made the states that depend on the Bay recognize the need for ecological restoration. States such as Maryland have implemented bills and started preliminary research on coastal acidification to address the marine ecological needs, industrial protocol, and better understand consequences of acidification (Brady et al. 2018).

Researchers in the preliminary stages of monitoring the water quality of the Chesapeake Bay have better understood the Bay's overall health. However, scholars and state agencies have only begun to understand the carbonate chemistry throughout the Bay. While studies have assessed pH in select areas of the Chesapeake Bay, the data does not provide a full understanding of the relation between atmospheric CO_2 and aqueous CO_2. Instead, previous studies generalize on the effects of coastal acidifications with data from a small range of parameters such as pH and dissolved oxygen (Task Force to Study the Impact of Ocean Acidification on State Waters 2015). Unless there are many monitoring sites, it is difficult to assess coastal acidification in estuaries given their varying salinities, anthropogenic effects, and differing habitats. The limited data on pCO_2 and other elements of the carbonate system hinders identification of the causes of coastal acidification across the Bay and knowledge on how to restore the Bay and lessen impacts of coastal acidification. While more data is needed, the high cost for sensors that monitor carbonate chemistry parameters represent a major hurdle for acquiring more data (Dinauer and Mucci 2017). Since CO_2 sensors can cost $10,000 or more, a more economical method is necessary to deploy the amount of CO_2 sensors needed to simultaneously capture various Bay zones.

To better correct for the limited amount of spatial and temporal monitoring, this project was implemented to build a deployable autonomous CO_2 sensor (DACS) at a price of under $1000. The DACS design was based off a recent off deck sensor suggested by Hunt et al. (2017) with modifications made for autonomy. While organizations such as the University of Maryland Center for Environmental Sciences, the Chesapeake Bay Foundation, NOAA, and others have attempted to fill in the gaps in our knowledge by deploying a new buoy that collects real-time

CO_2 measurements (Task Force to Study the Impact of Ocean Acidification on State Waters 2015), there are still many areas in the Bay without CO_2 monitors that experience the effects of coastal acidification. Countless coastal communities within the Chesapeake Bay region, specifically Maryland counties, are exposed to acidification, making it necessary to understand these processes to assist in strategizing adaptive procedure (Ekstrom et al. 2015). Efficient spatial and temporal analysis of the Chesapeake Bay, in addition to inexpensive and dependable sensors, can improve understanding of the complexities of coastal acidification so that its negative implications can be combated in a more effective manner.

Materials and Methods

Construction of CO_2 Sensors

The DACS was constructed using Hunt et al. (2017) as a reference. There were modifications made to the original design to make the sensors deployable and autonomous. The main components needed to construct the sensors are as follows: K33 ELG 10,000ppm CO_2 + RH/T Data Logging NDIR Sensor (CO2 Meter, Ormond Beach, Florida), Brushless Pump NMP 05 S (KNF Neuberger, Trenton, New Jersey), Lithium Iron Phosphate 12V 14AH Battery for Katana GSX-R 750 1100 (ACE Comp Solutions, Edison, New Jersey), DROK L298 Dual H Bridge Motor Driver DC 6.5V-27V 7A Motor Control Board (Drok, Hong Kong, China), 4.7 K Resistors, and an Arduino Due (Arduino). Figure 2 shows a full schematic of all the electrical components.

Once the DACS electrical components are constructed, they are packaged in a junction box and then placed on top of a PVC base. The main components that were used for packaging the sensors are PVC pipes, pool noodles, scotch Velcro, O-Rings, and an 8'' x 8'' x 4'' Waterproof Junction (Lowes). It was decided to give the DACS autonomy so continuous carbonate chemistry data from various regions throughout the Choptank River could be collected simultaneously. The battery powers all the electrical components and the DACS uses an Arduino to elongate the life of the battery and overall product by toggling power between the K33 CO_2 sensor, pressure sensor, and brushless pump (Figure 3). The final cost of the DACS is approximately $835.

The DACS works as an Arduino code is set to the Arduino mega, which then controls when the air pump turns on and off, as well as when K33 CO_2 sensor and pressure sensor take measurements. The Arduino code allows for DACS frequencies to be changed dependent on the tests being run. First, the Arduino activates the air pump. It runs for a given cycle and circulates air that is at equilibrium with the seawater (Figure 4). When the air pump finishes running for the set frequency, the K33 CO_2 sensor takes a CO_2 measurement, and then the pressure sensor records the pressure of the junction box at the time of the measurement. This process repeats itself throughout the testing time.

Calibration and Sampling Frequency

To ensure the accuracy of the sensors, they were first calibrated with nitrogen and carbon gases to 0 ppm and 400 ppm. During the calibration process, a software called GasLab (CO2 Meter, Ormond, Florida) was used to control the K33 CO_2 sensor. GasLab is the software that comes with the K33 CO_2 sensor and is used to download data, set timing, read live time data, and calibrate the K33 CO_2 sensor and other sensors made by the CO_2 meter. While the K33 CO_2 sensor was attached to the GasLab software (CO2 Meter, Ormond, Florida), it was placed in a New Brunswick Excella E24 Incubator Shaker Series at 26.7 degrees Celsius to model the outdoor temperature in which the DACS monitors. The K33 CO_2 sensor was then placed in a

bag with nitrogen gas (0ppm) flowing inside so the sensor could be calibrated to 0pmm using GasLab. The same procedures were then repeated at with the sensor in 400ppm and then it was again calibrated through the program.

Throughout analysis in and outside of the laboratory, the sampling frequencies varied from monitoring continuously to once every hour. With the use of an Arduino code, the pump and CO_2 and pressure sampling frequencies were set to the desired monitoring frequency at the time of every test.

Deployment

Before the deployment of the DACS, the sensor was calibrated to ensure the most accurate results. After calibration, the Arduino code was set with the frequencies that read CO_2 continuously so that DACS accuracy measuring CO_2 and battery capacity were best understood. Once the components were in the junction and the K33 CO_2 sensor had its time set, the junction box was fully sealed to ensure it was air- and watertight. Securely sealing the junction box was imperative for the study to ensure the DACS read the CO_2 at equilibrium with the seawater instead of the atmospheric CO_2. When the junction box was secured, it was placed with the stem attached (Figure 3) on top of the PVC base, making the DACS ready for deployment. The stem was the access area for air circulation throughout the junction box, making it imperative to have attached before deployment.

For the lab experiments that examined design features (pumps, stem lengths, etc.), the DACS was deployed in an iterative fashion that allowed us to optimize the design and component configuration. The pump of the DACS was interchanged between a brushed and brushless pump to achieve the best equilibration time. A food coloring test was also conducted with the DACS to determine water exchange in the stem. The DACS was set in a 200 ml tank with seawater from the Choptank River and set to run. Food dye was then placed in the water to verify the flow created by the air pump. Once the DACS had shown the expected flow and equilibration, it underwent testing that compared its data from the Horn Point Laboratory (HPL) Oyster Hatchery to laboratory-data-calculated CO_2 results. The laboratory results were calculated using an online software called CO2Sys. CO2Sys requires salinity, temperature, total alkalinity and dissolved inorganic carbon measurements to calculate pCO_2. Other laboratory analysis consists of the same deployment procedures and then placing them into various testing areas.

Field studies of CO_2 were completed in the Choptank River, specifically in the Horne Bay tributary adjacent to the HLP. The Choptank River is 114.263 km in length and 2,600 km^2 in overall area (Task Force to Study the Impact of Ocean Acidification on State Waters 2015). The tributary that it feeds into is approximately half a kilometer in length. The entire region tends to have a salinity range from 8.59 to 9.77, a temperature range of 18.49 to 26.94 °C, and a dissolved oxygen range of 6.99 mg/L to 4.40 mg/L during the summer months (Task Force to Study the Impact of Ocean Acidification on State Waters 2015). Once the DACS was set for deployment, it monitored various areas of the Choptank River, including once at a pier and another instance further into the tributary.

Total Alkalinity and Dissolved Inorganic Carbon Analysis

Alongside the measurements from the DACS sensors, water samples were taken at various times throughout laboratory monitoring to measure the dissolved inorganic carbon (DIC) and total alkalinity (TA). The DIC and TA measurements are used to verify the DACS and constrain

the carbonate chemistry. Laboratory monitoring for this study took place in a tank in the HPL oyster hatchery, using water that flowed in from the Choptank River. The water samples were taken at various intervals through testing periods and mixed with mercuric acid to kill any microorganisms and reduce their impact on the carbonate chemistry of the sample (i.e. respiration). After testing was completed, the samples were analyzed with a model AS-ALK2 Total Alkalinity Titrator and Model AS-C3 Dissolved Inorganic Carbon Analyzer to gather the TA and DIC measurements, respectively.

Data Analysis

After the laboratory data was retrieved, it was then analyzed so an understanding of the carbonate chemistry throughout the various areas of the river and lake was identified. CO2Sys was used to interpret the TA and DIC measurements that were taken throughout lab and field analysis. Visual plots were then used with the collected DACS data to demonstrate the carbon fluxes and general interactions of the carbonate system throughout the test. Once collected, the DIC, TA, and DACS data was compared with the use of regression analysis. Pressure data was collected and analyzed to check for drastic increases in environmental pressure which would affect the reading of the K33 CO_2 sensor.

Equilibration Tests

Throughout the construction of the DACS, various designs were tested to ensure the final product was the most accurate and best optimized. A component that constantly changed throughout the DACS design was the air pump. Throughout the designing process a Brushless Pump NMP 05 was repeatedly interchanged with a Brushed Pump NMP 850 to test equilibration time. Other variables were compared during this process, such as stem size and the use of an air stone. The stem size was changed from a ¾ in stem to a 1 in stem to see which allowed for more flow. The use of an air stone was also tested to see if the presence increased circulation or had no effect. It was seen throughout designs that there must be approximately twenty minutes of continuous pumping for the junction box to achieve equilibrium. When looking at Figure 5, each sampling time indicates a sixty second interval and when a curve asymptotes, it has reached equilibrium. Therefore, when looking at the most recent design, the DACS takes twenty minutes to equilibrate.

Results

DACS Final Design

After comparing six different designs, the equilibration time decreased over time (Figure 5). It was expected for our final design to have the least amount of equilibration time, which is seen in our most recent design (Figure 5, line 6). The decreased equilibration time informed our design, leading us to modify it from a ¾ in stem and brushless pump with no air stone to a 1 in stem and brushed pump without an air stone. These modifications were one of many preliminary tests that lead to a DACS configuration that produced the most reliable and accurate results to date.

Comparison of Laboratory and DACS CO_2 Preliminary Results

When comparing the CO_2 data from the laboratory and the DACS, a one-to-one relationship would be expected if the DACS measurements were perfectly accurate. However, when comparing the CO_2 readings of the DACS and laboratory analysis on the water from the Choptank that enters the HPL oyster hatchery, there is not a one-to-one relationship in

measurements, although their readings were similar (Figure 5). When comparing DACS results over the laboratory results, the DACS readings did not fall out of the linear line of laboratory results and both slopes varied from each other (Figure 6). The R^2 value of the DACS results was 0.6732, indicating that there was a weak relationship, whereas the laboratory results R^2 was 1, indicating a very strong relationship. The slope values for the laboratory results was 1 and for DACS it was 0.4297.

Field Tests

The DACS was tested for twenty-four hours in the Choptank River. The field deployments have been conducted in moments of rain or sun, proving the DACS capability of monitoring in outdoor environments. When analyzing the data that the DACS recorded in the Choptank, they followed what was expected for a sunny day with clear skies (Figure 8). It was seen that during the day CO_2 was at its lowest due to the activity of phytoplankton. As phytoplankton goes through photosynthesis, more CO_2 was taken up by algae, which was responsible for the lower levels of CO_2 during the day or times of higher light intensity. A tidal drift was then seen, which was followed by an increase in CO_2 at night when there was not as much respiration from bacteria due to limited sunlight (Figure 8). The levels of CO_2 then decrease again during the middle of the following day (Figure 8).

Discussion

Assessments of the DACS thus far have provided the foundation to gather more spatial and temporal monitoring, to better understand the carbonate chemistry in estuarine ecosystems at a price which is less than a tenth of the high-quality commercial CO_2 sensors currently available (Hunt et al. 2017). Such a low-cost CO_2 sensor would be groundbreaking, as it would give the opportunity to understand local and regional estuaries' vulnerability to acidification. However, the results collected at this time in the process show that there are further ongoing laboratory and field assessments that the DACS must undergo before commercialization or releasing plans to the public. While the DACS can read CO_2 in the field and in the laboratory, greater optimization and validation of the DACS' data must be completed.

The equilibration rates of the DACS thus far suggest that a twenty-minute time span is needed for the junction box to achieve equilibrium due to the asymptote of the most recent design. Knowing this, further assessments can be used to further optimize the product. For example, to improve battery and component life, instead of running at a continuous pumping and sampling rate, the DACS can pump air for twenty minutes continuously before sampling CO_2 and pressure, after which it turns off for forty minutes before repeating the cycle. If the DACS were to run the twenty-minutes on, forty-minutes off cycle, the sample would be taken every hour, which will save power and take samples in a way that corresponds with what was identified through the rates of equilibration. Further tests, with optimization, should not be limited to the alterations of sampling frequencies. Instead, it is a hope for the DACS to run for a week or ten-day time span before being collected out of its sampling site. To further optimize the DACS, it is expected in the future to have solar power cells attached to the battery that can be recharged while sampling. The proposed feature combined with controlled sampling frequencies would optimize the DACS and allow it to conserve power while in use.

The results from the DACS and laboratory assessments show that the water from the Choptank River that is being filtered into the HPL oyster hatchery was high in CO_2. From an oyster production perspective, high concentrations of CO_2 can harm their business due to potential consequences such as acidification, which threatens the growth of oysters. Understanding the

CO_2 concentrations in marine ecosystems is necessary to best prepare for the rehabilitation of marine ecosystems and to prepare adaptations for stakeholders who are dependent on such resources to combat acidification. In future assessments of the DACS in comparing its results to laboratory calculated results, different iterations of the DACS design should be tested alongside other variables that affect pCO_2 concentrations.

As of now, differences in the accuracy of DACS and laboratory results were approximately fifty percent in each sampling site, whereas other commercial high-quality sensors range from one to five percent inaccuracy (Hunt et al. 2017). Understanding factors such as light exposure, pressure, and temperature will provide insight into why the DACS data disagrees with the laboratory results. The addition of the pressure sensor to the DACS was to potentially correct for increased pressure within the junction box that may have influenced the CO_2 reading of the K33 sensor, however, the pressure was not an interfering factor at the time. Therefore, further tests comparing the DACS results with lab results should be conducted until there is less inaccuracy and the relationships are closer to the expected outcome.

Furthermore, collecting a variety of carbonate chemistry parameters with the assessments of the DACS results compared with the laboratory results will give insight into the expected CO_2 levels and if the DACS is accurately reading what is present. Comparing other carbonate chemistry parameters such as dissolved oxygen would provide more evidence to the true CO_2 levels at the sampling site, which is necessary for correcting the DACS in the way it must be done. Despite current inaccuracy, the DACS can record reasonably accurate data, which was observed throughout our studies. It was seen through previous analysis that the carbonate chemistry trends recorded by the DACS follow typical diurnal cycles. Through more tests that further verify and optimize the DACS, the product can reliably provide greater spatial and temporal CO_2 data in estuarine environments.

Ultimately, verification of low-cost methods of CO_2 collection at higher frequencies than done in the past will allow for greater understanding of carbonate system complexities in estuaries. Studies have previously shown that estuaries have additional anthropogenic factors that affect the water chemistry such as ranges in salinity, temperature, sunlight exposure, and other physical aspects (Drake 1992). These complexities are not fully understood because of the inability to deploy large amounts of sensors at once to collect variance in data. A low-cost data collection approach allows for greater opportunities in future research and understands the carbonate system in estuaries and marine ecosystems across the world. In addition to ecological knowledge, such data is needed to identify to what extent coastal and estuarine communities that are reliant on natural resources (e.g. crabs, oysters, etc.) are vulnerable to the effects of coastal acidification. In recent studies, Dorchester County was found to be highly susceptible to the effects of coastal acidification due to increased run off and other anthropogenic factors, making it imperative that there be spatial analyses conducted so that policy might effectively combat the negative implications of coast acidification (Ekstrom et al. 2015). Better understanding benefits local communities as well as those nationwide who are dependent on the productivity of estuaries.

Conclusion

While the DACS is not a fully complete product, this was the start for providing an economical way to monitor CO_2 in complex ecosystems that we have limited information on. While the data that resulted from the few experiments did not have a relationship when compared, they are indicative of a promising future for DACS development and the possibility to further optimize and verify. The data also revealed that water from the Choptank River is in fact high in CO_2

concentrations, which can affect the stakeholders who depend on the natural resources of the river. The potential for oyster hatcheries, fishermen, and other individuals to be further affected by ocean acidification stresses the importance of solidifying the design of the DACS and getting it out onto the market. In recent literature by Kelly and Hoffman (2013) they've stated, "Detailed information on natural temporal and spatial variation in [pCO_2], and tests of local adaptation to [pCO_2] conditions will be critical priorities for future [ocean acidification] research." This call to action must be answered and furthering the DACS' accuracy would be one step in understanding ocean acidification so that society can mitigate its potential impacts.

Acknowledgments

First, I would like to thank Dr. Matthew Gray for his mentorship and guidance throughout the summer on the REU project. I would like to thank Maryland Sea Grant for providing the opportunity to conduct research with the University of Maryland Center for Environmental Science at Horn Point Laboratory. Additionally, I would also like to acknowledge Rainier Hood for his engineering expertise and designing the electrical components along with the code. This study was supported by NSF grant OCE-1756244.

References

Brady, D. C., Depinto, J., Chapra, S., Friedrichs, M. A., Gray, M. W., Jordan, T., & Xia, M. 2018. Scientific and Technical Advisory Committee Panel Report: Chesapeake Bay Water Quality and Sediment Transport Model 2017 Review. Edgewater, MD: STAC Publication Number 18-00.

Dinauer, A., & Mucci, A. 2017. Spatial variability in surface-water pCO2 and gas exchange in the world's largest semi-enclosed estuarine system: St. Lawrence Estuary (Canada). Biogeosciences, 3221–3237.

Drake, B. G. 1992. A Field Study of the Effects of Elevated C02 on Ecosystem Processes in a Chesapeake Bay Wetland. Australian Journal of Botany, 579–595.

Ekstrom, J., Suatoni, L., Cooley, S., Pendleton, L., Waldbusser, G., Cinner, J., . . . Portela, R. 2015. Vulnerability and adaptation of US shellfisheries to ocean acidification. Nature, 207–214.

Hönisch, B., Ridgwell, A., Schmidt, D., Thomas, E., Gibbs, S., Sluijs, A., . . . Ziveri, P. 2012. The Geological Record of Ocean Acidification. Science, 1053–1068.

Hunt, C., Snyder, L., Salisbury, J., Vandemark, D., & McDowell, W. 2017. SIPCO2: A simple, inexpensive surface water pCO2 sensor. Limnology and oceanography: methods, 1–12.

Kelly, M. W., & Hoffman, G. E. 2013. Adaptation and the physiology of ocean acidificaiton. Functional Ecology, 980–990.

National Marine Fisheries Service. 2017. Fisheries of the United States 2016. Silver Spring: NOAA Current Fishery Statistics.

Orr, J., Fabry, V., Aumont, O., Bopp, L., Doney, S., Feely, R., . . . Rodgers, K. 2005. Anthropogenic ocean acidification over the twenty-first century and its impact on calcifying organisms. Nature, 681–686.

Scavia, D., Field, J., Boesch, D., Buddemeier, R., Burkett, V., Cayan, D., . . . Titus, J. 2002. Climate Change Impacts on U.S. Coastal and Marine Ecosystems. Estuaries Vol. 25, No. 2.

Task Force to Study the Impact of Ocean Acidification on State Waters. 2015. Task Force to Study the Impact of Ocean Acidification on State Waters Report to the Governor and the Maryland General Assembly. Maryland General Assembly.

Figures and Tables

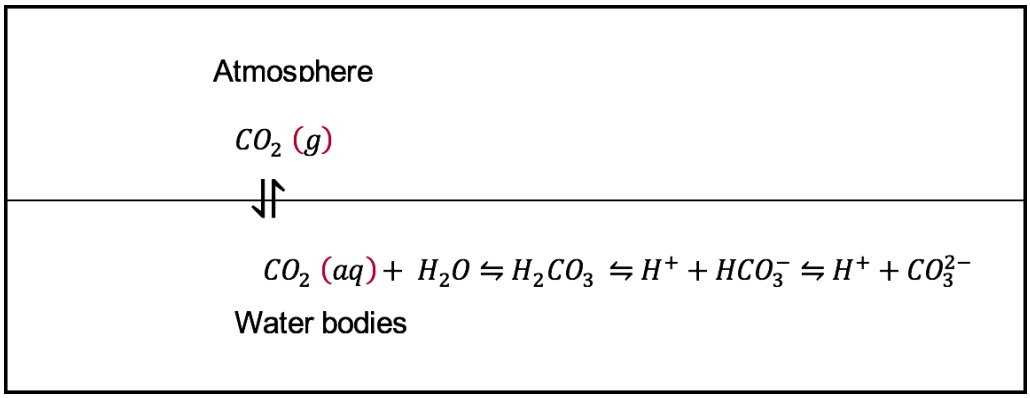

Figure 1. The carbonate system, showing the exchange between atmospheric CO_2 and aqueous CO_2 in the ocean being at equilibrium. It then shows dissolved CO_2 interactions in water, which includes bicarbonate and carbonate ion.

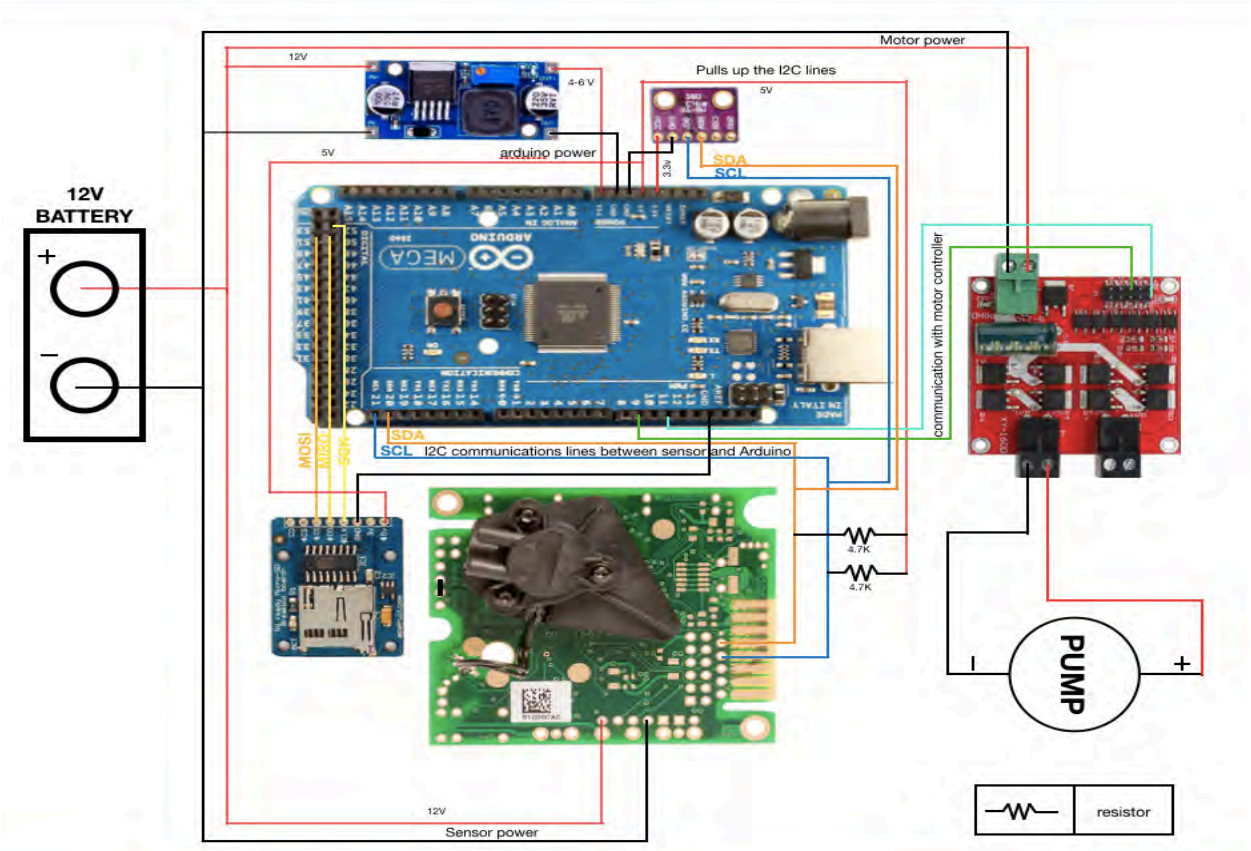

Figure 2. The interior schematics of the DACS, showing how to connect all components together.

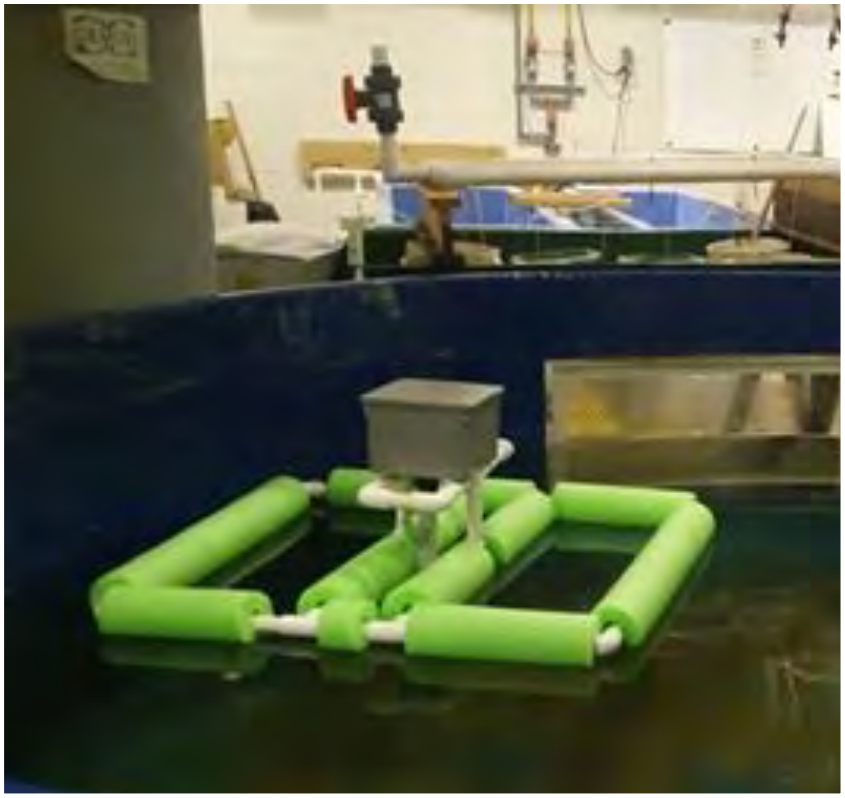

Figure 3. The DACS interior and exterior components fully together. The electrical components sit in the air-tight junction box that sits upon a PVC piping base. That base then sits upon a PVC-noodle base, which allows for it to float. Then stem in a one-inch PVC pipe with holes at the end to assist with water circulation throughout the stem.

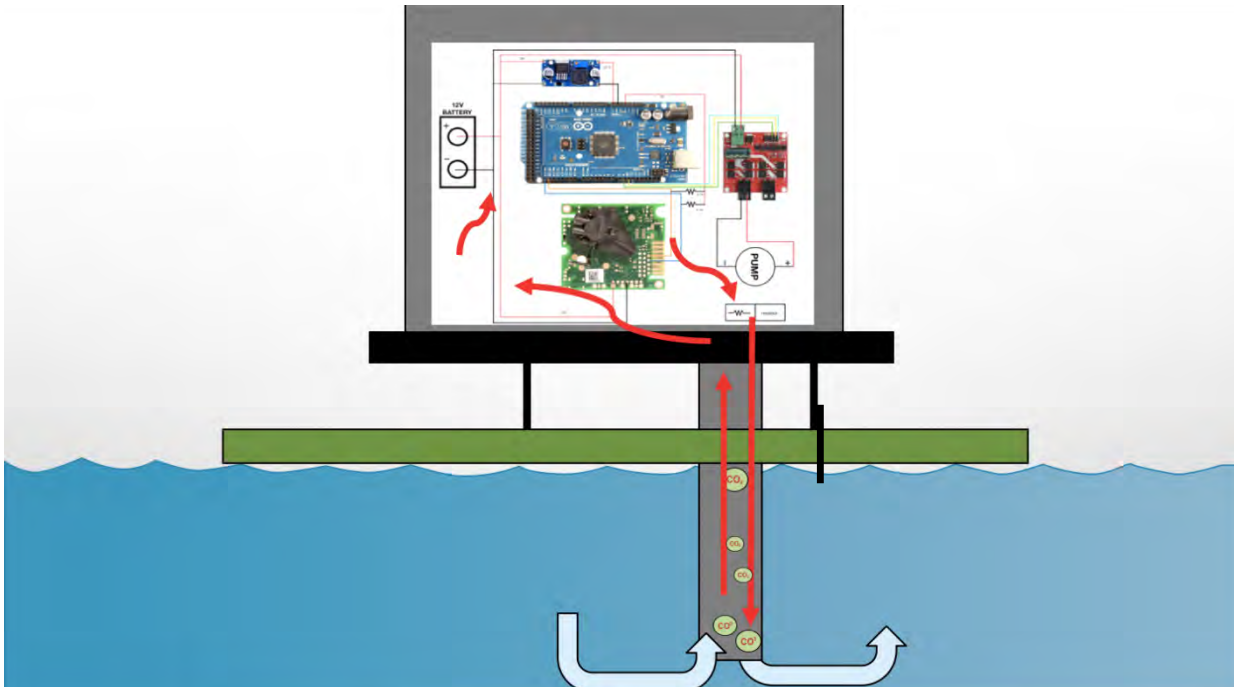

Figure 4. The red arrows show the flow of air throughout the stem and junction box, initiated by the air pump. The air pump is also responsible for driving seawater throughout the stem.

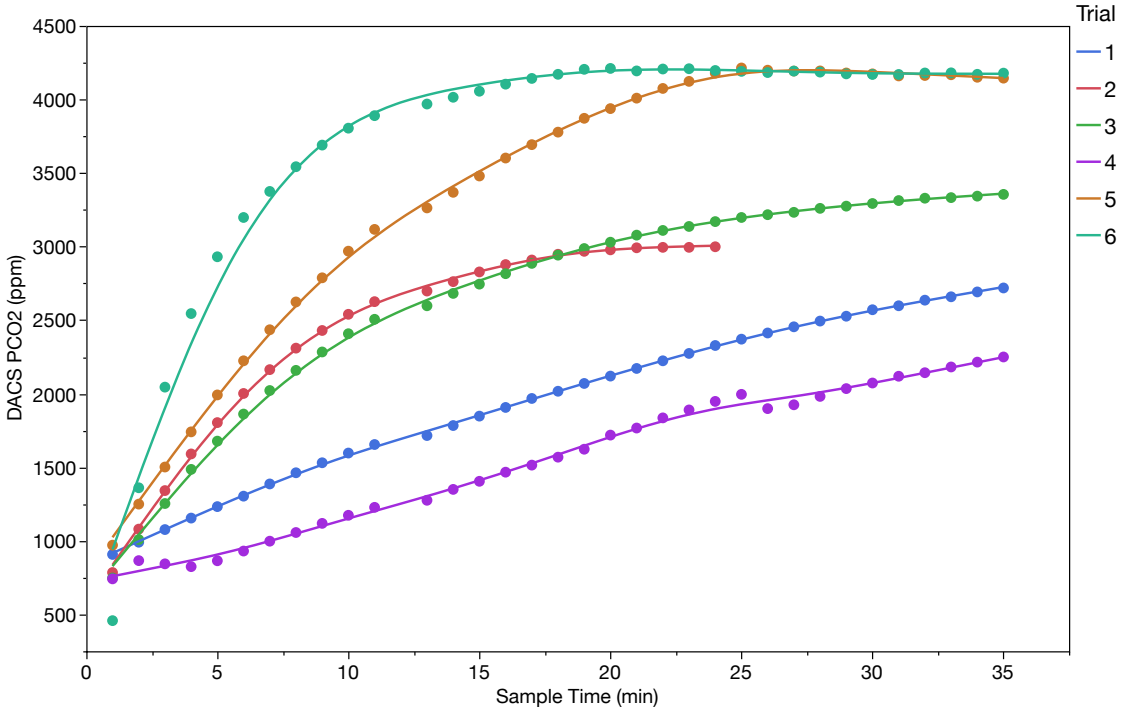

Figure 5. This graph shows pCO_2 over time from different iterations of our design with Trial One being the oldest and Trial Six the most recent. Asymptotes indicate the DACS reaching equilibrium. Trial One is our oldest design with the longest equilibration time. Line Six is our most recent design, with the design phases increasing with numerical value.

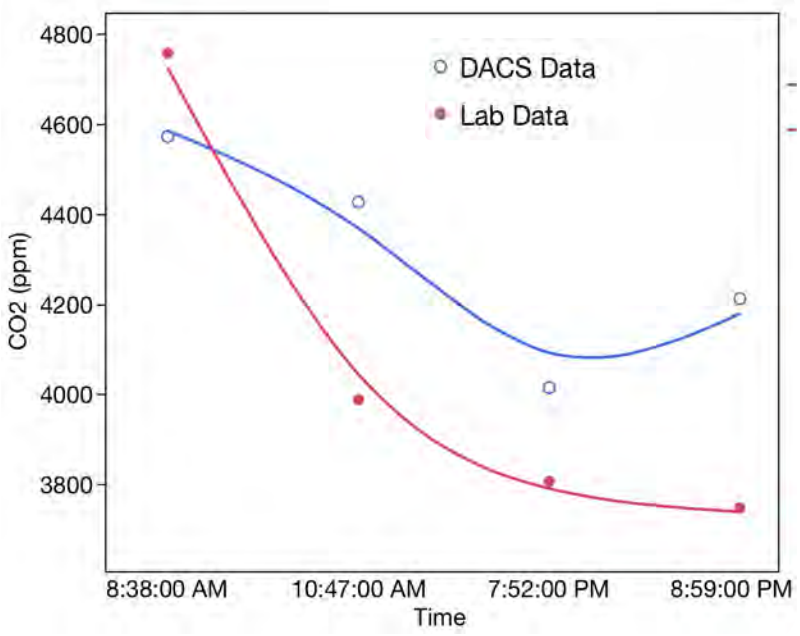

Figure 6. The graph shows CO_2 over time comparing DACS and Lab CO_2 results from water that flows into the HPL oyster hatchery from the Choptank River.

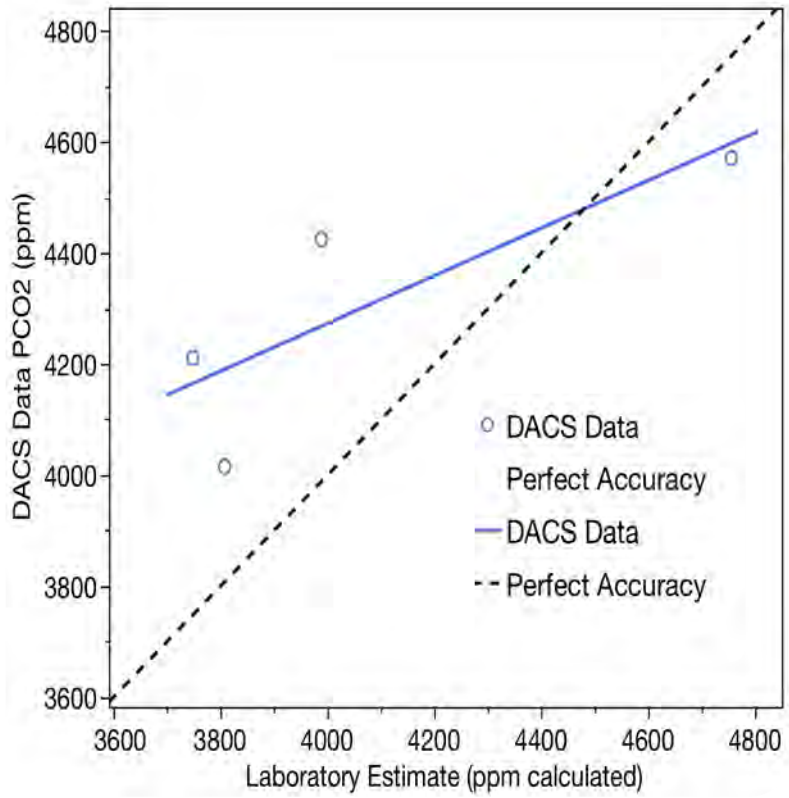

Figure 7. The graph shows DACS CO_2 over Lab CO_2 results from water that flows into the HPL oyster hatchery from the Choptank River.

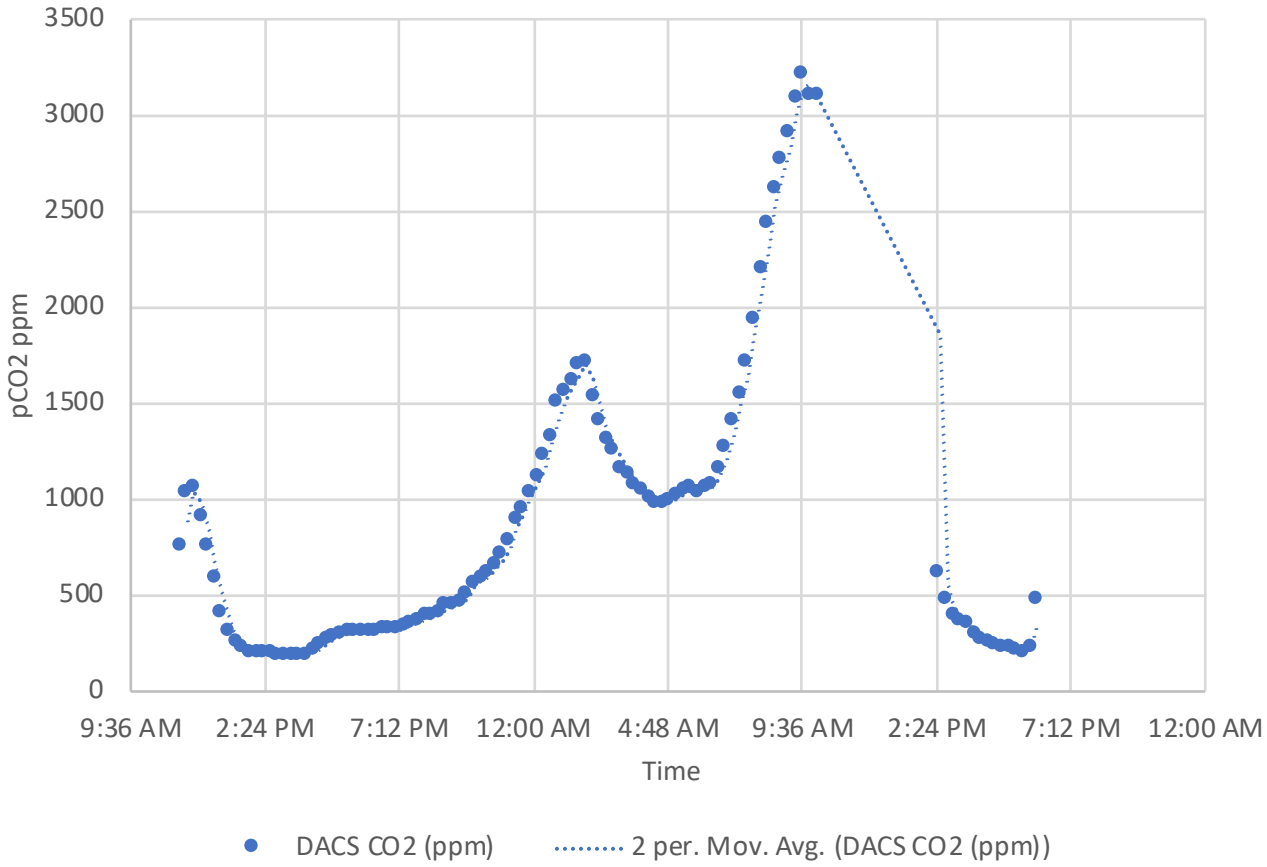

Figure 8. The graph shows pCO_2 over time from DACS measurements in the Choptank River. From around 10:00am to 2:15pm the DACS was taken out of the water, which is reason for the visual gap seen.